

Magnetism of Iron Nanoparticles in Rare Earth Matrices

Thesis submitted for the degree of
Doctor of Philosophy
at the University of Leicester

by

Gail N. Iles BSc (Open)

Department of Physics and Astronomy
University of Leicester

August 2007

Magnetism of Iron Nanoparticles in Rare Earth Matrices

Gail N. Iles

Abstract

This thesis details three main studies. The first is an investigation of the effect of coating Fe nanoparticles in a gas to isolate the magnetic moments. An isolation or enhancement of the already increased magnetic moment of a Fe nanoparticle would have the potential for exploitation in high-moment materials. The two other investigations are of the behaviour of Fe nanoparticles in the rare earth matrices Ho and Dy. Transition metals and rare earth metals normally couple antiferromagnetically at their interface, however the intention of this work was to determine if this also happens when the Fe is incorporated as pre-formed clusters. The motivation for this is that if the interactions between the rare earth and the transition metal is switched to be ferromagnetic then the Curie temperature of the rare earth could be increased without a large decrease in its saturation magnetisation.

Fe nanoparticles consisting of ~200 atoms and ~2nm in diameter were manufactured using a gas aggregation source then coated with $H_2(g)$. VSM, XMCD and TEM measurements were taken of these samples and the magnetic moment per atom of Fe was found to drop significantly compared to that of isolated clusters in Ag matrices. A comparative study using $N_2(g)$ was conducted yielding similar results. This is attributed to the gas permeating the whole cluster rather than forming a shell.

Addition of atomic Fe to a rare earth matrix decreases the total magnetisation due to antiferromagnetic coupling. Fe nanoparticles deposited into rare earth matrices heavily quench the rare earth moment. Samples of 2-35% Fe by volume contain Fe nanoparticles large enough to disrupt the rare earth spin wave. The Fe nanoparticles couple ferrimagnetically to the rare earth producing the low overall magnetic moment. Several magnetic phase transitions were observed in all Fe/rare earth alloys. Structural measurements using EXAFS indicate that the Fe clusters may have changed to an expanded lattice within the Dy matrix.

Acknowledgments

This thesis is dedicated to my grandfather, Dr Edward James Iles, who devoted many hours of his time enthralling me with talk of his scientific experiments. He instilled in me the belief that we are *never* too old to learn.

My heartfelt thanks go to Professor Chris Binns for supervising me throughout this project, to Dr Steve Gurman for being the internal examiner of this thesis, to Dr Stephen Baker for guidance in experimental practice and to Mr Stuart Thornton for his expert engineering. Special thanks to Sharon Louch, Mark Sturgess, Merv Roy and Mark Everard for much help and advice during my studies. Thanks to all other CMP members past and present for the total lack of decaf coffee and copious amounts of beer. Thanks to all Daresbury staff and scientists who helped me with my synchrotron studies. Thank you to Rebecca Smith for help with VB code and to Peter Cossins for proof-reading this thesis.

Thank you to the unsung heroes; technicians - Pete Glew, Nick Dorsey, Ray Macerlean and both Toms; admin bods - Lucy, Pam, Ranjna and Stuart; Dean the Potty Porter; stores blokes – Phil and Nigel and the workshop guys - Steve and Andy for all your help at fixing stuff and organising me.

I am exceedingly grateful to the University of Leicester and EPSRC for supporting me financially and to TDK, Japan for their partial funding of this project.

Thanks to the people who got me here in the first place namely, Peter Huggard (RAL), Ray Macintosh (OU) and Chris Nicklin.

Love, hugs and best wishes to the Lab Ladies (Becks, Rhian & Cat), all the Cheerleaders / Pirates / Apes / Witches / Charlie's Angels / Superheroes / Emergency Workers / Spaaaartans , the So Quantum Crew (Matt, Rob, Sally & Ian), the International Consortium (Antonios, Chen, Dave, Emma, Franci, The Goat, Halim, Isidre, Magda, Mikal, Nick, Rafal, Ricky, Seve, Ugur, Yan & Yueheng), Team Alpha (Get Awesome

Coach, Balls of Steel, Lucy Lightening, Ninja Pixie, Doc, Swedish Chef & Driver Dan), Team Omega, The White Knight and my family (Mum, Dad, Ali, PJ, Coz, Tin, Krorgs, Teeds, Unly, Gran Iles and Grandad Anderson).

A big shout out to Leicester U/G's (Sophie, Chris, Andy M, Tom, Ed, Matt, Charley, Jamie, Jo, Dave & Lucy), Leicester P/G's (Craig & Dan) Leicester post-docs (Das & Kim), surrogate cave-dwelling colleagues (Jal, Lee, Paddy & Alex), fellow footballers (Ken, Graham, John, Gordon, Andy, Yohann, Mike & Johnny), Langar DZ (Harry, Milko, Rich & Can-Can), my French teacher, Yvan Tardy; my Russian teacher, Alexandra; LAC; Big Band; all my i-Science students; Tania Burchell; Carlyne Cotton; Ed & Gloria; John Nimmo; 48 Signal Sqn - Rodders, Lenny, Mags, Nav & Wendy; my wonderful tutees who taught me so much – Fergus, Ross & Annie, Ali & Lauren, Grace & Mel, Matty & Hannah, Emma & Becka, Kerry & Kelly, Charlie and Richard; school chums of yesteryear – Sal, Hugs, Tris, Penny, Hayley, Jude, the Kennerleys and Dan H; random physicists - Ben Carpenter and Hand Zenia. Thank you to Papillon.

Thanks to Madonna, Martin Luther King, Ellen Macarthur, Ghandi, Helen Sharman, Nelson Mandela, Kelly Holmes, New Order, Jo Rowling, the Dalai Lama and Princess Diana for inspiration.

Special mention to the charities FAAB, MATCH, NSPCC, Samaritans and ChildLine for all the fabulous work you do.

To the love of my life, Daisy – thanks for always being there. You make the loneliest nights resonate with the sound of your purring. To my noble steed, Tallula – thanks for getting me to where I need to be. You may have a chip in your windscreen and an oil leak but you'll always be perfect to me.

Finally, to my two gorgeous sons, James and Charlie, "The higher they build their barriers - the taller we become."

Contents

Abstract	i
Acknowledgments	ii
Contents	iv

Chapter 1

Introduction	1
--------------	-------	---

Chapter 2: Magnetism

2.1 Atomic Magnetism	8
2.2 Nanoscale Magnetism	12
2.3 Bulk Magnetism	19

Chapter 3: Experimental Procedure

3.1 Sample Preparation	29
3.2 Measurement Techniques	40
3.3 Preliminary Investigations	46

Chapter 4: Gas-coated Fe

4.1 Gas-coating models	59
4.2 VSM Data	60
4.3 XMCD Data	65
4.4 TEM Imaging	74
4.5 Summary	75

Chapter 5: Ho Studies

5.1 Ho MBE	80
5.2 Fe clusters in Ho	86
5.3 H ₂ (g) coated Fe in Ho	97
5.4 Summary	99

Chapter 6: Dy Studies

6.1	Polycrystalline Dy	103
6.2	Fe/Dy alloys	108
6.3	Structure	118
6.4	Summary	121

Chapter 7

Conclusion	123
------------	-------	-----

Appendix A: Periodic Table of Elements	125
Appendix B: Ground State Electron Configurations	126
Appendix C: Sample Details	127
Publications	129
References	130

“Whatever you do, or dream you
can, begin it.

Boldness has genius and power and
magic in it”

Johann Wolfgang von Goethe

(1749-1832)

Chapter 1

Introduction

Iron has intrigued the peoples of the world for thousands of years. Revered as one of the two most magically charged items, since Neanderthal times there has been much mystique and fascination associated with this element and its hidden power – magnetism.

Magnetism is a highly complex phenomenon which is condition- and element- specific. Most atoms are magnetic due to the movement of electric charges, however atoms do not exist on their own and once a bulk material is formed most elements lose this atomic magnetism. There are only three bulk metals that are naturally magnetic, that is there is a permanent magnetic moment at each atomic site, at room temperature. When neighbouring atomic moments are aligned this property is termed ferromagnetism (FM) of which the transition metal (TM), iron (Fe), is an example. In non-uniform applied fields a FM material is drawn into the field. FM materials contain microscopic regions in which millions of dipoles are aligned. These regions, which are called magnetic domains, can align with an external field. When the external field is removed, if the domains do not relax back to the zero magnetic state, the magnetism remains. It is this property that makes recording onto audio tape or magnetic disk storage in computers possible. Applying a field to the tape or disk magnetises a small portion of the material which remains magnetised until another magnetic field changes it.

Other types of magnetism have been identified pertaining to different behaviours in applied magnetic fields. Antiferromagnetic (AFM) materials have adjacent dipole moments that are equal in size but reversed in direction; AFM materials in which adjacent dipoles are of unequal size are ferrimagnetic (FiM). In reality most AFM materials are FiM because the dipole moments do not cancel each other out exactly. Diamagnetic (DM)

materials are repelled by magnetic fields, but the effect is small compared to FM materials. Bi is the most DM element (Periodic Table in Appendix A); its DM susceptibility¹ is $(-1.31 \pm 0.01) \times 10^{-6}$ which is about 20 times higher than that of graphite or water.

In a paramagnetic (PM) material the dipole moments try to line up with an applied magnetic field but are prevented from becoming perfectly aligned by their random thermal motion. As long as the strong magnetic field is present, it will attract and repel other magnets in the usual way but once the external field is removed the magnetic alignment is lost as the dipoles relax back to their normal random motion. Finally, superparamagnetism² (SPM) is a phenomenon by which magnetic materials display similar behaviour to PM below a critical temperature. This critical temperature is the Curie Temperature (T_C) used to describe the onset of FM behaviour. For example, Fe is PM above 1043K but below this temperature it is FM. A material displaying PM below T_C would be indicative of superparamagnetism. SPM occurs when a material is composed of very small isolated crystallites (1-10nm or 10-100 atoms). In this case the atomic magnetic moments in the particle are locked together by the exchange interaction to form a single giant magnetic moment, which fluctuates due to thermal energy. When an external magnetic field is applied, the magnetic moment of the entire crystallite aligns with the magnetic field.

SPM is found in abundance in cluster studies due to their size and structure. The high proportion of surface atoms in clusters magnifies the importance of the surface energy and it is the competition between this and the local bonding forces that determines the clusters' morphology³.

Simple metal clusters with highly isotropic bonding are pulled into spheres with the system behaving very much like a liquid drop. Abundance spectra show magic numbers⁴ that correspond to especially stable electronic configurations within a spherical jellium model⁵. For TM the magic numbers always correspond to stable atomic geometries rather than filled electronic shells. For example, the body-centred cubic (bcc) metals, Fe, Nb and Ta show magic numbers at $n = 7, 13$ and 15 corresponding to a pentagonal pyramid (fig.

1.1a), an icosahedron (fig. 1.1b) and a double icosahedron (fig. 1.1c) respectively. In the case of metals with close-packed cubic crystal structures, the clusters tend to form truncated octahedrons (fig. 1.1d).

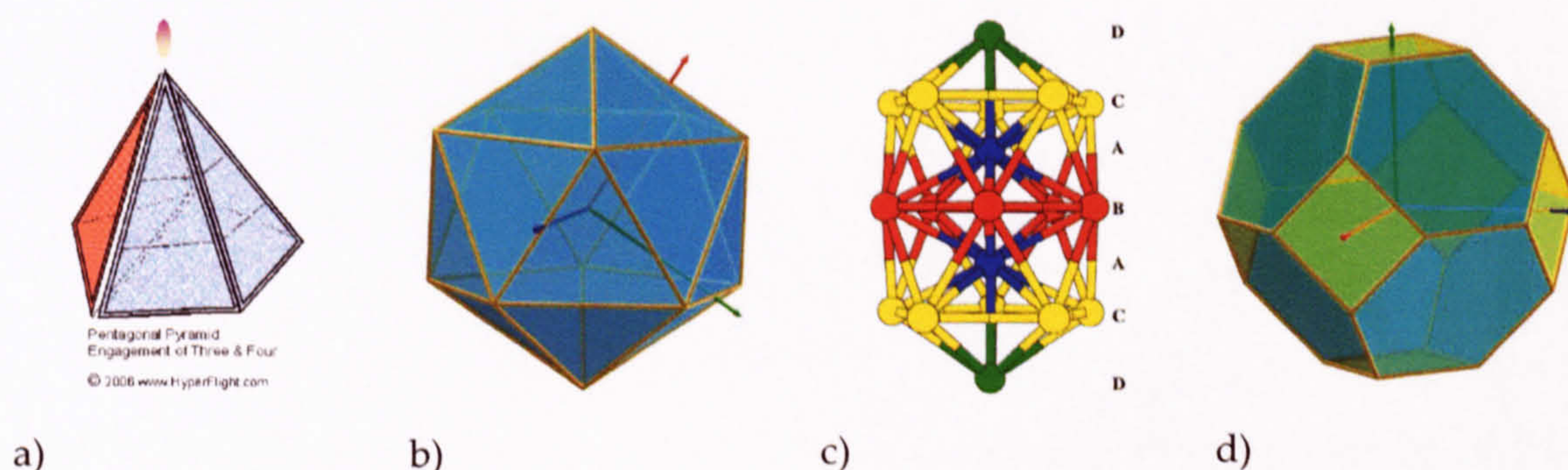


Figure 1. 1 Atomic structures. (Images b and d courtesy of www.mathcurve.com)

The atomic structure and nearest neighbour distance are critical in determining the magnetic properties of clusters. A cluster of Fe_{12} has a moment of $(5.4 \pm 0.4) \mu_B/\text{atom}$ i.e. close to the atomic limit whilst Fe_{13} has a moment of only $(2.5 \pm 0.4) \mu_B/\text{atom}$ i.e. close to that of the bulk⁶. So although the magic numbers show the abundance of particular molecules these stable configurations do not relate to the associated magnetic moment of the cluster. The enhanced magnetic moments arise from the reduced average coordination number of atoms within the cluster. The reduced co-ordination produces a narrowing of the 3d band due to a decreased overlap of atomic orbitals. Within a simple tight-binding model, the bandwidth is proportional to the number of nearest neighbours. Reducing the width of the 3d band in a transition metal will increase the spin polarization per atom since the minority spin band will empty and the proportion of the majority spin band that is full will increase. The increased proportion of atoms at the surface of a cluster will also increase the orbital moment. The quenching effect seen in the bulk requires a highly symmetrical crystal field and reducing this symmetry will decrease the quenching effect and lead to an increase in the orbital moment.

The metals with the highest atomic moments are the rare earth metals (RE) whose magnetism arises from unpaired spins within the 4f shell (Ground State Electron Configurations in Appendix B). These moments are largely shielded by the 6s electrons in the outer shell, thus in the bulk the magnetic moment localised at the atomic sites is close

to that of free atoms. Although RE can have a saturation magnetisation much higher than TM they also have low Curie temperatures. Much of the work in this thesis is devoted to trying to increase the Curie temperature of RE by embedding within them TM nanoparticles. High-moment materials are industrially important as the available write fields in digital recording systems are a limiting factor on data storage densities.

A wealth of research has been conducted on alloys of TM and RE in various forms, e.g. multilayers with varying thicknesses of TM to RE; TM matrices doped with RE atoms and vice versa. All multilayer studies report perpendicular anisotropy at the interfaces between the TM and the RE⁷. Much work has centred around compositionally modulated films (CMF); pure metal films doped with ions in a specific ratio. Patents are registered for the utilisation of CMF in magnetic tunnel junction devices⁸ as used in magnetic memory or high sensitivity sensors.

Avenues for investigation are dilute alloys, clusters of alloys and clusters within matrices. A dilute alloy could be made by the process of molecular beam epitaxy (MBE) whereby two metals are vapourised simultaneously and co-deposited onto a substrate. The deposition of each metal is controlled by the evaporation rate so the relative concentrations can be varied easily. For clusters of alloys, gas phase clusters can be formed from one metal then coated in a substance, either a gas or another metal, and lastly gas phase clusters of a TM metal can be deposited within a RE matrix formed by MBE.

For a coated cluster, if the coating were of a gas which formed a non-magnetic shell around the cluster it may be possible to deposit a high concentration of clusters without a quenching effect. Such a shell would effectively 'lock' the magnetic moment of the cluster, isolate it from the next cluster itself also in a shell and enable the high moments to remain despite being in a bulk material. Conversely, a TM cluster deposited into a RE matrix may induce FM coupling with the matrix. The RE moments adjacent to a cluster would be forced into a FM arrangement with medium range order. If the distance to the next cluster were not so great for the FM ordering to be lost the entire sample would become FM.

In a sample containing a TM and a RE the working materials of choice would be iron and holmium as these have the highest atomic moments of the elements in their group. The RE dysprosium (Dy) is also a good choice as it has a magnetic moment of $10.2 \mu_B$ which is almost as high as Ho ($10.9 \mu_B$) but with a much higher Curie temperature (Dy: 89K, Ho: 20K). This work specifically investigates the two combinations Fe in Ho and Fe in Dy.

The structure of the thesis is as follows. Chapter 2 begins by describing the physics behind magnetism in the three main magnetic regimes of the atomic, nano and bulk scales. Chapter 3 contains a description of the experimental equipment used, how the samples were made and the results of some preliminary investigations. There then follow three main data chapters. Firstly, chapter 4 describes the results of coating clusters with hydrogen or nitrogen. Various measurements techniques are utilised namely vibrating sample magnetometry, X-ray magnetic circular dichroism and transmission electron microscopy. Secondly, chapter 5 details all studies undertaken on a number of holmium samples. The changes in magnetisation of pure Ho and Fe/Ho alloys are measured with respect to temperature in fields ranging from 0.1T up to 8T. The third data chapter on dysprosium samples is detailed in chapter 6. Magnetometry data is accompanied by structural data to obtain a clearer picture of the interactions between the iron and the rare earth on the nanoscale. Chapter 7 concludes the work highlighting other areas for investigation and making suggestions for future work.

“I think I can safely say that no-one
understands quantum mechanics.”

Richard Feynman

1918-1988

Chapter 2

Magnetism

There are three distinct magnetic environments. At the atomic scale single atoms are magnetic as a result of charged electrons which produce an overall magnetic moment with orbital and spin components. On the macroscopic scale bulk magnetism is seen in everyday life (e.g. compasses, fridge magnets) where the physics relies on the behaviour of magnetic domains. Magnetic domains are typically of the size of several microns and therefore contain millions of atoms. This thesis is concerned with nanoscale magnetism whose effects lie somewhere in between the latter two descriptions. In order for a comprehensive model of nanoscale magnetism to be plausible, both classical and quantum effects must be considered.

2.1 Atomic Magnetism

Classical models involve particulate electrons travelling in circles around a central nucleus. This orbital motion of an electric charge gives rise to a magnetic moment due essentially to a current loop. However, this is not the complete story of atomic magnetism. The Stern-Gerlach experiment showed evidence of additional intrinsic electron angular momentum dubbed 'spin'. The combination of the orbital angular momentum, L , and spin angular momentum, S , gives the total angular momentum, J , of an atom, which produces the total magnetic moment. The natural unit of the magnetic moment is the Bohr magneton, μ_B where

$$\mu_B = \frac{e\hbar}{2m} = 9.27 \times 10^{-24} \text{ JT}^{-1} \quad (2.1)$$

m = mass of electron

The values of L , S and J for the state of lowest energy in an atom are given by Hund's rules. These relate only to partially filled shells because full shells and subshells do not contribute to total L or S .

Hund's rules, in the order they must be obeyed, are:

- i) S takes the maximum value allowed by the exclusion principle – as many as possible of the electrons must have parallel spins;
- ii) L takes the maximum value consistent with this value of S ;
- iii) $J = |L - S|$ for a shell less than half-full and $J = L + S$ for a shell more than half-full.

Hund's rules i and ii, which determine the values of L and S , are associated with the Coulomb forces between electrons. The Pauli Exclusion Principle states that no two electrons in the same system can be in the same quantum state. This is a consequence of the fundamental property of electrons being identical in the sense that they are completely indistinguishable from one another. Parallel spins therefore stay further apart due to Coulomb repulsion to keep the lowest energy. The Coulomb forces are much larger than magnetic forces so the application of a magnetic field does not interfere with these. The third rule, which determines the value of J , is associated with the spin-orbit interaction. This is the interaction of the magnetic dipole moment of an electron's spin with the magnetic field associated with its orbital angular momentum. It is responsible for the fine structure in atomic spectra. The energy of the system is slightly higher when the orbital and spin magnetic moments are parallel than when they are antiparallel. The spin-orbit interaction is of the order of 10T so there is a possibility that this rule can be disrupted by an applied field of this order.

An extract from Appendix B is reproduced in figure 2.1 to show the ground state electronic configurations of the main elements used in this thesis. A term symbol (final column) is used as an abbreviated description of the angular momentum quantum numbers in a multi-electron atom. This follows the convention for labelling as follows

$$^{2S+1}L_J$$

where 2S+1 is the spin multiplicity and L is the total orbital quantum number in spectroscopic notation.

Element	No. d electrons	m _l =					L	S	J	State
		-2	-1	0	1	2				
Fe	6	↓↑	↓	↓	↓	↓	2	2	4	⁵ D ₄

Element	No. f electrons	m _l =							L	S	J	State
		-3	-2	-1	0	1	2	3				
Dy	10	↓↑	↓↑	↓↑	↓	↓	↓	↓	6	2	8	⁵ I ₈
Ho	11	↓↑	↓↑	↓↑	↓↑	↓	↓	↓	6	3/2	15/2	⁴ I _{15/2}

Figure 2. 1 Ground state electron configuration of Fe, Dy and Ho. (reproduced from Appendix B)

Quantum systems such as atoms and molecules exist in stationary states in which the total energy of the system has discrete values called the energy levels of the system. The first direct experimental evidence for the existence of energy levels was provided by the Franck-Hertz experiment which demonstrated the existence of excited states in mercury atoms. The experiment confirmed that electrons occupy only discrete, quantized energy states.

When enough atoms combine to form a solid, the separations between energy levels become correspondingly smaller and smaller as shown in fig. 2.2.

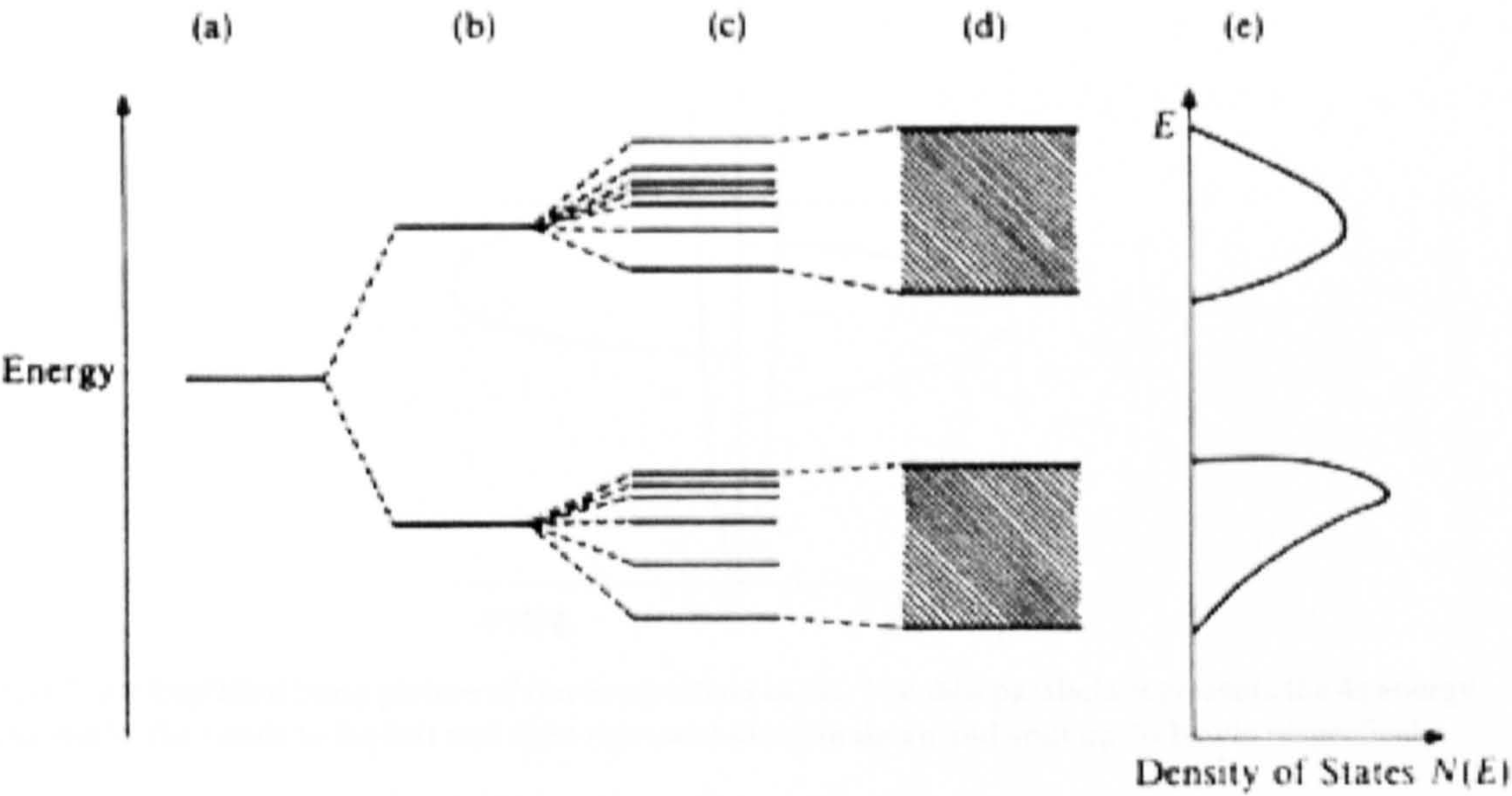


Figure 2. 2 Orbital energies of (a) atom, (b) small molecule, (c) large molecule, (d) solid, and (e) density of states corresponding to (d). (Reproduced from University of Waterloo, California)

The original bonding and antibonding orbitals of a diatomic molecule now evolve into the valence and conduction bands respectively. The energy separation between the top of the valence band and the bottom of the conduction band becomes the band gap. Solids are categorized according to the nature of this band gap: in metals there is no energy gap separating the conduction band from the valence band; insulators have a wide band gap; semiconductors have a small band gap so although they are non-metallic they are still able to conduct electricity due to thermal excitation of electrons across the band gap. All of these solid structures are ordered crystals with a variety of arrangements of atoms, these different arrangements ultimately dictating their different behaviours.

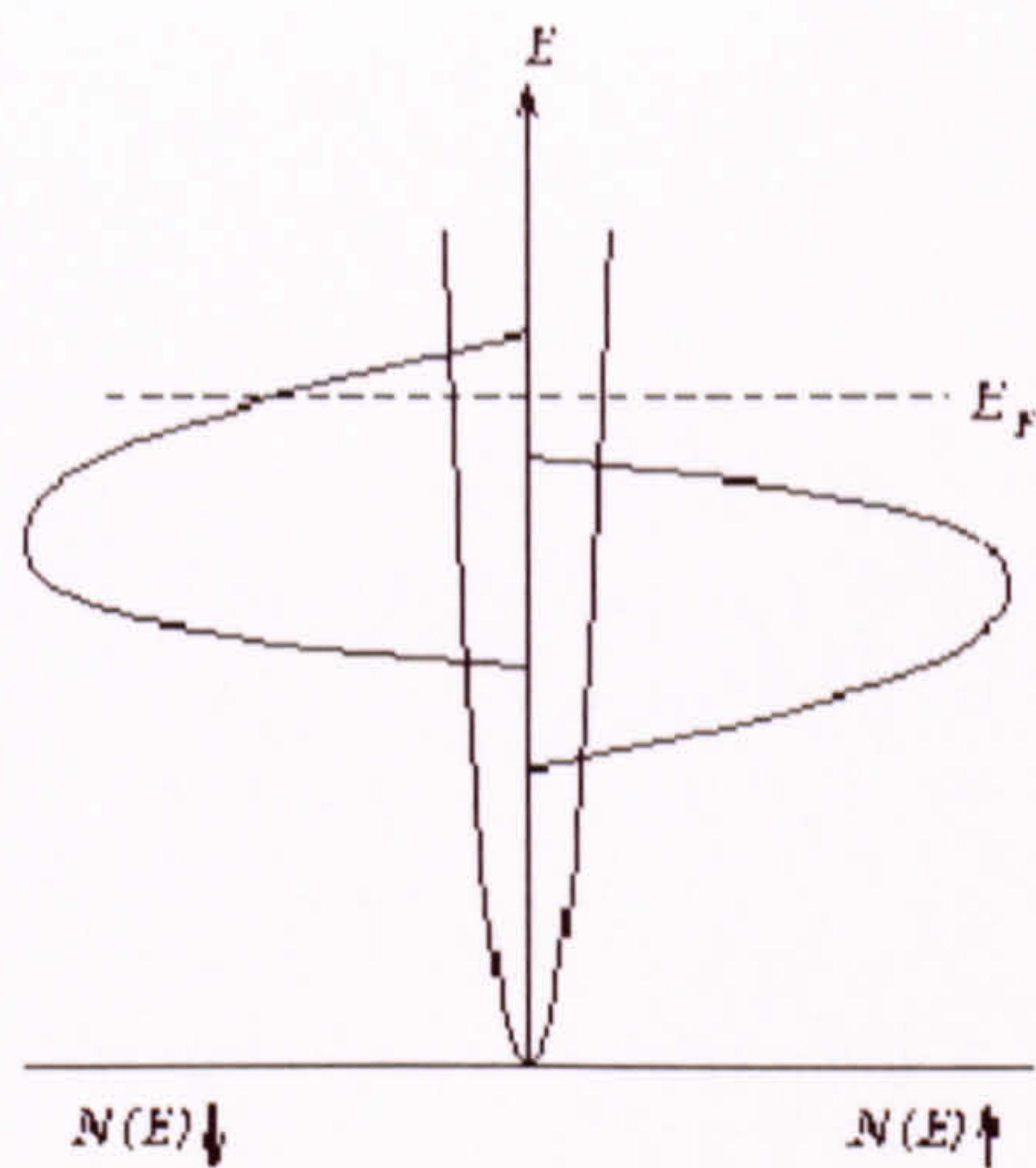


Figure 2.3 Simplified band picture of ferromagnetism in Fe. The thin parabola represents the 4s energy band whilst the bands to the left and right represent the spin down and spin up 3d bands respectively.

Band magnetism can be considered qualitatively. Fe has a partly filled d-band. This band is divided in two sub-bands which are spin-up and spin-down occupied respectively as shown in figure 2.3. These bands have different energy, i.e. one band is filled while the other is only partly filled. This is due to the exchange interaction as detailed in the next section.

2.2 Nanoscale Magnetism

For minimum energy the atoms pack themselves as closely together as possible in solids. A common structure is face-centred cubic (fcc) (fig. 2.4a) with a rhombohedral primitive unit cell. Many of the transition metals have the fcc structure. Another cubic structure less close-packed than fcc is body-centred cubic (bcc) (fig. 2.4b) and the third most common stacking sequence gives a hexagonal close-packed (hcp) structure (fig. 2.4c). This has alternate layers in successive planes in the c-direction.

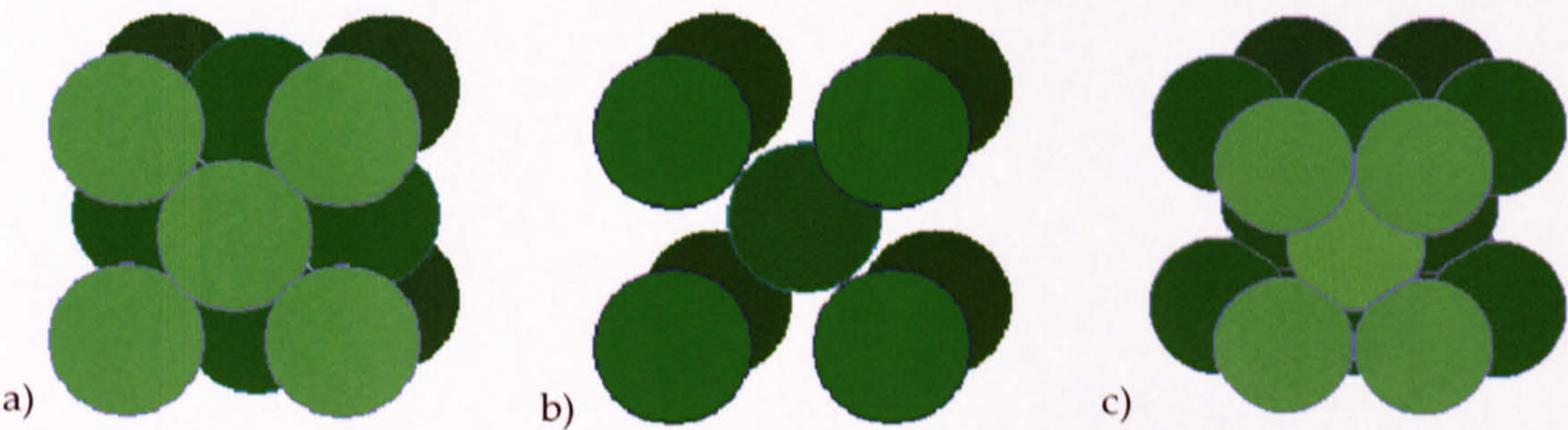


Figure 2.4 Crystal structures a) fcc b) bcc c) hcp

In the case of hcp a , b and c are used to describe the unit cell edge lengths whilst α , β and γ are the angles between (α between b and c , etc). These are shown diagrammatically in figure 2.5.

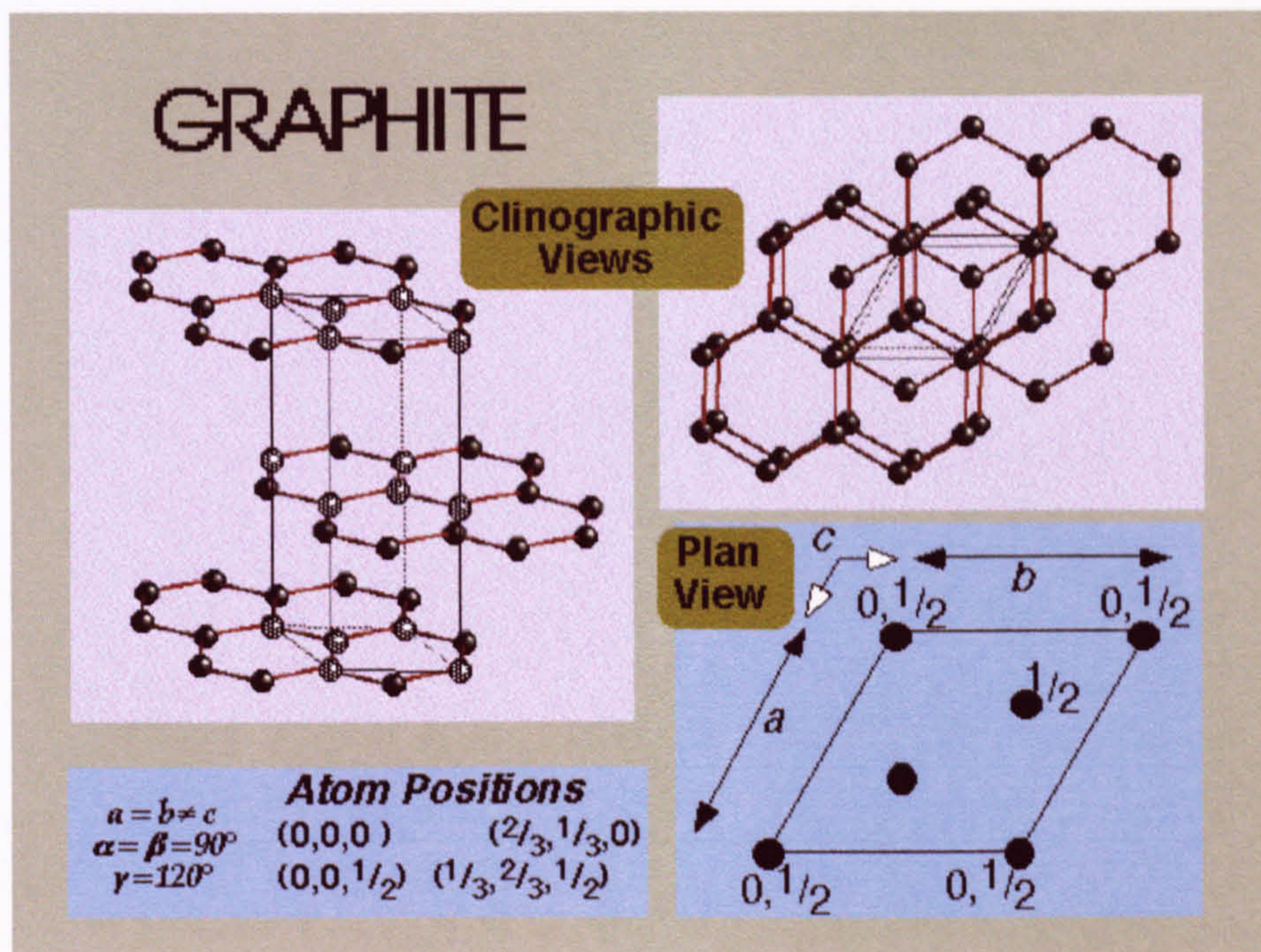


Figure 2. 5 HCP definition according to atomic parameters (Image © S.J. Heyes, Oxford, 1996-2000)

The reciprocal lattice is generated from three reciprocal lattice vectors a^* , b^* and c^* analogous to the three primitive translation vectors a , b and c used to define the lattice points of a crystal in real three-dimensional space. K-space (or reciprocal space) is the appropriate space for plotting wavevectors.

As all ferromagnetic solids are metals, which in turn are crystalline in structure, it is essential to know how the atoms are arranged within materials. Magnetism in the transition elements as a group arises as a result of their partly filled d subshells. It is this fact, and a high density of states at the Fermi energy, that explains the FM properties of Fe, Co and Ni. In TM ions a dominant effect is the crystal field. The orbital angular momentum of the TM ions is quenched because in a solid the electronic wavefunctions are affected by the electric field produced by neighbouring atoms. The mechanism of magnetic interaction observed in lanthanides differs very much from that in magnetic TM.

The heavy lanthanides arrange in a hcp crystal structure with their inner 4f electron shells only partially occupied, while the outer shells are completely filled. The 4f levels are located close to the core and therefore are well screened from Coulomb interaction with the surrounding ions. Figure 2.6 shows the relationship between the relative energy levels in Ho. The 6s subshell is full but at a slightly lower energy than the 4f subshell.

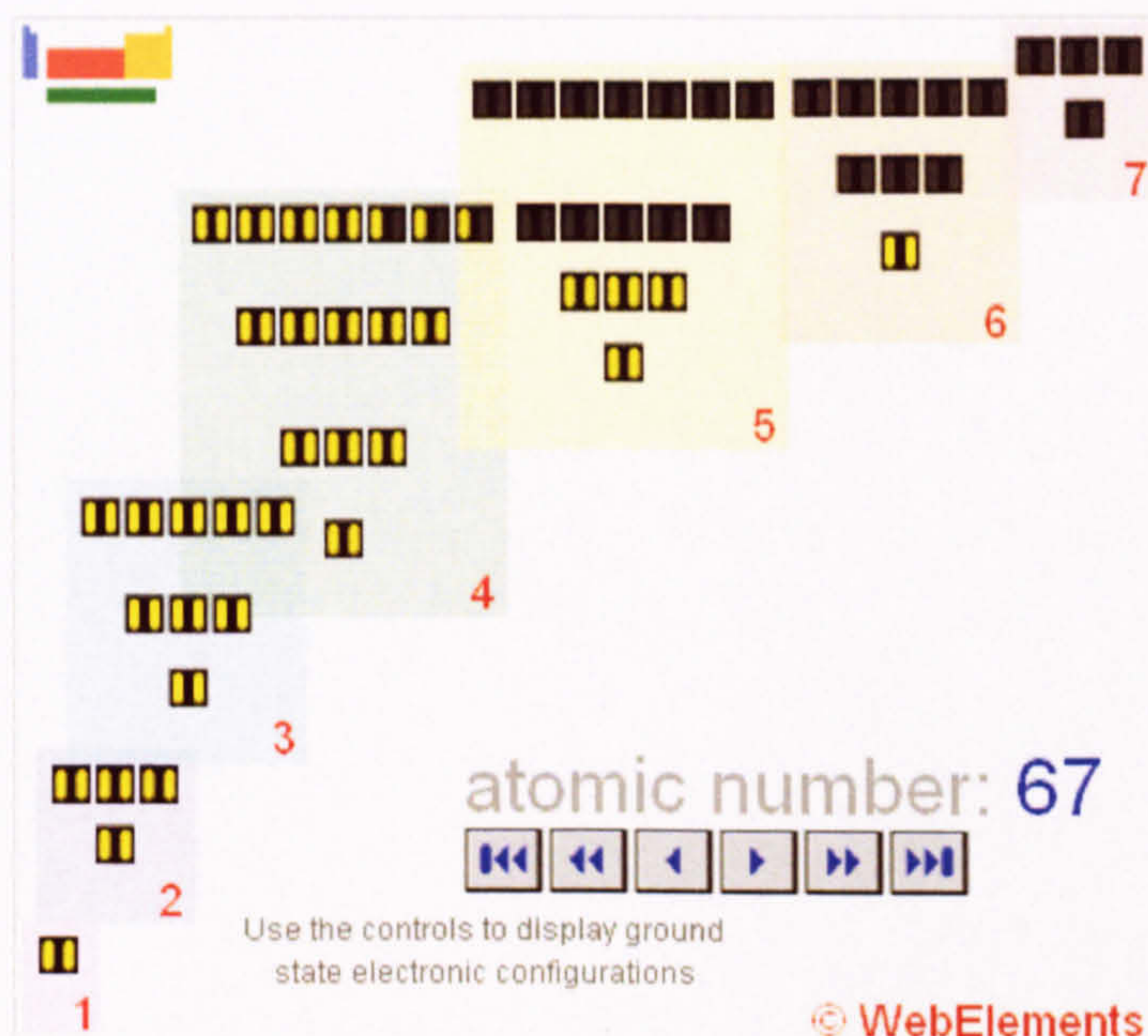


Figure 2. 6 Ground state electron configuration of Ho arranged in increasing energies. (Image © WebElements)

The open 4f-shells supply non-vanishing magnetic moments, which are localized at the lattice sites. In the ordered state these moments interact indirectly, with the exchange being mediated via delocalized electrons (RKKY exchange). Indirect exchange couples moments over relatively large distances. It is the dominant exchange interaction in metals where there is little or no direct overlap between neighbouring magnetic electrons. It therefore acts through an intermediary which in metals are the conduction electrons (itinerant electrons). This type of exchange was first proposed by Ruderman and Kittel⁹ and later extended by Kasuya¹⁰ and Yosida¹¹ to give the theory now generally known as the RKKY interaction. The localization of the 4f electrons within screening orbitals generally results in both the orbital and spin moments maintaining their full atomic values in the bulk. The large orbital moment and spin-orbit coupling is responsible for the very high values of the magnetic anisotropy energy observed in RE.

2.2.1 Magnetic Anisotropy

The most stable domain or spin configuration is obtained by minimizing the total free energy, which is the sum of four main energy factors:

$$E_{\text{Tot}} = E_{\text{ex}} + E_{\text{H}} + E_{\text{K}} + E_{\text{Z}} \quad (2.2)$$

E_{ex} = exchange energy

E_{H} = magnetostatic energy

E_{K} = anisotropy energy

E_{Z} = Zeeman energy (in the presence of an external magnetic field)

In the absence of an applied magnetic field the direction of the moment is determined by the anisotropy, K , and the anisotropy energy is defined as the dependence of the free energy of a homogeneously magnetized film (single-domain state) on the orientation of magnetization. This depends on the direction in which the magnetic vector is pointing and leads to hard and easy magnetisation directions. All pointing directions of the cluster magnetic anisotropy are not equally probable and in real crystals crystalline anisotropy provides an 'easy' direction for the magnetisation. Anisotropy can arise from several different sources, the three main ones being; magnetocrystalline anisotropy, favouring magnetisation along a particular crystallographic direction due to spin-orbit coupling; shape anisotropy favouring magnetisation within the plane of a thin film and stress which also induces anisotropy.

The exchange energy, E_{ex} arising when the spin magnetic moments, s_1 and s_2 of adjacent atoms lie at some angle to one another is incorporated into the exchange interaction, $-2E_{\text{ex}}s_1 \cdot s_2$. The exchange interaction lines up spins in a magnetic system and keeps electrons of parallel spins apart. For a FM system E_{ex} is positive and for an AFM system E_{ex} is negative. Although the exchange interaction produces strong interactions between neighbouring magnetic atoms it can also be mediated by various mechanisms, producing long range effects.

It is an elementary observation that unless some special effort is made to stop it a 'magnetic' material demagnetizes so that it generates no external field. This is in order to minimize the 'magnetic self-energy' of the atomic magnetic moments in the material. If they obey the exchange force and all line up then the magnetization generates a field within the material in which the dipoles are aligned such that they have maximum magnetostatic energy, $E_H = \mu_0 H$ where μ_0 is the permeability of free space. Of course reversing the magnetization is no use because the generated field reverses and again they are aligned in the least favourable direction to minimise energy. The exchange interaction and the magnetostatic self energy are thus competing, which at first glance doesn't appear to be much of a competition considering that the exchange interaction between nearest neighbours is 3-4 orders of magnitude stronger than the magnetostatic one. The dipolar interaction however is long range while the exchange interaction only operates between atomic neighbours so there is a compromise that will minimize the energy relative to the totally magnetised state. If the material organises its magnetisation into domains of opposite magnetisation it can be shown that the magnetic energy is reduced relative to the state of uniform magnetisation. Minimisation of the magnetostatic energy demands that the material forms as many domains as possible but every new domain introduces a boundary of oppositely aligned atomic spins thereby increasing the exchange energy within the material. The energy balance works because only atoms at the boundary feel the powerful exchange force whereas a much larger number of atoms benefits from the reduction in the dilute magnetostatic energy.

The energetics driving domain formation depends on a large number of spins in a mesoscopic volume decreasing their (small) magnetostatic energy by a total greater than a relatively small number of spins at the domain boundary increasing their (large) exchange energy. Clearly there is a minimum volume required for the process to save energy and for particles smaller than this critical volume it is energetically unfavourable to form a single domain boundary. Thus sufficiently small particles will consist of a single domain.

2.2.2 Spin Waves

Spin waves propagate through a three-dimensional crystal according to a dispersion relation. A quantum mechanical calculation of spin waves generates quantized values of the energy of a mode with wavenumber k . The quanta associated with the spin wave modes are called magnons. The contribution of the spin waves to the heat capacity of FM at low temperatures can be calculated in much the same way as calculating the heat capacity due to lattice vibrations. This contribution is proportional to T ; the magnon heat capacity varies as $T^{3/2}$ at low temperatures.

A spin glass is a disordered material exhibiting high magnetic frustration, or the inability of the system to remain in the ground state. Time-dependence distinguishes spin glasses from other magnetic systems. Up to the spin-glass transition temperature, T_g , the magnetisation in a spin glass is inversely proportional to temperature. At T_g the magnetisation becomes constant and marks the onset of the spin glass phase. When the external field is removed the magnetisation of the spin glass decreases rapidly to remanence followed by a slow decay to a magnetisation of zero. This differs from FM materials whose remanence value is constant in time. A variety of RE alloys have been shown to exhibit spin glass behaviour.

Spin ice materials are characterized by disorder of magnetic ions even when at very low temperatures. They consist of tetrahedra of spins, which must satisfy a two-in, two-out rule analogous to the behaviour of the protons in water ice. Spin ice materials therefore exhibit the same residual entropy properties as water ice. The only known spin ice materials are the pyrochlores $\text{Ho}_2\text{Ti}_2\text{O}_7$, $\text{Dy}_2\text{Ti}_2\text{O}_7$ ¹², and $\text{Ho}_2\text{Sn}_2\text{O}_7$ all compounds containing the RE of interest¹³.

2.2.3 Magnetic Phases

Water can exist in the solid, liquid and gaseous phases of matter as ice, water and steam respectively. Magnetic systems exist in magnetic phases according to temperature, applied field and pressure¹⁴. The Curie temperature defines the transition from PM to FM

and is a second-order phase transition (SOPT) whilst the Néel temperature defines the transition from PM to AFM and is a first-order phase transition (FOPT). The first-order phase transitions are those that involve a latent heat. During such a transition, a system either absorbs or releases a fixed (and typically large) amount of energy. Because energy cannot be instantaneously transferred between the system and its environment, first-order transitions are associated with mixed-phase regimes in which some parts of the system have completed the transition and others have not. Second-order phase transitions have a discontinuity in a second derivative of the free energy. With the FM phase transition in Fe, the magnetisation, which is the first derivative of the free energy with the applied magnetic field strength, increases continuously from zero as the temperature is lowered below the Curie temperature. The magnetic susceptibility, the second derivative of the free energy with the field, changes discontinuously. SOPT have no associated latent heat. Thermal hysteresis (subsection 2.3.1) is used to characterise FOPT. However, a difference between the traces obtained from heating or cooling a sample does not necessarily mean that thermal hysteresis is occurring. It is common to observe differences between the data collected in the two circumstances but this must always be considered to be an experimental artefact rather than an intrinsic behaviour of the sample.

In a superheating phase transition (SHPT) a sample is colder after heat has been added to it and during supercooling the converse is true. SHPT have been observed in the RE at the SOPT of the Curie temperature.

Spin-reorientation transitions (RT) can occur deep in the FM regime. The associated change of symmetry results from the combination of different anisotropy contributions whose magnetism can be controlled or driven by temperature, thickness or even composition variations. An example would be if all spins were aligned with the applied field then at a particular temperature switching occurs such that the spins align at some angle to the applied field.

The large thermodynamic fluctuations observed near T_c are termed critical fluctuations. These dominate the behaviour of the susceptibility (section 2.3) just above, and the

spontaneous magnetisation just below, T_c . The critical behaviour of the susceptibility is described by the temperature dependence

$$\chi \propto (T - T_c)^{-\gamma} \quad (2.3)$$

with the critical exponent $\gamma = 1.33$

There are other critical exponents which have been measured and found for all materials. The critical exponents for different SOPT appear to depend only on the nature of the symmetry change involved.

2.3 Bulk Magnetism

Observing low temperature nanoscale magnetic spin waves is impractical so magnetisation measurements must be made on bulk systems made as thin and small as possible. The behaviour of the spins on the nanoscale can then be inferred from the results.

2.3.1 Magnetometry

The magnetisation, M , of the sample is defined as the magnetic moment per unit volume. Dimensions of magnetisation are current/length measured in amperes per metre.

$$M = \frac{m}{V} \quad (2.4)$$

Where m = total magnetic moment of the sample

The magnetisation is proportional to the magnetic field strength with the constant of proportionality being the magnetic susceptibility, χ .

$$M = \chi H \quad (2.5)$$

If the magnetisation of a material is measured with respect to temperature in a constant or zero applied field the resulting traces are called isofields. If magnetisation is measured with respect to applied field at fixed temperature the traces are known as isotherms. FM materials generate varying isofields and isotherms represented by hysteresis curves. Hysteresis is the property of magnetic memory. As a FM sample is cycled through an increasing applied magnetic field the dipoles will gradually align with this external field up to the point of saturation at which all the dipoles are aligned. As this applied field is then decreased, instead of relaxing, the dipoles retain the majority of their alignment even to the point at which there is no applied field. Hysteresis measurements of a sample produce a curve or 'loop' as shown in figure 2.7 and these loops are characteristic of FM materials.

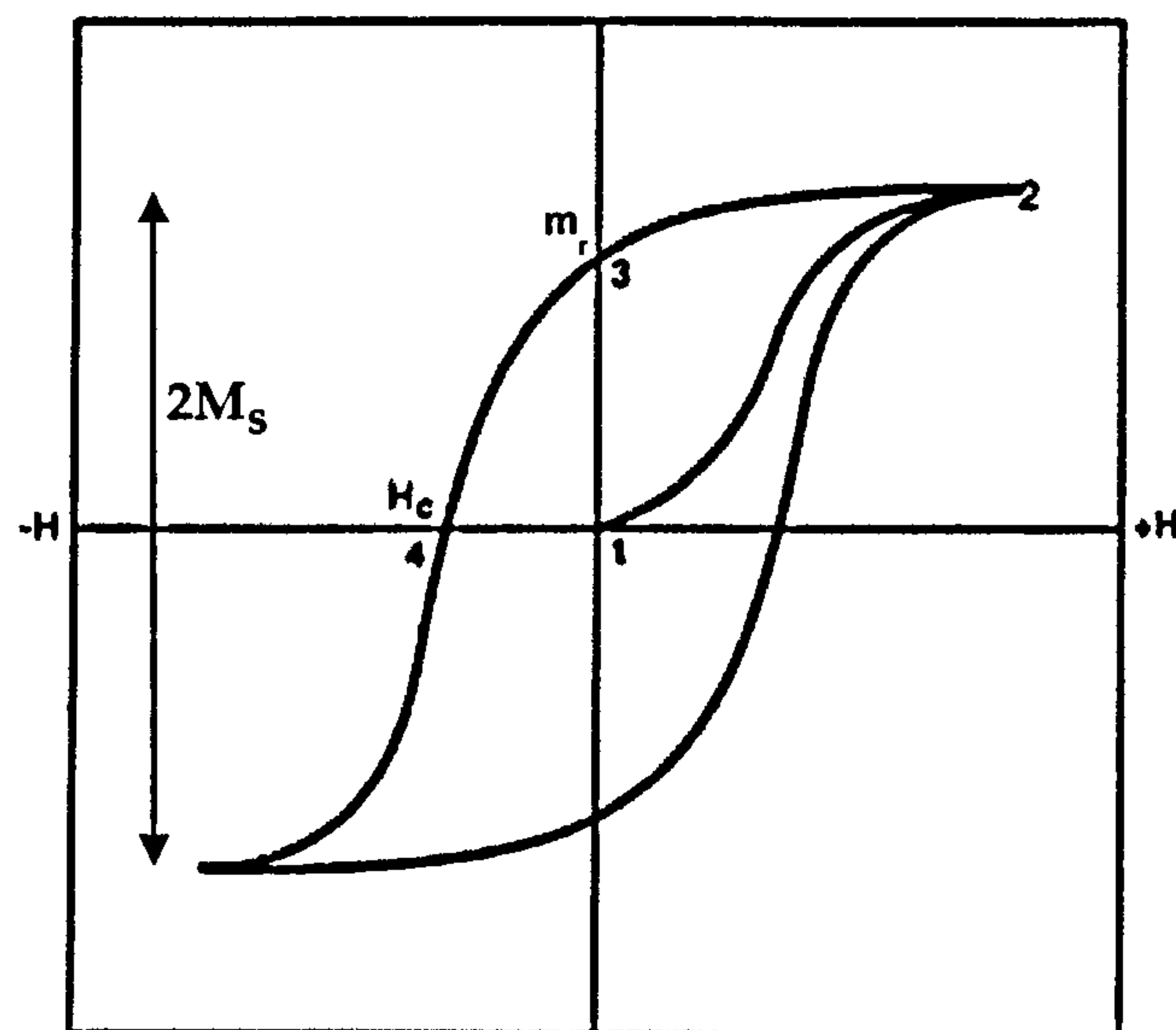


Figure 2.7 Characteristic isotherm for a FM material showing hysteresis. Magnetisation is measured on the abscissa

Point 2 shows the maximum magnetisation or saturation magnetisation, M_s , that the material acquires when all the dipole moments to become aligned with the external field. The coercivity, H_c , of the sample is taken from where the curve crosses the x-axis (point 4). The coercivity of a FM material is the intensity of the magnetic field required to reduce the magnetisation of that material to zero *after* the magnetisation of the sample has reached saturation. The remanence, m_r , is the value taken from the y-axis intersection (point 3). Remanence is the magnetisation left behind in a medium after the external

magnetic field has been removed. The material of a recording head must be magnetically soft so that it can be easily magnetised therefore it must have a large M_s and small H_c . For magnetic storage the material should be able to retain the spatial magnetisation patterns stored in it by the recording head requiring high m_r . The H_c should be high enough so it is difficult to erase magnetic information from it under stray fields but not so high that it is impossible to record magnetic data on it.

At different temperatures the thermal energy of a material will change and this will generate a different curve. If the entire hysteresis curve is shifted to the left this is an example of exchange bias and is indicative of an oxidised sample. Exchange bias is the exchange interaction between an AFM and FM at their interface¹⁵. All the iron oxides couple AFM therefore this measurement is a direct indicator of a damaged (i.e. oxidised) sample.

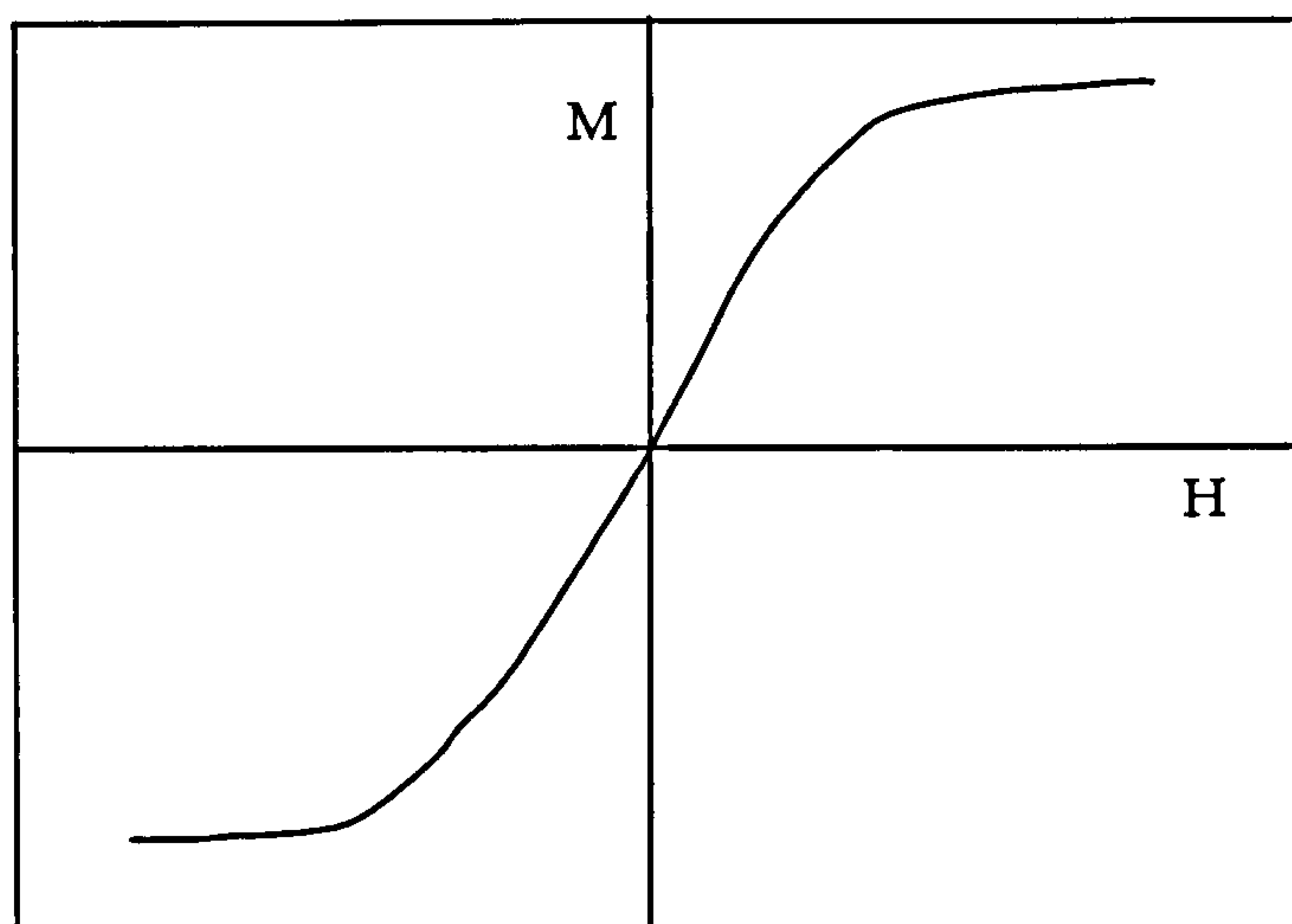


Figure 2.8 Characteristic isotherm for a PM material

The PM isotherm in figure 2.8 would trace out the same path with increasing and decreasing H showing no hysteresis, merely a response to the applied field.

Typically SPM samples will also show a lack of hysteresis in the magnetisation curve. The temperature at which the curve just begins to form a loop is an indication of the location of the blocking temperature. Different magnetisation curves will also be seen depending

on whether a sample is field-cooled (fc) or zero-field-cooled (zfc). Some such behaviour can be characteristic of SPM particles with a particle size distribution¹⁶.

Isofields showing thermal hysteresis reveal the onset of phase transitions. Plotting susceptibility against temperature, a sharp increase in gradient marks the onset of the FM phase whilst a change in sign of the gradient marks the onset of the AFM phase.

Figure 2.9 shows characteristic isofields for AFM, PM and FM systems upon cooling.

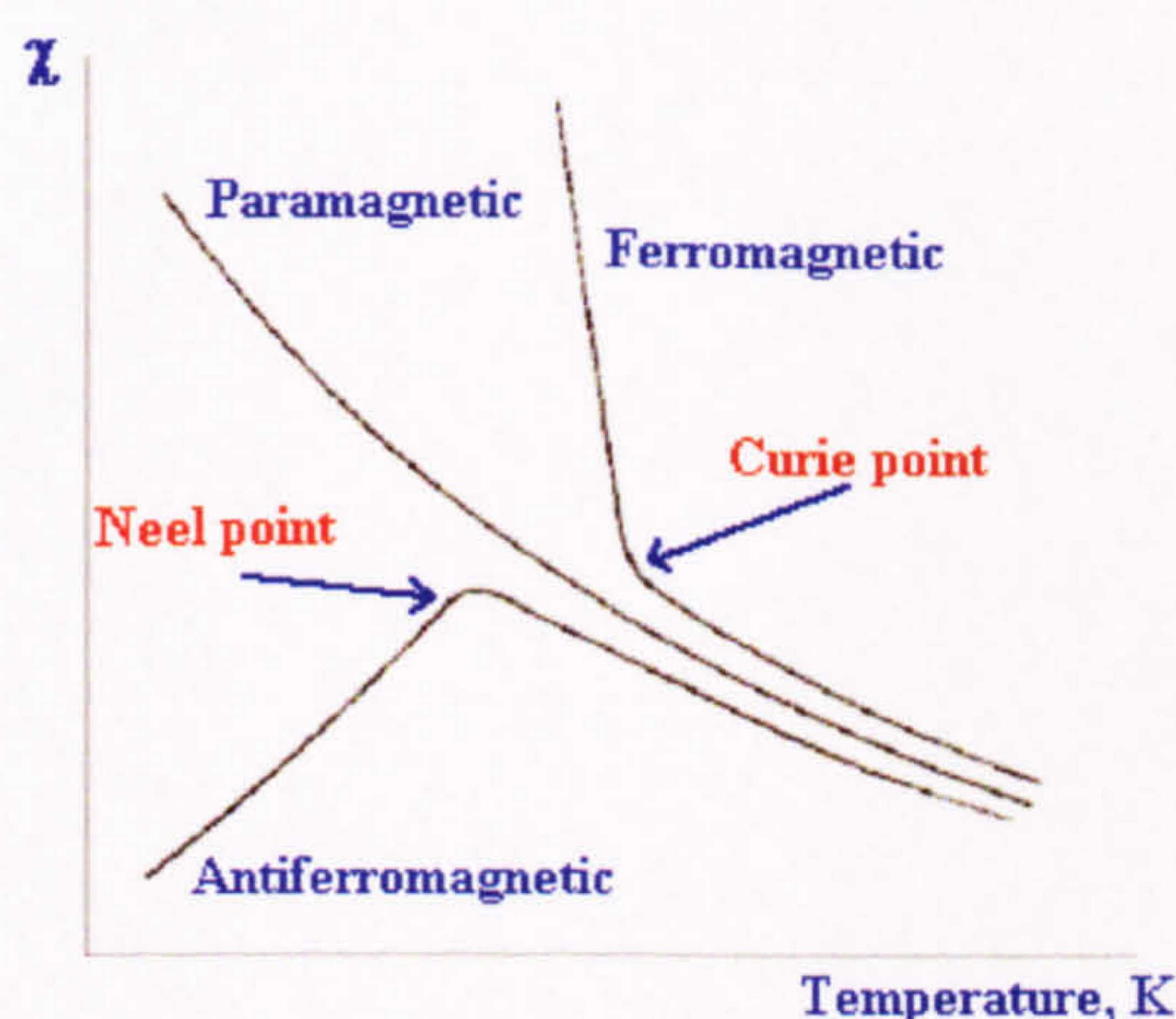


Figure 2. 9 Characteristic isofields for magnetic systems

At temperatures below 30K isofields can show spin glass transitions but there is still much conjecture¹⁷ as to their validity in diagnosing such behaviour.

2.3.2 X-Rays

X-ray radiation is a valuable tool as its frequency range is such that it interacts with the electrons of atoms. X-rays are therefore the perfect probe for magnetism.

In X-ray magnetic circular dichroism (XMCD) a sample is placed in a magnetic field and the absorption of circularly polarised x-rays is measured. Measurements are made with the magnetic field and photon spin aligned parallel and then antiparallel. There is a difference in the absorption of the sample between the 2 cases and this is the dichroism, see figure 2.10.

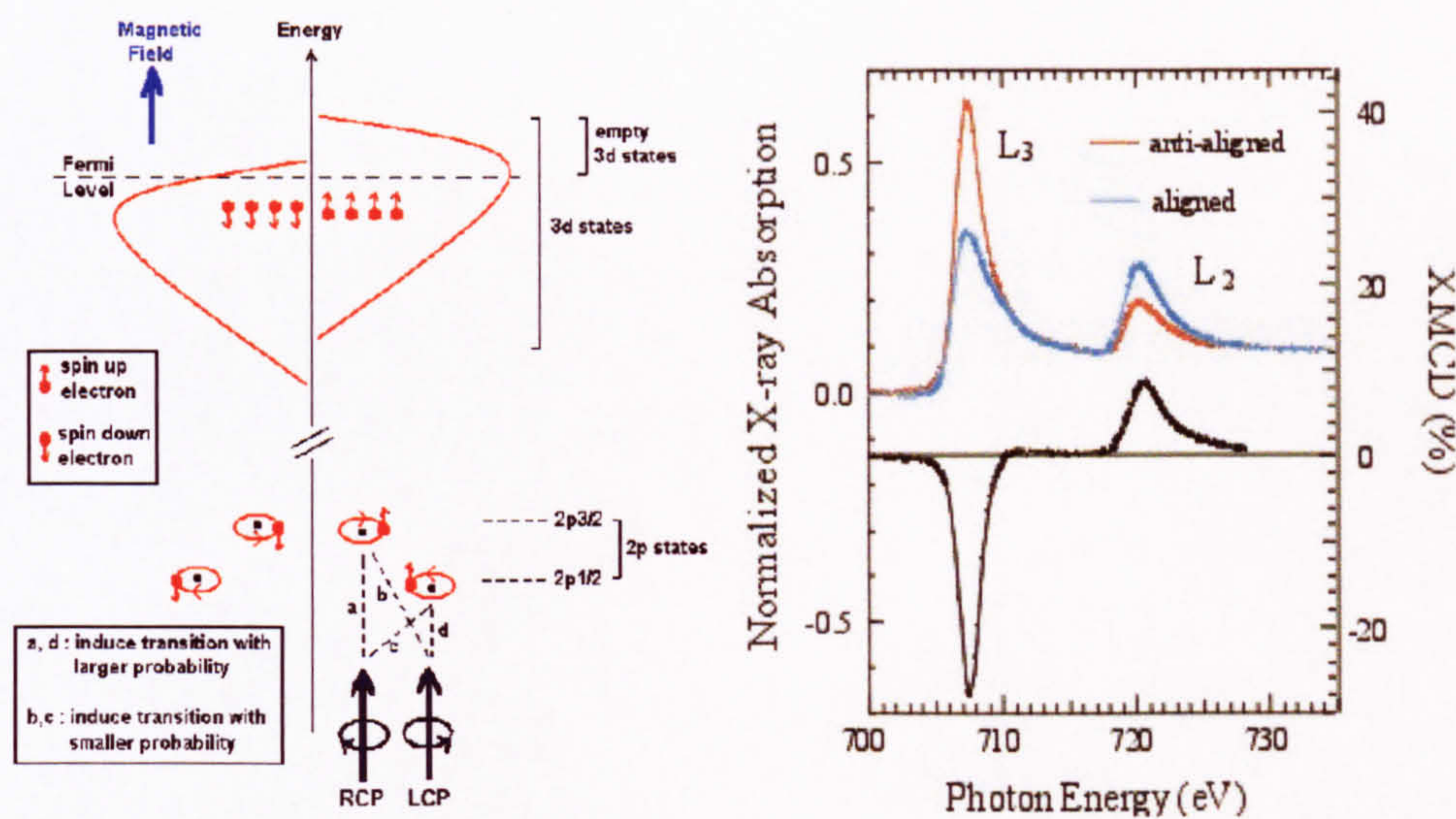


Figure 2. 10 Differential absorption of circular polarized X-Rays

If there is a non-zero spin or orbital moment in the valence band, the absorption of the right-handed circularly polarized (RCP) light differs from that of the left-handed circularly polarized (LCP) light at resonance absorption edges. The integrated area of the difference in the two absorption spectra, also called dichroism spectra, can be directly correlated to the spin and orbital magnetic moments. In the case of bulk Fe, circularly polarized X-rays trigger core-to-valence ($2p \rightarrow 3d$) excitation of the atom. The L absorption edge is split into L_3 and L_2 due to the strong spin-orbit coupling in the 2p shell. For this reason the XMCD technique is element specific and can generate the spin *and* orbital magnetic moments of an element.

The absorption process in XMCD can be described using the one-electron approach together with a two-step model proposed by Wu et al¹⁸. Step 1 describes how a single electron is excited by a single photon of energy $\hbar\omega$. X-rays are absorbed by the spin-orbit split 2p electrons and this results in the production of spin-polarised photoelectrons. These electrons acquire an angular momentum of $+\hbar$ or $-\hbar$ from a RCP or LCP x-ray photon respectively. This angular momentum can be transferred in part to the electron spin via the spin-orbit coupling. The spin-polarised photoelectrons are subsequently excited into empty states in the 3d valence band above the Fermi level (step 2).

Two important sum rules were derived for the orbital¹⁹ and spin²⁰ magnetic moments by Thole et al and Carra et al respectively. The rules are valid for dipole-allowed electron transitions from core levels to empty valence band states in magnetically ordered materials.

The sum rules for 3d shells used in the analysis of data in chapter 4 of this thesis are quoted below.

$$m_{orb} = -\frac{4 \int_{L_3+L_2} (\mu_+ - \mu_-) d\omega}{3 \int_{L_3+L_2} (\mu_+ + \mu_-) d\omega} (10 - n_{3d}) \quad (2.6)$$

$$m_{spin} = -\frac{6 \int_{L_3} (\mu_+ - \mu_-) d\omega - 4 \int_{L_3+L_2} (\mu_+ - \mu_-) d\omega}{\int_{L_3+L_2} (\mu_+ + \mu_-) d\omega} (10 - n_{3d}) \left(1 + \frac{7\langle T_z \rangle}{2\langle S_z \rangle}\right)^{-1} \quad (2.7)$$

m_{orb} = orbital magnetic moment

μ_+ = right-circularly polarized (RCP) dichroism trace

μ_- = left-circularly polarized LCP dichroism trace

ω = frequency

n_{3d} = number of valence electrons in the 3d shell

m_{spin} = spin magnetic moment

$\langle S_z \rangle$ = expectation value of spin

$\langle T_z \rangle$ is the expectation value of the magnetic dipole moment, which is much smaller than S_z and in bulk samples it is often ignored. In systems of low symmetry (for example nanoparticles) however it is enhanced and must be determined by doing measurements as a function of the angle of the sample with respect to the X-ray beam. With certain types of sample it can be eliminated by doing a single measurement at the so-called 'magic angle' (55°) at which the T_z contribution should go to zero.

Each integral is represented graphically in the experimental data. For example, the numerator in equation 2.6 is the integral over both L-edges of the RCP dichroism trace subtracted from the LCP dichroism trace. Conversely, the denominator in both equations is the integral over both L-edges of the two dichroism traces added together. By utilising the following identities,

$$p = \int_{L_3} (\mu_+ - \mu_-) d\omega \quad (2.8)$$

$$q = \int_{L_3+L_2} (\mu_+ - \mu_-) d\omega \quad (2.9)$$

$$r = \int_{L_3+L_2} (\mu_+ + \mu_-) d\omega \quad (2.10)$$

equations 2.6 and 2.7 can be simplified greatly to the following expressions,

$$m_{orb} = -\frac{4q}{3r} (10 - n_{3d}) \quad (2.11)$$

$$m_{spin} = -\frac{6p-4q}{r} (10 - n_{3d}) \quad (2.12)$$

Equations 2.11 and 2.12 show that the separate orbital and spin moments are the ratio of the amount of dichroism to the amount of absorption.

Figure 2.11 shows the type of XMCD graphs that would be generated by an Fe sample. The values p, q and r are shown.

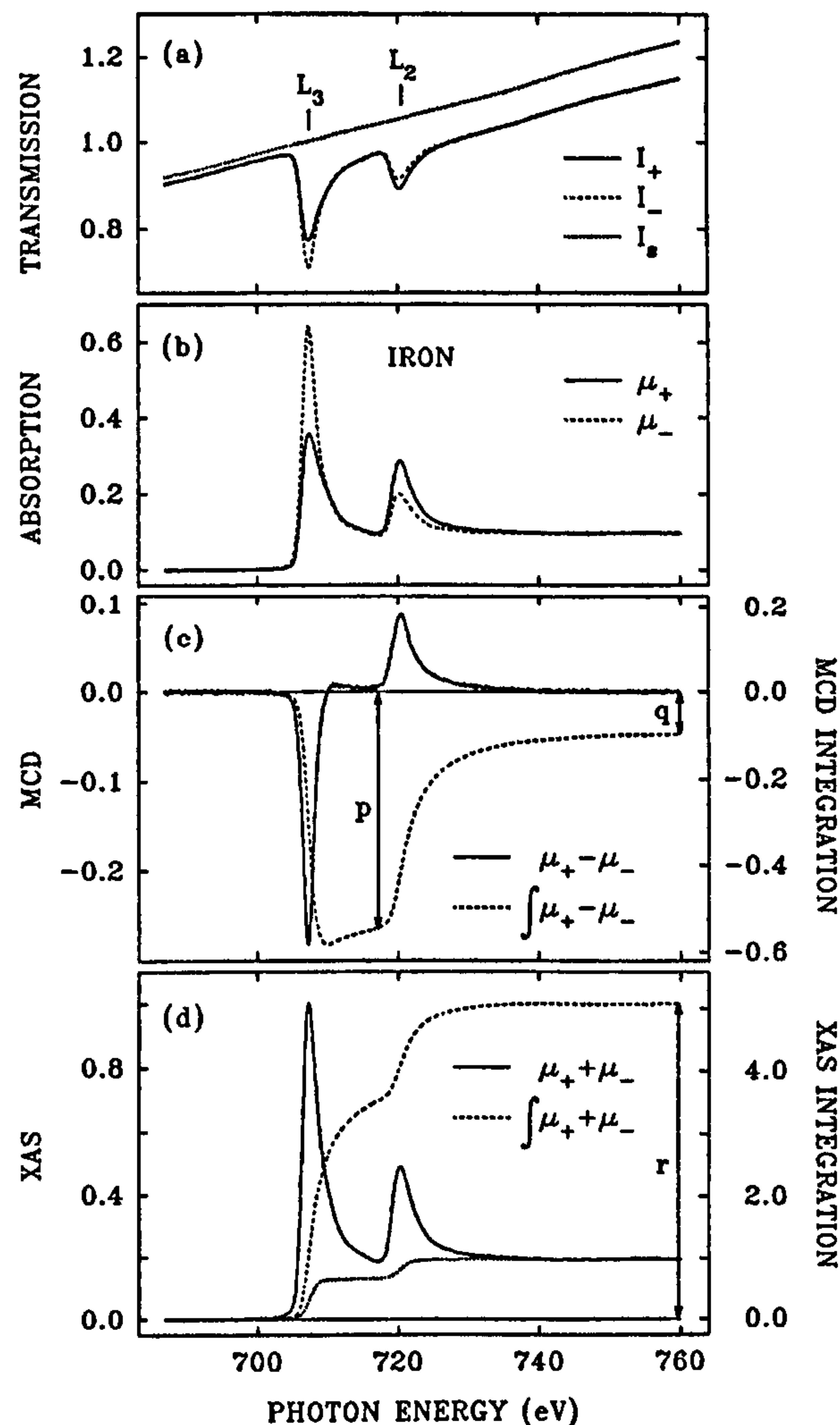


Figure 2. 11 The main stages of XMCD graphical analysis. (Image reproduced from Chen et al²¹) a) transmission spectra of Fe where I_+ represents transmission of RH light and I_- represents LH light and I_s shows the transmission of a blank substrate of parylene b) absorption spectra calculated from a) by subtracting the signature of the substrate to produce a level trace c) integration of the difference of the two dichroism traces (dichroism) d) integration of the sum of the two traces (absorption).

The dotted trace in 2.11 (d) represents the two-step-like function which is removed from the absorption trace before integration. It removes the L_3 and L_2 edge jumps with thresholds set to the peak positions of the L_3 and L_2 white lines. The height of the L_3 (L_2) step is set to $2/3$ ($1/3$) of the average intensity of the last 15eV of the spectra according to its quantum degeneracy, $2j + 1$.

Another X-ray technique utilised for magnetism studies is Extended X-ray Absorption Fine Structure (EXAFS). A monochromatic X-ray beam is directed at the sample. The photon energy of the X-rays is gradually increased such that it traverses one of the

absorption edges of the elements contained within the sample. Below the absorption edge, the photons cannot excite the electrons of the relevant atomic level and thus absorption is low. However, when the photon energy is just sufficient to excite the electrons, then a large increase in absorption occurs known as the absorption edge. The resulting photoelectrons have a low kinetic energy and can be backscattered by the atoms surrounding the emitting atom. The probability of backscattering is dependent on the energy of the photoelectrons. The backscattering of the photoelectron affects whether the X-ray photon is absorbed in the first place. Hence, the probability of X-ray absorption will depend on the photon energy (as the photoelectron energy will depend on the photon energy). The net result is a series of oscillations on the high photon energy side of the absorption edge. These are due to interference effects between outgoing and backscattered photoelectrons. These oscillations can be used to determine the atomic number, distance and coordination number of the atoms surrounding the element whose absorption edge is being examined.

X-ray absorption spectra are generally produced in the range 200 - 35 000 eV.

“I am among those who think that science has great beauty. A scientist in her laboratory is not only a technician: she is also a child placed before natural phenomena which impress her like a fairy tale. “

Marie Curie

1867 - 1934

Chapter 3

Experimental Procedure

The samples in this thesis have been made using a gas aggregation cluster source (GAS) coupled to an in-house, custom built ultra high vacuum (UHV) deposition chamber and measured using a vibrating sample magnetometer (VSM) to obtain bulk magnetisation data; XMCD for atomic magnetic moments and EXAFS/transmission electron microscopy (TEM) for structural information. All equipment and sample manufacturing methods used in this work will be described within this chapter concluding with a description of the initial studies conducted in order to investigate the properties of the experimental set-up. Appendix C details the fifty samples made throughout this work.

3.1 Sample Preparation

UHV is used to ensure the samples stay clean. At a few hundred atomic layers in thickness, a sample will be rendered useless by any impurities.

3.1.1. Leicester University Mesoscopic Particle Source (LUMPS)²²

LUMPS is an in-house GAS producing clusters in the size range 1-5 nm which in turn form very clean cluster beams with a high flux. Figures 3.1 and 3.2 show images of the source and its main features whilst the diagram in figure 3.3 and its description focus on the internal mechanics of the chambers.

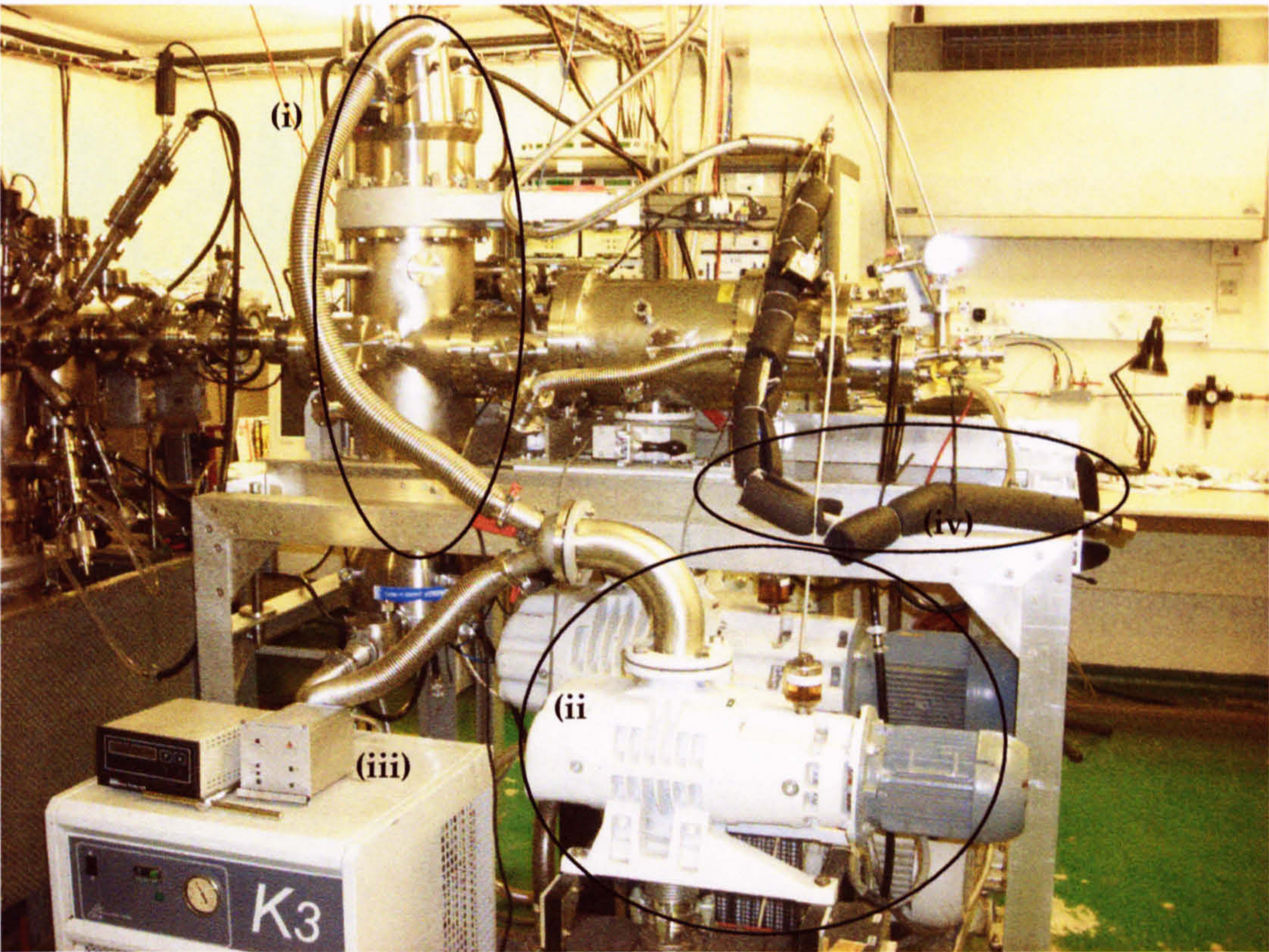


Figure 3. 1 Rear view of LUMPS showing (i) turbo pump backing lines into the (ii) rotary pump, (iii) chiller unit and (iv) $N_2(l)$ feed.

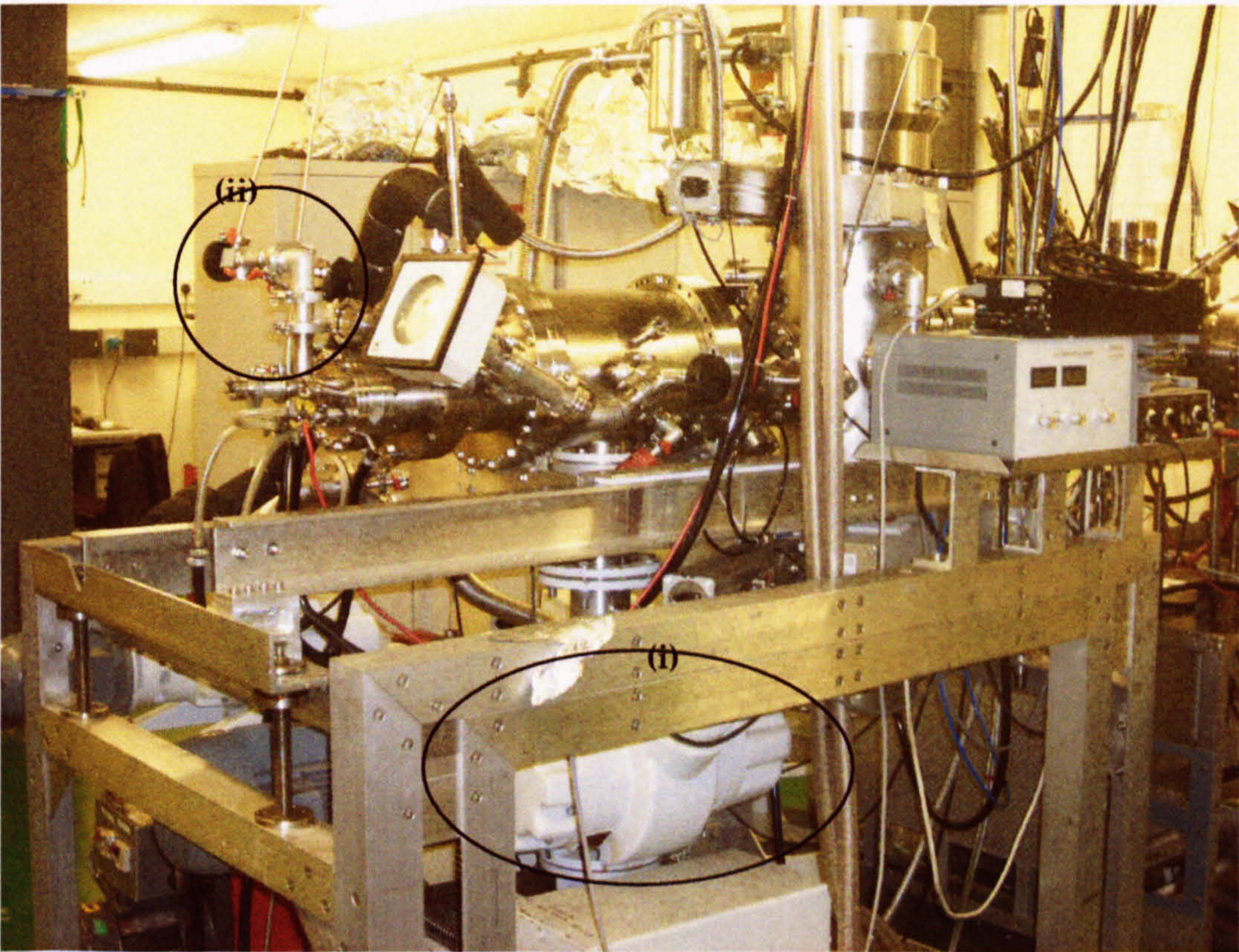


Figure 3.2 Front view of LUMPS showing (i) roots pump underneath and (ii) gas feeds

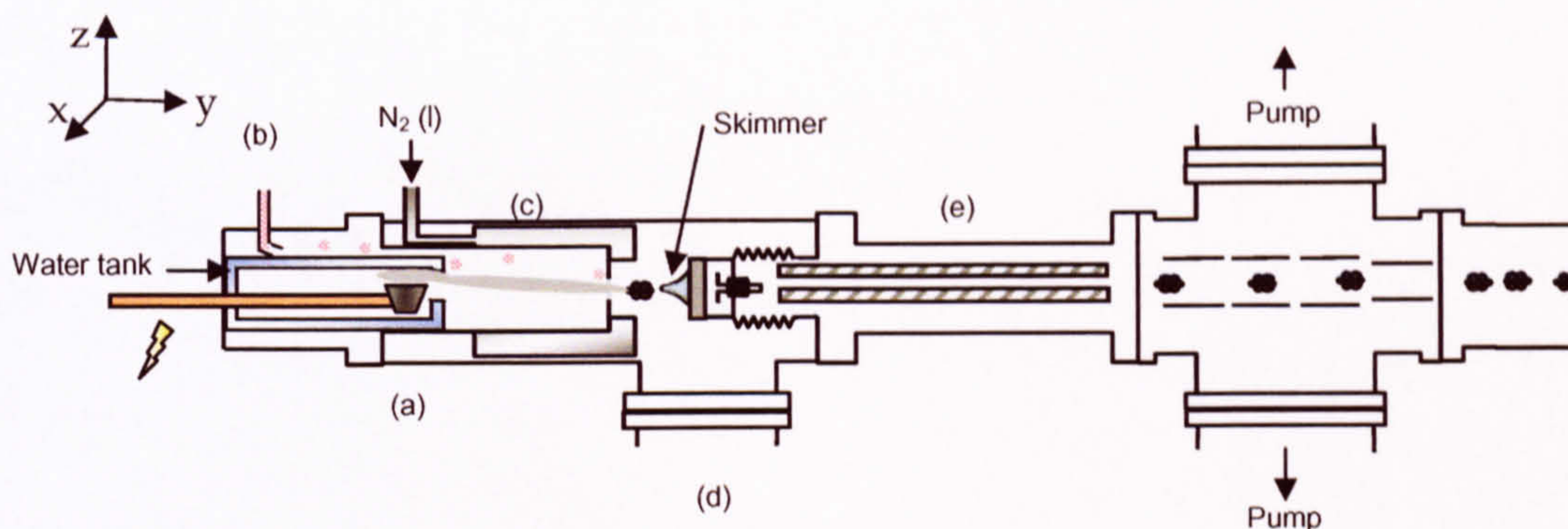


Figure 3.3 Diagram of the internal features of the main chamber within LUMPS

- a) The heater is a ceramic crucible with an internal metal contact. This is attached via two Mo rods to Cu feedthroughs and connected to a power supply. The heater operates at a power of $\sim 550\text{W}$ to evaporate $\sim 10\text{g}$ of FM material.
- b) The metal evaporates into a cloud of helium gas, He(g) where it condenses and the clusters form. At this stage the He(g) is maintained at a constant pressure of 3mbar (P_1).
- c) The clusters travel through a hole in a Cu plate attached to the end of the water tank. From here a pressure gradient within the chambers pushes the clusters through the aerodynamic focusing lenses; a series of cylinders of decreasing radius which focus the clusters into a particulate beam. These lenses culminate in the aperture, a hole in a larger Cu plate, the pressure at this point typically being 0.12mbar (P_2). (Lenses not shown in figure 3.3 for clarity.)
- d) The region between the aperture and the skimmer is pumped out with a roots/rotary pump in order to remove the He(g) . The skimmer with its parabolic structure maximises the dynamic flow of the bath gas towards the pump. Within this main chamber the pressure drops to 10^{-4}mbar (P_3) at which pressure the flow is molecular and the clusters form a free beam. The main chamber is cryogenically cooled with liquid Nitrogen, $\text{N}_2(\text{l})$. This performs two functions; to draw any stray water molecules away from the cluster beam and to ensure the aperture remains cool. The cooler the aperture the greater the throughput of clusters. For rates higher than 0.5nm/min the skimmer becomes blocked and the turbo pumps would struggle to maintain the vacuum. Dendrites form after a couple of hours of

deposition at a rate of just 0.2 nm/min with a resulting drop in pressure and deposition. This is quickly and easily remedied by use of a 'wobble stick' within the main chamber controlled by external bellows.

- e) Finally the clusters are ionised so that upon entry into the quadrupole they can be mass filtered and measured according to their mass distribution. The RF quadrupole is connected to a frequency modulator and is modulated on a DC offset

$$U = V \cos \omega t \quad (3.1)$$

U = d.c. voltage

$V \cos \omega t$ = a.c. component

$$\omega = 2\pi f$$

The mass range, m of the quadrupole is proportional to

$$m \propto \frac{V}{f^2 d^2} \quad (3.2)$$

V = voltage

f = frequency

d = pole diameter

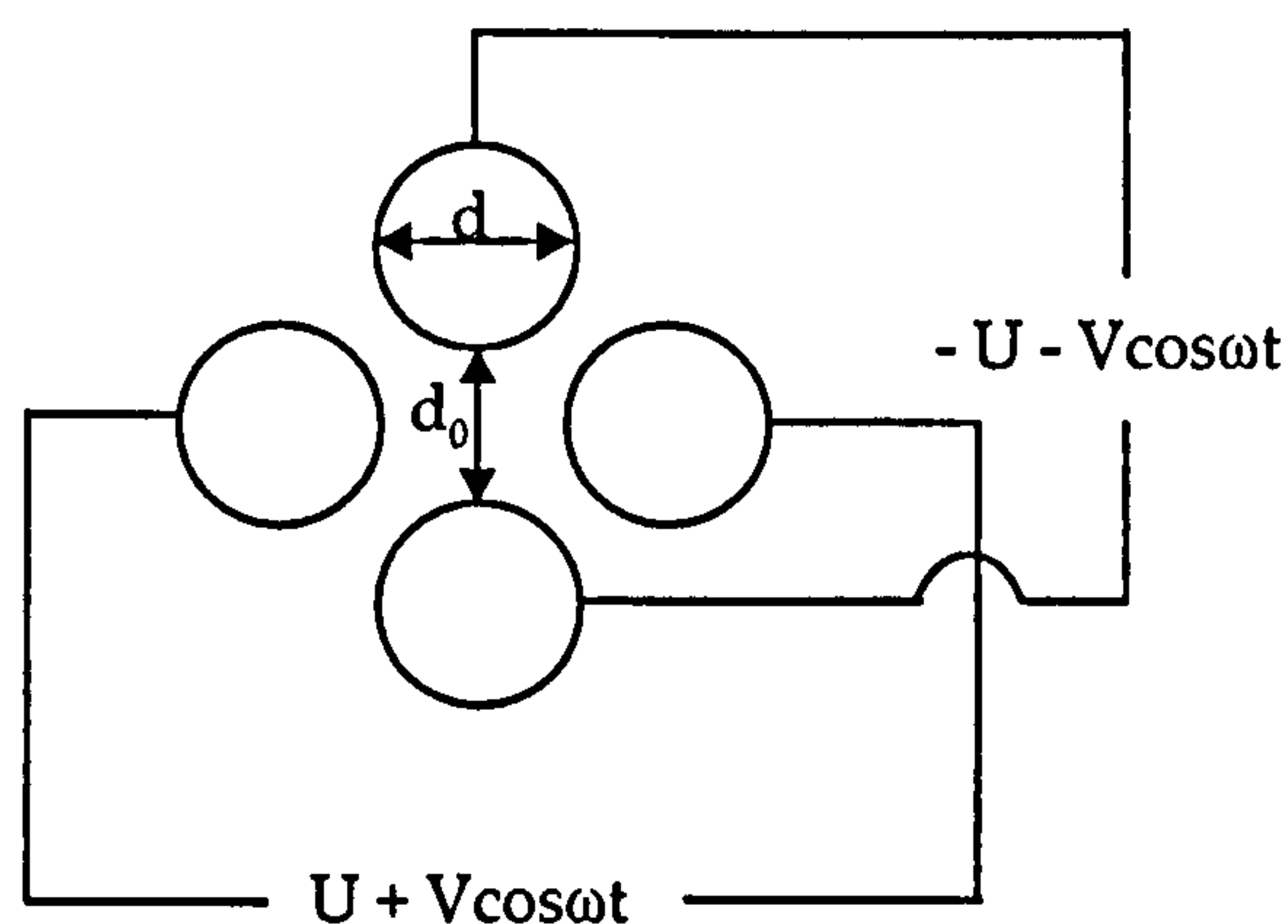


Figure 3.4 Electrical circuit of quadrupole showing DC offset

The U/V ratio determines the mass resolution and can be varied from the intrinsic quadrupole resolution determined by the mechanical precision ($\Delta M / M \sim 0.5\%$) to 'wide open' where all ionised clusters are passed. This condition is used to monitor the total ionised flux.

The smallest cluster size typically resolved is 2,000 a.m.u. (~36 Fe atoms) whilst the maximum is 50,000 a.m.u. (~900 Fe atoms).

3.1.2 ESCA

ESCA (Electron Spectroscopy Chemical Analysis) is a UHV deposition chamber separated from and opened to LUMPS via a gate valve (figure 3.5i). This chamber can be fitted with ovens to bake out the majority of water contamination. The ovens will typically stay at $\sim 122^\circ\text{C}$ over the period of a weekend. The UHV is maintained with a Turbo pump, an Ion pump and a cryogenically cooled Titanium Sublimation Pump (TSP). Typically the chamber maintains a vacuum of 10^{-10} mbar when not open to LUMPS. When LUMPS and ESCA are in operation the TSP trap must be kept cool with $\text{N}_2(\text{l})$. This remains the most effective way of achieving a UHV of the order of $<10^{-10}$ mbar. The TSP draws stray molecular contaminants away from the samples in the same manner as described for LUMPS in figure 3.3(d).

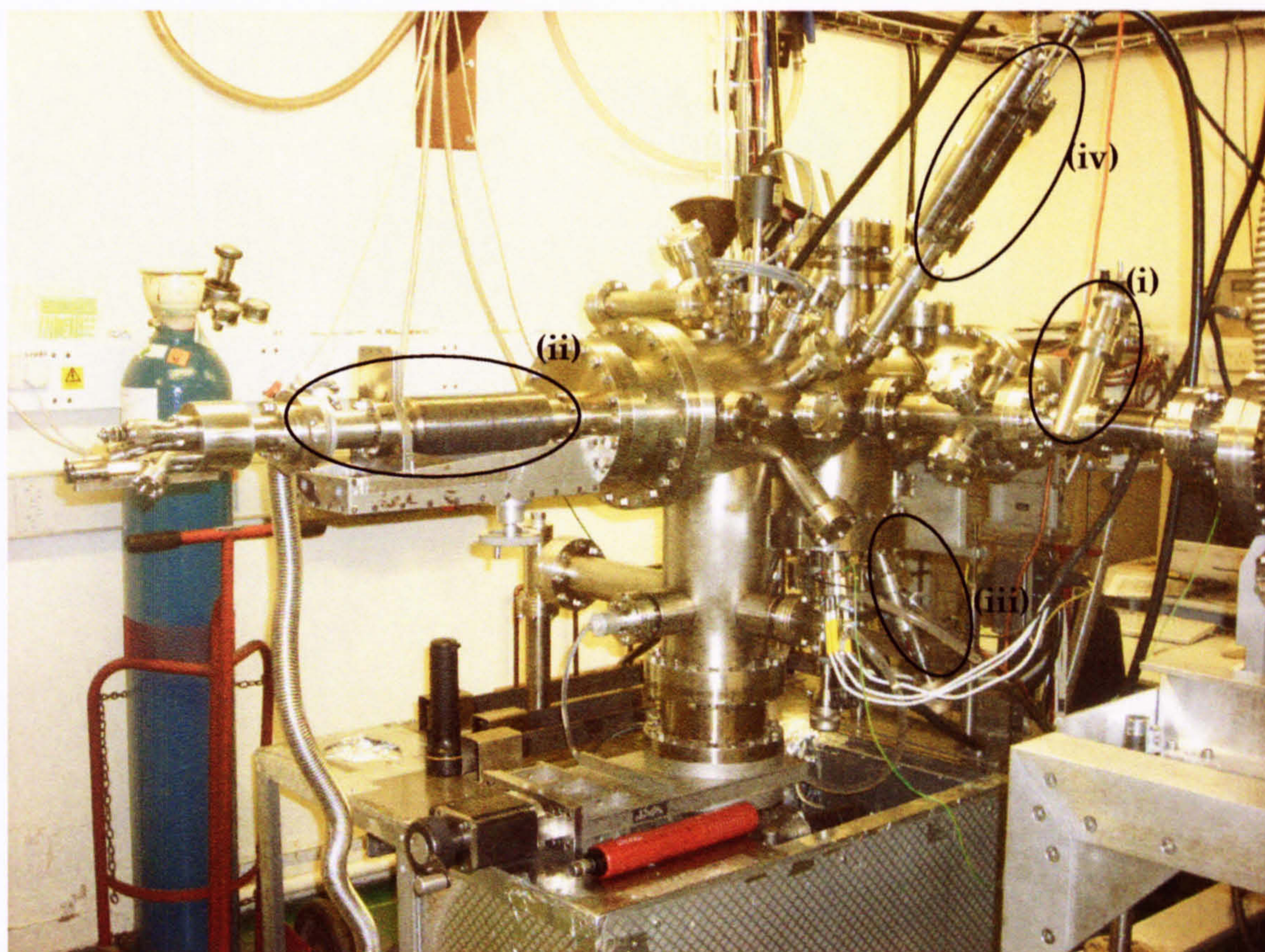


Figure 3.5 ESCA: MBE deposition chamber

Figure 3.5 shows a sample arm (ii) with capacity for up to 6 substrates which lie perpendicular to the cluster beam. It can be rotated a full 360° on its axis and laterally into the chamber. The matrix material is deposited by the method of MBE using evaporators (iii) again custom built at the university²³. Alternatively a C sputter head can be attached for sputtering C layers using Ar gas to induce the plasma. The evaporators must be outgassed fully before use. This process involves passing a current through the evaporators generally higher than that used under normal operating conditions. This results in all surface contaminants evaporating away as gas, being taken out of the chamber by the pumps. An RGA monitor measures the levels of contaminants according to mass i.e. a bar chart plots a.m.u. against pressure as shown in figure 3.6.

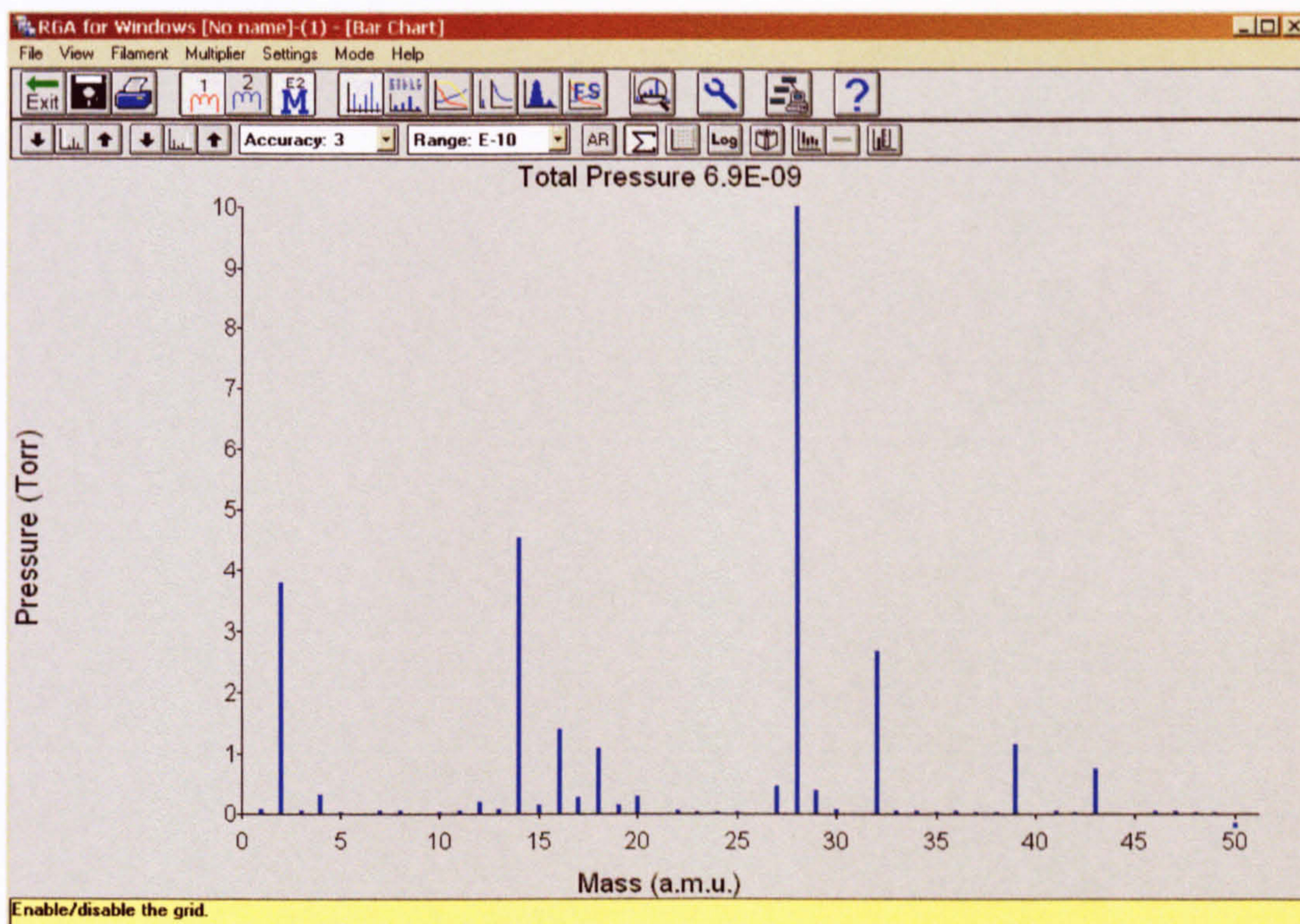


Figure 3.6 Example of screen output of RGA showing contaminants of the vacuum in ESCA

The majority contaminants are presumed to be N_2 and CO but in fact many hydrocarbons have similar masses to normal atmospheric molecules and could be within the chamber. After approximately an hour of outgassing however, these contaminants reduce to give a final chamber pressure of 10^{-10} mbar. During outgassing the pressure can be as high as 10^{-8} mbar. When ESCA is coupled to LUMPS the chamber pressure rises into the 10^{-6} mbar range of He but RGA scans show that the total partial pressure of all contaminant gases remains in the 10^{-10} mbar range.

A crystal thickness monitor (XTM) (figure 3.5 iv) can be wound into the path of any of the particle beams; clusters or evaporators, to measure their respective deposition rates. The XTM must first be programmed to the density of a particular element, the crystal measures the mass of the material that impacts upon it and from this it calculates the thickness of the deposition. By recording this thickness and the time taken to deposit it the deposition rate can be calculated.

After venting ESCA with $N_2(g)$ the samples can be removed for analysis.

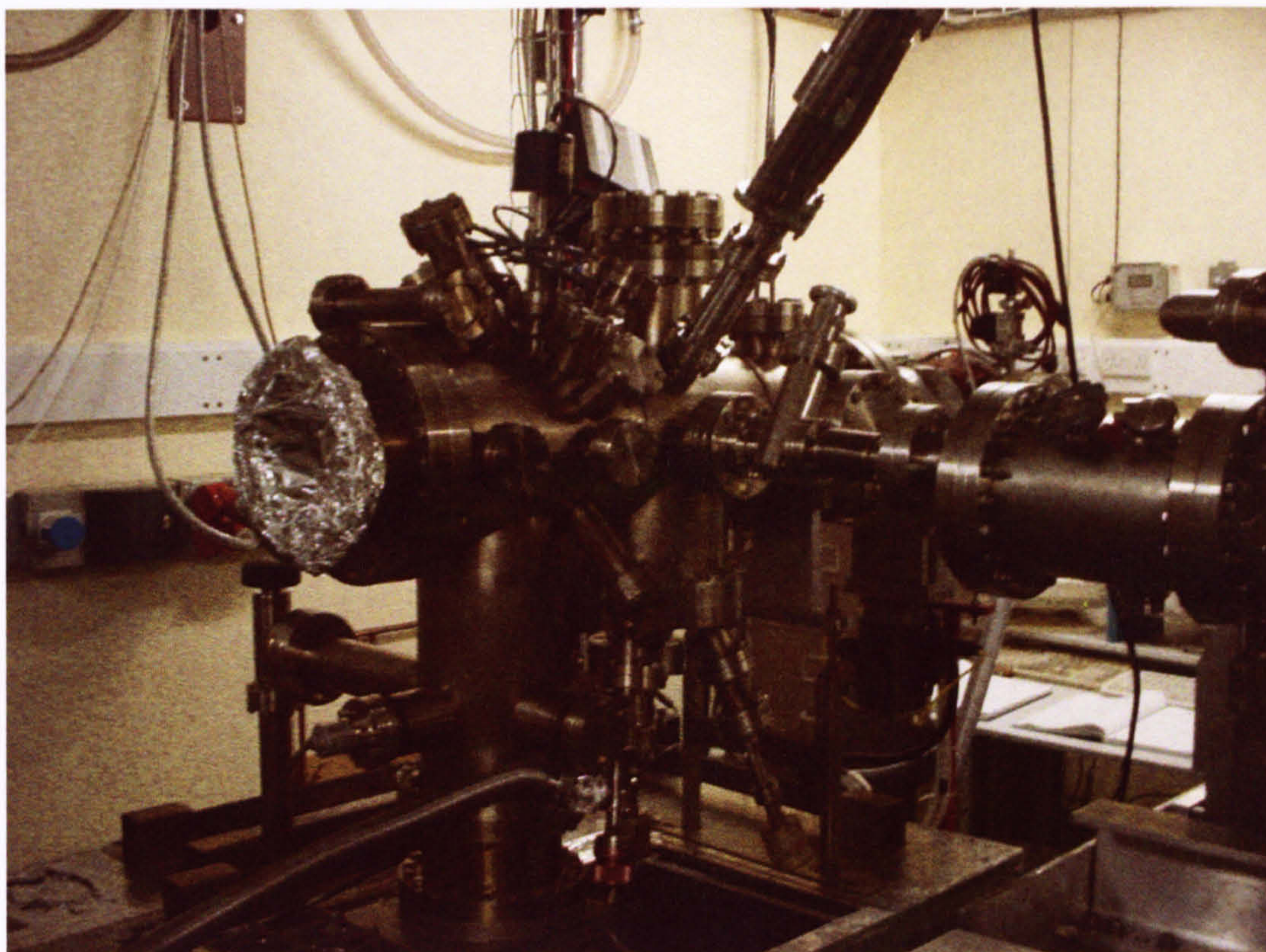


Figure 3.7 ESCA showing the removed sample arm

3.1.3 Samples

A sample consists of 2 parts; a substrate and the deposited material. Substrates must be chosen depending upon the measurement technique to be employed. For example magnetometry measurements require a non-magnetic material. The hydrocarbon polyetheretherketone (PEEK) has been used for all VSM samples in this work. Its chemical structure is shown in figure 3.8.

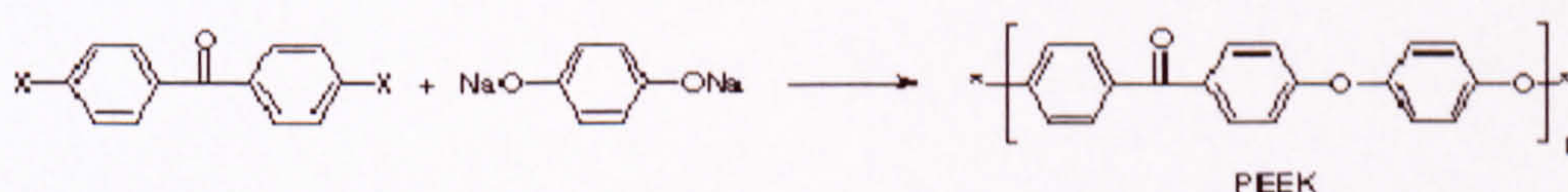


Figure 3.8 Chemical structure of PEEK

PEEK is partially crystalline, and has a glass transition temperature of 143 °C and a melting temperature of 334 °C. The material is resistant to both organic and aqueous environments and is used in bearings, piston parts, pumps, compressor plate valves, and cable insulation applications. Its malleable properties are essential for insertion into the cylindrical sample space of the magnetometer. Figure 3.9 shows the plastic ampoule within which the sample must be placed. This ampoule is also non-magnetic and generates a small DM signal.

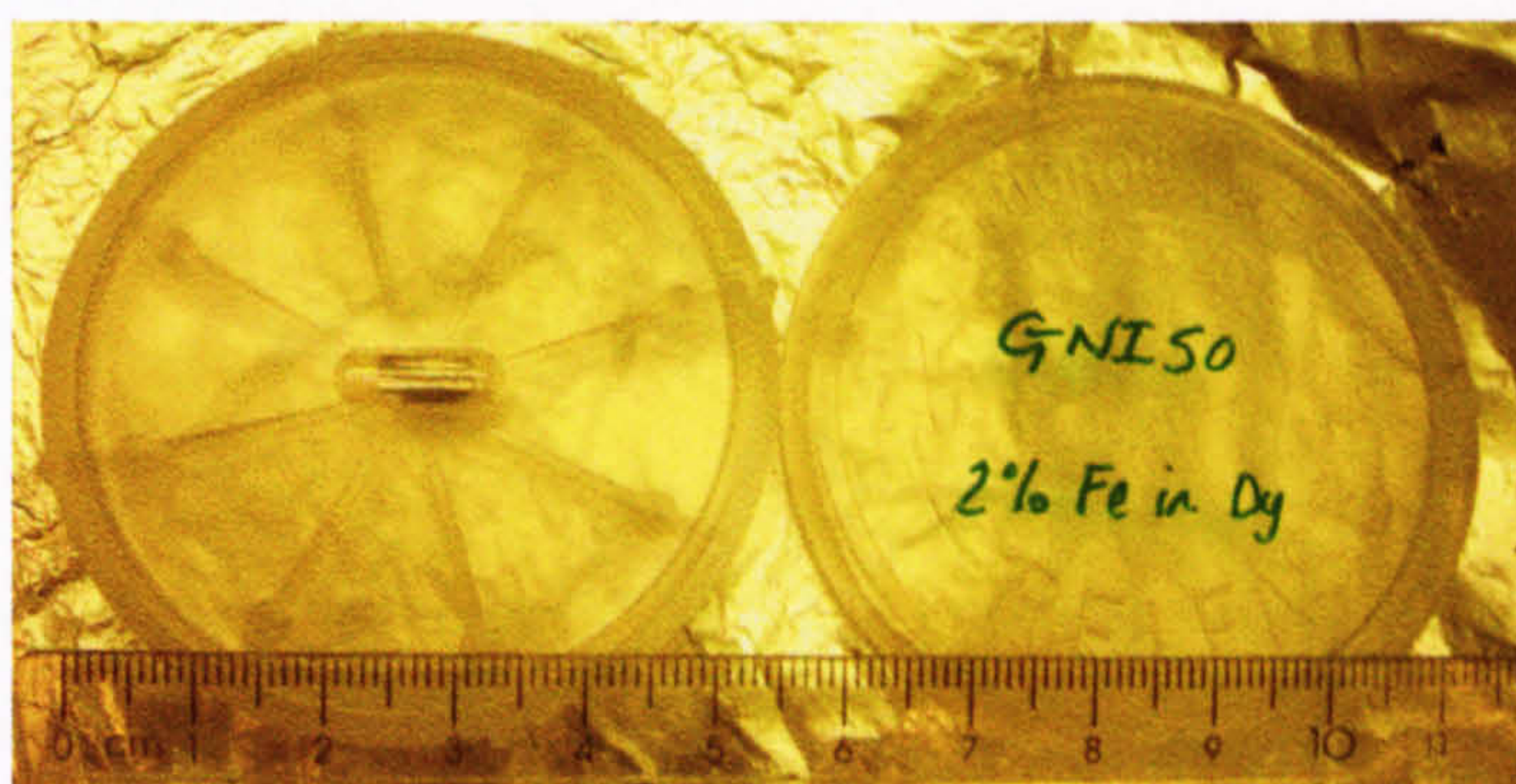


Figure 3.9 Circular plastic sample case keeps plastic ampoule protected from the atmosphere. The ampoule contains a rolled up piece of PEEK upon which the dark circular shape of the deposition can just be seen.

The PEEK VSM substrates in this work were cut to a rectangular size 11x20mm and cleaned using a process of acid etching (in a solution of 10% nitric acid) and two ultrasonic treatments first in acetone then in IPA (Propan-2-ol). The PEEK substrates are 1 μm in thickness.

Mylar is a trade name of DuPont Teijin Films for biaxially-oriented polyethylene terephthalate (BOPET) polyester film. It was used as the substrate for the first batch of XMCD samples as detailed in Chapter 4 of this thesis. Mylar was chosen because of its high tensile strength, chemical and dimensional stability and transparency. Mylar has been used successfully in many experiments, Leuenberger et al used a Mylar-foil for Gd samples²⁴, however, it transpired that this substrate was entirely unsuitable for our experimental arrangements.

C-coated TEM grids as shown in figure 3.10 are used as substrates for transmission mode XMCD samples and in the TEM itself. The slit width in the copper mesh is 0.15mm. The 3mm diameter TEM grids are coated in a 5nm layer of carbon.

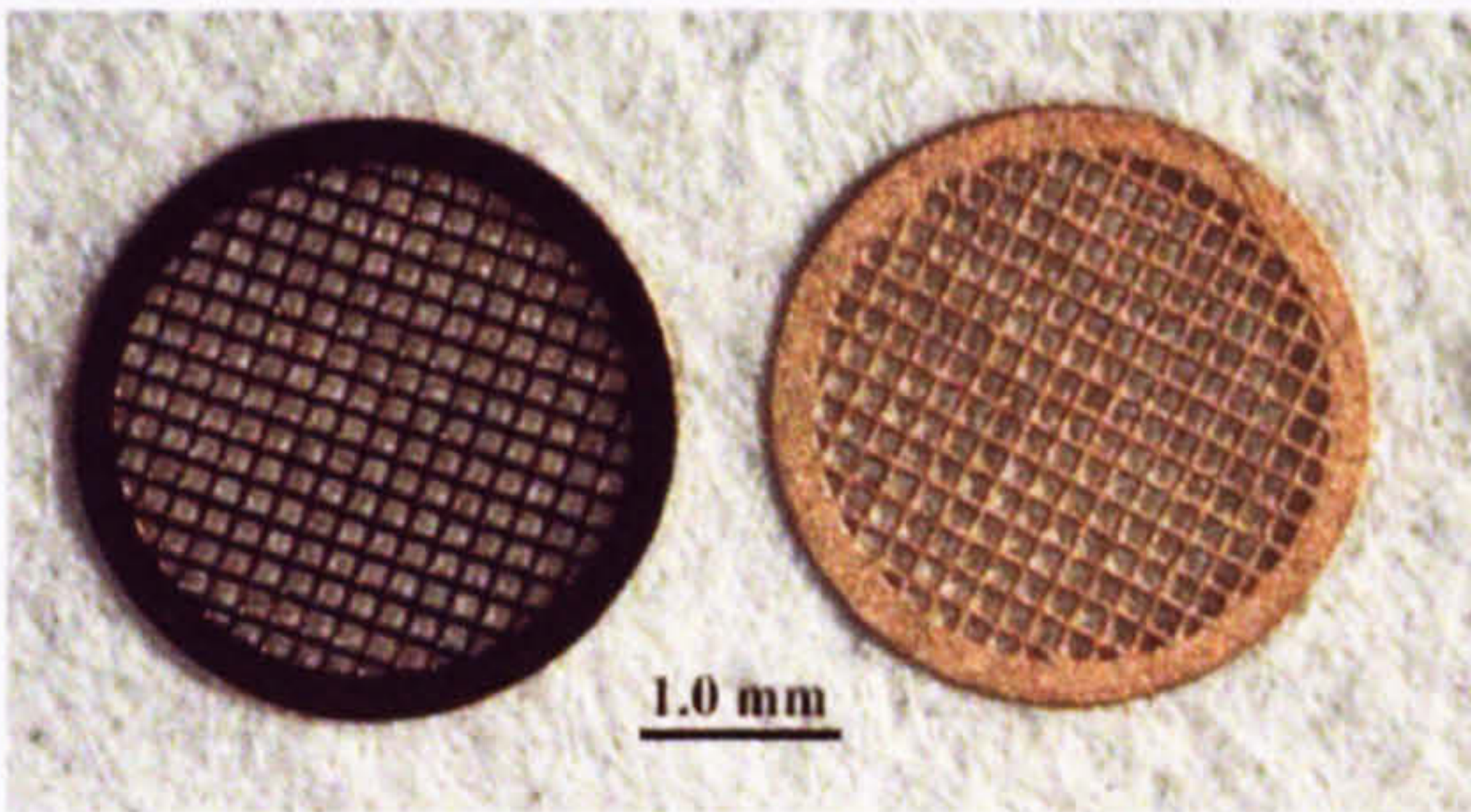


Figure 3.10 TEM grids. (Photo courtesy of Radboud Universiteit, Nijmegen)

Once the correct substrate is chosen the deposited material is built up in layers up to tens of nm in thickness. The sample will then consist of 3 main layers as in figure 3.11.

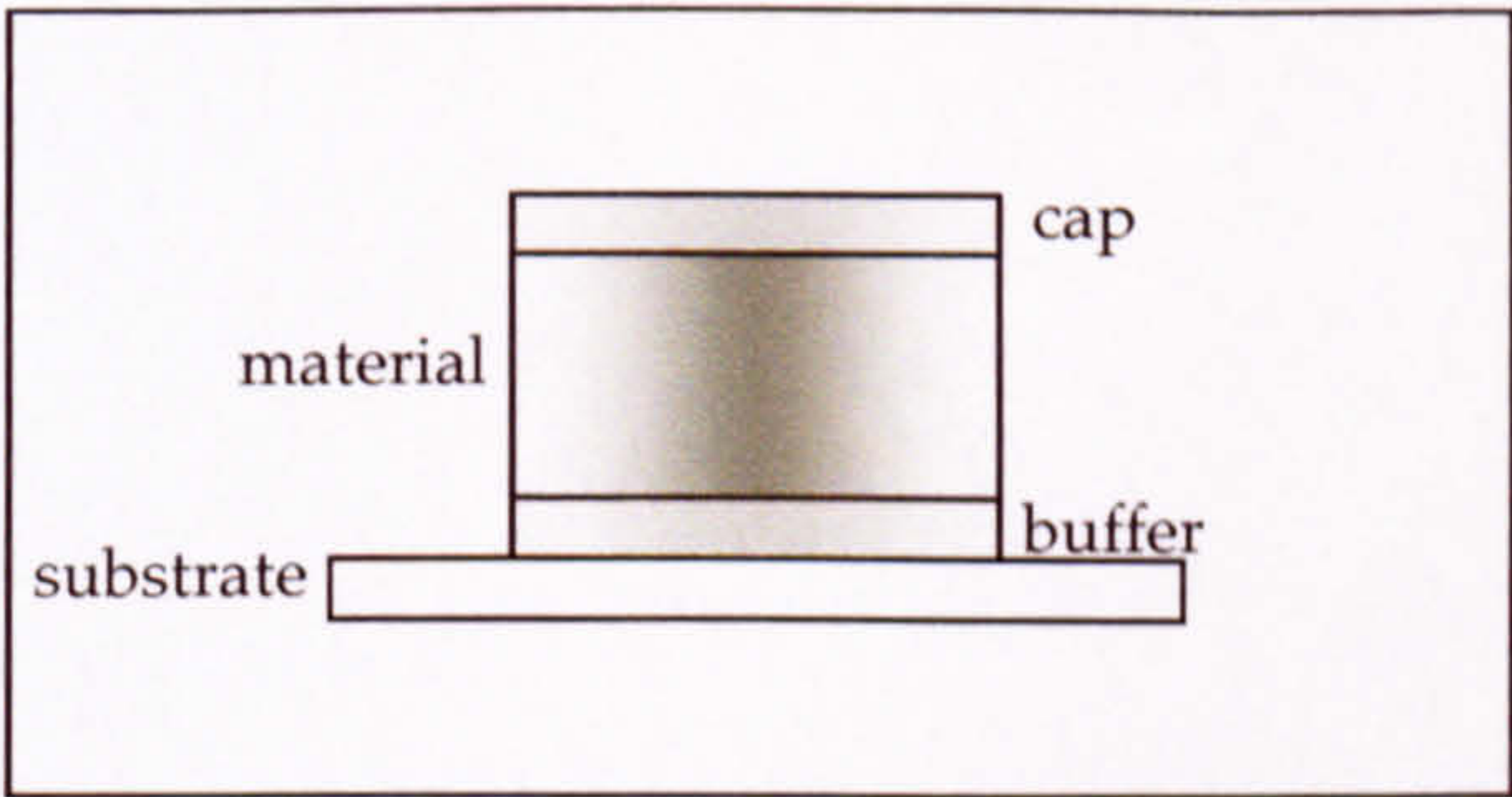


Figure 3.11 Sample representation diagram

In reality a sample will look more like the diagram in figure 3.12,

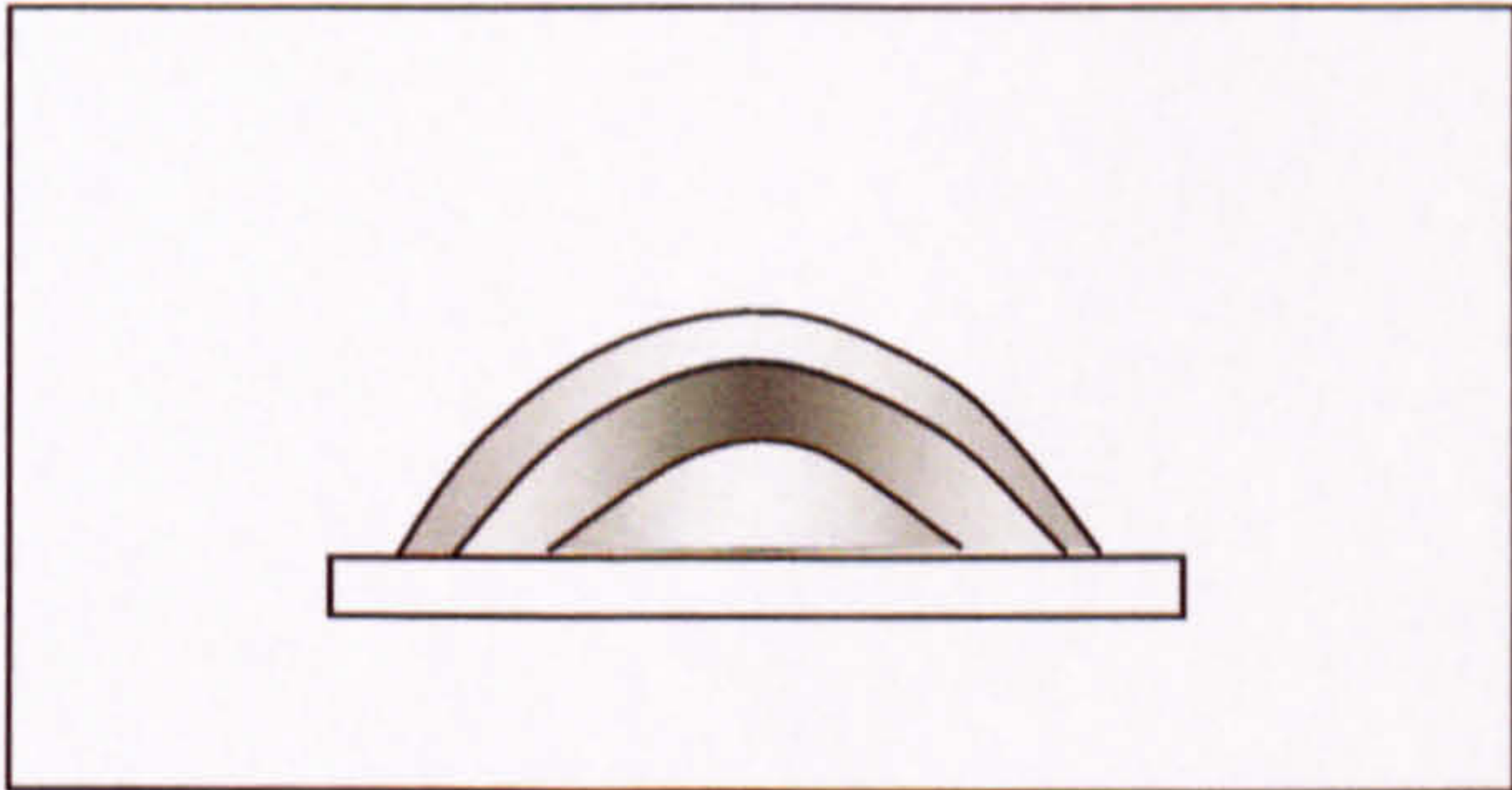


Figure 3.12 Subsequent layers of a sample will overlie those deposited first.

however, for clarity they are usually represented as in figure 3.11. The cap isolates the material from the air where oxidation can irreparably damage the sample and the buffer is to ensure that the sample properties are independent of the substrate material.

Typically a batch of 6 samples will contain 2 control samples and 4 other samples. Control samples will consist of just one material to provide a contrast for any alloyed samples. The diagrams in figure 3.13 are used to describe the construction of the samples.

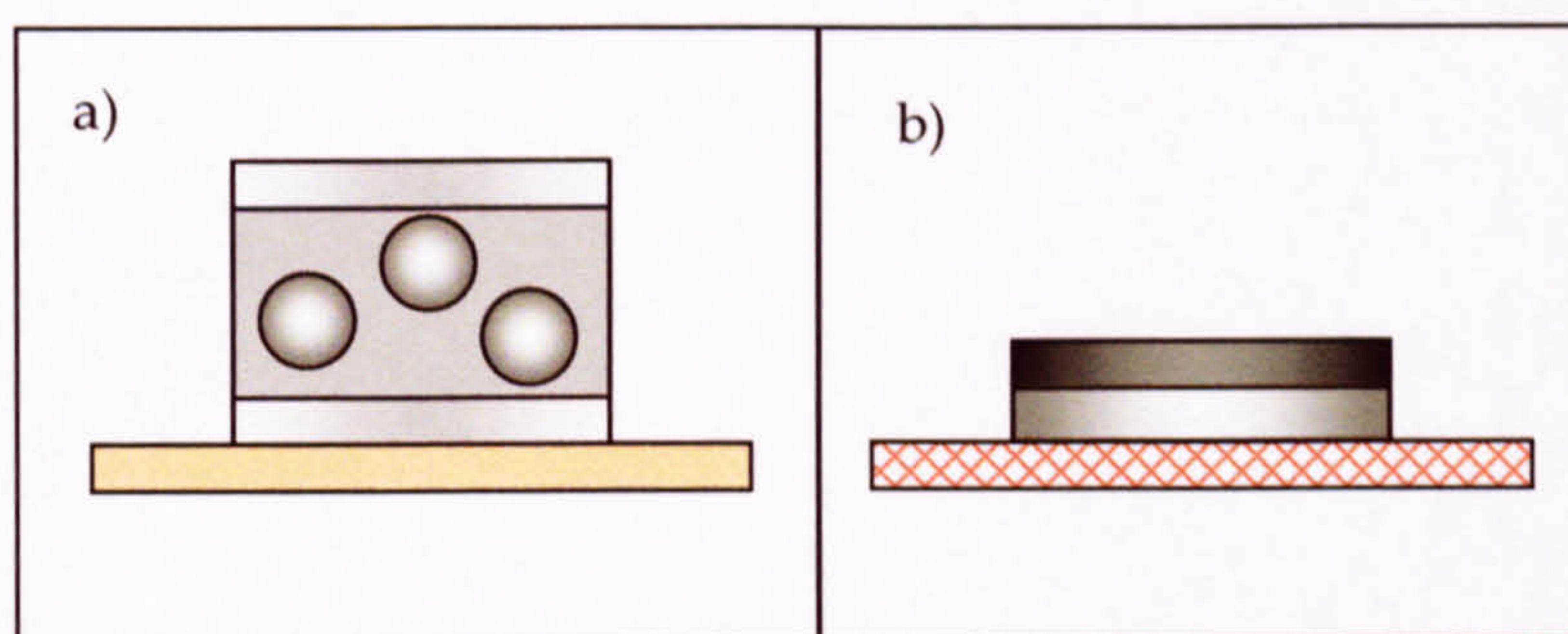


Figure 3.13 Sample diagrams; a) PEEK substrate, Ag buffer and cap, Fe clusters in a matrix; b) TEM grid substrate, no buffer, Fe MBE film, C cap.

When a sample is made from the clusters produced by the source and deposited into a matrix formed by MBE it is described in terms of the volume filling fraction (v.f.f.). The source delivers a cluster flux in a limited range producing a deposition rate in the range 0.05-0.5 nm/min. Evaporators can deposit in the range 0.1-5 nm/min for a number of hours. This means control of the v.f.f. must be managed by the deposition rate of the evaporators in ESCA. The nanoparticles are typically of a diameter of 2nm. This means that when they are deposited into a matrix with a v.f.f. of 10% there is only a distance of ~2.5nm between them. By the time the v.f.f. has risen to 25% this distance has reduced to ~1nm and at least half of the clusters will be in contact with a neighbouring cluster. 20-25% represents the percolation threshold²⁵.

Whilst the sample is described in terms of the v.f.f. of clusters within the matrix, the clusters are described as an equivalent thickness of material. So if a sample was 10% v.f.f. Fe in Ag of total thickness 100nm, it would contain an equivalent thickness of Fe of 10nm and therefore an equivalent thickness of Ag of 90nm.

Typically it takes one day to make one sample. MBE films can be made in a few hours once the deposition rates of the evaporators have been established using the XTM. When a capping layer of an unreactive substance, typically Ag or C, has been deposited the samples can be safely removed from ESCA ready for analysis.

3.2 Measurement Techniques

The in-house VSM magnetises samples to provide data about the bulk magnetic moment of a sample. Daresbury synchrotron run by the former CCLRC has several beam lines of which the author used 5U.1 and 7.1. XMCD data was collected during three allocations of beamtime on line 5U.1 which produces a beam of circularly polarized X-rays. EXAFS data was collected on one run at station 7.1 consisting of a double crystal Si(111) monochromator to measure atomic structure.

3.2.1 VSM

The VSM built by Oxford Instruments is capable of generating magnetic fields up to ± 9 Tesla using coils made from superconducting NbTi in a Cu matrix. These coils are cryogenically cooled with liquid helium, He(l) which provides a minimum sample space temperature of 1.4K. When a sample is placed within a uniform magnetic field and made to undergo sinusoidal motion (i.e. mechanically vibrated), there is some magnetic flux change. This induces a voltage in the pick-up coils, which is proportional to the magnetic moment of the sample.

The VSM consists of four concentric internal chambers. An outer vacuum chamber (OVC), a N₂(l) chamber, a He(l) chamber housing the superconducting coils and the sample chamber which can be evacuated or brought to an atmosphere of He(g) by opening a needle valve.

The complete pumping-down procedure takes 3 days to complete. This needs to be done infrequently and usually only if a major fault develops.

Maintaining the cryogen tanks however is a daily commitment with the $N_2(l)$ chamber losing 10% of its contents per day and the $He(l)$ chamber losing 5% of its contents per day when not in use. A 50% $He(l)$ fill takes ~30 minutes. This needs to be done once a week if not in use but for scans using very high fields ($>8.0T$) the $He(l)$ can decrease by as much as 20% per day. Therefore maintenance of the magnetometer is a time consuming and expensive activity.



Figure 3.14 University of Leicester 9T magnetometer

The system measures the total sample magnetisation in units of Am^2 . To obtain the magnetic moment per atom it is essential to know how much material is in the sample. This data is obtained from measurements made by the XTM. The thickness of the sample is used to calculate the expected moment. For a Fe MBE sample this calculation can be compared to the magnetometry data to effectively calibrate the magnetometer.

3.2.2 XMCD

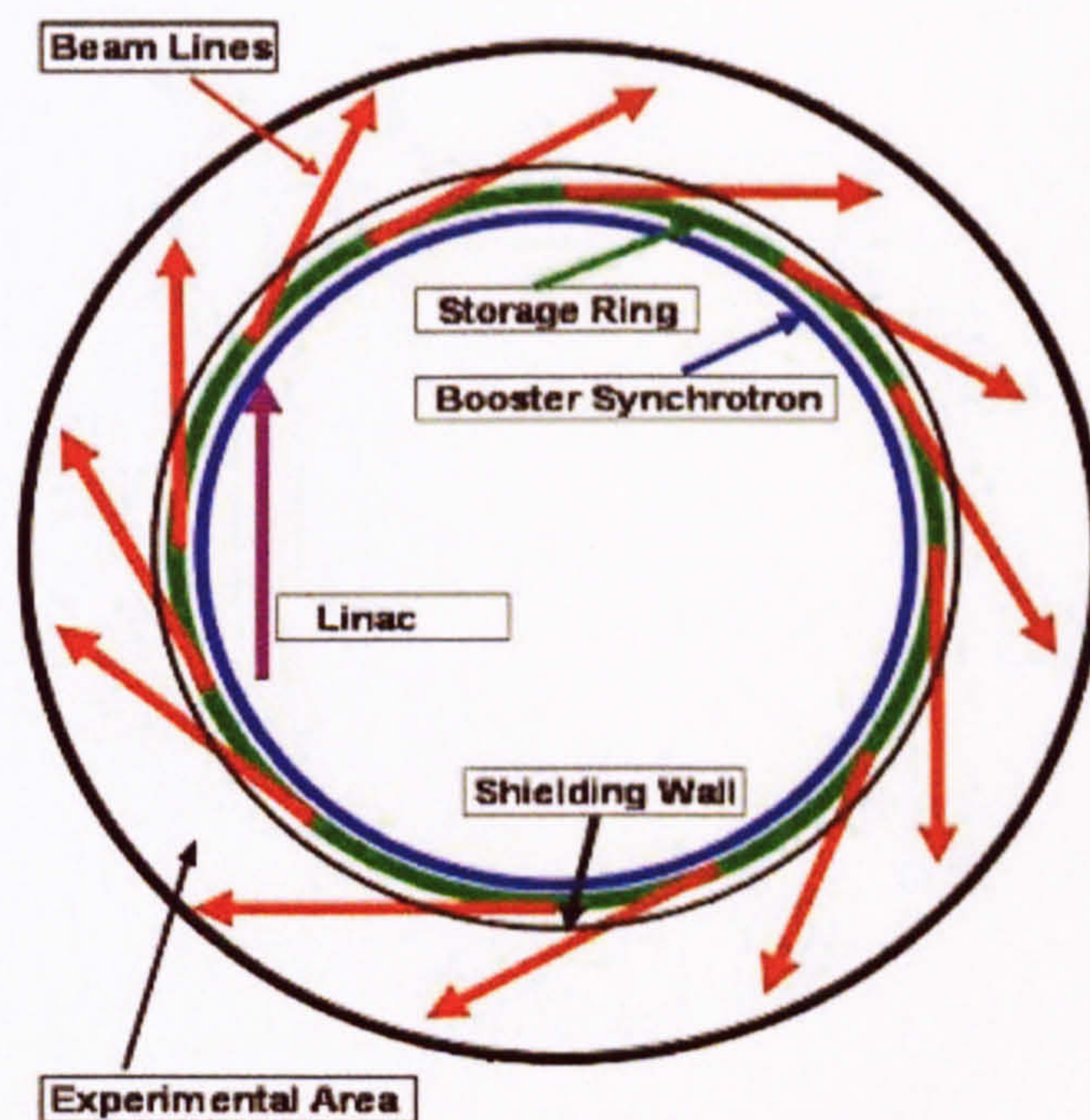


Figure 3.15 Diagram of a synchrotron. (Picture courtesy LLS, Barcelona)

Electrons are inserted into the Linac (Linear Accelerator) then accelerated to speeds close to the speed of light around the booster until X-Rays are emitted which are channelled along beam-lines for use in end-stations. Many techniques can be employed for probing the atomic and sub-atomic properties of samples using these X-Rays such as surface diffraction and linear or circular dichroism.

The X-ray beam generated at Daresbury passes through magnetic undulators before exiting down beamline 5U.1. The undulators circularly polarise the beam either left-handed or right-handed whilst the end station incorporates flipping magnets to reverse the sample magnetisation. The sample is placed in the path of the beam within the magnetic array. Figure 3.16 shows a photograph taken of the end station octopole with samples mounted on the cryostat (top centre) and red crane cage (right) supporting the He(l) dewar for cooling to $\sim 30\text{K}$.

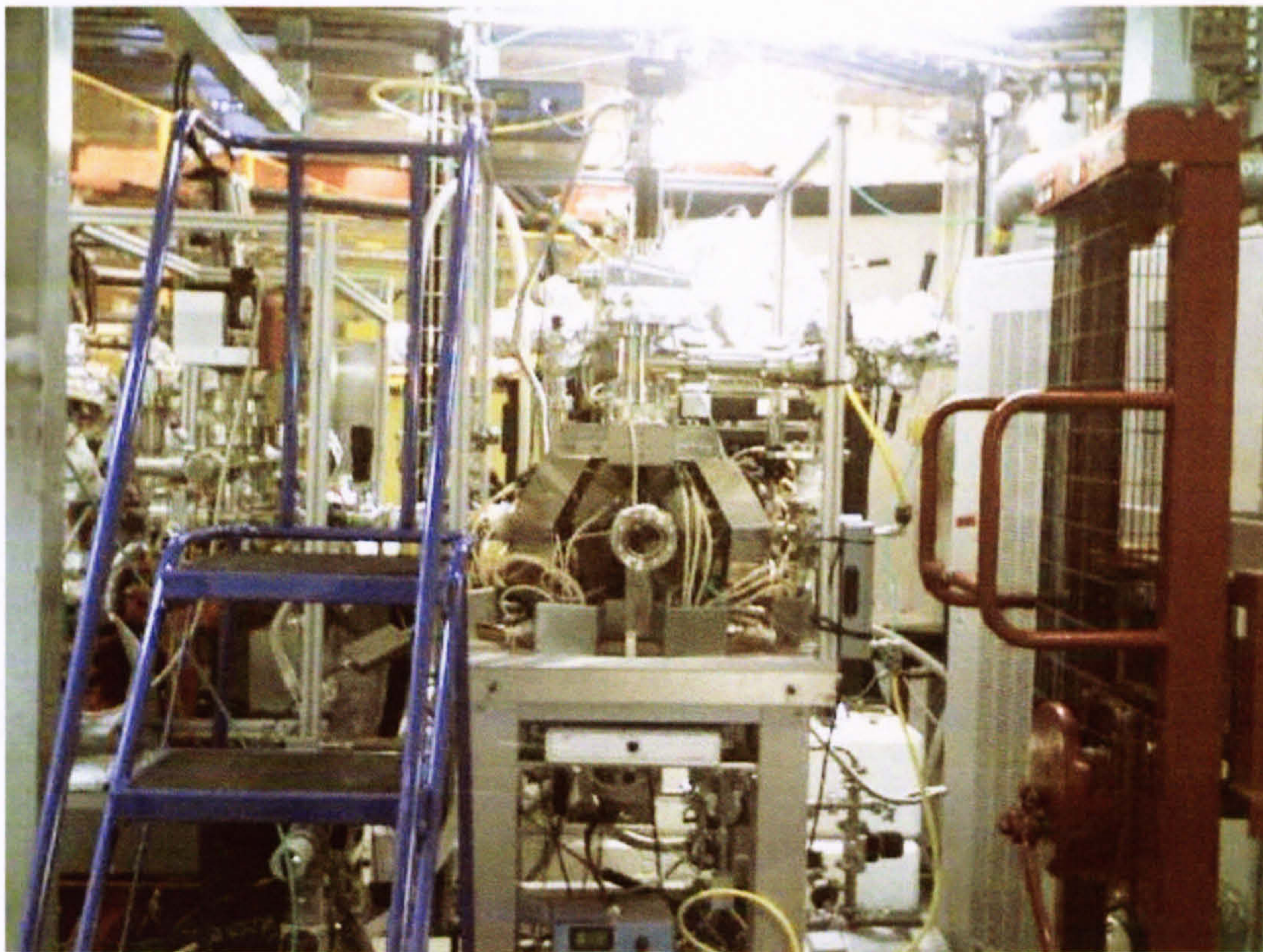


Figure 3.16 POMS Octapole magnet on the 5U.1 end station (Photo used courtesy of Daresbury Laboratory - Magnetic Spectroscopy Group)

There are 2 methods of obtaining the magnitude of the X-ray absorption required to obtain the XMCD signal. Firstly by measuring the sample drain current or secondly by measuring the change in transmission of the x-ray beam as it passes through the sample. In transmission mode, the absorption of the sample I_{sample} is proportional to I_t / I_0 .

$$I_t = I_0 e^{-\mu x} \quad (3.3)$$

I_t = transmitted current

I_0 = incident current

μ = absorption coefficient of sample

x = sample thickness

A Au evaporator was used to deposit a new, clean, highly electrically conductive Au layer onto the I_0 and I_t meshes so that the background would normalise out completely and reproducibly. Contaminated I_0 and I_t meshes introduce spurious features into the spectra,

and charging of the meshes causes deformation of the backgrounds. In XMCD normalisation is extremely important because the normalised spectra from opposite magnet or light polarisations are subtracted, so the difference may be very small, and the transmission mode is very sensitive to the background absorption level. A high voltage is needed on the measuring grids.

If both the drain current and transmission are measured the two sets of data can be used to better normalise the data.

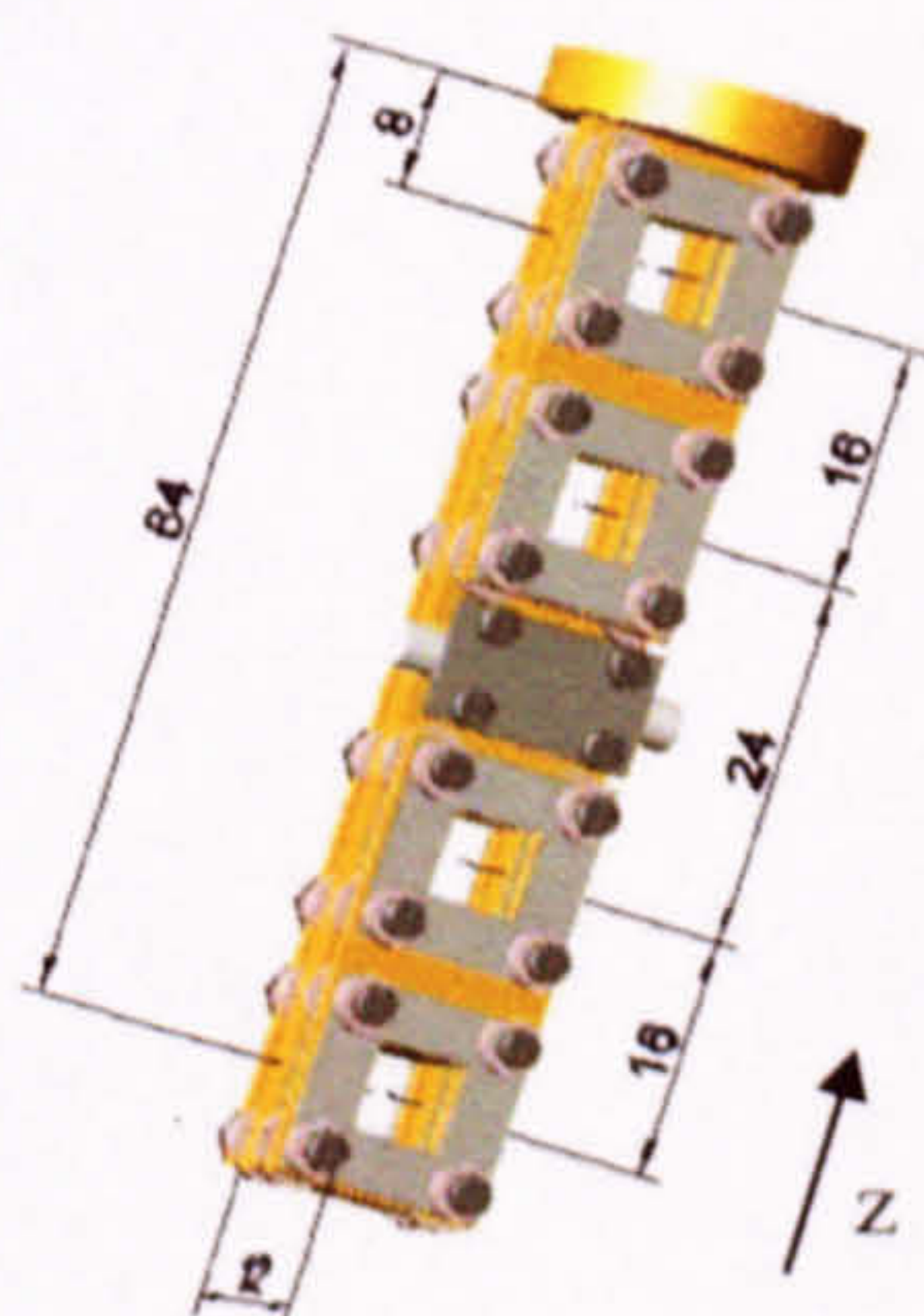


Figure 3.17 Sample holder for XMCD samples (scale in mm)

Samples for transmission measurements are mounted on a sample holder as shown in figure 3.17. This is then manipulated in the z direction to move different samples into the path of the beam.

3.2.3 TEM

The University of Leicester Engineering Department has a JEOL-JEM 2100 TEM which has been used to generate the images used in this thesis. TEM is an imaging technique whereby a beam of electrons is focused onto a specimen causing an enlarged version to appear on a fluorescent screen. The maximum resolution that one can image is determined by the wavelength of the particles that are being used to probe the sample. The set up used is shown below in figure 3.18.

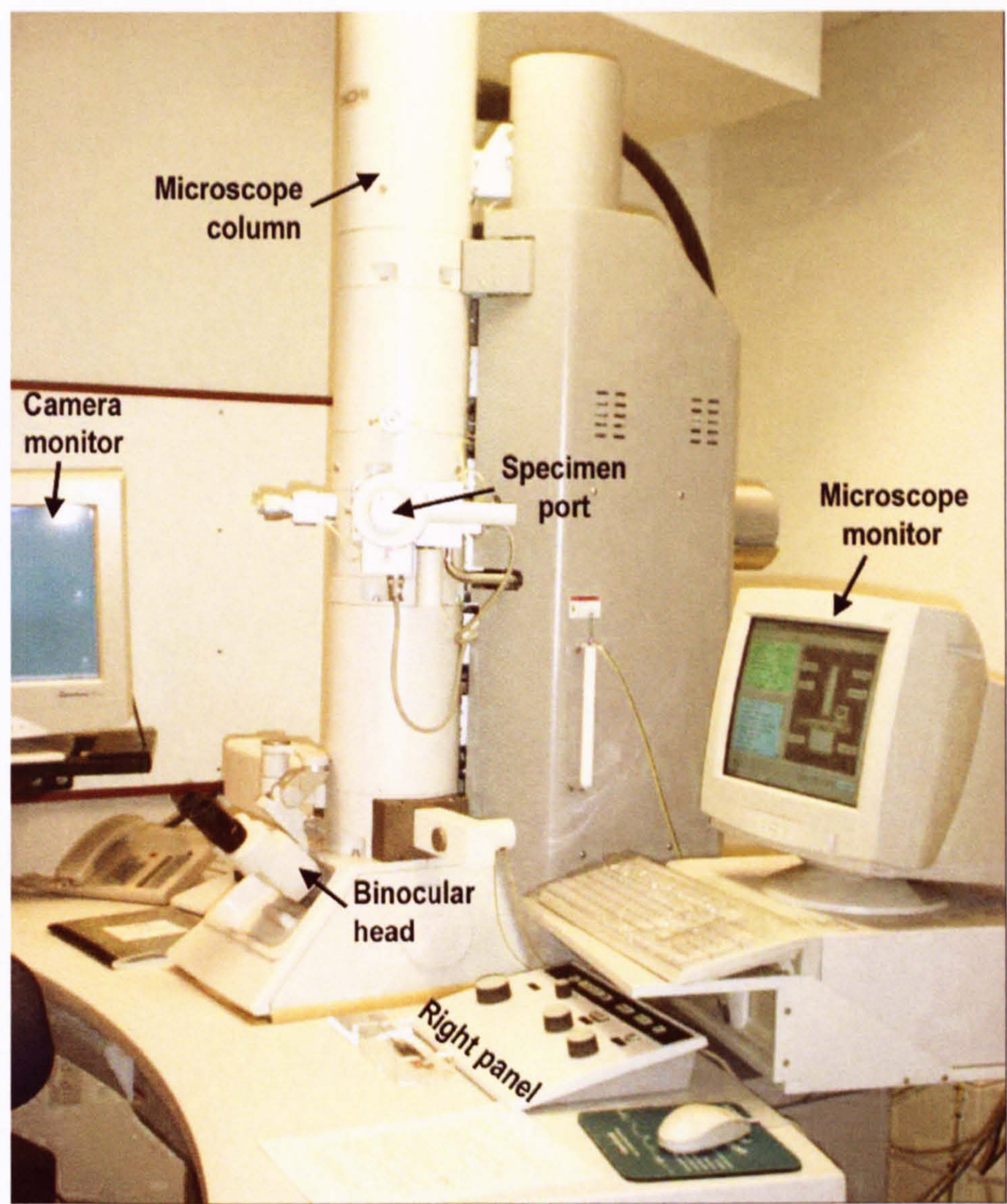


Figure 3.18 Image of a TEM microscope, manual controls and PC acting as a camera.

The JEOL-JEM 2100 works thermionically such that the electrons are produced from a heated filament. Samples must not be too thick. If the thickness is of the order of the extinction length, some reflected beams may have very small intensities because they are diffracted back into the primary beam. The objective lens will then not be able to reconstruct the spatial frequencies contained in these reflections; the image will look like a different lattice.

3.3 Preliminary Investigations

In order to gain experience in operation of the source two magnetometry samples were made. The capabilities of the source were then investigated by altering the configuration of the internal parts of the source (see fig 3.3) and measuring the resultant effects on the mass distribution. Clusters made from different materials can be produced by the source however, to change from Fe to Co, for example, involves changing the entire crucible assembly, cleaning the Cu feedthroughs with acetone and IPA and removing the water tank including the first Cu plate for thorough cleaning.

3.3.1 SQUID Samples

Two SQUID (Superconducting QUantum Interference Device) samples were made with 1% and 10% v.f.f. Co in an Ag matrix. A SQUID substrate shown in figure 3.19 holds 4 PEEK discs in place. Each disc is 3mm in diameter and 1mm thick. Two such substrates were mounted into ESCA.



Figure 3.19 SQUID substrate

The sample diagram is shown for clarity in figure 3.20.

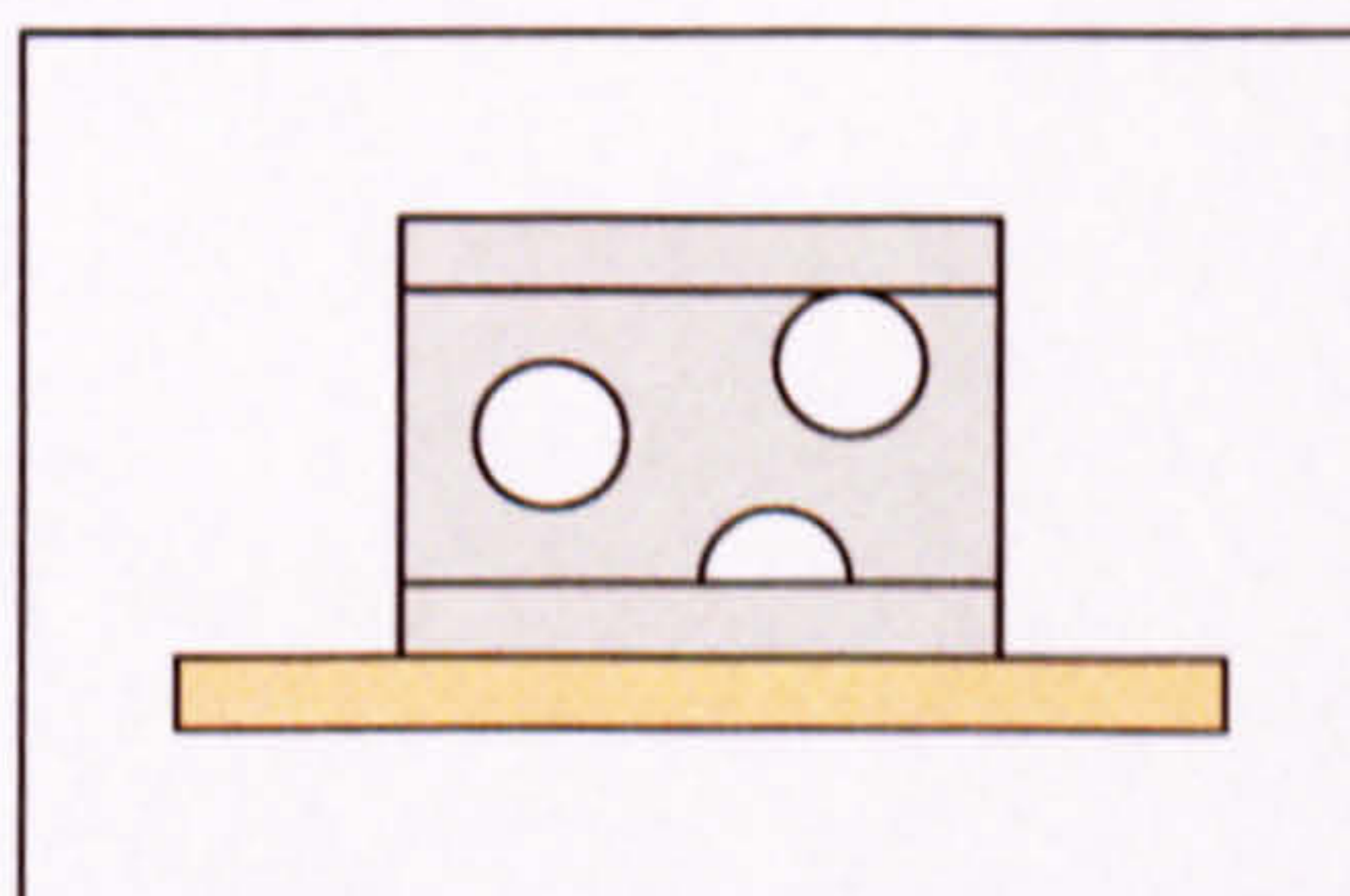


Figure 3.20 SQUID substrate, Ag buffer, Co in Ag matrix, Ag cap

Measurement of the Co cluster beam produced the mass spectra in figure 3.21 showing the distribution of cluster sizes produced by the source.

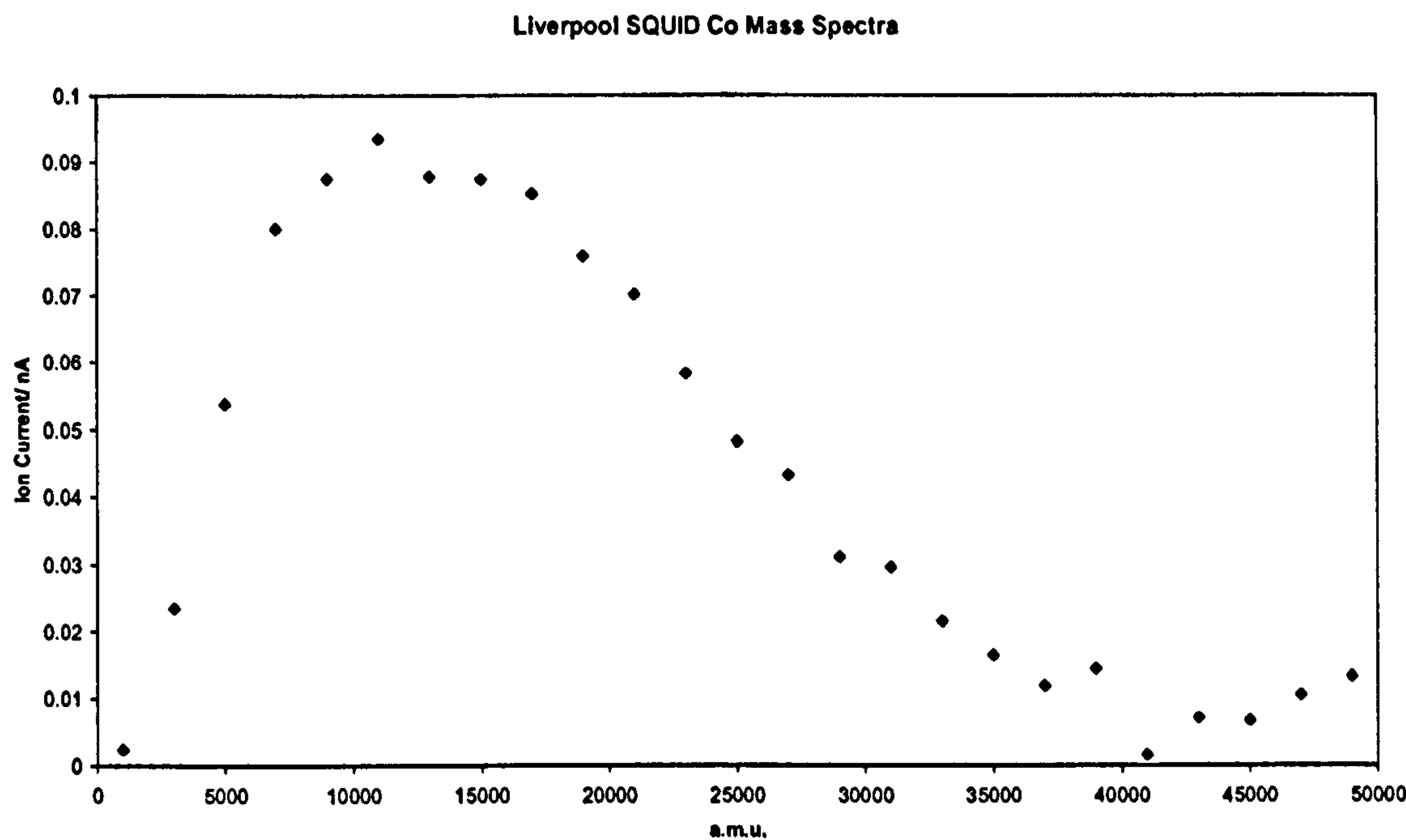


Figure 3.21 Mass spectra of Co as used in both SQUID samples.

The peak at ~12,000 a.m.u. corresponds to a majority cluster diameter of approximately 1.7nm. This value, when combined with the VSM magnetometry data, can be used to calculate the anisotropy constant of the material.

The two Co samples were sent to the University of Liverpool for measurement in their SQUID Magnetometer. Figure 3.22 shows a basic schematic of how a SQUID magnetometer works.

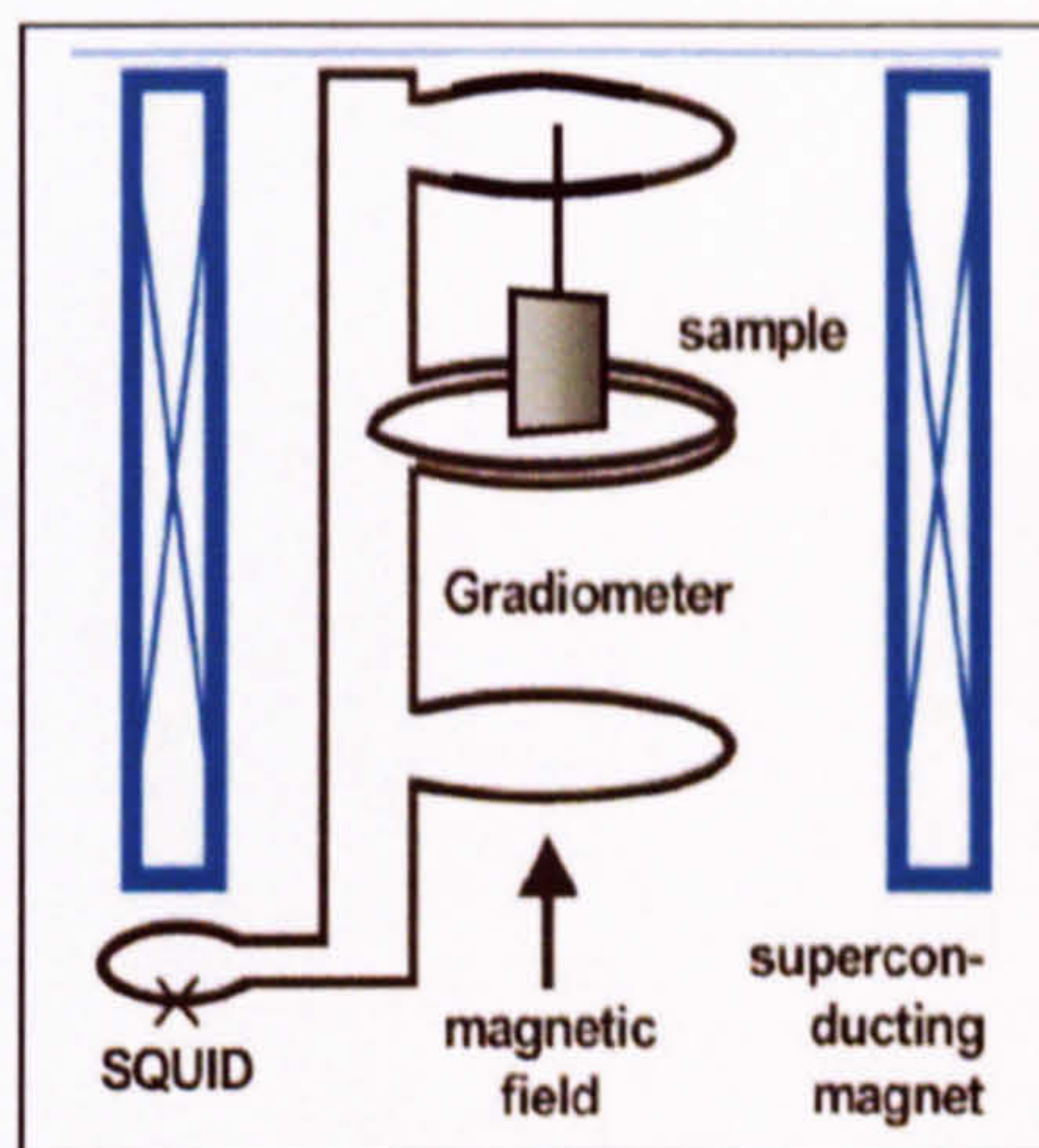


Figure 3.22 Diagram of a SQUID magnetometer

Superconducting magnets kept at He(l) temperature ($\sim 4\text{K}$) produce a uniform magnetic field. A superconducting detection coil acts as a pick-up system within the uniform magnetic field region. The SQUID device is usually a thin film that functions as an extremely sensitive current-to-voltage-converter. The magnetic moment of the sample induces an electric current in the pick-up coil system. A change in the magnetic flux of these coils changes the persistent current in the detection circuit, which produces a variation in the SQUID output voltage proportional to the magnetic moment of the sample.

Isofields were generated upon cooling the samples both within an applied magnetic field and without. Figure 3.23 shows the fc data and zfc data illustrating the blocking temperature, T_b , of the 1% sample. The blocking temperature indicates the point above which a sample is SPM. The open circles show the fc data whilst the filled squares show the zfc data.

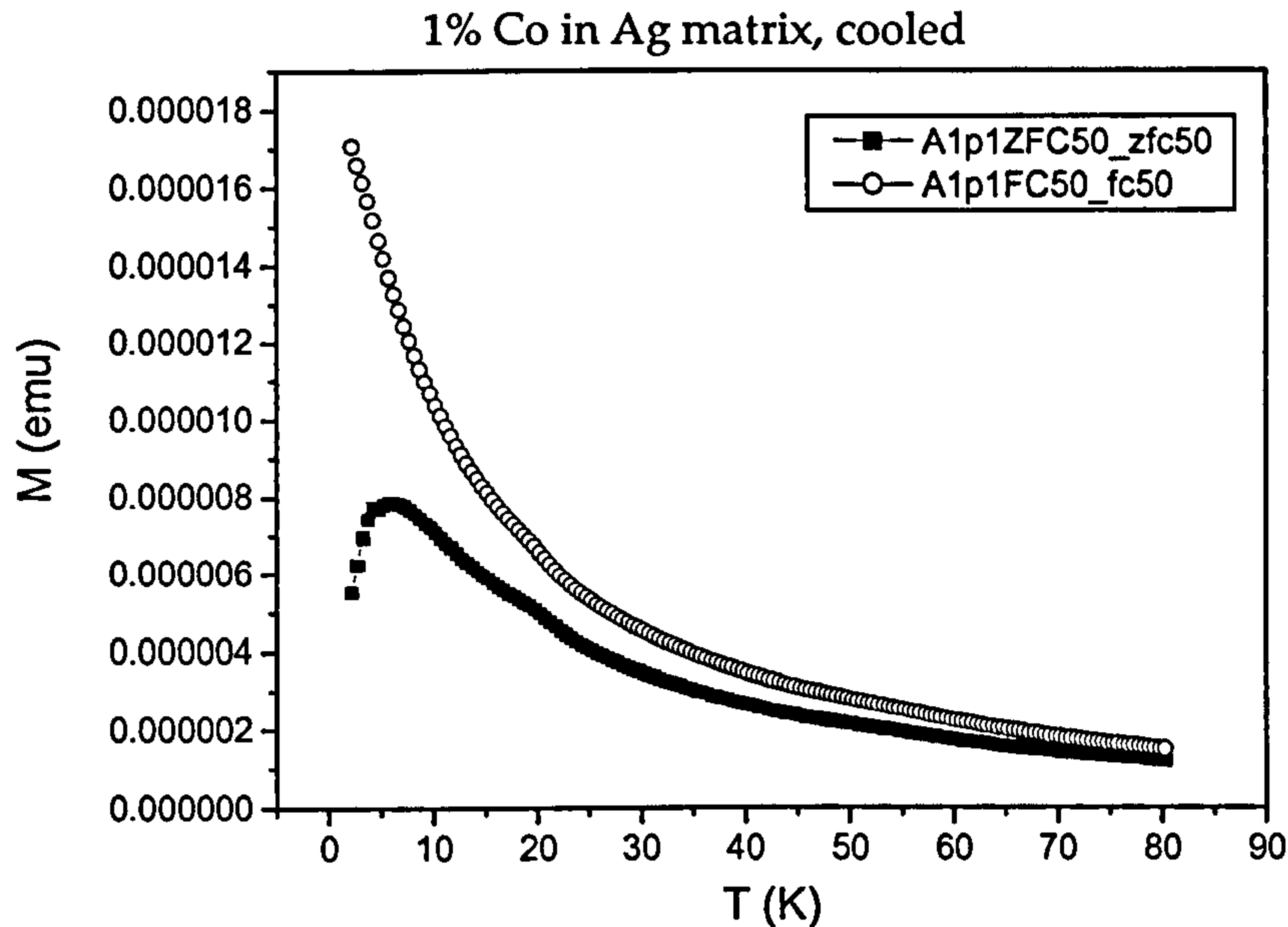


Figure 3.23 VSM data obtained from Liverpool University on the 1% SQUID sample

The blocking temperature of a cluster with a volume V , and anisotropy constant, K is given by:

$$T_b = \frac{KV}{k_B \ln \left(\frac{\tau}{\tau_0} \right)} \quad (3.4)$$

τ = measurement time (~1000s for a DC magnetometry sample)

τ_0 = lifetime due to the natural gyromagnetic frequency of the particles and is normally taken to be 1ns

From this equation the anisotropy constant can be calculated. Reading from the graph the zfc sample has a blocking temperature of ~6K. The volume of each cluster can be calculated using the diameter values obtained from fig. 3.21 combining to give a magnetic anisotropy energy, $K = (1.5 \pm 0.7) \text{MJ m}^{-3}$. This is much larger than the anisotropy constant of bulk Co.

3.3.2 GAS Optimisation

An investigation was carried out to see how a change in the gas pressure in this aggregation region would affect the cluster mass distribution. A significant shift in the mass distribution to a range of 0-5000 a.m.u. would mean clusters containing <20 atoms could be resolved. If this was the case then Fe₁₂ samples, with their enhanced magnetic moments, could be made. This would corroborate the results quoted in the introduction. Three possible options to achieve a significant change in mass distribution were investigated. Firstly, a change in pressure of the He(g) at the agglomeration stage, secondly, a change of gas at the agglomeration stage and finally a reconfiguration of the crucible arrangement within LUMPS. The details of these changes follow.

The metal evaporates into a cloud of He(g) normally maintained at a pressure of 3mbar. This was changed to pressures of 1 and 5mbar and the resulting mass spectra were compared to that of the 3mbar condition. These results are shown in figure 3.24.

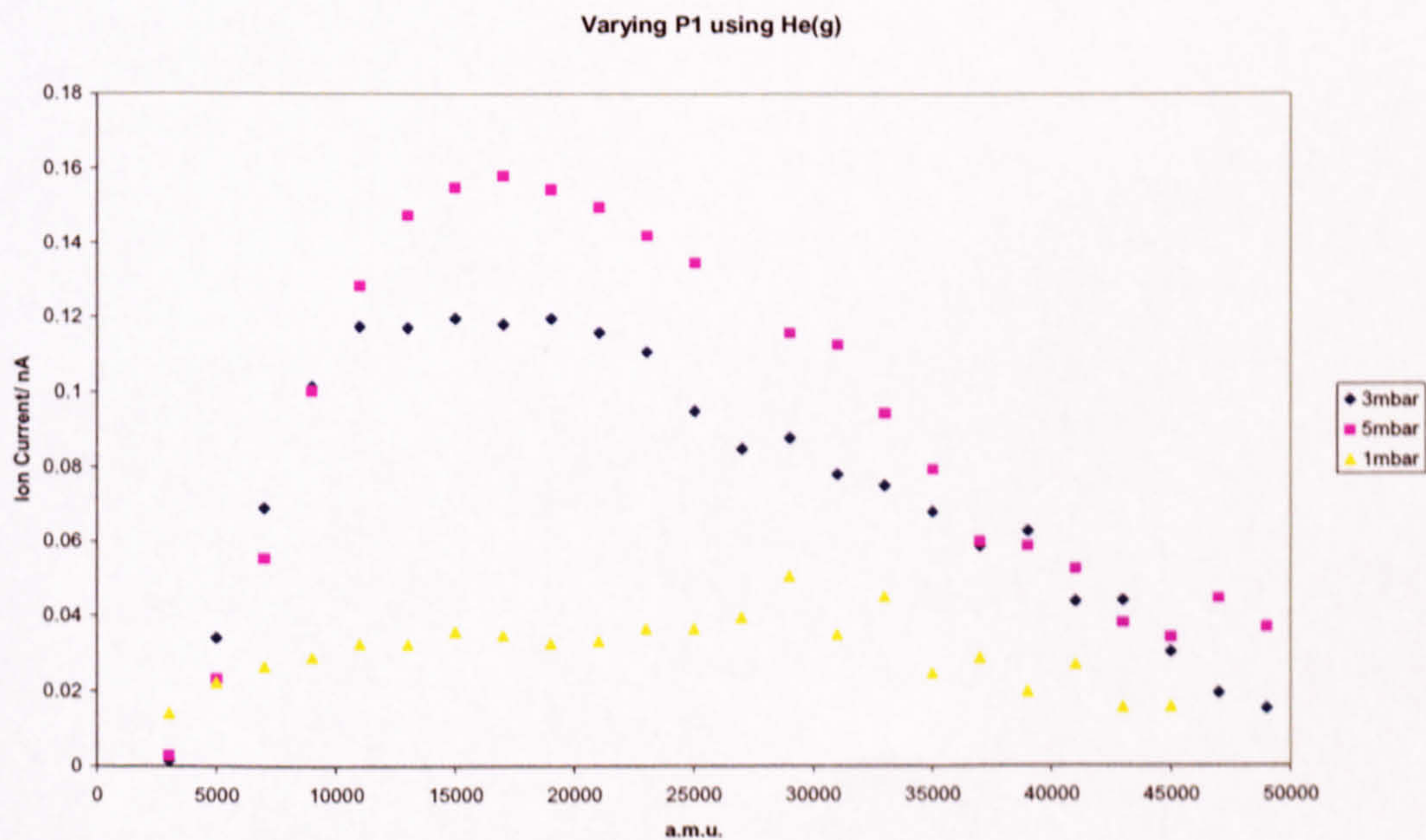


Figure 3.24 Mass spectra taken of Fe clusters formed in differing aggregation pressures.

The results show that cluster flux is proportional to the gas pressure. The mass distribution peaks at $\sim 17,000$ a.m.u. in the 3 and 5 mbar cases. This change is insufficient to decrease the distribution sufficiently for the purpose.

The aggregation gas was then changed to a mixture of He(g) and Ar(g) in varying ratios and varying total pressure. Mass spectra were taken of the cluster beam to measure the effect that this gaseous mixture had on cluster size and flux the results of which are shown in figure 3.25.

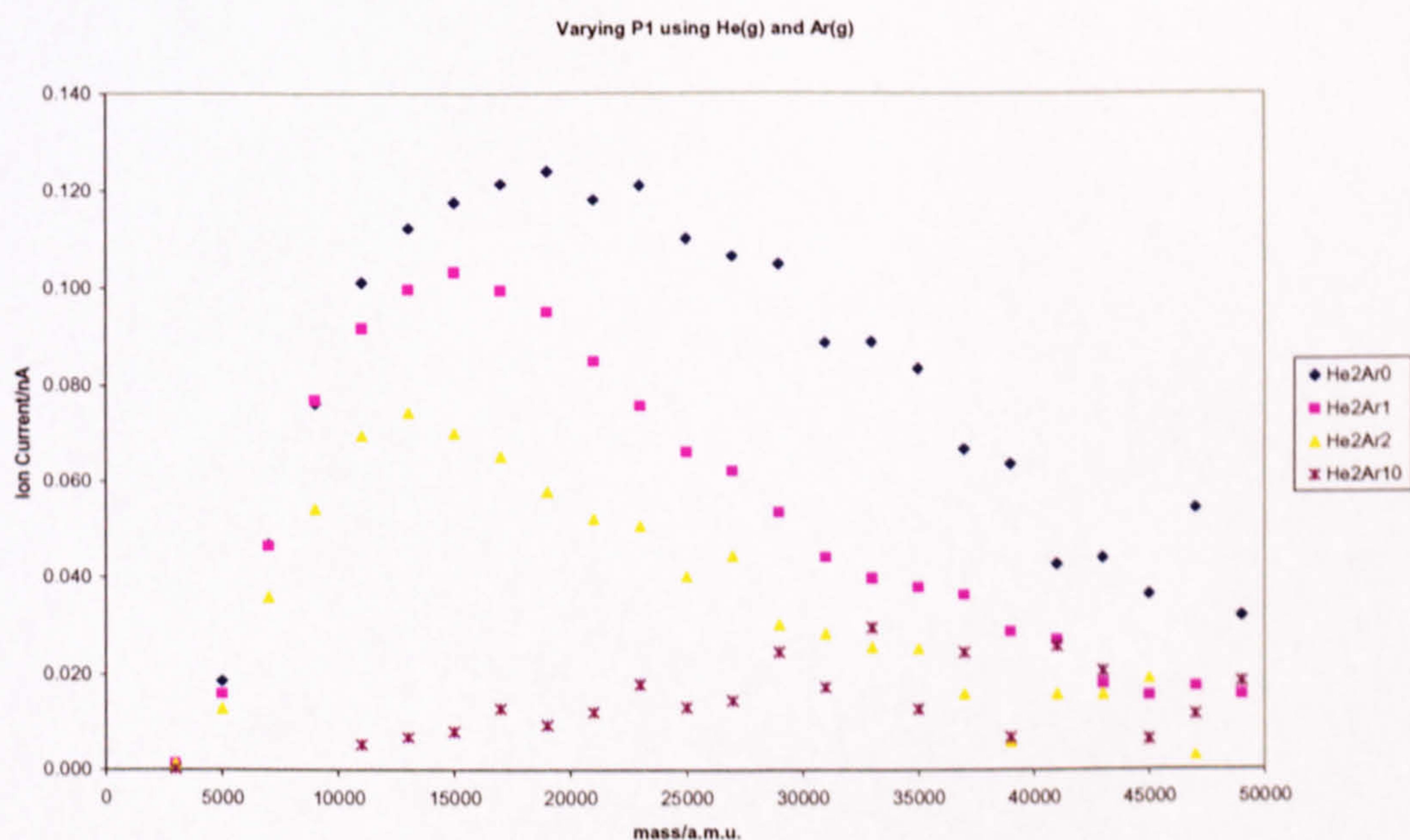


Figure 3.25 Mass spectra taken of Fe clusters formed in differing aggregation pressures in varying He(g):Ar(g) mixtures.

An increasing concentration of Ar(g) decreases the cluster flux and decreases the number of atoms in the majority cluster size. These results could have been improved by changing the position of the skimmer in the y-direction as by changing the pressure at the source, the consequent flux after the focusing lenses changes and this means the skimmer must be realigned for optimum flux. The frequency settings on the quadrupole were changed in an attempt to resolve at the lower masses. Again, the gas mixture was insufficient to obtain a low mass distribution.

The configuration of the crucible assembly was altered such that the position of the heater changed within the chamber. The diagram in figure 3.26 shows the configurations that were tested.

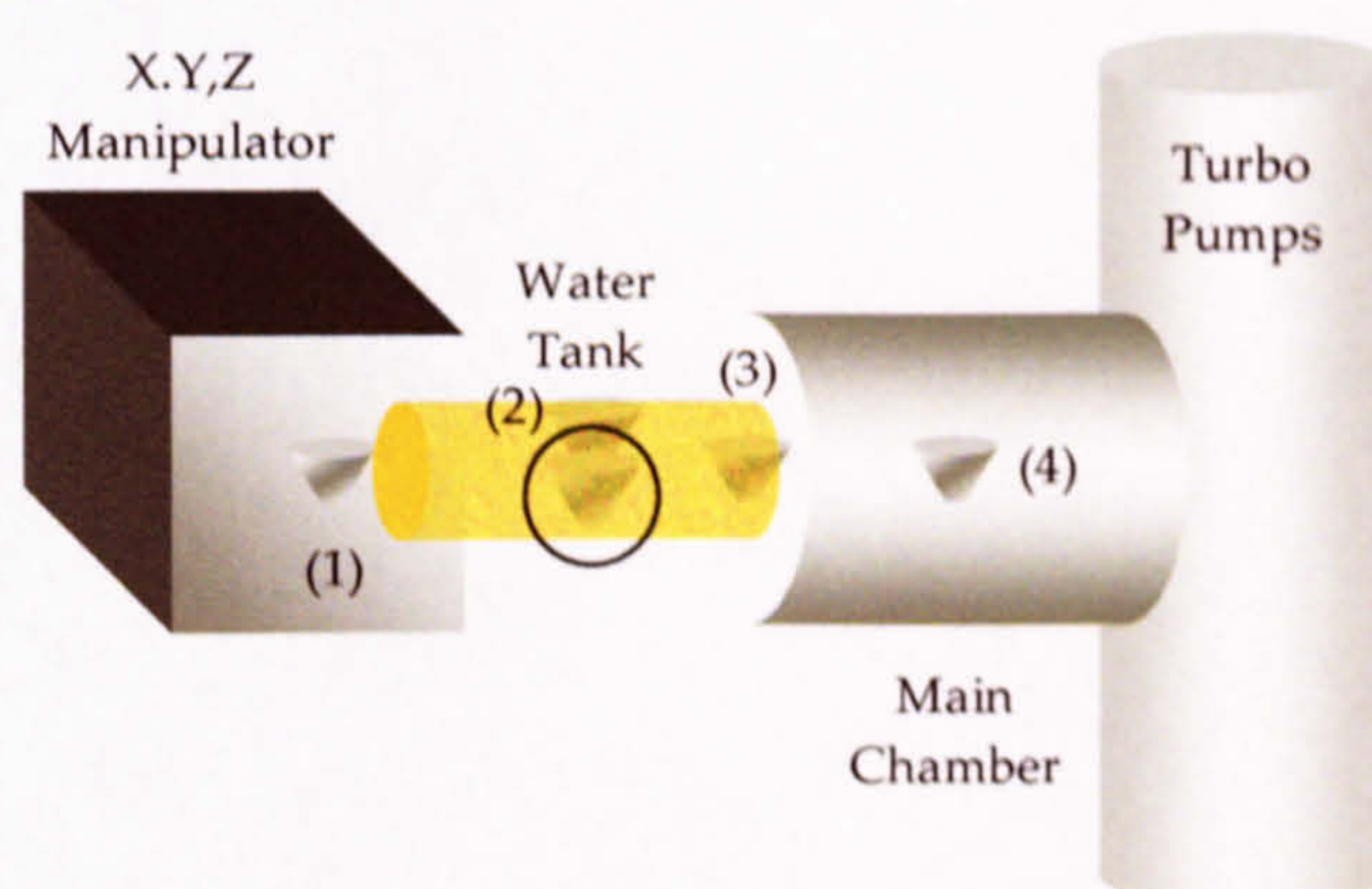


Figure 3.26 Changes to the position of the crucible within the LUMPS chambers. The circled position indicates the original starting position.

An X,Y,Z manipulator was fitted to the water tank such that the crucible could be wound in and out of the water tank. Position (1) held the crucible far back and out of the water tank. Position (2) held the same y-distance as the original position but raised the crucible higher within the water tank i.e. directly in front of the first Cu plate. Position (3) wound the crucible as far in as possible to the limit of the water tank. Position (4) was achieved by removing the X,Y,Z manipulator altogether, using custom built Cu rods of double length and removing the focusing lenses. The final position resulted in the crucible sitting directly in front of the second Cu plate.

The pressures and frequencies were varied in these 5 positions. With so many variables under investigation a simple test was made by bleeding Ar(g) into the chamber, without any Fe(s) evaporating, and the mass distribution measured. The results showed a very clear peak as soon as Ar(g) was introduced however this peak occurred at 100 a.m.u. With an atomic mass of 40 a.m.u. this introduces a 2.5 correction factor on any mass measurements. So in order to see a cluster of Fe₁₂ with a mass of 670 a.m.u. the mass spectra would instead show a peak at ~1700 a.m.u.

The optimum results from three of the configurations are shown in the table of figure 3.27 and graph of figure 3.28.

	f (kHz)	Min (a.m.u)	Peak (a.m.u).	Max (a.m.u)
Original	25	2000	14000	50000
(1)	10	11000	30000	300000
(2)	250	50	100	500

Figure 3.27 Quadrupole optimum frequency settings

These settings indicate that the small cluster could easily be resolved, especially at a high quadrupole frequency. However, the flux in this configuration was very low and the cluster beam was very volatile i.e. the deposition rate was inconsistent. This would make it very difficult when making a sample to know how much material had been deposited. In fact flux and reliability of the cluster beam were poor in all of the new configurations chosen.

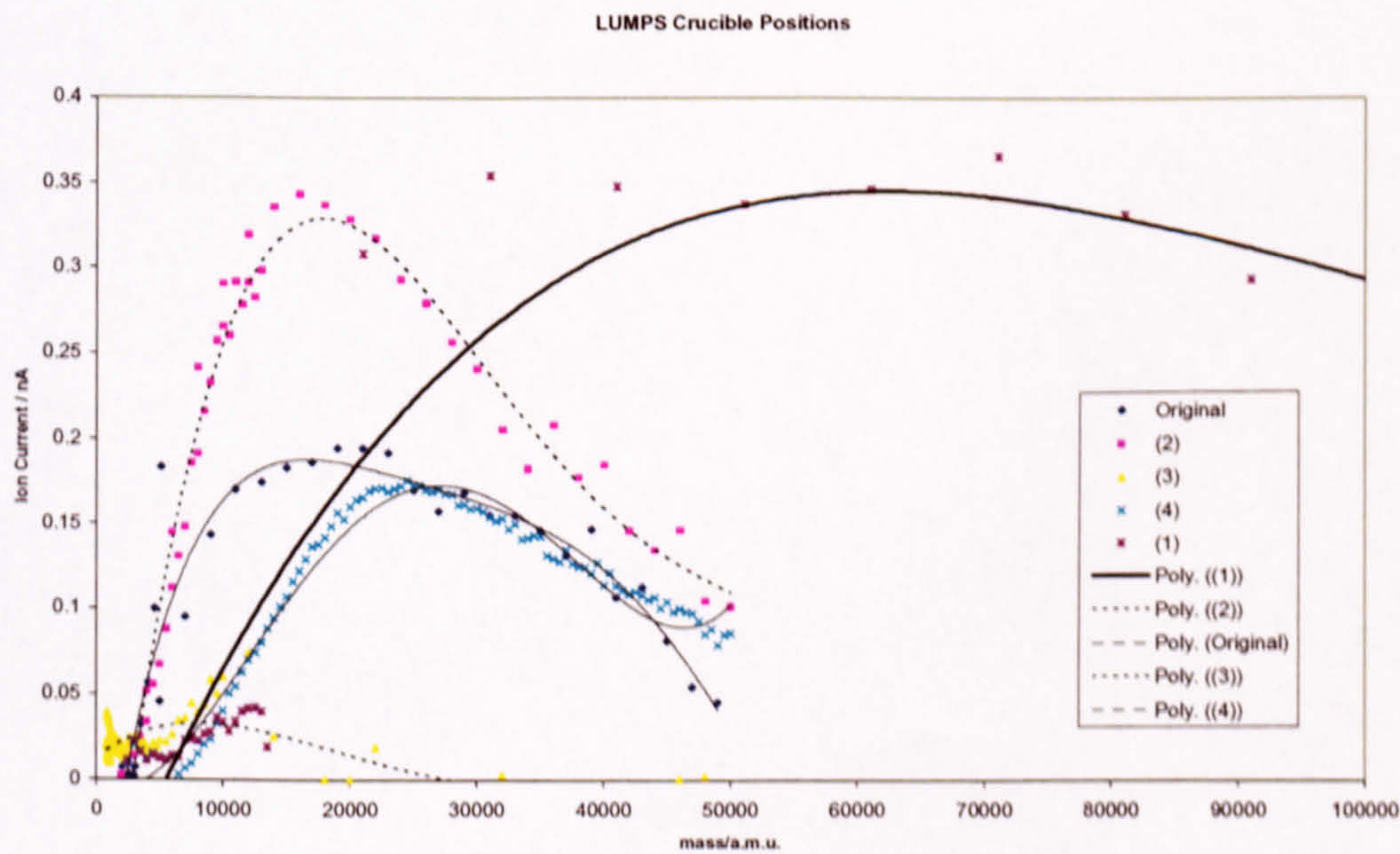


Figure 3.28 Mass spectra of Fe clusters in varying GAS configurations

The interesting feature from the graph in figure 3.28 is that very heavy clusters have been manufactured from the configuration with the heater in position (1) i.e. far back. With the

heater so far back the clusters gain a much longer path in which to form and collect atoms. The optimum position for smaller clusters was (2) as this yielded the largest flux relatively although not at a high enough rate with which to deposit a sample. Also having the heater in position (2) caused spatial problems as the heater mounts were shorting out by contacting with the inside of the water tank so the heater was put back to its original position. This is in accordance with the curve 'Original'. The gas aggregation was reset to 3mbar and the quadrupole was set to 25kHz. With the properties and limitations of the GAS now fully investigated the first samples could be deposited.

“The scientists of today think deeply instead of clearly. One must be sane to think clearly, but one can think deeply and be quite insane. “

Nikola Tesla

July 1934

Chapter 4

Gas-coated Fe

It is well known that gas-phase magnetic nanoparticles containing a few hundred atoms have an enhanced magnetic moment per atom.²⁶ It has also been shown that when the particles are deposited on a surface or embedded in a matrix they maintain enhanced spin and orbital magnetic moments²⁷.

When the magnetic nanoparticles are deposited onto a substrate the magnitude of the magnetic moment of the entire sample depends upon their proximity to each other. Embedded nanoparticles show a decrease from the maximum total magnetic moment, m as the volume-filling fraction is increased²⁸. Eventually the value of m will equal that of a bulk Fe sample such that the effect of addition of the nanoparticles is negligible. This is essentially because the clusters have become so closely packed that the exposed surface atoms responsible for the enhanced magnetism no longer have a reduced number of nearest neighbour atoms. The width of the 3d band increases back again as the clusters physically approach each other and effectively the sample reverts back to a bulk substance.

The studies detailed in this chapter focus on isolating the embedded clusters from one another in order to prevent the formation of a bulk substance by coating the clusters with a monolayer of gas. This would, in theory, protect the individual moments of each cluster and simultaneously allow them to be packed closer together in order to produce a high-moment film.

The motivation for using gas to coat the clusters was inspired by the extensive studies of reactions of iron clusters with hydrogen at the Argonne National Laboratory, Illinois. Mark Knickelbein et al found that the magnetic moment of iron clusters was particularly enhanced for Fe_nH_m systems with $n=13-18$ and $m=12-18$ ⁶. For example Fe_{13} has a magnetic

moment of $2.5 \mu_B/\text{atom}$ whilst $\text{Fe}_{13}\text{H}_{12}$ has a magnetic moment of $4.9 \mu_B/\text{atom}$. Also, Chen et al conducted studies on $\alpha''\text{-Fe}_{16}\text{H}_2$ which was shown to have an increased magnetic moment²⁹. The work of these two groups and the ready availability of $\text{H}_2(\text{g})$ and $\text{N}_2(\text{g})$ were the motivation for attempting to make $\text{Fe}_{18}\text{H}_{18}$ clusters. This is the largest size of cluster made at Argonne with the enhanced magnetic moment and therefore the most likely to be resolved by the quadrupole in LUMPS. With a molecular mass of 1017 a.m.u. and the mass filter resolving at ~ 2.5 times the atomic values this should register as ~ 2540 a.m.u. on a mass spectra. This is within the lower limits of the resolution of the quadrupole.

The gas inlet for the coating gases was positioned to inject after the focusing lenses (see fig. 3.3) such that the clusters had travelled approximately 1m from their point of formation before coating. Measurements of the amount of gas added were obtained by monitoring the total chamber pressure. Ideally a pressure that resulted in a single adsorbed monolayer was required. It was assumed that the difference in molecule size of nitrogen and hydrogen was negligible compared to the size of the cluster such that the same pressure calculations would apply in both cases.

The number of gas atoms required to form a monolayer was calculated using simple geometry. Assuming an Fe cluster contains ~ 250 atoms (corresponding to an equivalent mass of ~ 15000 a.m.u.) and with the density of Fe = 7870 kg m^{-3} , the volume of a cluster was calculated to be $3 \times 10^{-27} \text{ m}^3$. From this, the area can be calculated assuming the clusters are spherical. A nitrogen molecule containing two atoms was approximated to cover an area of covalent radius 75 pm^{30} . Thus it was found that ~ 500 atoms were required to coat the surface of a cluster with a single monolayer.

Assuming the clusters travel through the gas coating region in a time τ , kinetic theory shows that the pressure required to form a monolayer containing N_0 atoms of mass m is given by:

$$P = \frac{N_0}{\tau} \cdot \frac{1}{\sqrt{2\pi m k T}} \tag{4.1}$$

τ can be estimated to be 2.6×10^{-3} s (by dividing the chamber length by the speed of the clusters) so a pressure of the order of 10^{-5} mbar is required to deposit a monolayer of gas molecules around an Fe cluster of ~ 250 atoms.

Ten batches of samples were then made (Appendix C) and analysed in the studies of this chapter. Three batches were made for XMCD analysis, two for TEM analysis and five for VSM analysis.

Initial mass spectra studies of the gas-coated particles showed a general shift in the mass distribution between pure and gas-coated samples. Figure 4.1 shows the traces of a pure Fe cluster sample and a sample where the cluster passed through 1×10^{-5} mbar N_2 . Addition of the gas coating has shifted the mass distribution to higher masses by an amount approximately equal to a monolayer of N_2 and reduced the total flux of nanoparticles.

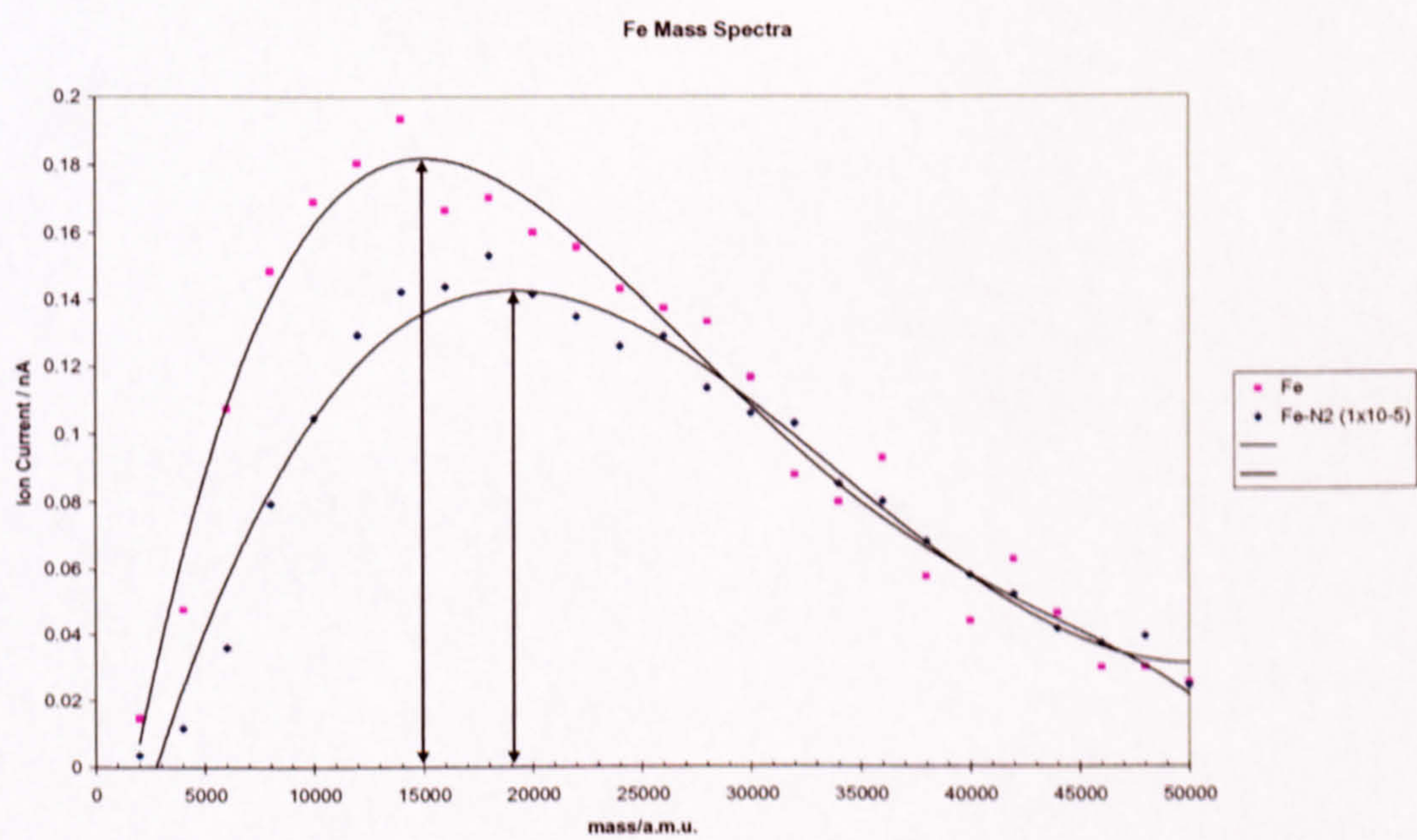


Figure 4. 1 Mass Spectra showing the size distribution of clusters produced at the source. The number in the legend refers to the pressure of gas used to coat the Fe clusters.

The pure Fe sample has a peak in the mass spectrum at 15,000 a.m.u. whereas addition of the gas has shifted this peak to 19,000 a.m.u. corresponding to 4,000 a.m.u. of nitrogen, equivalent to ~290 atoms. A monolayer was calculated to consist of 500 \pm 100 atoms so the gas coating is approximately 1 layer thick. The diameter of the pure Fe clusters was calculated to be (1.82 \pm 0.15)nm whilst the sample with a nitrogen shell would have a total diameter of (1.94 \pm 0.15)nm.

4.1 Gas-coating Models

E. K. Parks et al determined that above $n=30$ cluster hydride compositions comprise chemisorbed hydrogen on cluster surfaces³¹. Chemisorption is a type of adsorption whereby a molecule adheres to a surface through formation of a chemical bond. Its notable characteristic is it only takes place in a monolayer. At higher pressures of hydrogen additional hydrogens bind to the clusters as a second physisorbed layer. Physisorption is physical adsorption in which the adsorbate adheres to the surface only through weak Van der Waal's forces. However, in a previous paper³², in reference to chemisorption, the same group warn of both a reduced number of hydrogens in relation to the number of surface iron atoms and that during the ionization process (for the mass spectra) there is the possibility of cluster fragmentation.

Therefore it was postulated that gas coating of the clusters would have the following effect when compared to an uncoated cluster:

- a) the gas forms a monolayer around the clusters, bound to the surface by chemisorption. The expected result of this model would be to see an increased magnetic moment.
- b) the gas penetrates partway into the cluster leaving a cluster centre encased in a metallic/gas shell. This would 'inflate' the cluster thus increasing the next-nearest-neighbour distance and again it would be expected to see an increased magnetic moment.

- c) the gas penetrates the cluster entirely, modifying its structure and a Fe-gas compound is formed. This would be indicated by a decrease in magnetic moment.

Figure 4.2 shows these effects diagrammatically.

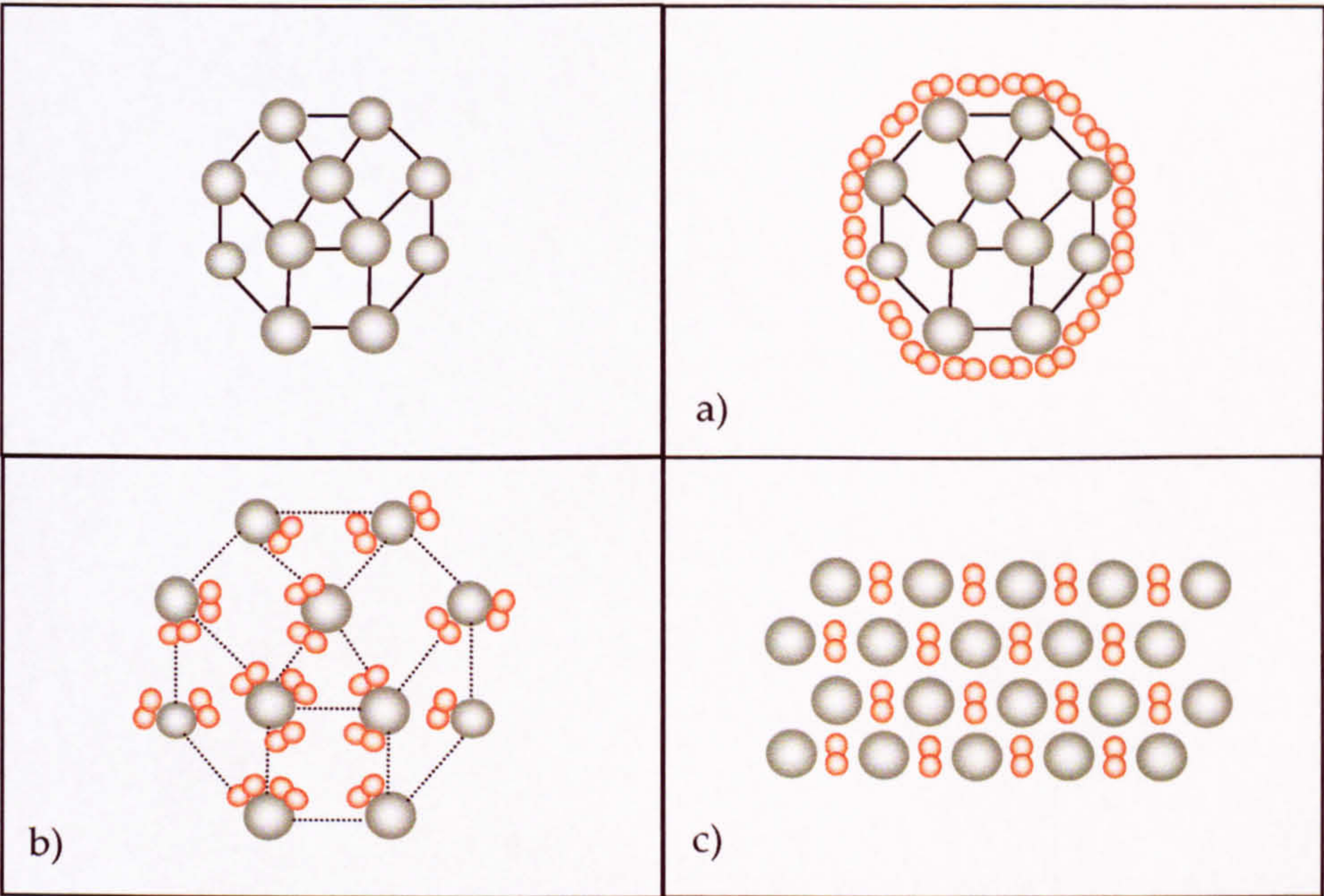


Figure 4. 2 Top left: A standard Fe cluster; a) an Fe cluster coated in a monolayer of gas; b) an Fe cluster inflated with gas; c) an Fe-gas compound

4.2 VSM Data

Batches 2 & 3 were gas coated samples of Fe clusters deposited to an equivalent thickness of 27- 50nm and coated with varying pressures of gas. The substrate used was PEEK.

Isotherms were taken on the samples using a saturation field of $\pm 5.0T$. Scans were made at 300K and at 2K without any field-cooling.

4.2.1 300K Data

A typical pair of magnetisation curves obtained by the VSM is shown in figure 4.3. The background generated by the PEEK substrate, which is linear, has been removed from the data. The saturation magnetisation is taken from the point where the data becomes horizontal.

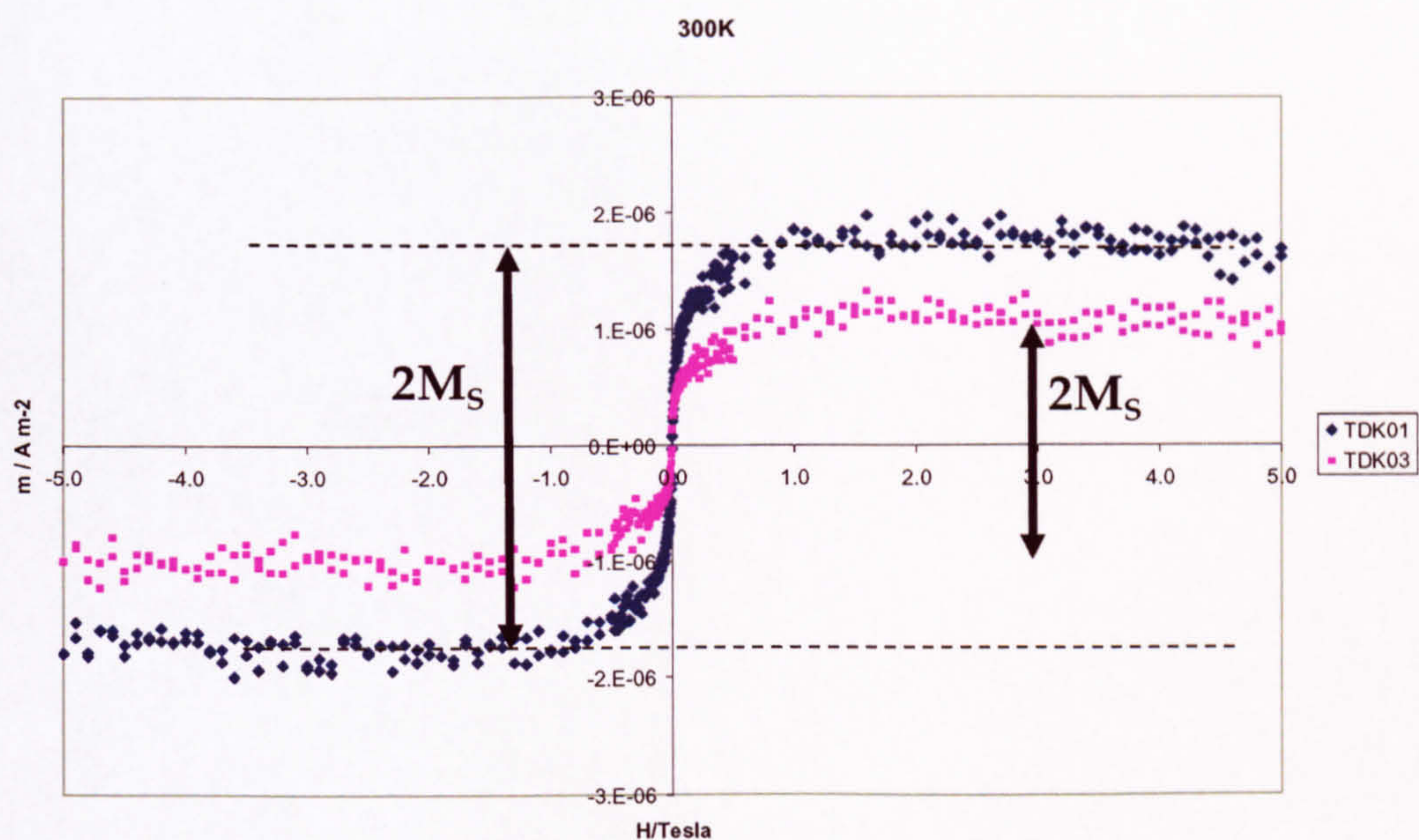


Figure 4. 3 Isotherms taken on Batch 2 samples at 300K

The blue trace represents a pure Fe film and the pink trace shows a sample with a hydrogen coating. Addition of the gas has decreased the saturation magnetisation. The following figures show how M_s (fig 4.4), m_R (fig 4.5), H_C (fig 4.6) and moment per atom (fig 4.7) values compare between pure Fe samples, an H_2 coated sample and N_2 coated samples. All samples have been normalised to an equivalent thickness of Fe of 30nm.

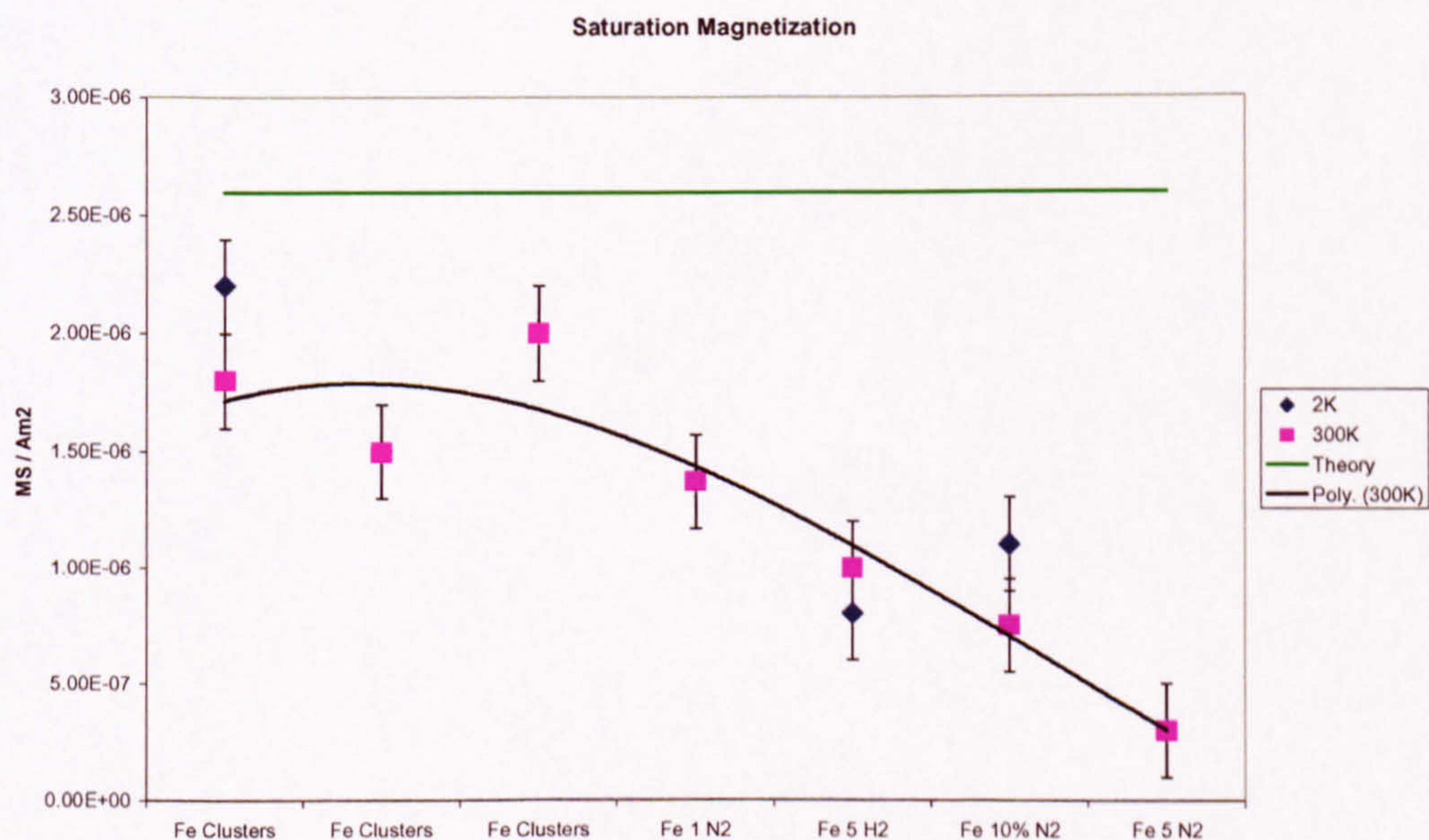


Figure 4. 4 Magnetisation values for gas-coated samples from batches 2,3,6 & 7. Labels refer to the amount of gas coating $\times 10^{-5}$ mbar. The theoretical curve shows the maximum value possible for a 30nm film of Fe.

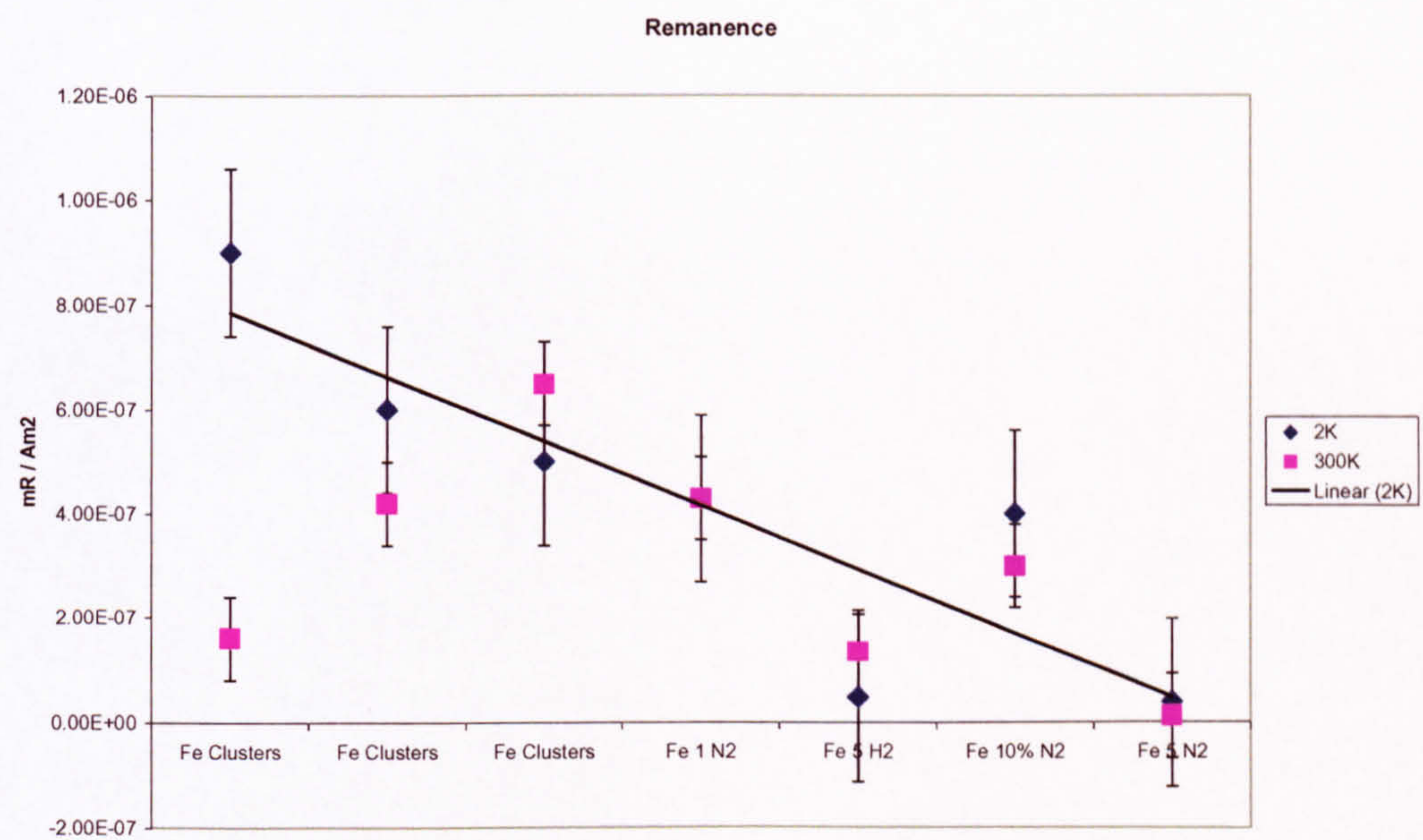


Figure 4. 5 Remanence values for gas-coated samples from batches 2,3,6 & 7. Labels refer to the amount of gas coating x 10⁻⁵ mbar.

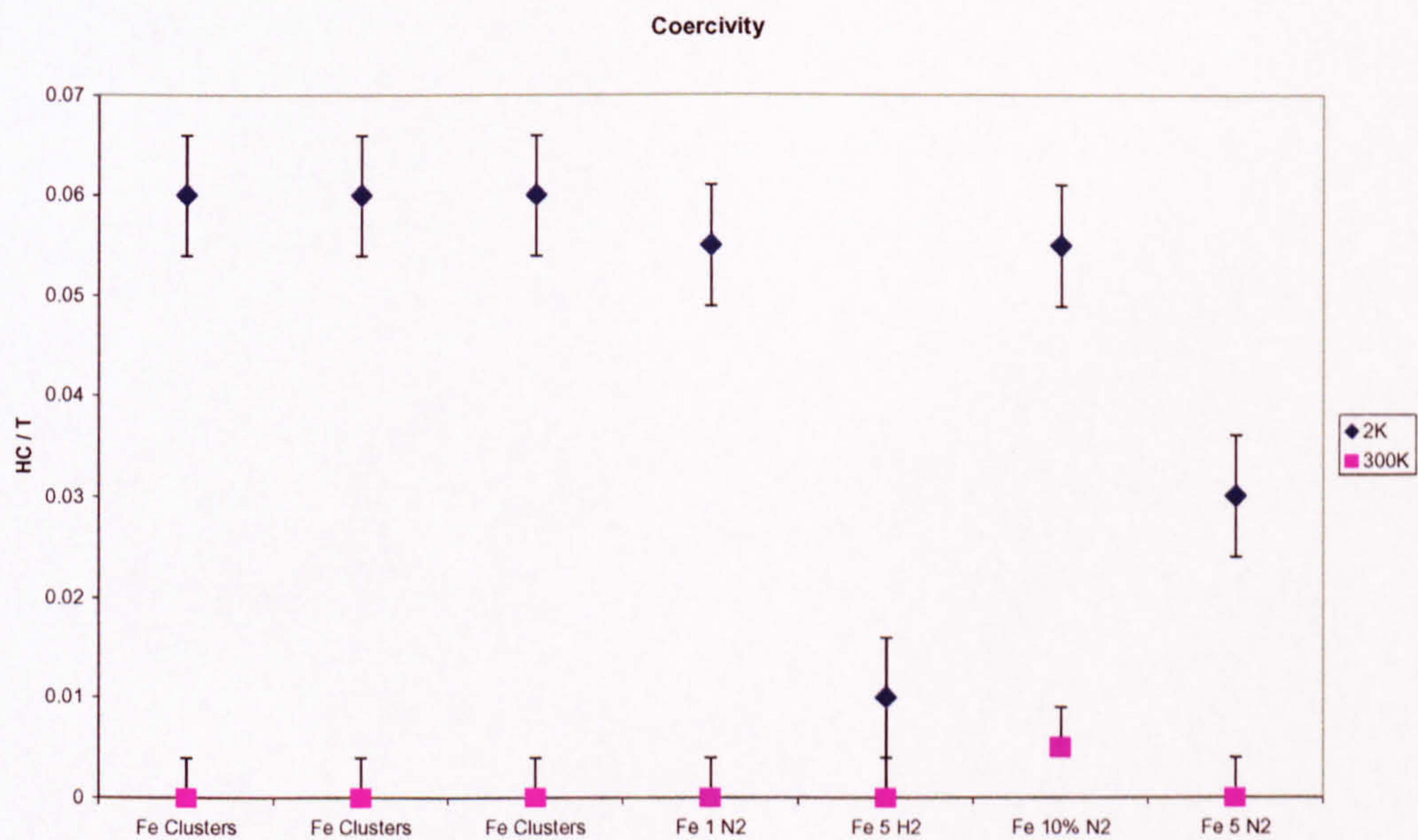


Figure 4. 6 Coercivity values for gas-coated samples from batches 2,3,6 & 7. Labels refer to the amount of gas coating x 10⁻⁵ mbar.

Figure 4.7 shows the values of average magnetic moment per atom calculated from the values in figure 4.4.

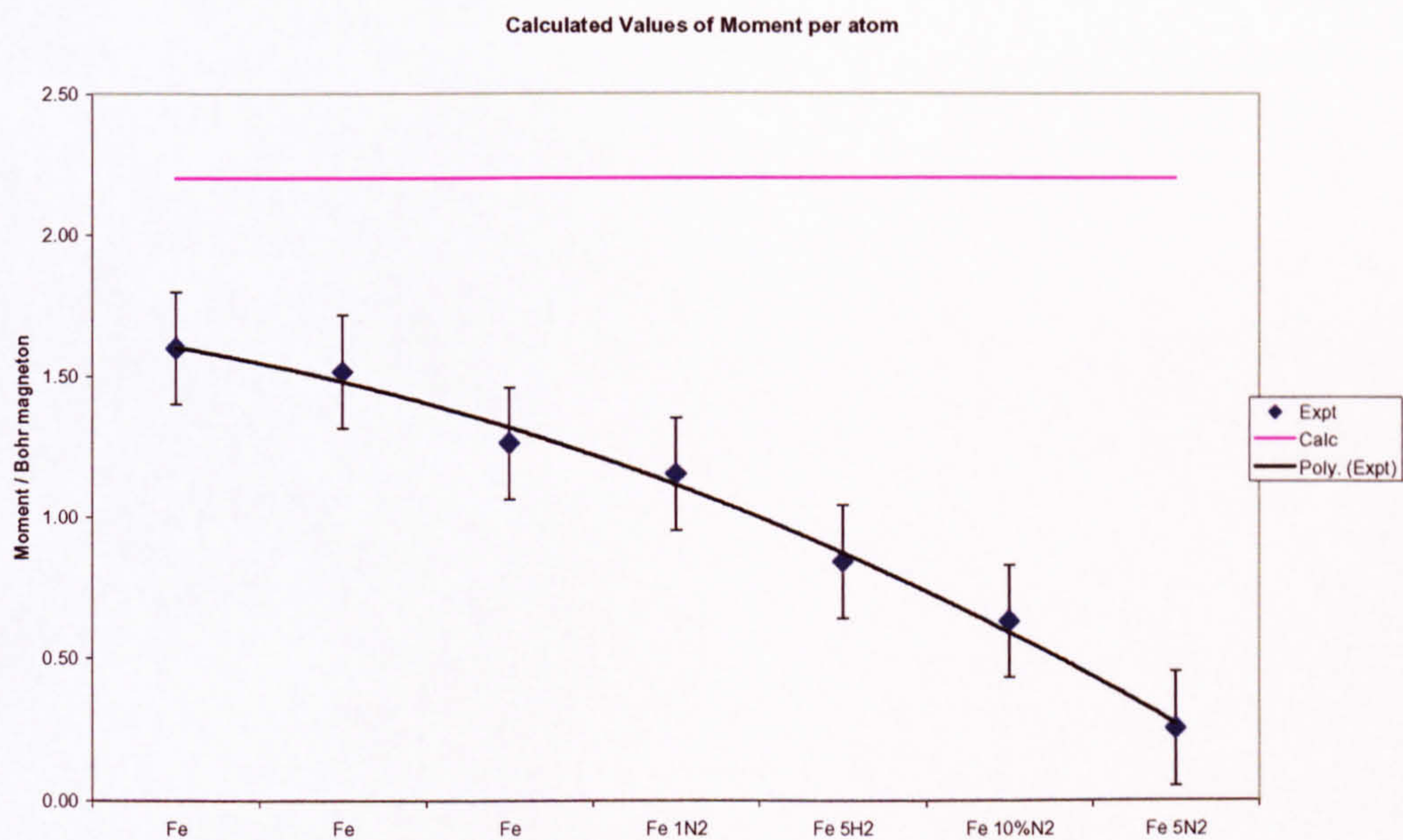


Figure 4.7 Magnetic moment per atom calculated from the experimental data of figure 4.4.

As can be seen from these results addition of a gas coating has decreased the moment. It should also be pointed out that the Fe samples without gas added are still lower than the calculated value and this is because these samples are oxidised. Oxidised Fe samples will contain a shell of ferrous oxide around the clusters which couple antiferromagnetically to the pure Fe cluster. This will decrease the overall magnetic moment of the sample. Causes of oxidation result from insufficient cleaning of the substrates, insufficient outgassing of the evaporators, lack of $N_2(l)$ in the TSP trap and accidental damage to the samples during removal from the sample arm and into the plastic ampoules.

4.2.2 2K Data

The 2K plots show the samples are FM ‘harder’ i.e. it is more difficult to magnetize them at this low temperature and the characteristic hysteresis loop of figure 2.7 can now be seen in figure 4.8.

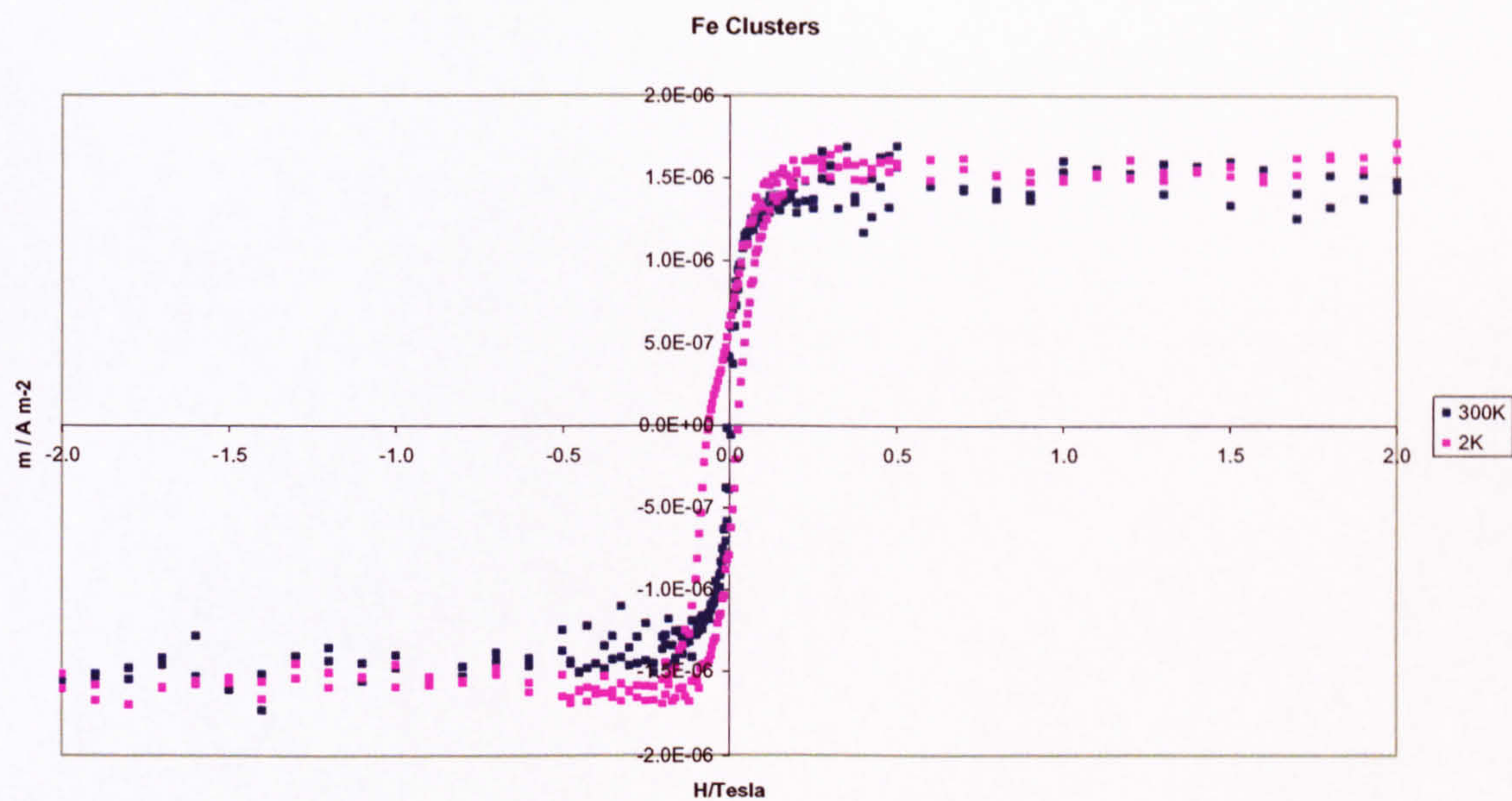


Figure 4. 8 Isotherms of pure Fe cluster sample at 300K and 2K

The pink 2K trace shows an interesting feature in the 3rd quadrant of the graph. The lower section has a fatter loop than the section in the 1st quadrant which suggests that two curves have been superimposed on one another. There is also a slight exchange bias which is likely to be as a result of oxidation of the sample.

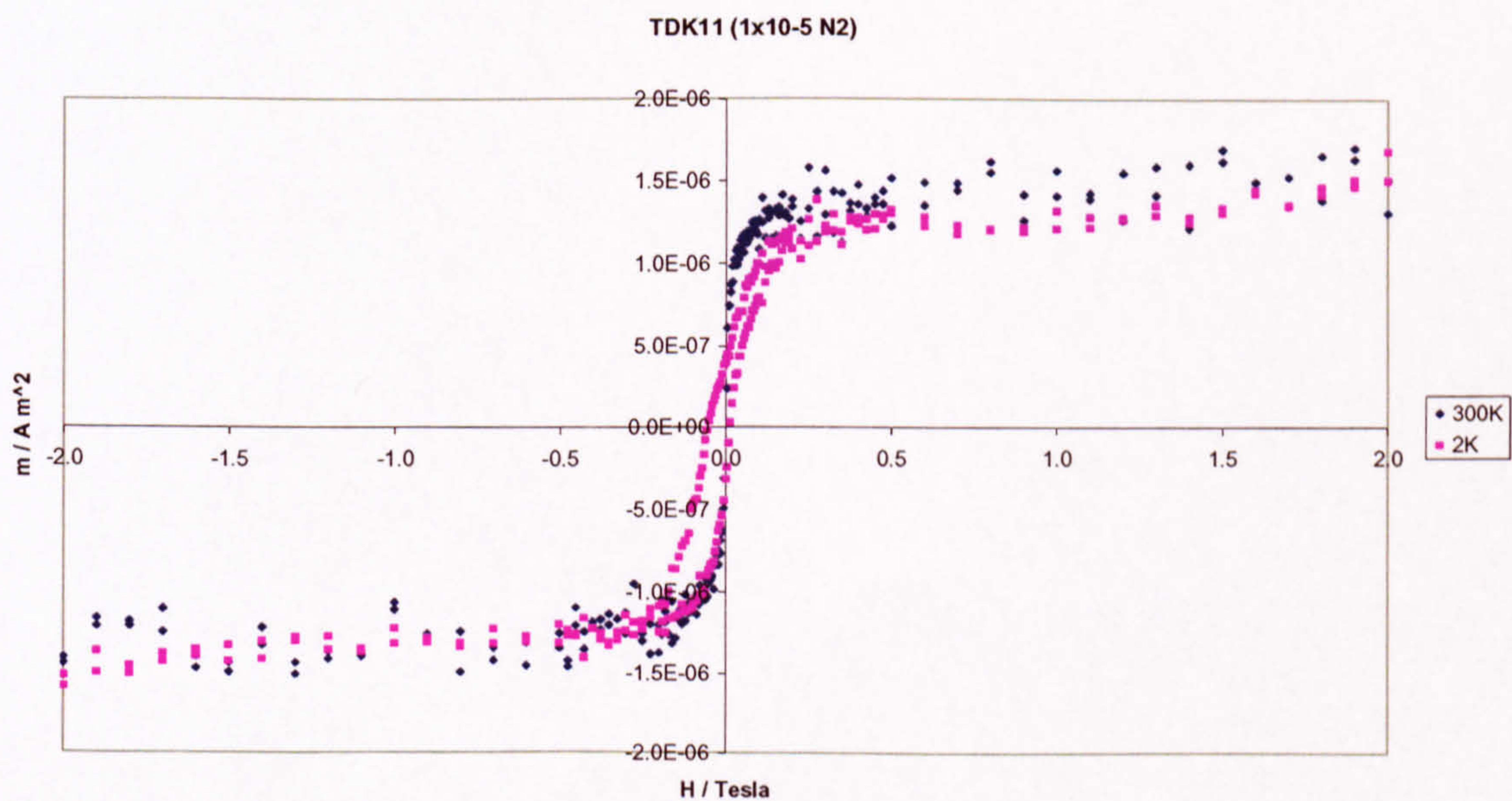


Figure 4. 9 Isotherms of N₂(g) coated Fe at 300K and 2K

Comparing figure 4.9 to figure 4.8, it can be seen that addition of N_2 has decreased both the saturation and remanence points at both temperatures.

Some samples were made with the gas introduced directly at the source in order that the gas was present as the clusters were being formed. This produced an interesting effect as shown in figure 4.10.

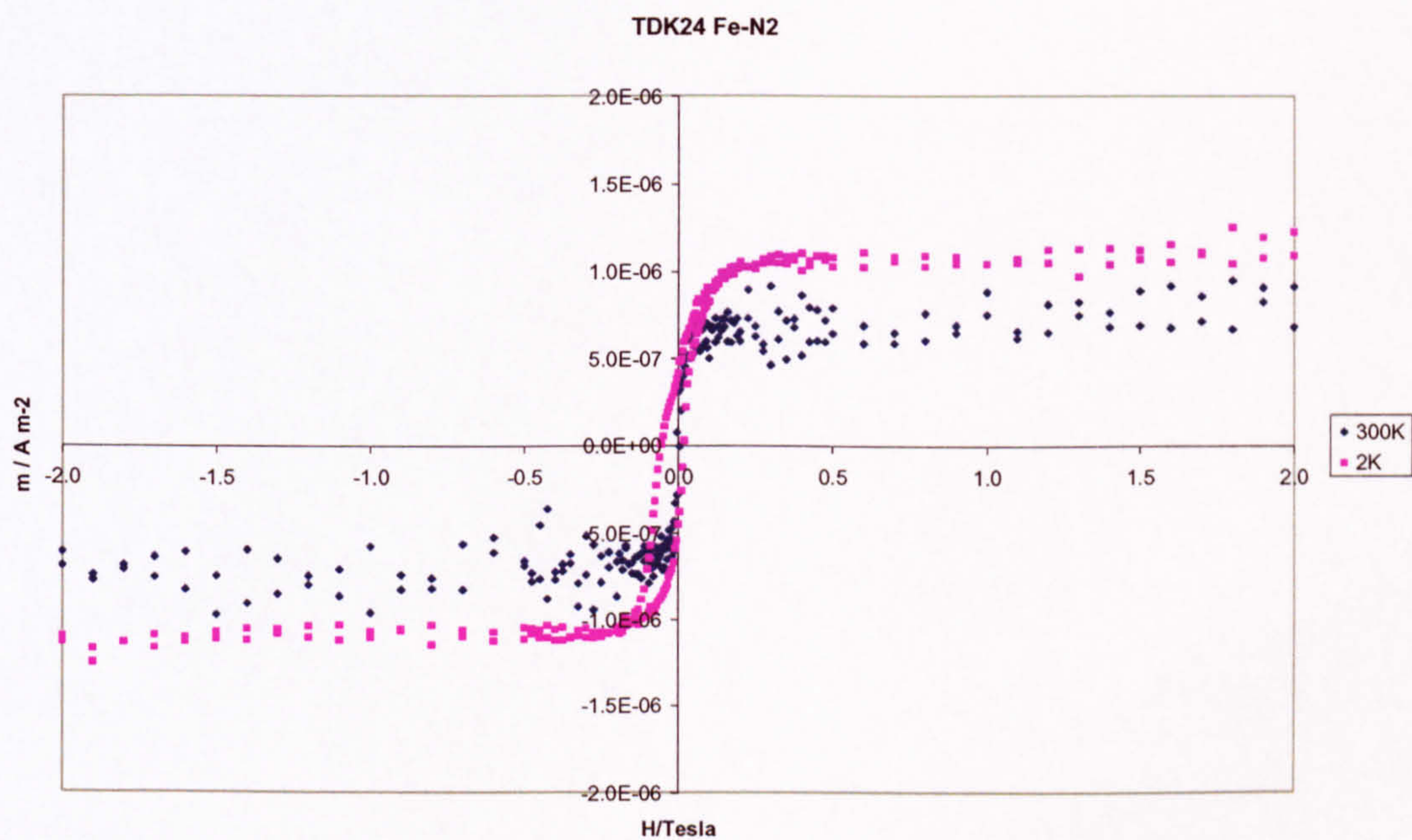


Figure 4. 10 Hysteresis scans of $N_2(g)$ coated Fe at 300K and 2K

This shows that the 2K scan has an increased magnetisation from that at 300K which may suggest the presence of FM and FiM layers within the sample.

4.3 XMCD data

Two allocations of beamtime were awarded in 2005 at the CCLRC synchrotron facility in Daresbury. Seven samples for H_2 studies were measured in May whilst five samples for N_2 studies were measured in November.

For each sample 5 transmission scans from 690 eV – 750 eV (i.e. across the Fe L-edges) were obtained for each relative orientation of the applied field and photon polarisation,

and averaged. Before each set of data, the Fe L₃ dichroism was measured as a function of the applied field to check that the samples could be saturated in the available field.

4.3.1 Fe-H₂

These samples were deposited on substrates of Mylar. As the X-ray beam impacted onto the sample during the experiment sample degradation occurred. This had the effect that transmission increased with each subsequent scan in a set of five. Some rectification of the problem was achieved by changing the position of the sample within the beam. Precise details of the samples made are given in Appendix C.

The following figure shows an example of how the raw transmission data normalised to the incident beam intensity appears after collection.

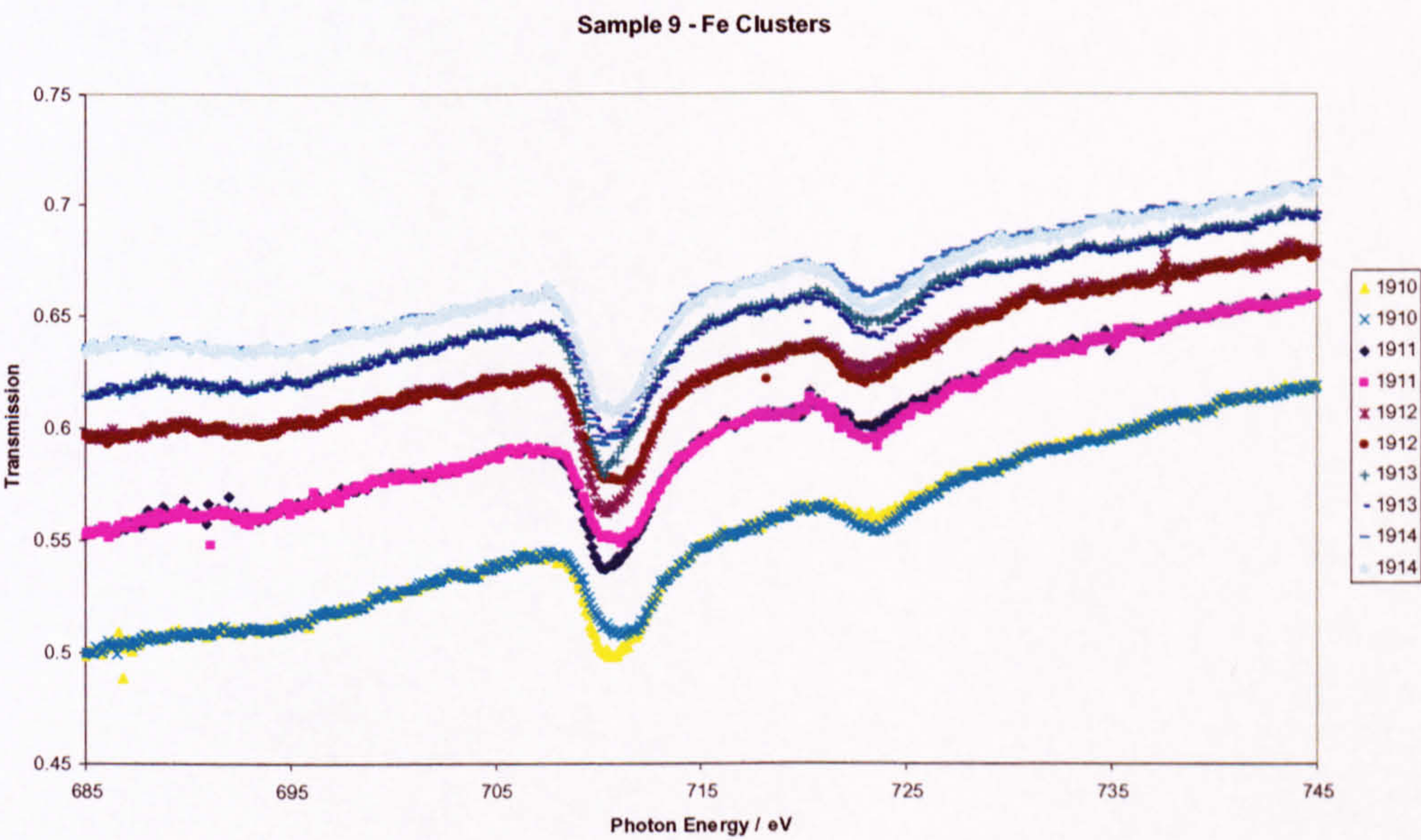


Figure 4. 11 Dichroism scans of 9.2% Fe in Ag sample

The lowest plot was taken first, subsequent spectra increase in intensity as the substrate decomposes. The underlying positive gradient of the graphs is a result of the superposition of the absorption spectra of the substrate with that of the Fe spectra. As these are dichroism scans each set contains pairs of traces. The legend has named the traces according to the computer filenames.

Subsequent scans should lie over each other, i.e. start and end positions should be the same. Each trace pair is taken one after another and requires approximately 45 minutes to complete. Over the course of the entire scan ~ 3 hours, the transmission of the beam through the sample has increased from 0.5 to 0.64 (a 20% increase). It was possible to see the physical deterioration of the sample, a black disc appeared on the material, visible to the naked eye. This occurred too with the spectra of the plain substrate, as indicated in the next figure.

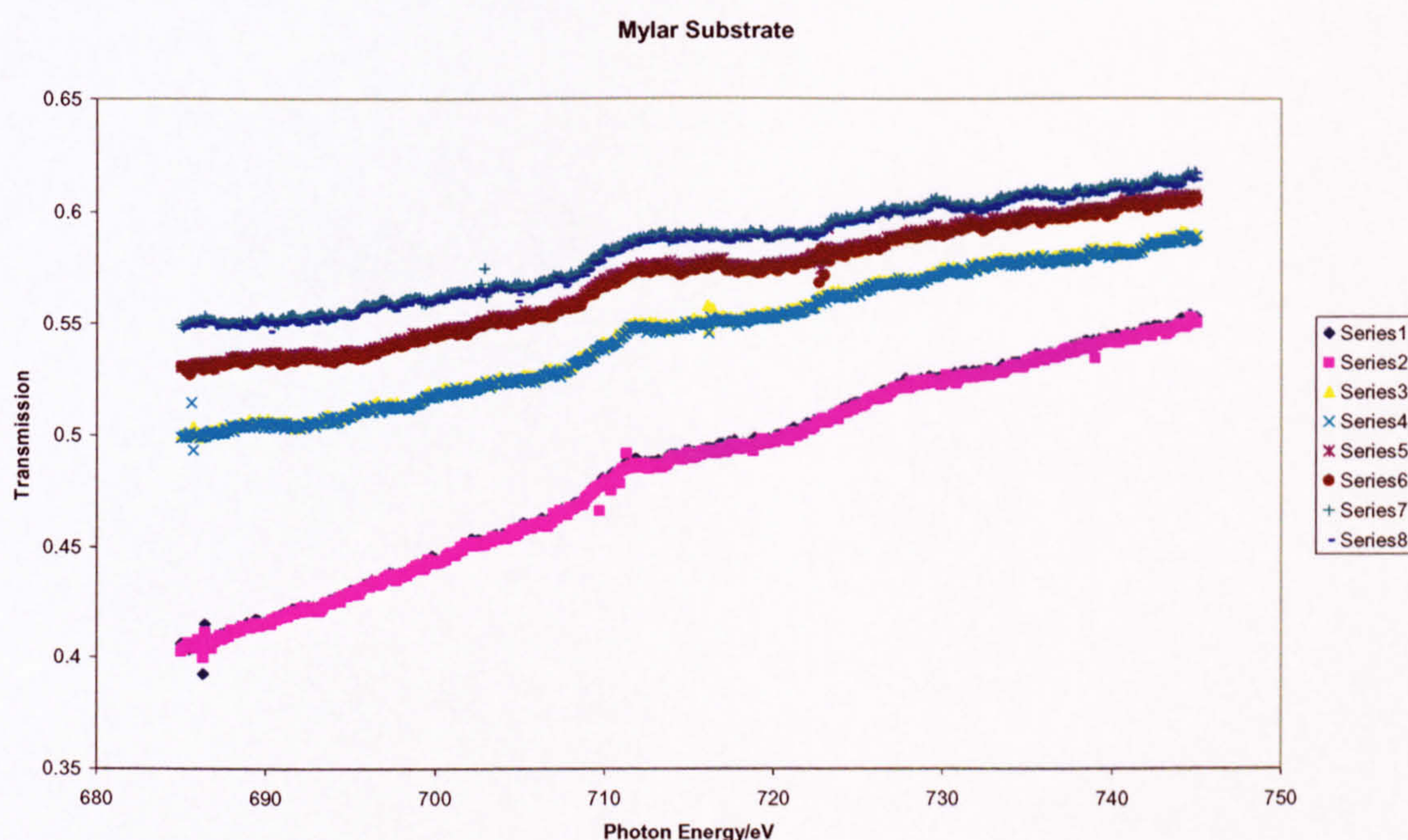


Figure 4. 12 Dichroism scans on blank Mylar substrate.

The plots in figure 4.12 show the same increased transmission with time and the increasing gradient characteristic of this material. It was concluded that the former effect was entirely due to the Mylar substrate and that for future experiments Mylar would not be used.

Each pair of scans of the Mylar background was removed from the corresponding pair of scans of each sample. Only 4 traces were obtained of the Mylar sample therefore every 2nd scan for each sample was disregarded. The remaining 4 pairs of scans were then averaged to leave 1 pair of scans of dichroism data. The next step of the normalization could then be performed.

In order for the magnetic properties to be obtained from the dichroism graphs it is essential that the leading edge begins at zero and is as horizontal as possible. Despite removal of the Mylar background the data from some of the samples still had a residual gradient so a further linear background was removed from the data. Figure 4.13 shows the graph generated after all linear backgrounds have been removed.

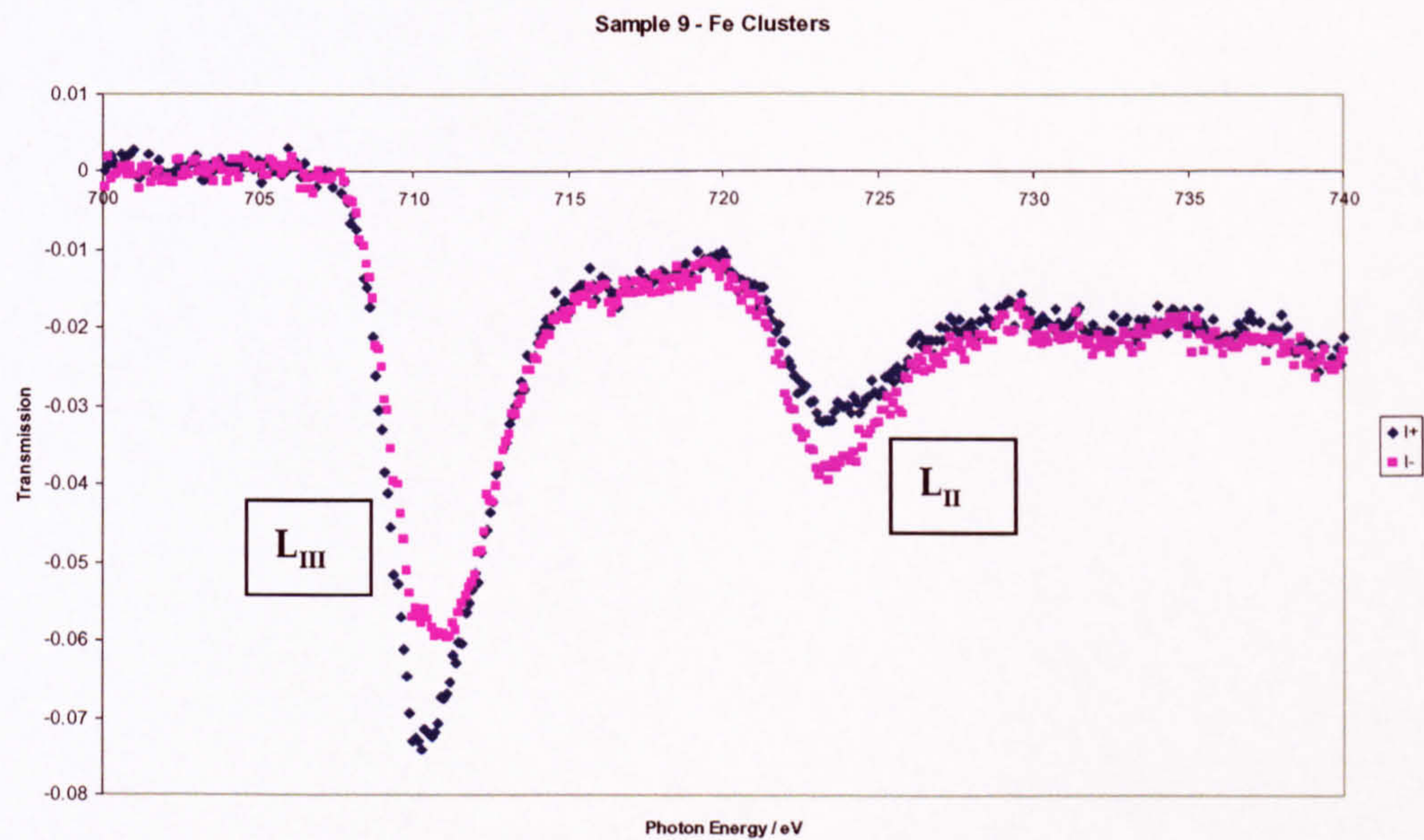


Figure 4. 13 Averaged dichroism traces for a pure Fe cluster sample showing L-edges.

Figure 4.13 shows the leading edge has been set to zero. The 2 peaks at 710 and 718eV show the $2p_{3/2}$ (L_{III}) and $2p_{1/2}$ (L_{II}) states of the Fe atom. Subtracting the pink trace (LHP) of figure 4.13 from the blue trace (RHP) produces the dichroism graph of figure 4.14.

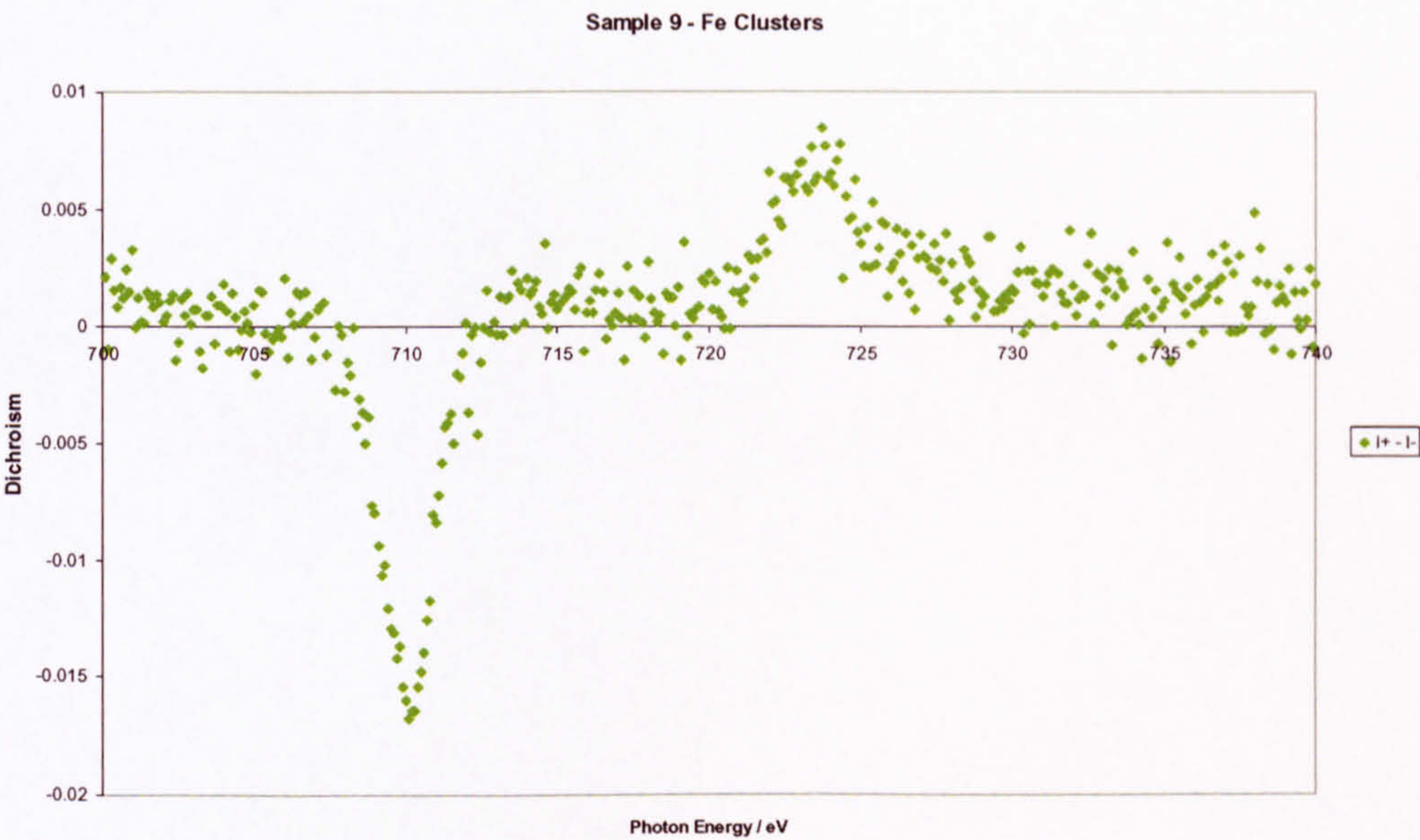


Figure 4. 14 Magnetic circular dichroism for a pure Fe cluster sample.

Adding the two traces of figure 4.13 produces the absorption graph of figure 4.15. These two steps are in accordance with the procedure detailed in subsection 2.3.2.

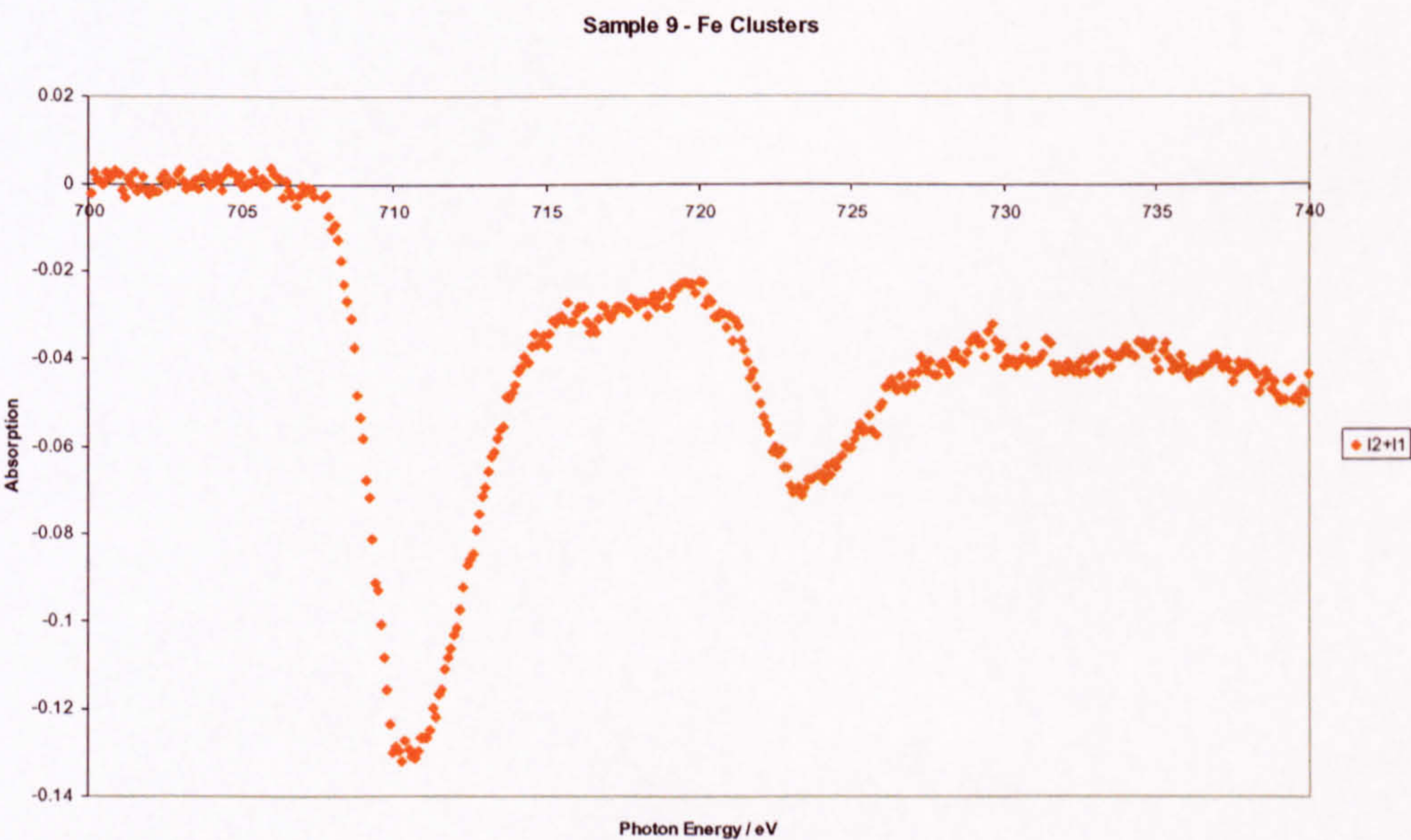


Figure 4. 15 Absorption for a pure Fe cluster sample.

Figures 4.14 and 4.15 must now be integrated to generate the total dichroism and total absorption respectively. Figure 4.16 shows the first of these integrals which will be used in the sum rules, equations (2.6) and (2.7).

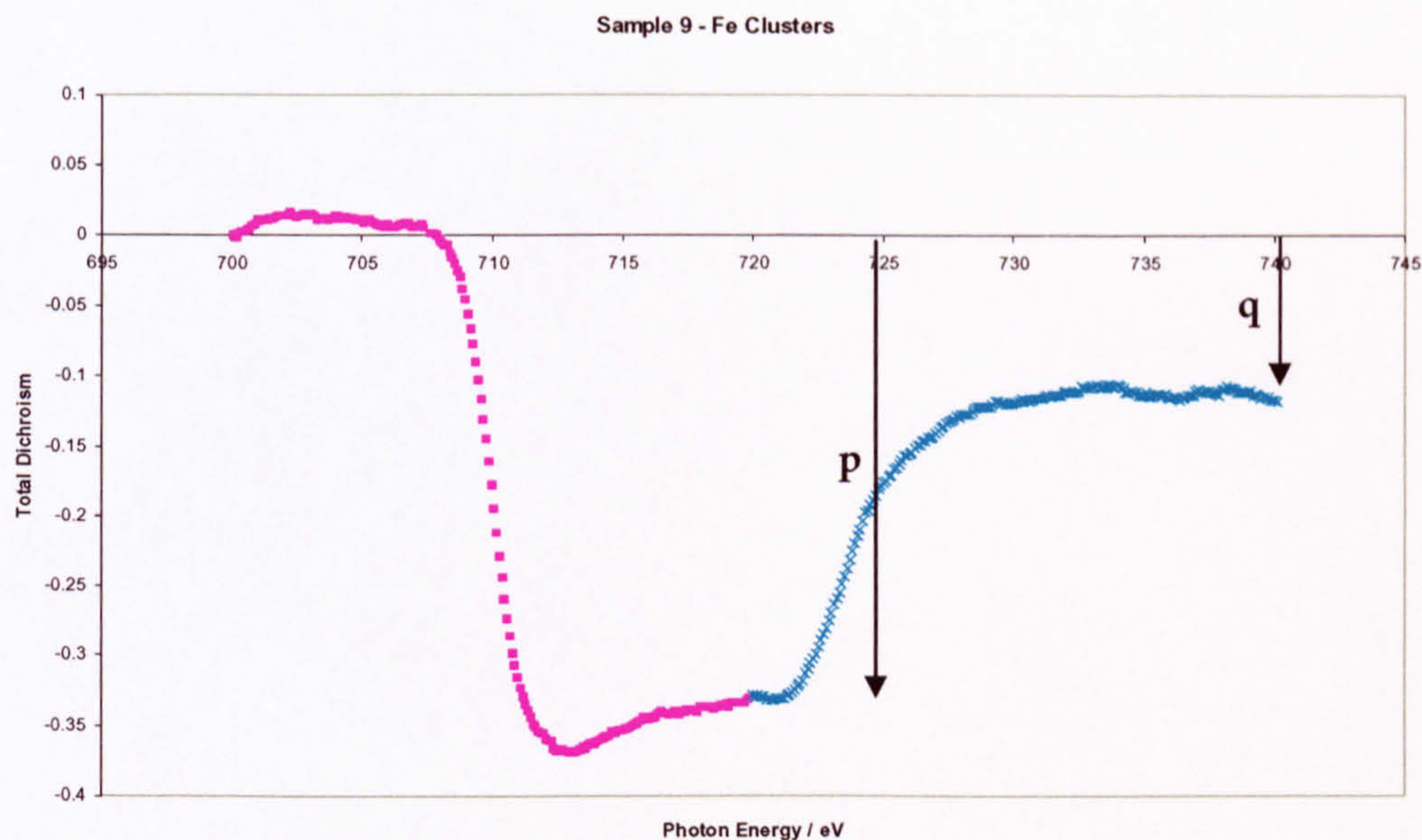


Figure 4.16 Total dichroism of pure Fe cluster sample.

The turquoise portion of the graph has been normalized such that the tail lies horizontally. The height between this tail and the x-axis (q) is one of the 3 values used in the sum rules. It is interesting to plot the differences in dichroism between the pure samples and the gas coated samples. This will not provide any numerical information but a quick comparison between samples can be made as dichroism is directly proportional to magnetic moment.

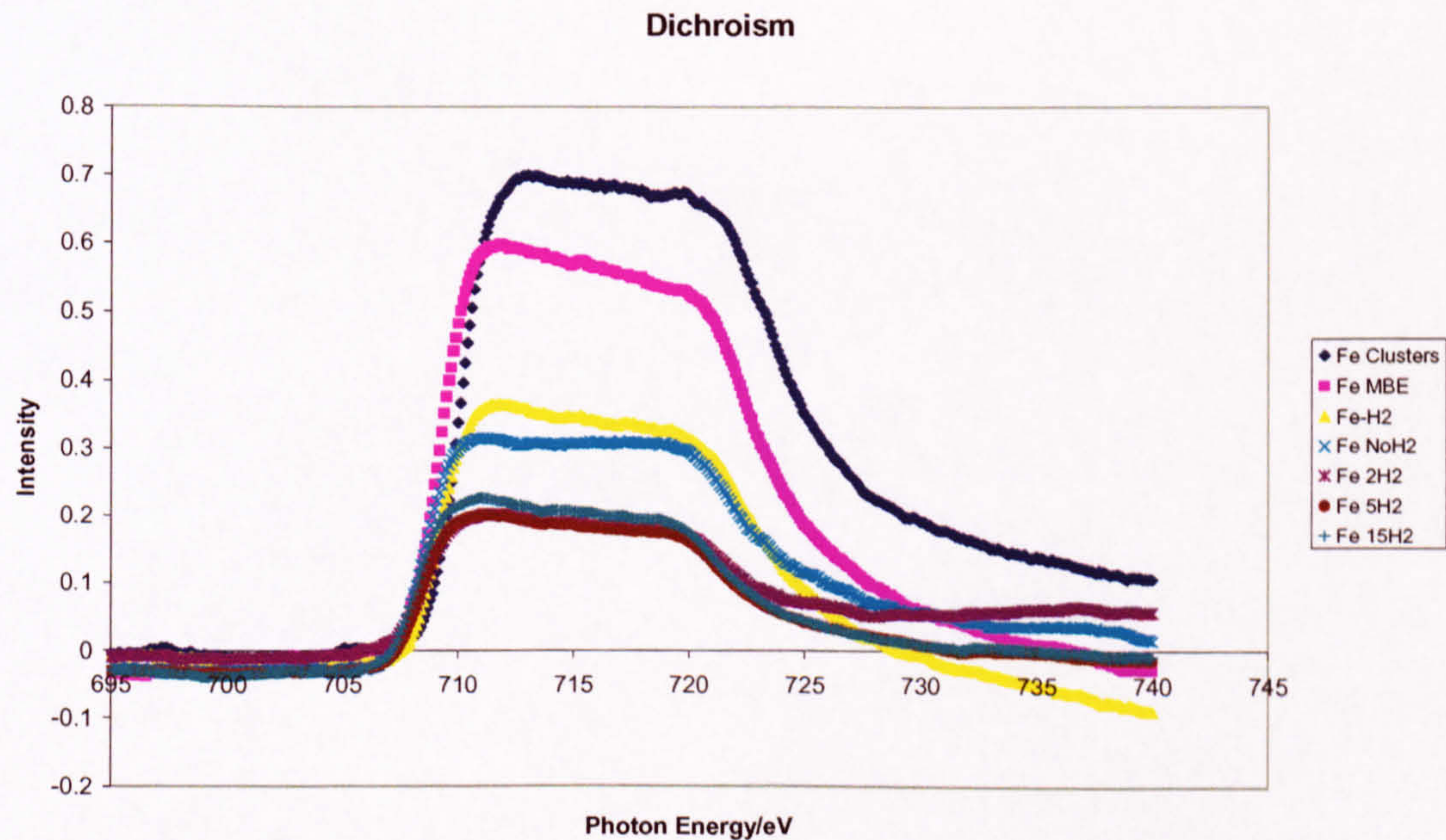


Figure 4.17 Total dichroism of 7 gas-coated samples.

The lowest three plots in fig. 4.17 are all samples coated in molecular H and these have the smallest dichroism. Pure Fe clusters (dark blue) have a larger dichroism than an MBE Fe film (pink). Despite the clear difference between these traces the data is not very clean. The trailing edge of each trace should be horizontal, any slight deviation from a linear tail will render actual values for the orbital or spin moment as inaccurate.

Figure 4.18 shows the result of integrating the graph in figure 4.15. It shows the total absorption of the sample.

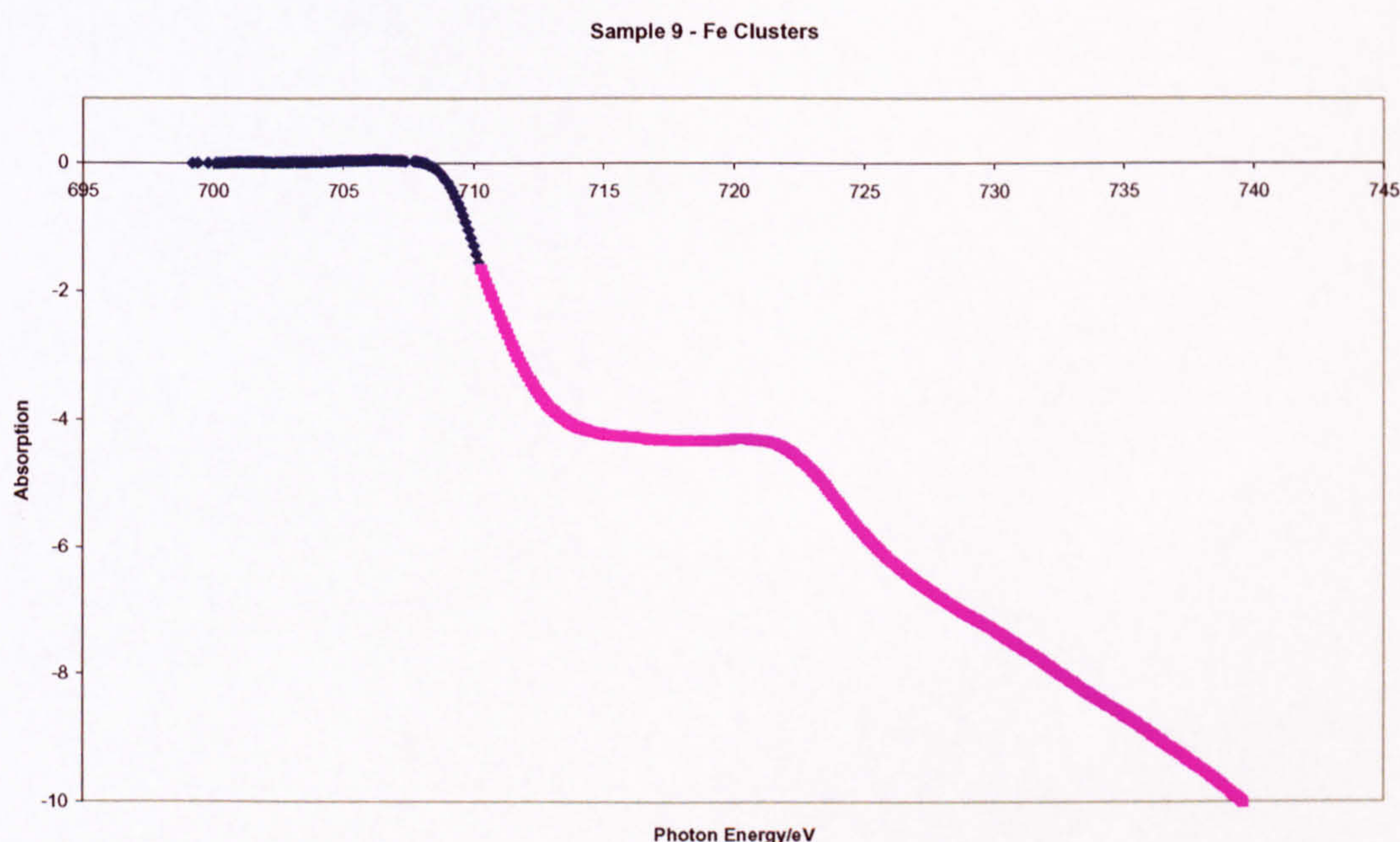


Figure 4. 18 Total Absorption of pure Fe cluster sample

As can be seen in figure 4.18 the tail of the graph is not level. Despite the two-step-like function having been removed from the data, the tail is not horizontal as it should appear as in figure 2.11(d). For this reason no values of r can be obtained and so no values of spin, orbital or total angular momentum have been generated for these hydrogen-coated samples. This is due to the poor quality of data and so the only conclusions to be drawn are from the relative data of figure 4.17 which shows that gas-coated samples have a smaller dichroism than the pure Fe samples. This in turn implies that addition of hydrogen has decreased the magnetic moment of the samples.

4.3.2 Fe-N₂

Five Fe-N₂ samples were made using C-coated TEM grids as substrates to eliminate any sample deterioration. The samples have an equivalent thickness of Fe of ~5nm and total thickness ~55nm. For this run the end station incorporated the new Portable Octopole Magnet System, POMS on station 5U.1 at Daresbury.

Again, full data analysis was carried out on the raw data and there were similar issues with an underlying background however, the clarity of data was improved such that magnetic moments could be generated. For instance, figure 4.19 shows a distinct levelling of the tail in the absorption after removal of the two-step-like function.

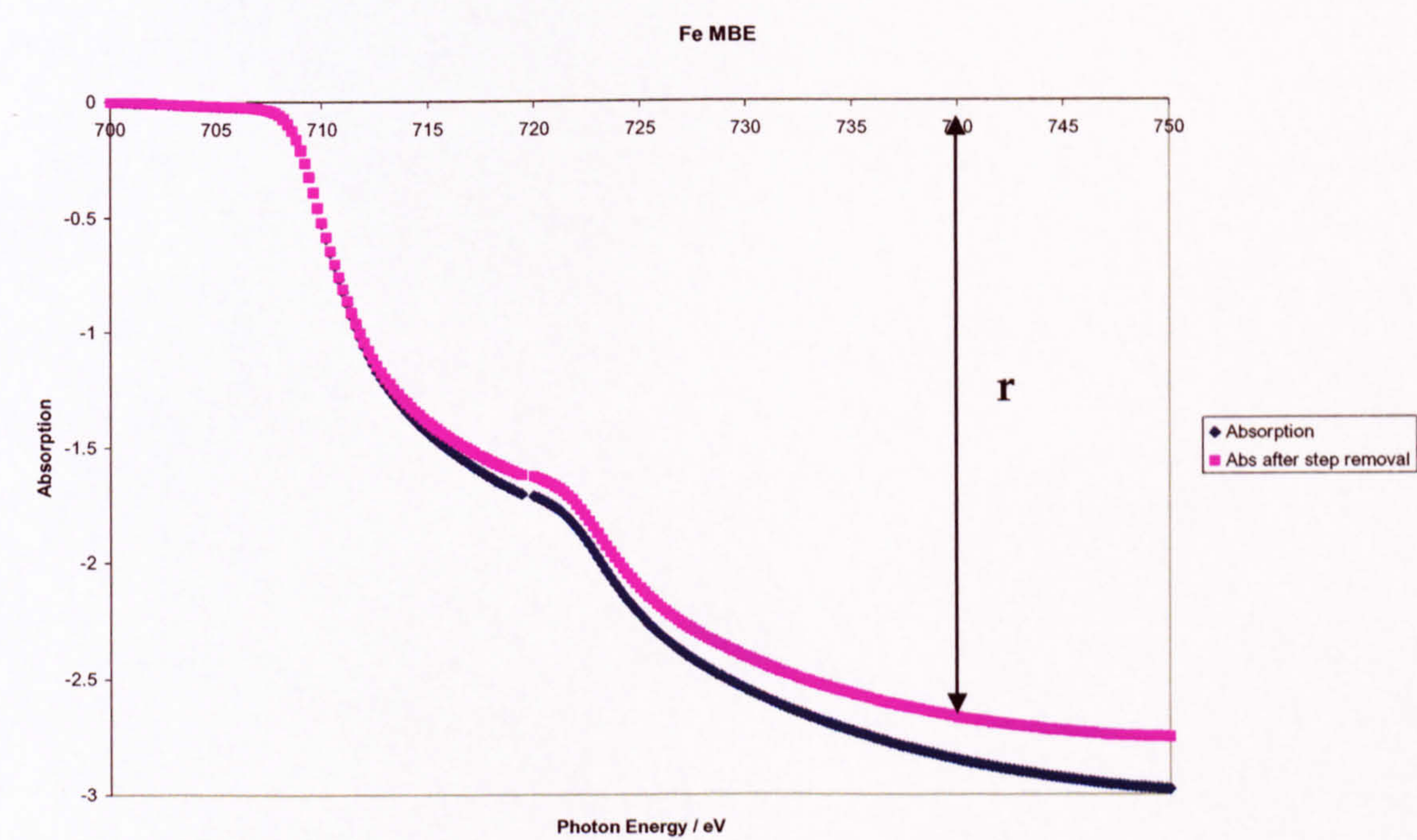


Figure 4. 19 Total Absorption of pure Fe MBE sample

The value of r in figure 4.19 has been chosen from the energy of 740eV as this is where the tail would be parallel if the data were completely clean. It is also the same energy from which the value of q has been obtained in the dichroism graph. Errors in the values of q and r have been obtained by taking the values at 5eV above and below this energy.

The values of p, q and r taken from the dichroism and absorption graphs are presented in the table of figure 4.20 with the resulting values of spin and orbital magnetic moment.

(1/cos45)/0.76=	1.860807	p	q	r	m orbital	m spin	m orb / m spin	total m	dm
Fe_n=	6.61	(μ _B / atom)							
Fe MBE		-0.081	-0.027	-2.667	0.62	0.89	0.69	1.50	0.03
Fe in Ag matrix		-0.039	-0.008	-1.372	0.09	0.49	0.19	0.58	0.43
Fe 5N2		-0.010	-0.005	-0.653	0.03	0.22	0.12	0.25	0.20
Fe 3N2		-0.019	-0.008	-0.733	0.05	0.39	0.13	0.43	0.31
Fe 2N2		-0.021	-0.009	-0.821	0.06	0.36	0.17	0.42	0.30

Figure 4. 20 p, q and r values taken from the dichroism and absorption charts of Fe-N2 samples. Magnetic moment values calculated from the sum rules.

The total m calculated in the final column of figure 4.20 is plotted in figure 4.21. The errors in the final column of figure 4.20 are not plotted in figure 4.21. Instead a general error of 0.2 μ_B/atom has been plotted as Excel could not plot individual points with individual errors.

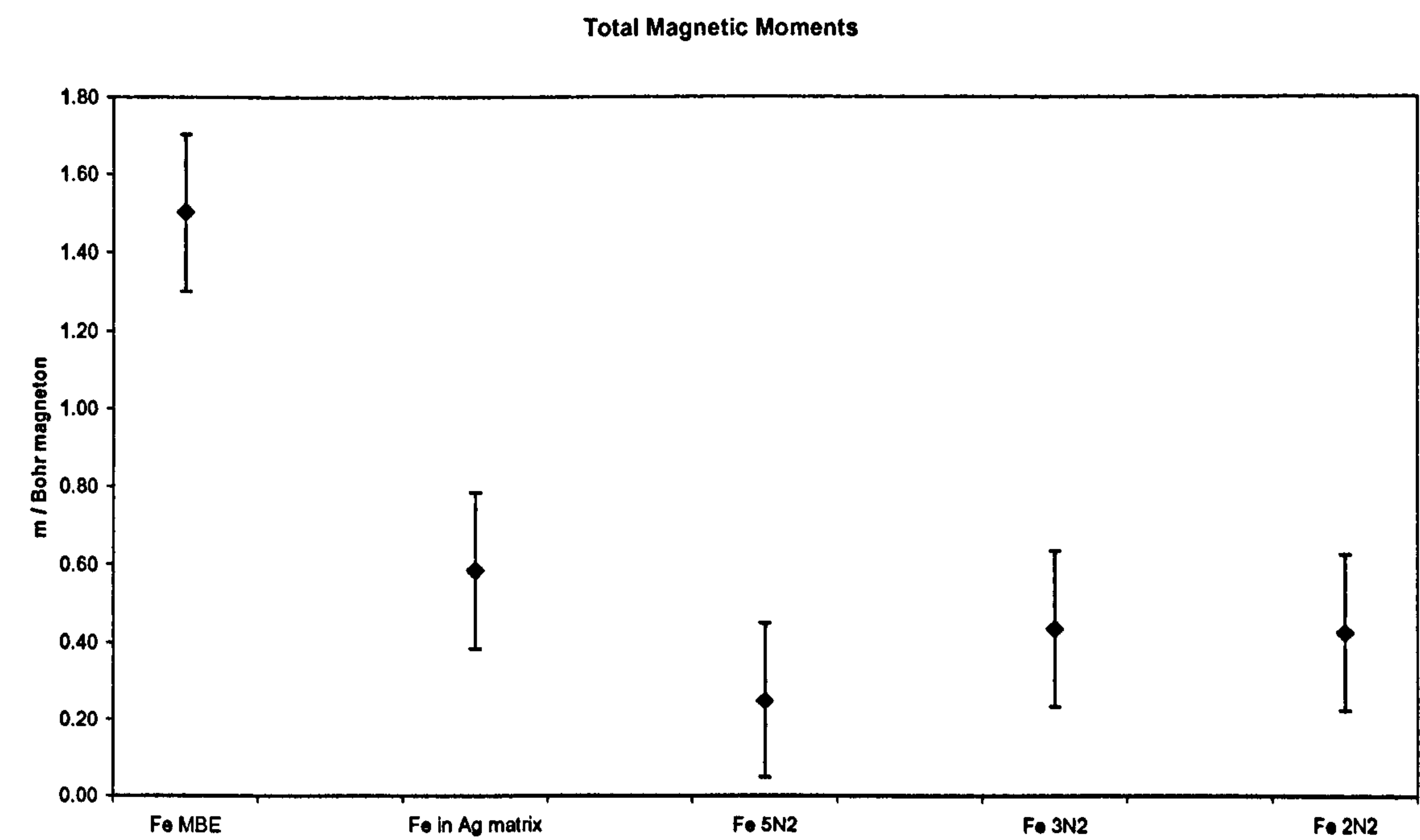
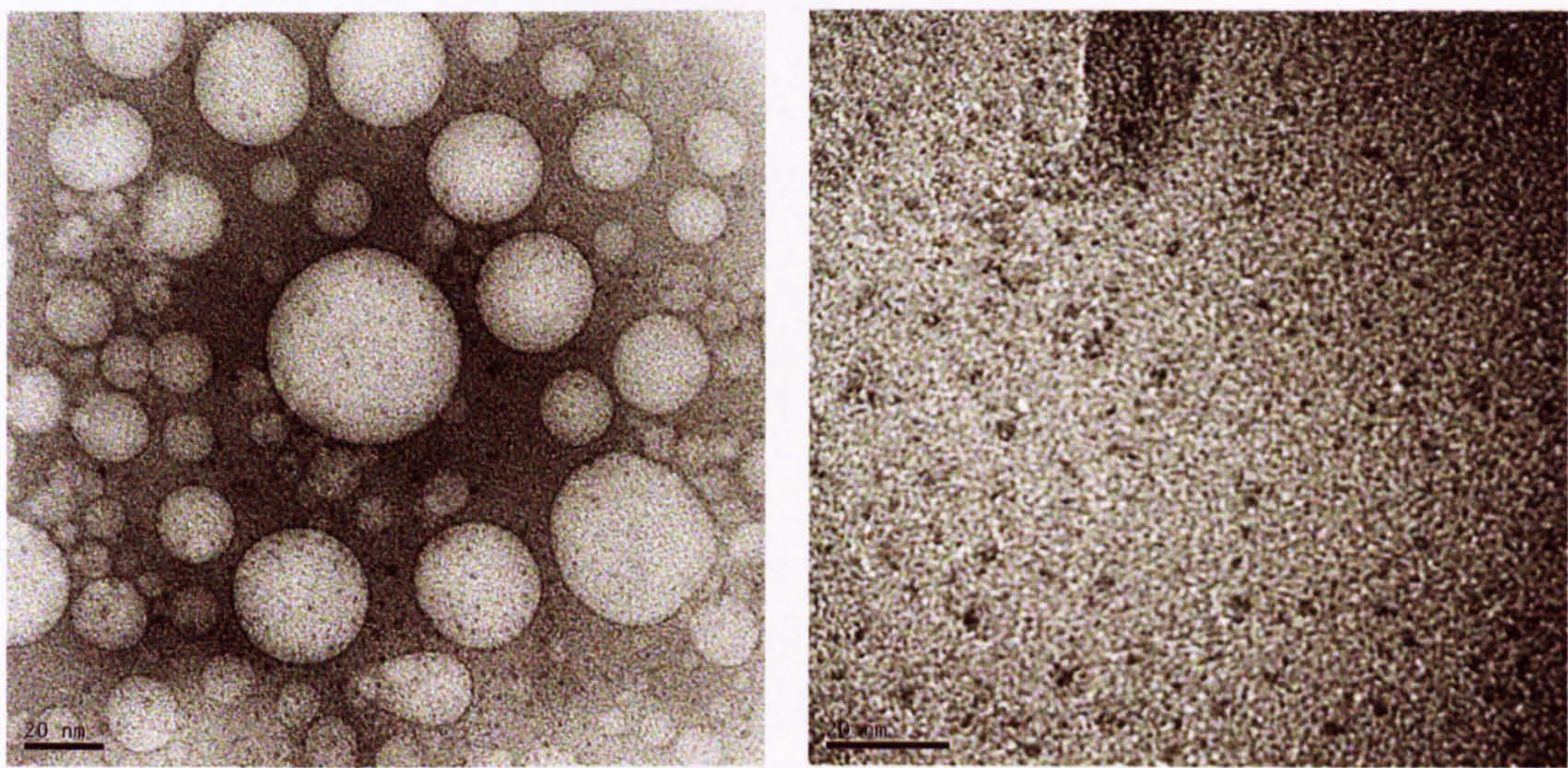


Figure 4. 21 Magnetic Moments plotted from the final column in figure 4.20.

Addition of the gas has decreased the moment. However, the Fe cluster sample in the Ag matrix should be higher than the Fe MBE film. This highlights the difficulty in producing accurate data from the XMCD technique for these samples. Very clean, high quality data is required to get reliable values for the spin and orbital moments. This means that the VSM data and the XMCD data corroborate each other. Both report a reduction in the overall magnetic moment with the addition of gas to the nanoparticles.

4.4 TEM Imaging

Two batches of samples were grown on C-coated TEM grids to investigate $H_2(g)$ coatings and $N_2(g)$ coatings respectively. These were then coated in situ with a thin C cap to prevent oxidation after removal from the UHV system.



a) 20nm scale image of a pure Fe sample b) 20nm scale image below the C capping layer

Figure 4. 22 TEM images taken of pure Fe sample (TDK18). Image (a) shows the C cap (large circles) and the Fe nanoparticles (small black dots) underneath. Image (b) shows the nanoparticles at a greater magnification, however, the underlying C buffer dominates the picture.

The image in Figure 4.22(a) is focused on a hole in the sample enabling us to see directly into the ferrous layer. This hole was due to a crack in the C capping layer. The electron beam is heating the Fe particles so that they coalesce and grow. As the sample was scanned the top layer could also be seen to deteriorate in real-time as the images were obtained. The thickness of the C cap in the majority of places has made it difficult to scan deeper through.

The clusters in figure 4.22(b) are approximately 2nm in diameter which corroborates the mass spectra and calculations presented at the beginning of this chapter.

4.5 Summary

The addition of a gaseous shell to the Fe nanoclusters is ineffective in enhancing the magnetic moment of the sample or the individual clusters. The Mylar is ineffective as a substrate in the range of energies of X-rays used for XMCD measurements on Fe. TEM grids provide a more suitable substrate for XMCD measurements.

Two gases, hydrogen and nitrogen, were used as coatings, both having a detrimental effect upon the magnetic moment. Technical difficulties were encountered throughout these studies, however most notably the $H_2(g)$, being highly reactive, destroyed the quad filaments within the main chamber of the LUMPS system.

The most likely explanation for the reduction in magnetic moment of these gas-coated samples is that addition of the gas has destroyed the surface structure of the clusters responsible for their enhanced moment. Some clusters may only have been partially coated by the gas through a combination of chemi- and physisorption whilst in others the surface structure is likely to have been broken down as gas atoms permeated into the clusters. Higher resolution TEM images may be able to better verify these speculations.

The key point is that the VSM data and the XMCD data corroborate each other. Both report a reduction in the overall magnetic moment with the addition of gases. This means the gas has not formed a shell around the clusters. All samples were oxidised but with the relative data showing the reduction of magnetic moment, the implication is that non-oxidised samples would yield reliable and consistent data.

Further work in this area could use atomic gases instead, although thermal crackers are expensive and until the reaction procedure between cluster and coating layers are understood fully this may well yield a similar study of gaseous coatings. An alternative

approach would be to inject the gas via a nozzle directly at the aperture before the focusing lenses (i.e. at the first Cu plate) in order to monitor the amount of gas entering the system better also to ensure that the clusters are coated directly.

“Element X”

Marc Delafontaine & Jacques Louis Soret

1878

Chapter 5

Fe Clusters in Ho

The rare earth metals Ho and Dy have exceptionally large atomic magnetic moments (10.9 and 10.2 μ_B /atom respectively) and despite their large atomic volume still generate a large flux density of 3.7T. This is much higher than the most magnetic TM alloy (FeCo), which generates a field of 2.45T. The problem with both Ho and Dy is that they have low T_C (20K and 89K respectively) and require very high applied fields to saturate hence they cannot be used in technological applications incorporating high-moment materials, which generally require a soft magnetic behaviour. Embedding TM nanoparticles in Ho and Dy matrices is hoped to both increase the T_C and the magnetic softness of the films. Although the coupling between TM and RE is generally AFM it may still be possible to achieve a magnetic composite that generates a field higher than 2.45T with a T_C above 300K. It is also possible that the giant moments offered by single domain magnetic nanoparticles of Fe (if embedded in a RE) may be large enough to induce FM coupling at the cluster/matrix interface and in the RE matrix, in which case an even higher average flux density will be achieved.

Firstly, studies were conducted on an MBE film of Ho then the effect of adding Fe clusters to a Ho matrix was investigated. The interactions of TM with RE have been well modelled³³ and there is a wealth of experimental data on RE multilayers, RE doped semiconductor systems and RE – TM alloys. However, the discussion in this chapter involves pre-formed TM clusters within a RE matrix.

Holmium is a complicated magnetic system. The single crystal structure in zero field is now well understood in terms of the spin-slip model originally proposed by Gibbs et al³⁴ and expanded upon by Cowley and Bates^{35, 36}. Not only does the metal exhibit 3 different magnetic phases at different temperatures, but these change according to the strength of an applied field. The T_N of Ho is 133 K above which the metal is PM. Below T_N the

magnetic moments exhibit 2 types of ordering. Firstly there is a helical ordering: within one crystal layer all moments are lined up parallel to each other, lying within the a-b plane, while between adjacent planes the direction of the moments is rotated by a small angle, leading to a full rotation of the moments with a period of several atomic layers in the c-direction.

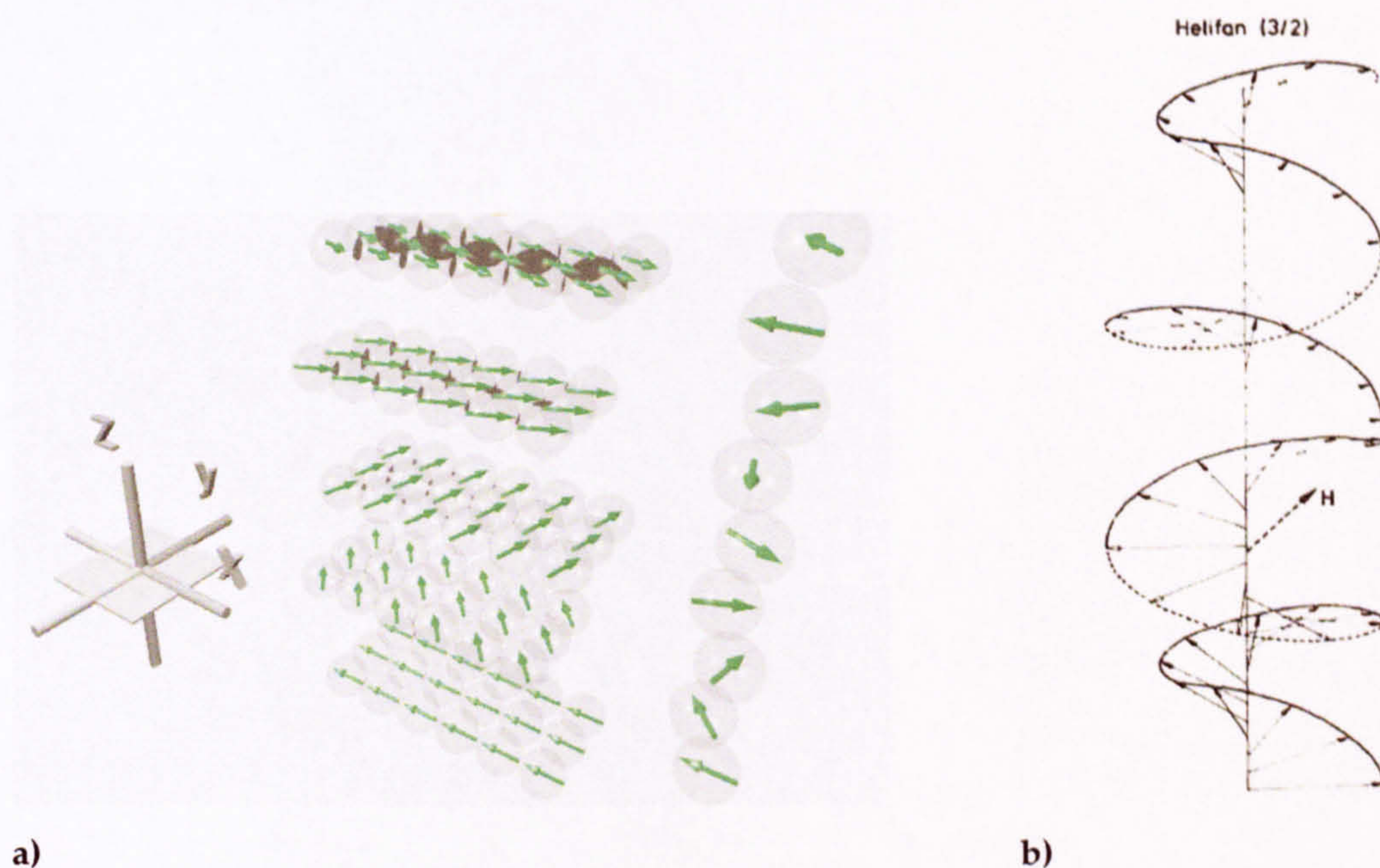


Figure 5. 1 Spin arrangements in Ho a) simple spiral (image courtesy of Konings³⁷) b) helifan (image reproduced from ref 35)

This arrangement is characterized by a wavevector, \mathbf{q} which decreases with decreasing temperature. On cooling \mathbf{q} decreases from $0.275c$ at 133K until a lock-in transition at about $T_c = 20\text{K}$ when the structure is described by a commensurate wavevector, $q_0 = \frac{1}{6}c^*$ such that the sequence repeats every 12 layers. Secondly, when approaching T_c , the magnetic moments become tilted out of the plane, leading to a total FM moment in the c -direction (perpendicular to the planes) with a circulating contribution in plane. The change in spin-slip spacing with temperature is driven by competition between the exchange term and the crystal field terms in the Hamiltonian. Secondly there is the AFM helifan arrangement as shown in figure 5.1(b) and in the magnetic phase diagram of figure 5.4.

Four batches of Fe in Ho samples were made, three for magnetometry measurements and one for XMCD analysis. The XMCD samples became oxidised so could not be used for that purpose but upon imaging in the TEM some interesting images were obtained.

Zfc isotherms were obtained between 300 and 2K, in 50K or 10K intervals and fc scans were taken from 300-100K and from 100-2K in a maximum field of ± 8.0 T. For the Ho MBE sample, the isotherms at 300K, 250K, 200K, 150K, 100K, then in 10K interval steps down to 20K did not show any clear hysteresis, there was no development of features and the data was very noisy. Finally, at 2K a weak FM hysteresis response was detected. The data was inconclusive regarding saturation magnetisation as the maxima reached were different at different temperatures. I.e. the sample had a higher saturation magnetisation at 2K compared to that obtained at 300K. For this reason and knowing the strong temperature dependence of the magnetism in RE materials, it was decided to focus on isofields rather than isotherms for these studies.

5.1 Ho MBE

Isofields taken in zero or low applied fields should show the magnetic phase changes of Ho at 20 and 133K. Much of the pioneering work on single crystals of Ho utilised low applied fields if any at all³⁸. The ground state isofield for Ho should look like the following figure.

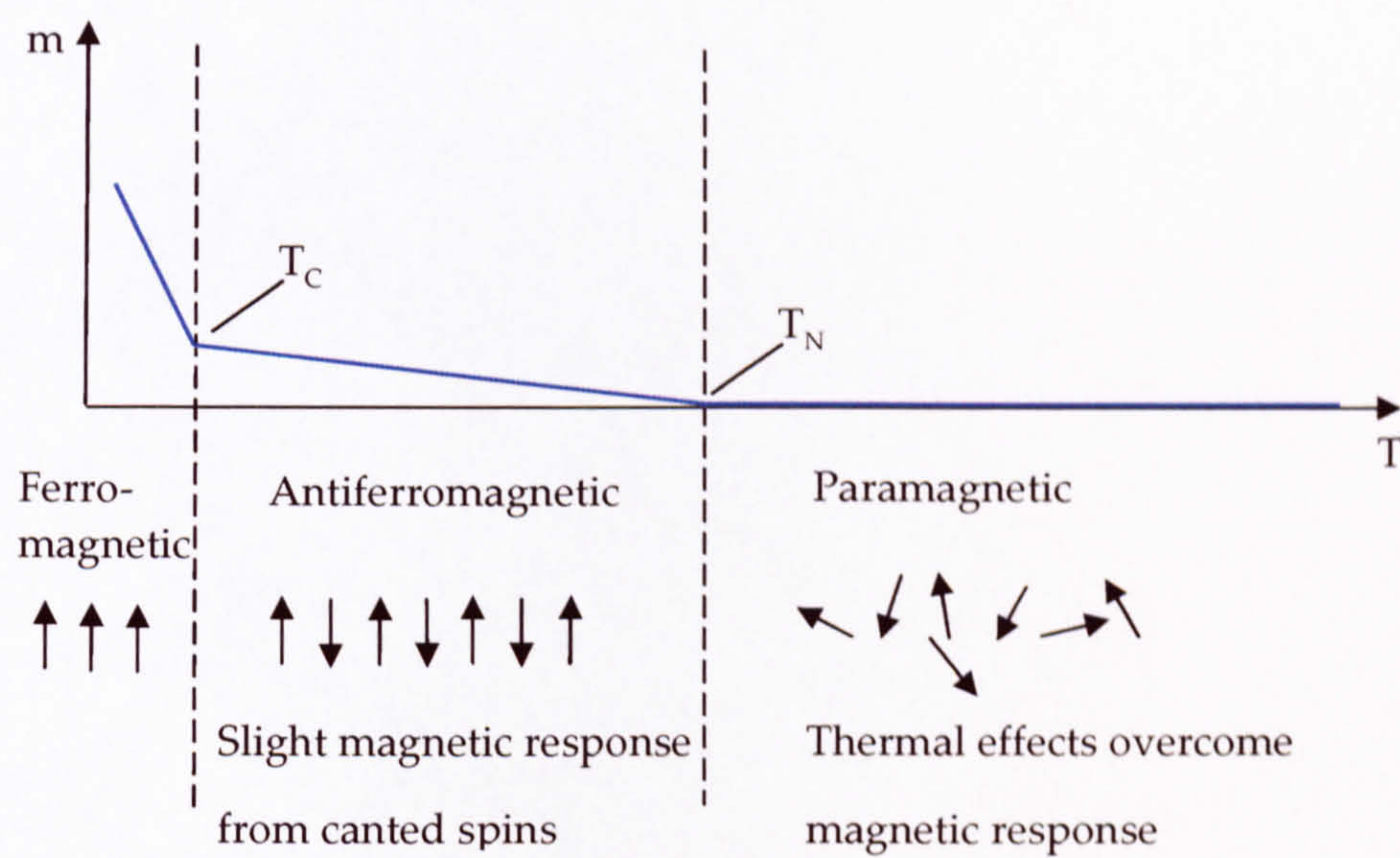


Figure 5. 2 Schematic diagram of a temperature sweep scan taken with a VSM.

Above T_N the moments are disordered and PM will be seen. Below T_N the system becomes ordered but AFM. If there is any mismatch between the up and down moments the FiM ordering will produce a slight magnetisation response. Below T_C the sample becomes FM and the gradient should increase noticeably.

The magnetic phases in a single crystal of Ho are seen when measured along the c-axis. Although this sample is a polycrystalline thin film sample and therefore axis direction varies with position, similar characteristics to the single crystal behaviour were obtained as figure 5.3 shows.

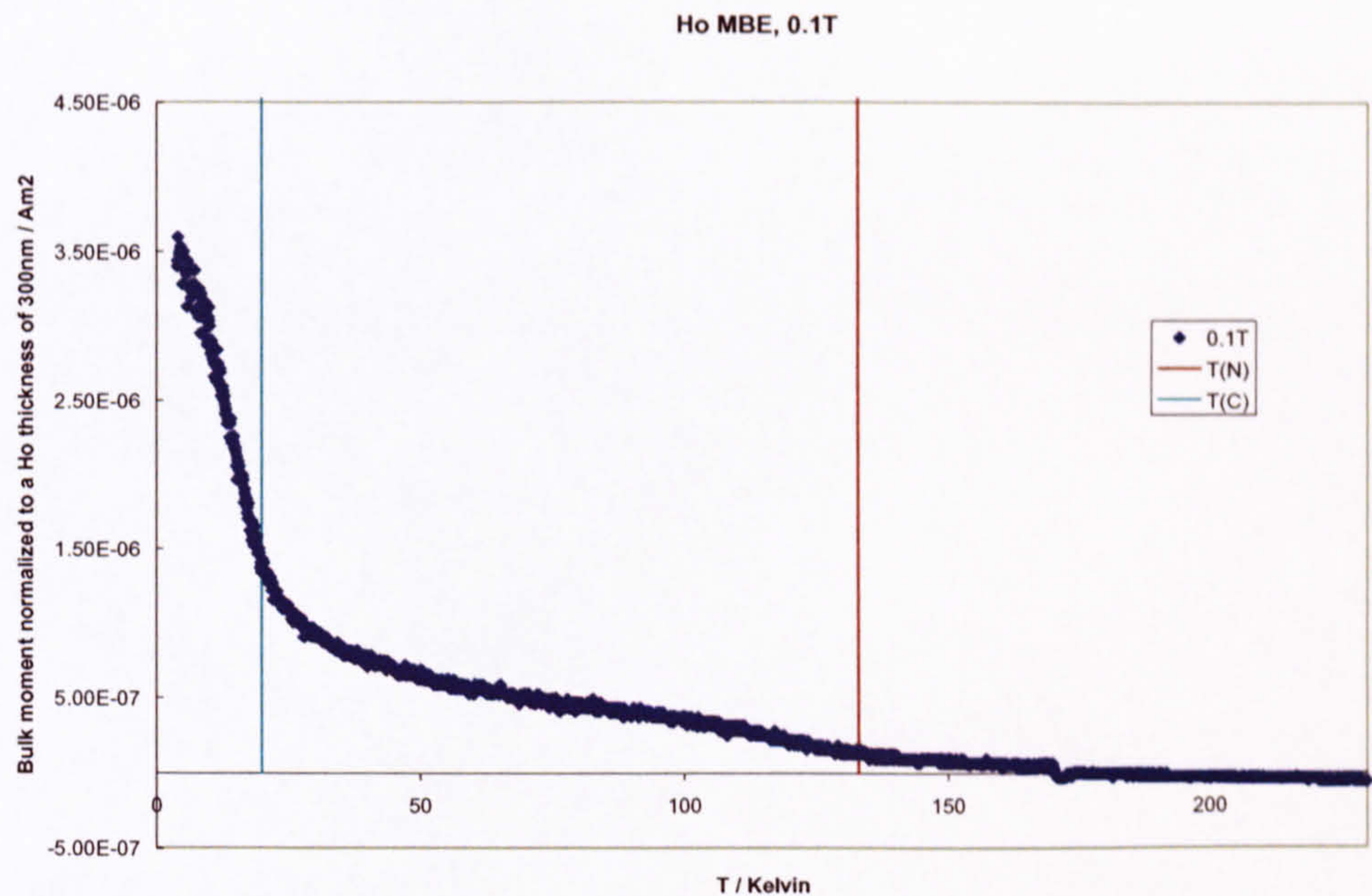


Figure 5. 3 Isofield from cooling Ho MBE in 0.1T applied field

The applied field of 0.1T was chosen here due to the work by Willis et al (1990)³⁹ and Jensen and Mackintosh (1992)⁴⁰. The gradient changes noticeably at ~130K and again at ~20K, T_N and T_C respectively. This is an important result as it means that the behaviour of the polycrystalline samples can be modelled on that of a single crystal, this being well understood. By relating the data of figure 5.3 to the phase diagram (figure 5.4) it is clear that in 0.1T applied field the sample is in the 1/6 structure.

The ordering of a single crystal of Ho is more complex than initially stated. Figure 5.4 shows the relationship between temperature and applied field and all the many magnetic phases that exist in the different combinations of these.

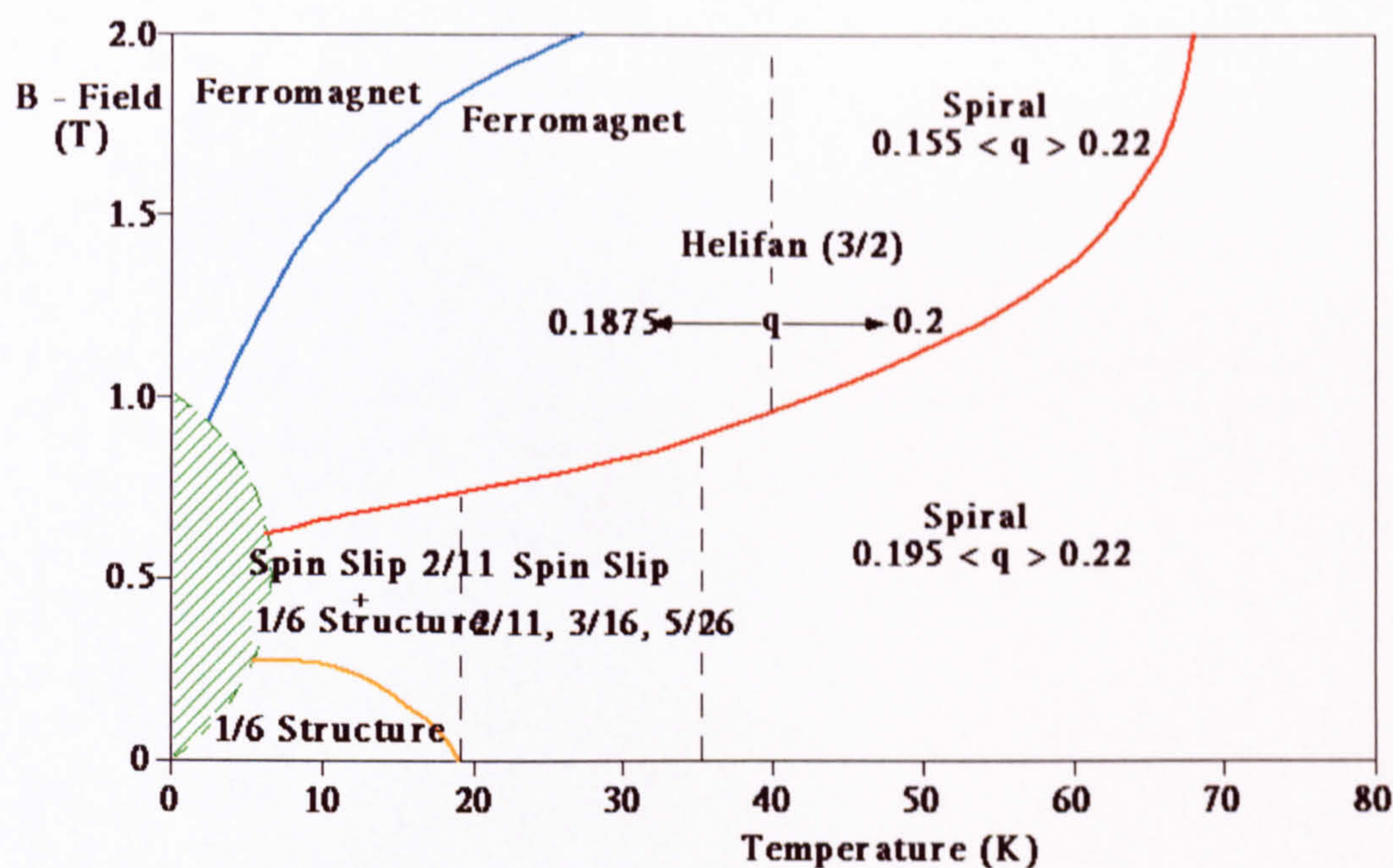


Figure 5.4 Phase diagram of holmium with a magnetic field applied along the easy b axis⁴¹

Increasing the field on the Ho MBE sample should force the sample into the FM regime at low temperatures. Figure 5.5 shows the effect of an applied field on the Ho MBE film.

Comparing figure 5.5 to the phase diagram of 5.4 there is a clear corroboration. The yellow 1.0T trace of figure 5.5 shows some magnetisation between 50-120K which is the helifan/spiral phase according to the phase diagram. The increase in gradient at ~40K marks the transition to FM. The maroon 2.0T trace shows the onset of FM at the higher temperature of ~70K almost avoiding the AFM stage altogether.

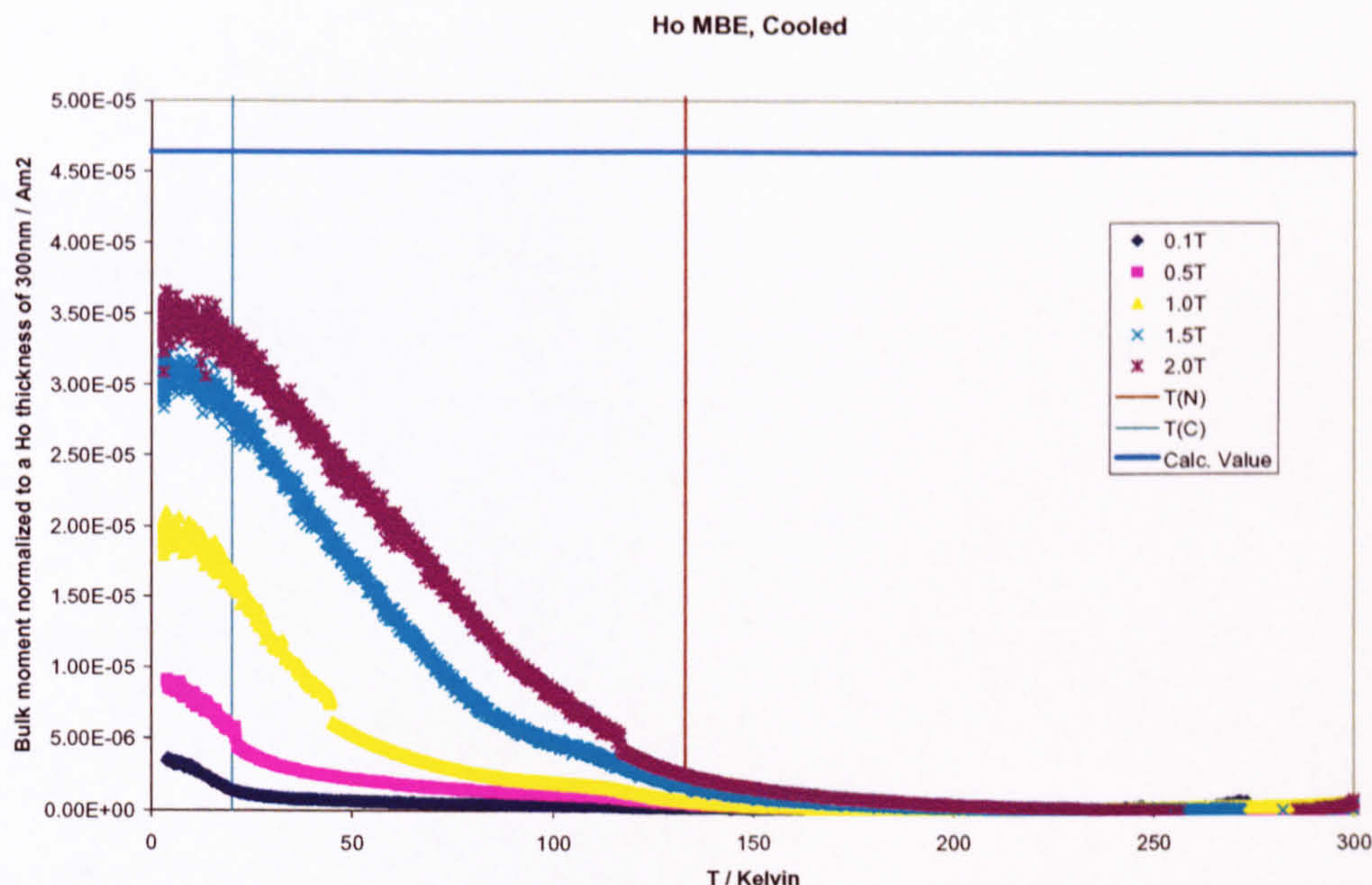


Figure 5. 5 Isofields from cooling a 300nm thick film of Ho. The horizontal blue line represents the calculated value of the saturation magnetisation ($4.64 \times 10^{-5} \text{ Am}^2$) of a 300nm thick film. The 'steps' seen in the 1.0T trace at ~45K and the 2.0T trace at ~115K are artefacts due to the lock-in amplifier increasing its range.

As the applied field is increased so the maximum magnetic moment increases. The polycrystalline sample is still following the behaviour of the single crystal in an applied field. The 1.5T trace shows an interesting feature at ~110K, the same being less prominent in the 1.0T trace. These changes in gradient in different applied fields between 20 and 200K are similar to those found by A. del Moral et al on $\text{Ho}_{30}\text{Dy}_{15}$ ⁴². In fields >1.0T the isotherms show a peak at ~10K. This implies that an increasing portion of the sample is becoming saturated as the FM ordering begins to dominate.

Snigirev, Tishin and Volkosub reported on a thermocycling hysteresis that extended into the PM state for a single Ho crystal⁴³. Isofields were obtained on heating the sample from 2K to 300K. The software sequence used to take these scans was only capable of scanning up to ~200K. Results presented in figure 5.6 show data from 3 scans taken in applied fields of 1.0, 1.5 and 2.0T.

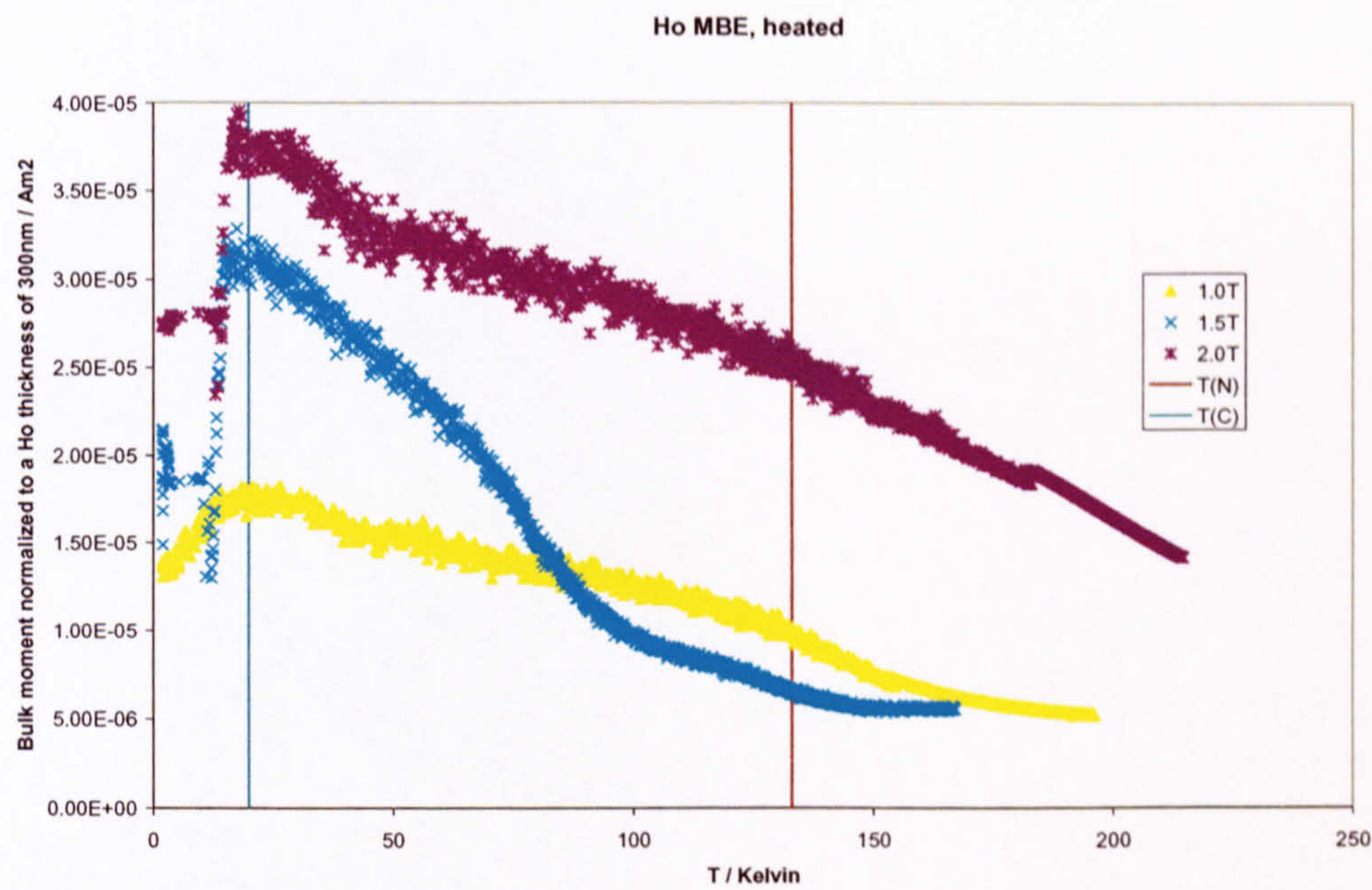


Figure 5. 6 Isofields from heating a 300nm thick film of Ho

The trough and peak structure <20K is similar to the data found on the single crystal by Snigirev et al. The trough and peak effect in these samples occurs between 0K and 20K but its origin is unknown. Figure 5.7 compares the effect of heating and cooling the Ho in the same field (2.0T).

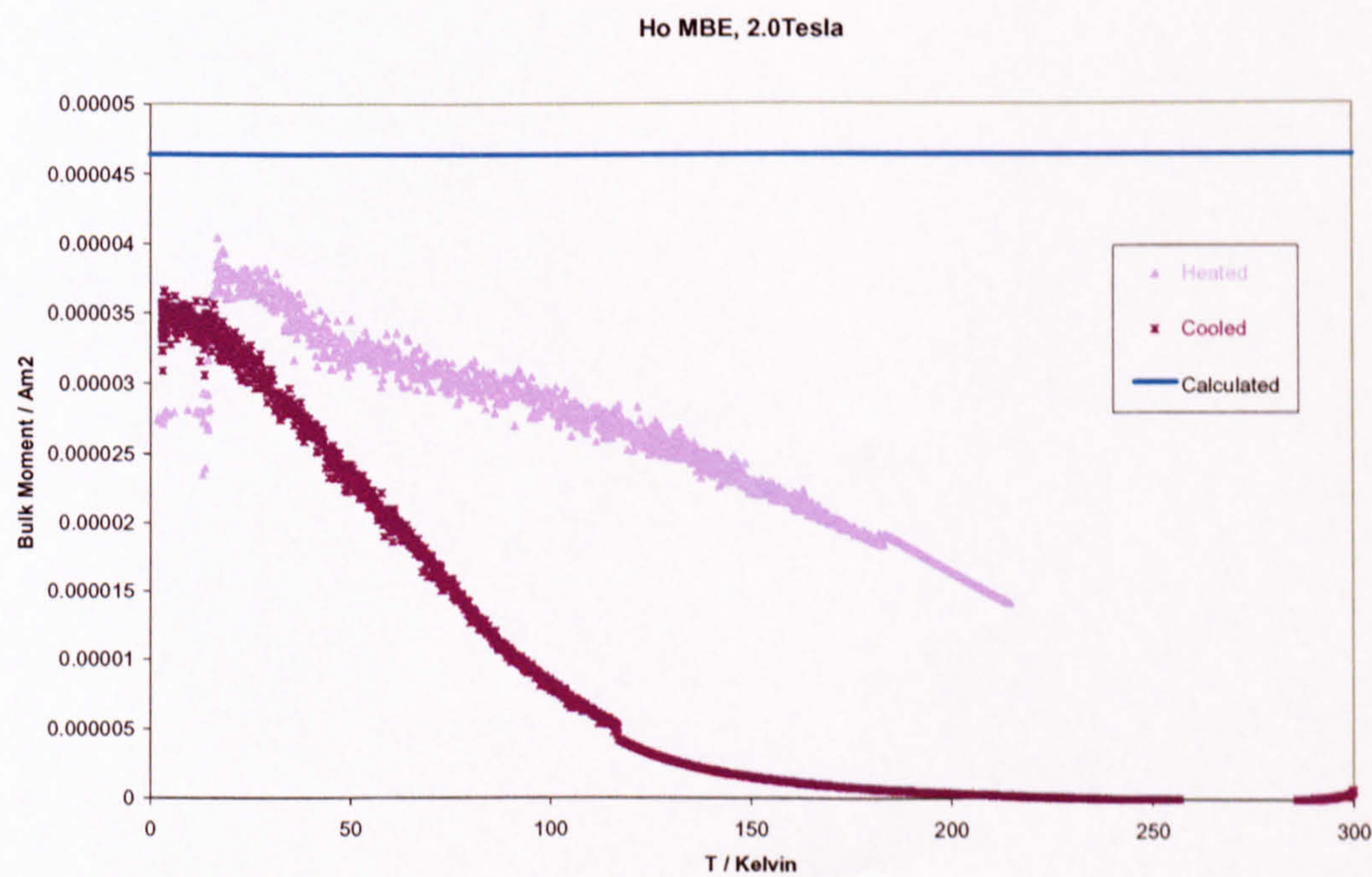


Figure 5. 7 Isofields from heating and cooling a 300nm thick film of Ho in an applied field of 2.0T

Note that the process followed to generate these isofields was not thermocycling. The heated isofield was generated by starting at room temperature, zfc to 2K, applying the field then heating whilst the field remained. There is a clear difference between the two traces implying that the FM remains locked in when the sample is cycled in such a manner.

5.2 Fe clusters in Ho

With the behaviour of pure Ho well modelled the investigation moved on to study the effects of addition of Fe nanoparticles to Ho as a matrix.

5.2.1 VSM Data

A 2% v.f.f. Fe cluster in Ho sample was measured at 0.1T applied field. The resulting isofield is shown in figure 5.8.

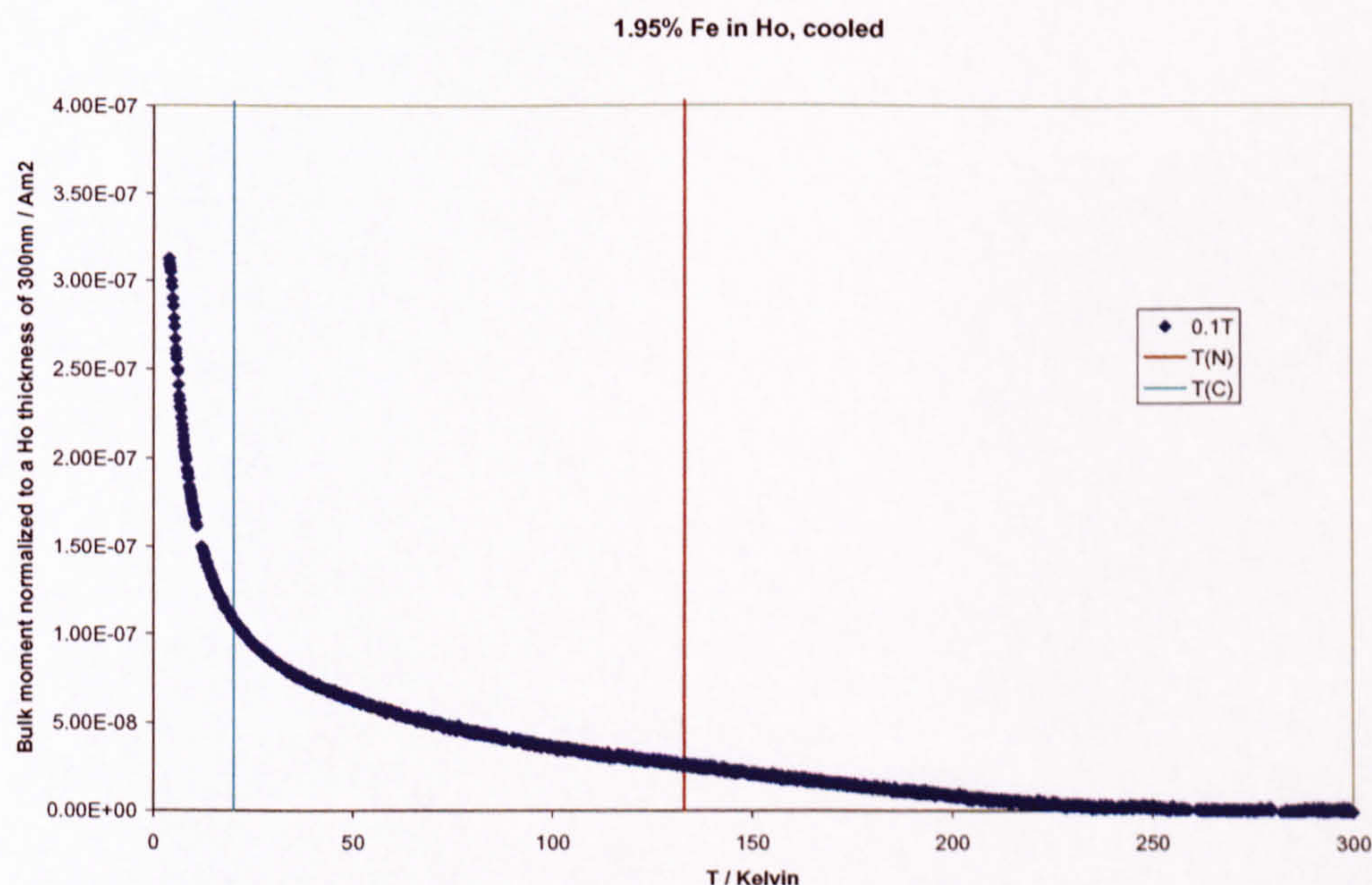


Figure 5. 8 1.95% Fe in Ho cooled in 0.1T applied field.

The isofield in figure 5.8 has a similar shape to the Ho MBE isofield in figure 5.3. However, the scales on the y-axis are completely different, as plotting the two samples on the same graph illustrates in figure 5.9.

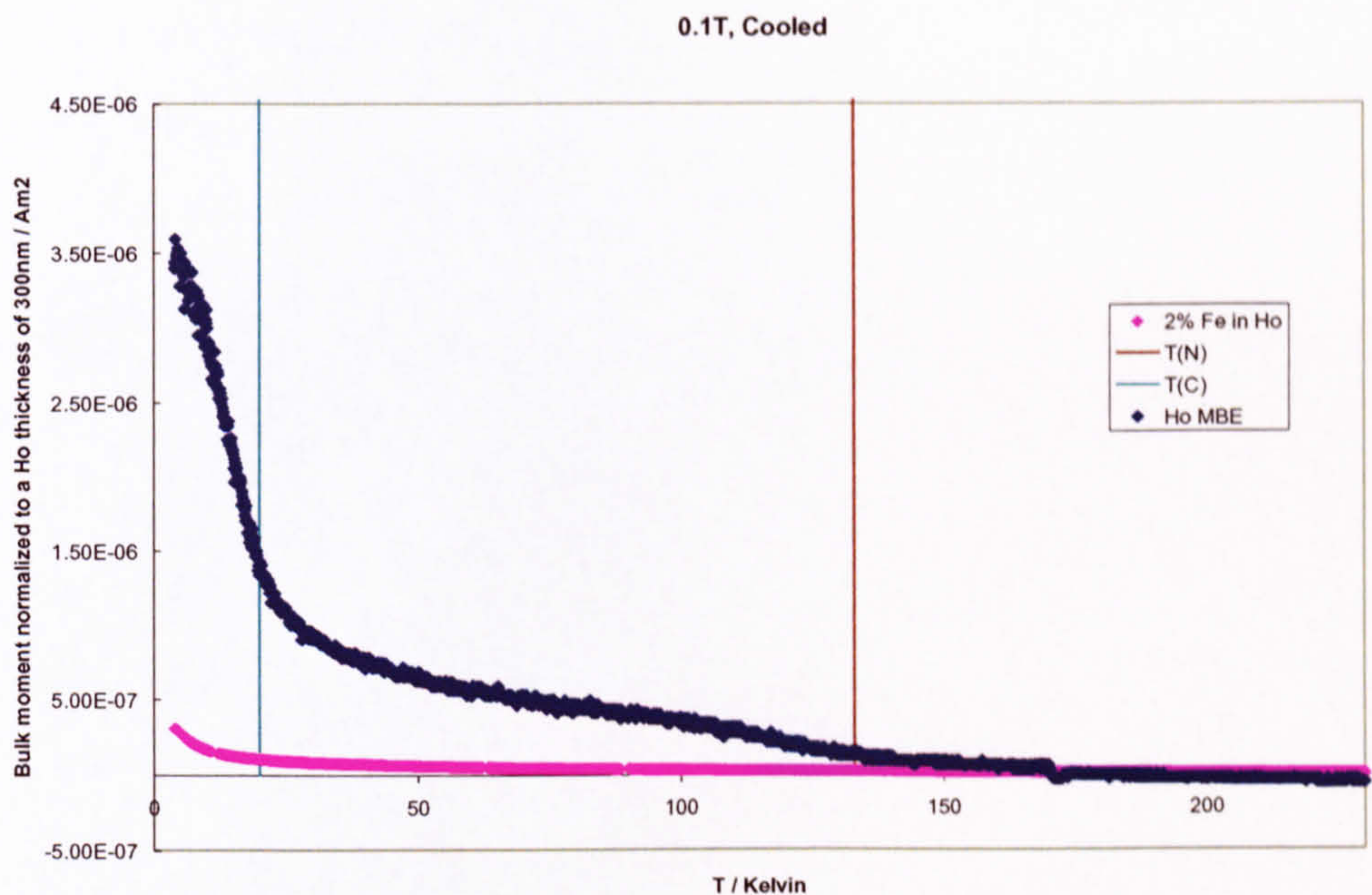


Figure 5. 9 Isofields comparing cooled 2% Fe in Ho and Ho MBE.

Addition of Fe to the Ho has reduced the moment significantly in this low field and the magnetic phases are difficult to determine.

An increase in the applied field produced the following isofields for the Fe/Ho alloy in figure 5.10.

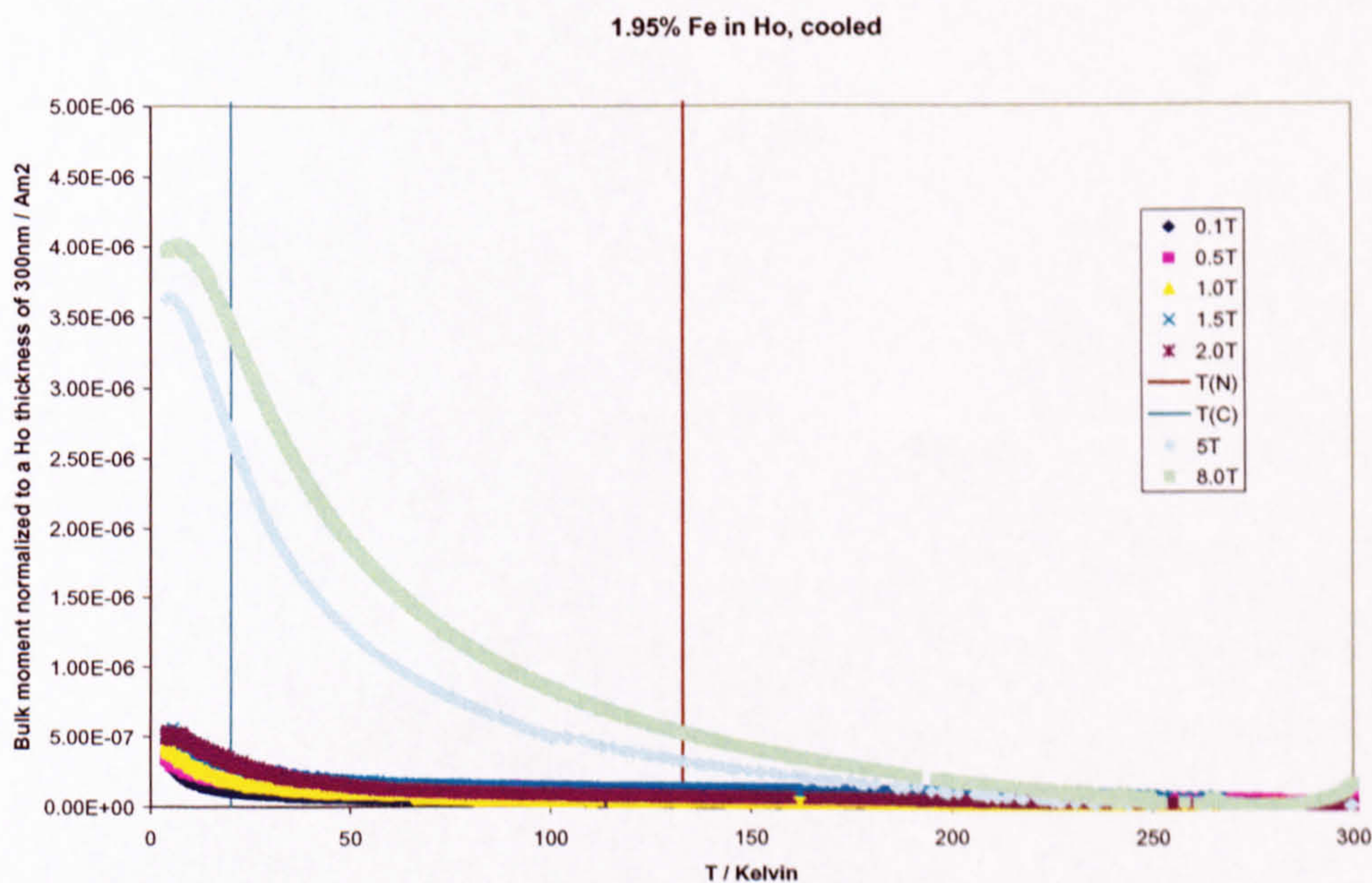


Figure 5. 10 Isofields comparing applied field on 2% Fe in Ho sample

Whereas with the Ho MBE a field of just 1.0T was required to produce the peaked curve, a much higher field of 5T is now required to achieve the same result in this Fe/Ho sample. Upon comparing heating and cooling isofields in these higher fields, there is again a difference in the traces.

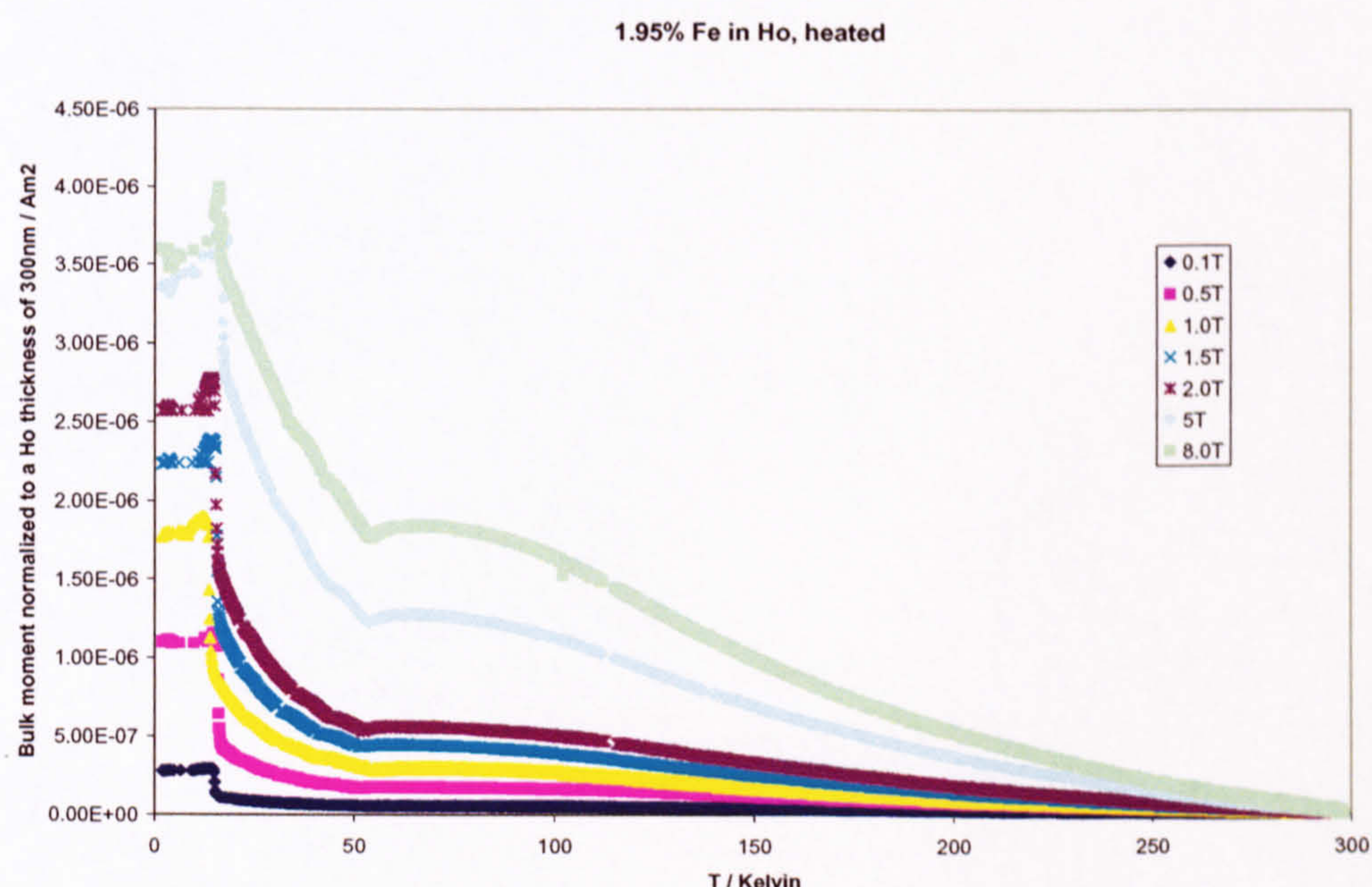


Figure 5.11 Isofields of heated 2% Fe in Ho

Figure 5.11 shows some interesting features at 16K and 50K. As the applied field is increased so too is the maximum saturation magnetisation. The heating response is different from the cooled response because of the sequence used prior to measurement. By cooling the sample in zero field the moments become frozen into random orientations at the lower temperatures. When the field is applied at these low temperatures a certain amount of energy in the form of heat must be added to the system before the moments can 'unfreeze' and align with the applied field. This is the peak seen at ~14K. The feature at 50K will be explored later in the chapter.

Increasing the v.f.f. of Fe in Ho also produces some interesting results. Figure 5.12 shows the 5 cooled isofields for a sample of 25.5% Fe in a Ho matrix.

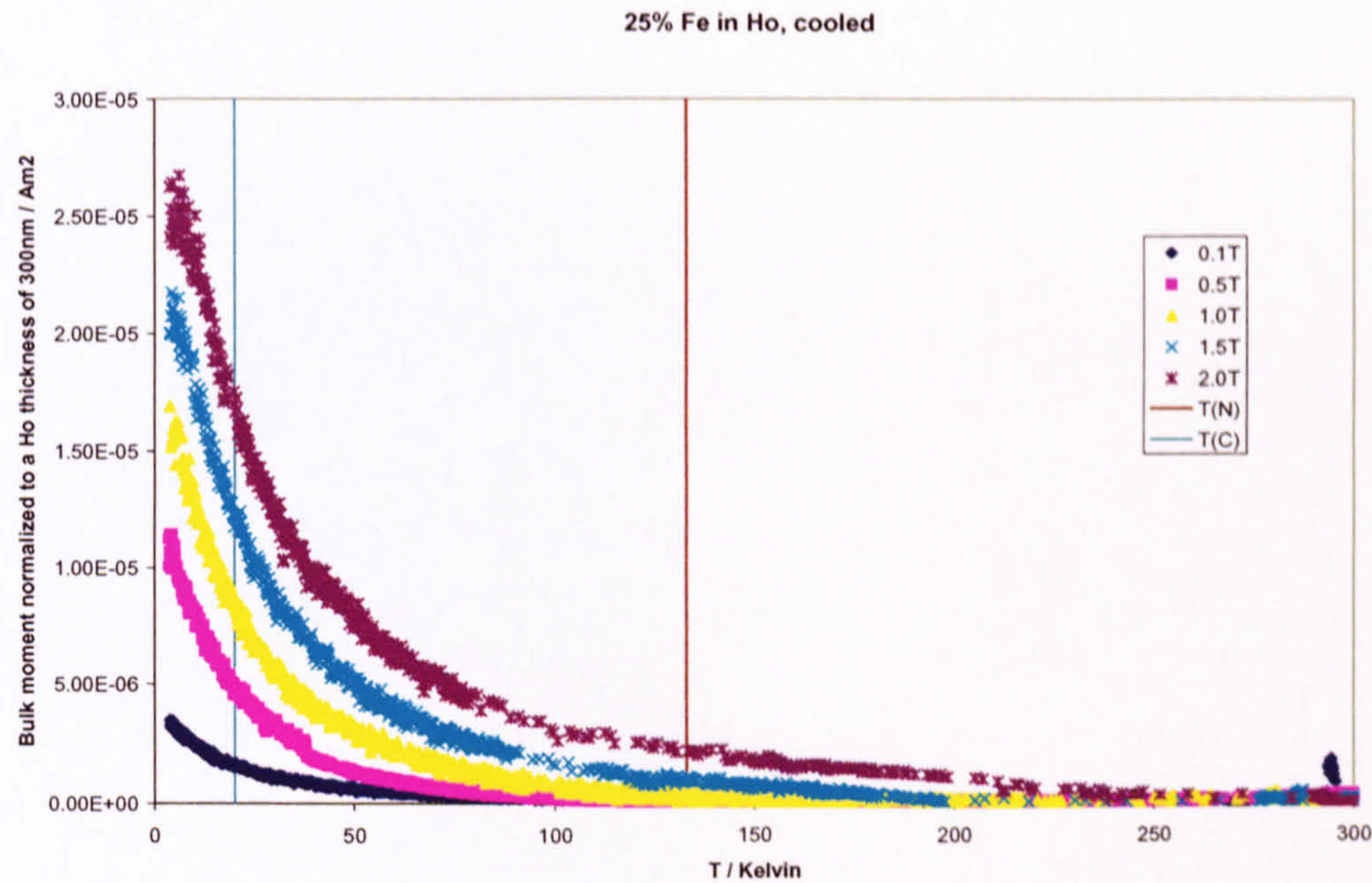


Figure 5. 12 Isofields from cooling 25.5% Fe clusters in a Ho matrix

The features in this graph are very different from those of the pure Ho sample. There is no sharp change of gradient at T_N or T_C but the gradient varies smoothly across the temperature range. These curves appear to be PM responses. There is no maximum reached with no associated saturation peak so addition of the Fe clusters in this proportion has affected the various low temperature spin-slip phases of holmium.

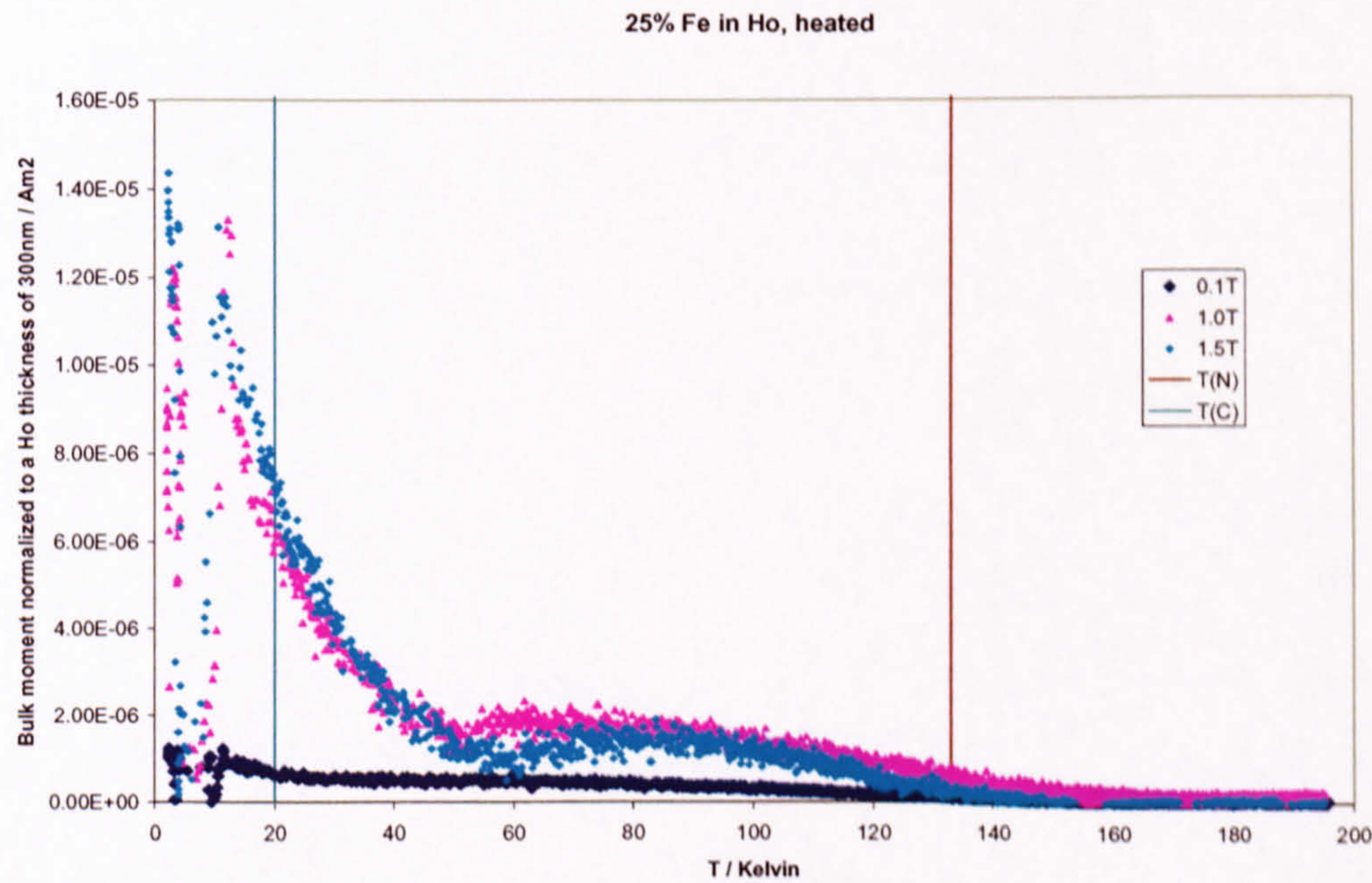


Figure 5. 13 Isofields from heating 25.5% Fe clusters in a Ho matrix

Figure 5.13 shows that heating the sample produces a different response from cooling. The low temperature structure in this sample shows the same complex behaviour as that of the pure Ho sample. There is the same trough/peak structure appearing at different applied fields. There is an interesting dip in the 2.0T trace at ~35K, whilst the 0.5, 1.0 & 1.5T traces show a dip at ~50K.

The feature developing at ~50K in figures 5.11 and 5.13 is similar to a feature found by S. Demirtas et al in tuneable magnetic thermal hysteresis studies of TM/RE multilayers⁴⁴. They report a 'bow-tie' effect whereby on heating and cooling the feature appears at different temperatures. Their effects are only seen in certain applied fields and for particular thicknesses of TM and RE however, the thermal hysteresis is clear and the feature in figures 5.11 and 5.13 at 50K is the same kind of feature as that in Demirtas' work. They attribute this feature to a switching of alignment of the moments within the sample. Their description involves discussion of 2 states; one whereby the TM is aligned parallel with the applied field and the RE is aligned anti-parallel, then after the 'switch' the opposite situation occurs. These are referred to as TM aligned or RE aligned. Extrapolating their description to this sample (when heated) it follows that between 20 and 50K the sample is Fe aligned. At 50K, there is too much thermal energy for the smaller Fe moments to remain aligned in the applied field and the sample switches to become aligned with the (larger) Ho moments. Upon cooling then, some anisotropy holds the Ho spins in place and the sample remains Ho aligned. In the lower applied fields the Ho moments have enough energy to combat the Fe moments and the samples appear disordered or showing a weak PM response.

This switching at 50K could be a superheating phase transition (SHPT). C.S. Arnold and D.P. Pappas talk of reorientation transitions⁴⁵ whereby at low temperature, continuous reorientation of the surface moment from in-plane to canted out of plane is characteristic of a second-order phase transition.

Camley and Tilley talk of a third 'twisted' phase in their work on magnetic superlattices⁴⁶ formed from two FM materials that couple AFM at the interfaces. Due to competing exchange and Zeeman interactions, a variety of phases exist in the superlattice where

there is alignment parallel and anti-parallel to the applied field or in the twisted phase the spins lie at a different angle with respect to the applied field.

The dips occurring in the Fe in Ho samples could also be explained as an artificial effect produced by the measurement process of the VSM. In order to maintain a temperature of 2K in the sample chamber the needle valve, N/V must be open by a particular amount, usually 25%. This opens the sample chamber (kept in a vacuum) to the He(l) tank. When the sequence is initiated to take the data the VSM automatically controls the heater in the sample space. This opposes the action of the open N/V which must then be closed. If the N/V is set straight to zero, when the heater is on, and a significant field is applied the temperature regulation is compromised. For example, there may be a sudden jump from 4K \rightarrow 12K, then back to 4K, rise slowly to 8K then shoot up to 14K. To combat this the technique was employed whereby the N/V was closed in 5% steps starting at 20K (i.e. at 20K close the N/V from 25% to 20%, at 30K close by another 5% etc). What this means though is that at 50K and 60K there is a significant change in the temperature of the sample space such that the dips in the isofields may be a systematic measurement error rather than a feature of the material.

Whilst this has been considered it is unlikely that such a large feature is due to the VSM measuring technique. For instance figure 5.6 does not show the feature at 50K. If there was a VSM error then it would appear on every graph. Figure 5.11 shows clear development of the 50K feature with increasing field. This feature, relative to the overall size of the graph, is too large to be a systematic measurement error. Focusing on the green 8.0T trace, the two smaller features occurring at \sim 30K and \sim 40K are most likely to be the effects of the N/V. Therefore the feature at 50K is definitely an intrinsic property of the material and not a measurement effect of the VSM.

Taking the maximum magnetisations obtained by each sample in each applied field will enable the different v.f.f. to be compared. Figure 5.14 plots pairs of traces for each sample tested; one for heating (h) and one for cooling (c) of the samples. The horizontal traces represent the expected magnetisation if all moments were to align with the external field.

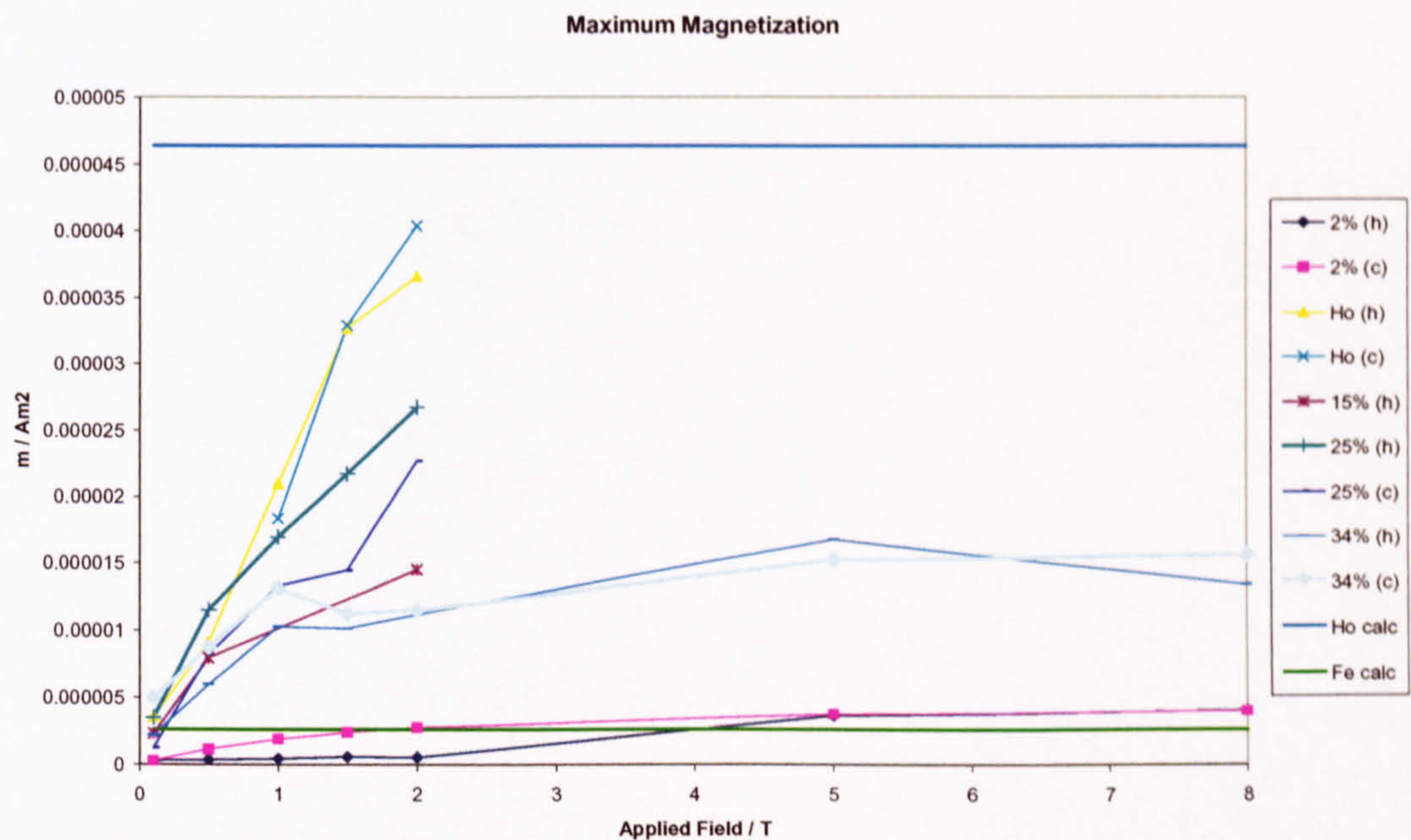


Figure 5. 14 Maximum magnetic moments taken from heated isofields at 2K

All traces show a positive correlation so all samples are aligning with the applied field. The lines at $2.6 \times 10^{-6} \text{ Am}^2$ and $4.64 \times 10^{-5} \text{ Am}^2$ are the calculated values of magnetisation for 30nm bulk Fe and 300nm bulk Ho respectively. These are the equivalent thicknesses used for all samples. Had the pure Ho sample been scanned in the higher applied fields it is expected that its trace would have converged with the calculated value.

Comparing the different samples, addition of the Fe clusters to the Ho has greatly reduced the maximum magnetisation obtained by the pure Ho sample. The 25% Fe in Ho sample has the closest magnetisation to that of the Ho MBE film.

It is important to highlight the main point again that whilst the traces of all Fe in Ho samples are interesting and show low temperature features, these are on a small scale when compared with the trace of the pure Ho sample. The overall moment of the Fe/Ho samples is still greatly reduced compared to that of the bulk.

5.2.2 TEM Images

The batch of 5 samples intended for XMCD measurement had become oxidised which rendered the XMCD data useless. One of the XMCD dichroism traces is shown in figure 5.15. Oxidation is evident from the shoulder on the first peak approximately halfway up the leading edge and also the L_{III} edge should only be twice the height of the L_{II} edge. The first peak is at least 4 times the height of the second.

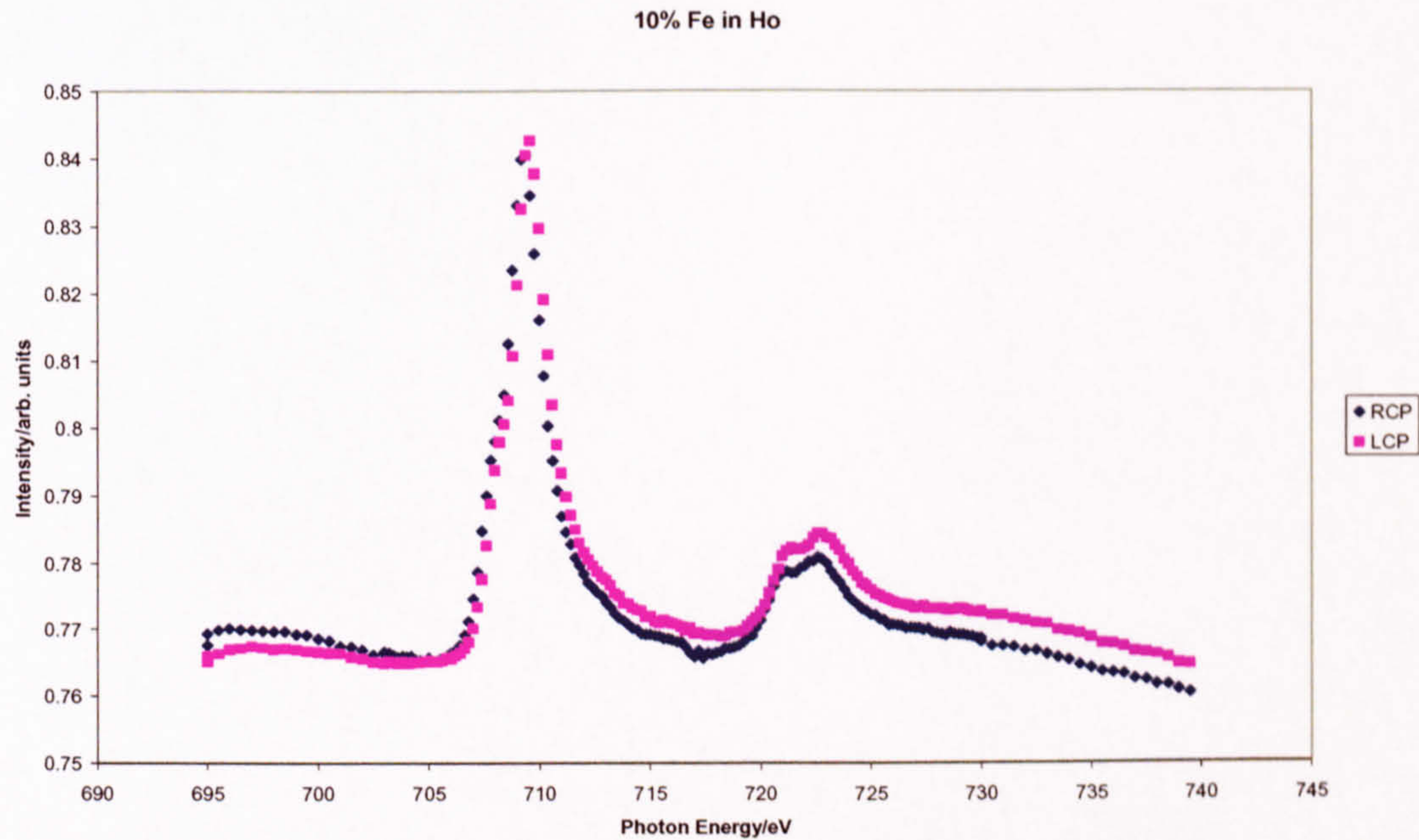


Figure 5. 15 XMCD data of sample TDK31, 10% Fe in Ho. Data taken at Daresbury in October 2006.

In order to make best use of the samples the 2% Fe in Ho sample was imaged in the TEM generating the images in the following figures.

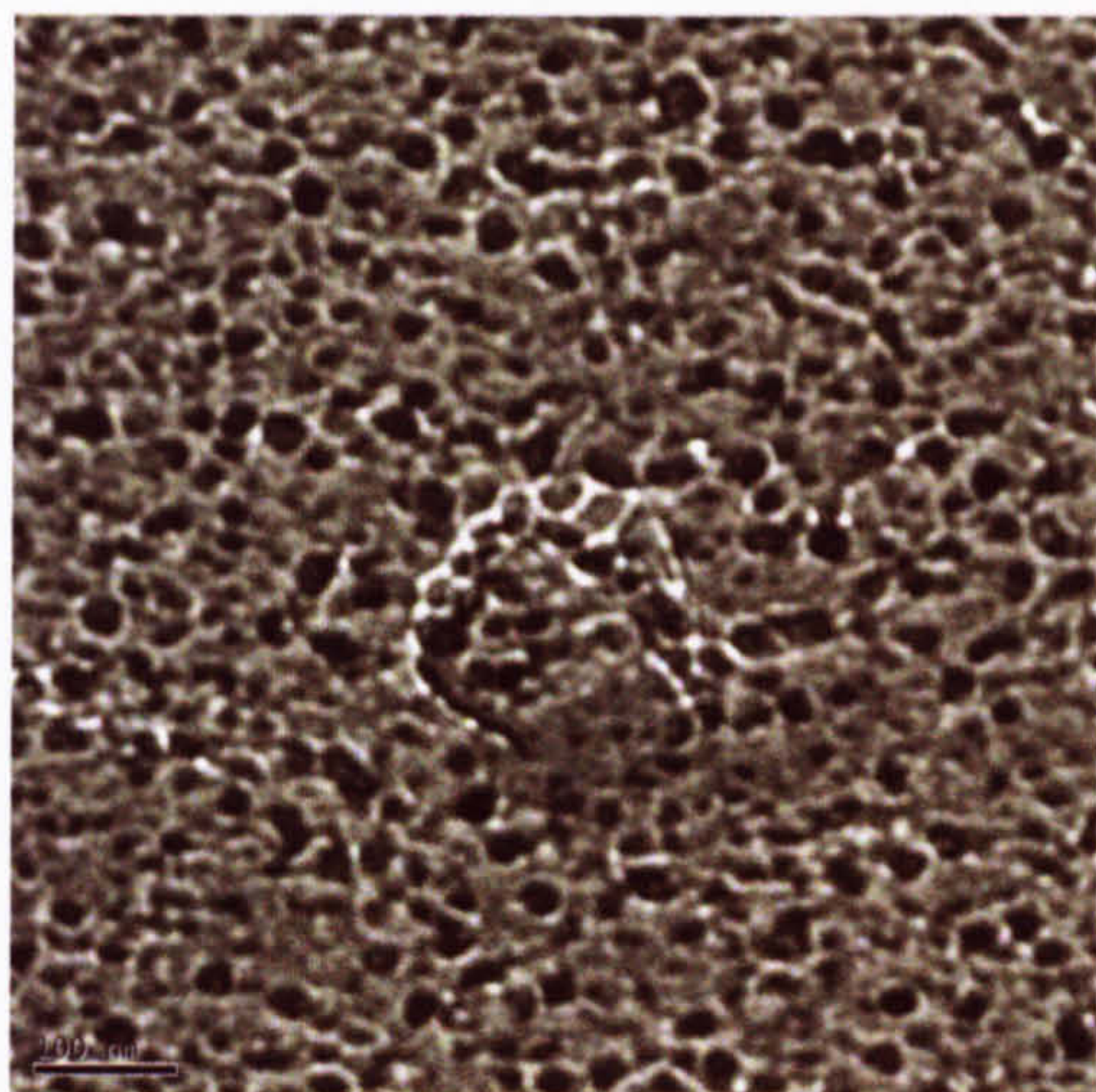


Figure 5.16 2% Fe in Ho TEM image (100nm)

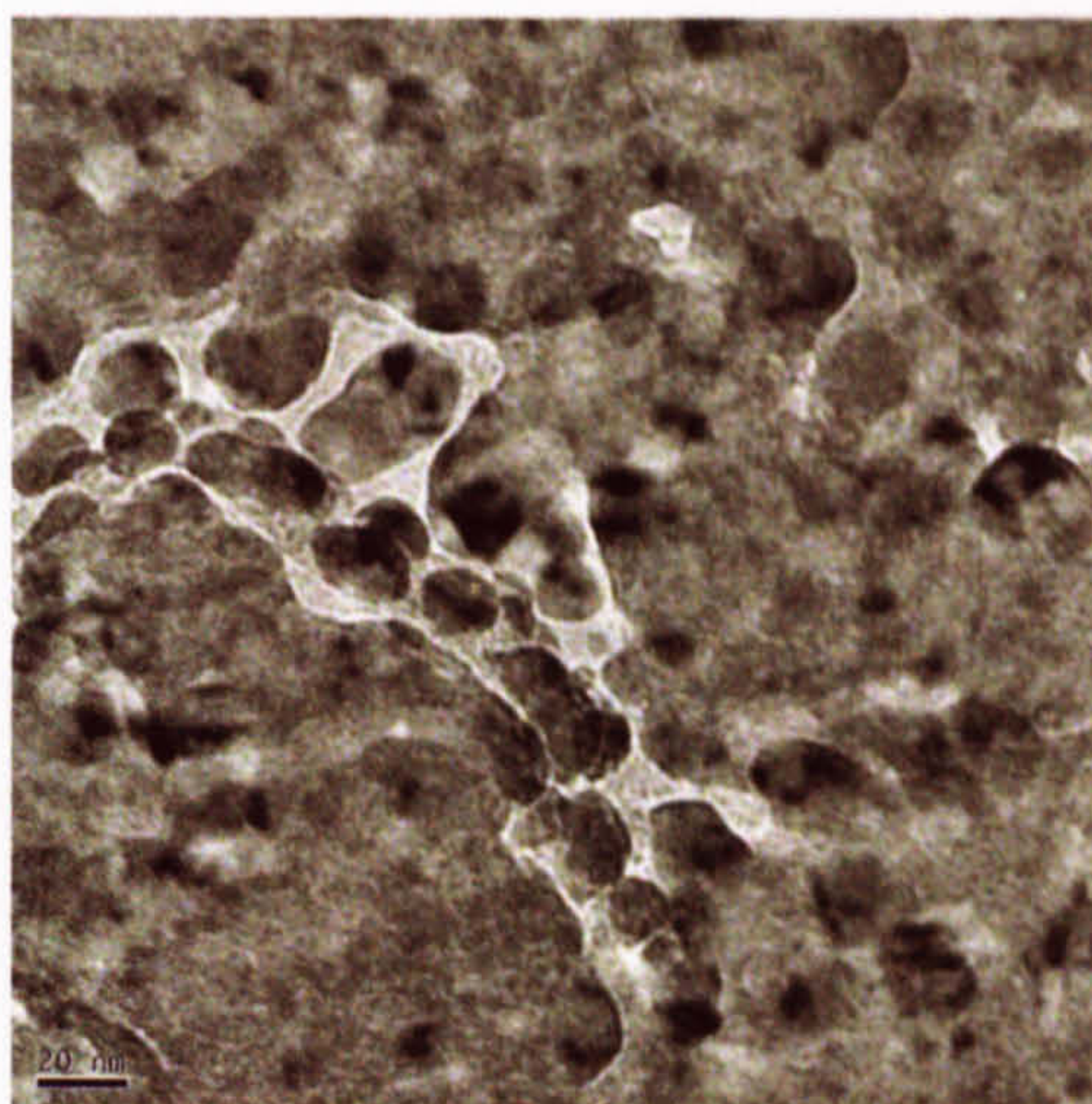


Figure 5.17 2% Fe in Ho TEM image (20nm)

The first image in figure 5.16 shows the lighter circles of the silver capping layer. This appears to have become compromised. The chain-like feature in figure 5.16 has been magnified in figure 5.17 where the darker circles beneath are more apparent. The medium gray colour is the C buffer whilst the black circles show holes in the sample right through the Cu mesh. This sample has a v.f.f. of just 2% Fe within a Ho matrix meaning individual clusters will be well separated from one another and should appear as small crystalline regions with a diameter of no more than 3nm.

Figure 5.18 shows a TEM image taken at a further level of magnification and it clearly shows the atomic layers. There are 17 layers in a 5nm length on the central region of this image. The atomic spacing is therefore $5\text{nm}/17 = 0.294\text{nm}$. There are 18 layers in a 5nm length on the top right region of this image. The atomic spacing is therefore $5\text{nm}/18 = 0.278\text{nm}$. The atomic masses and elemental densities of the 3 substances; Ag, Fe and Ho, in this sample can be used to calculate their respective atomic spacings which may lead to identification of the substance in the image.

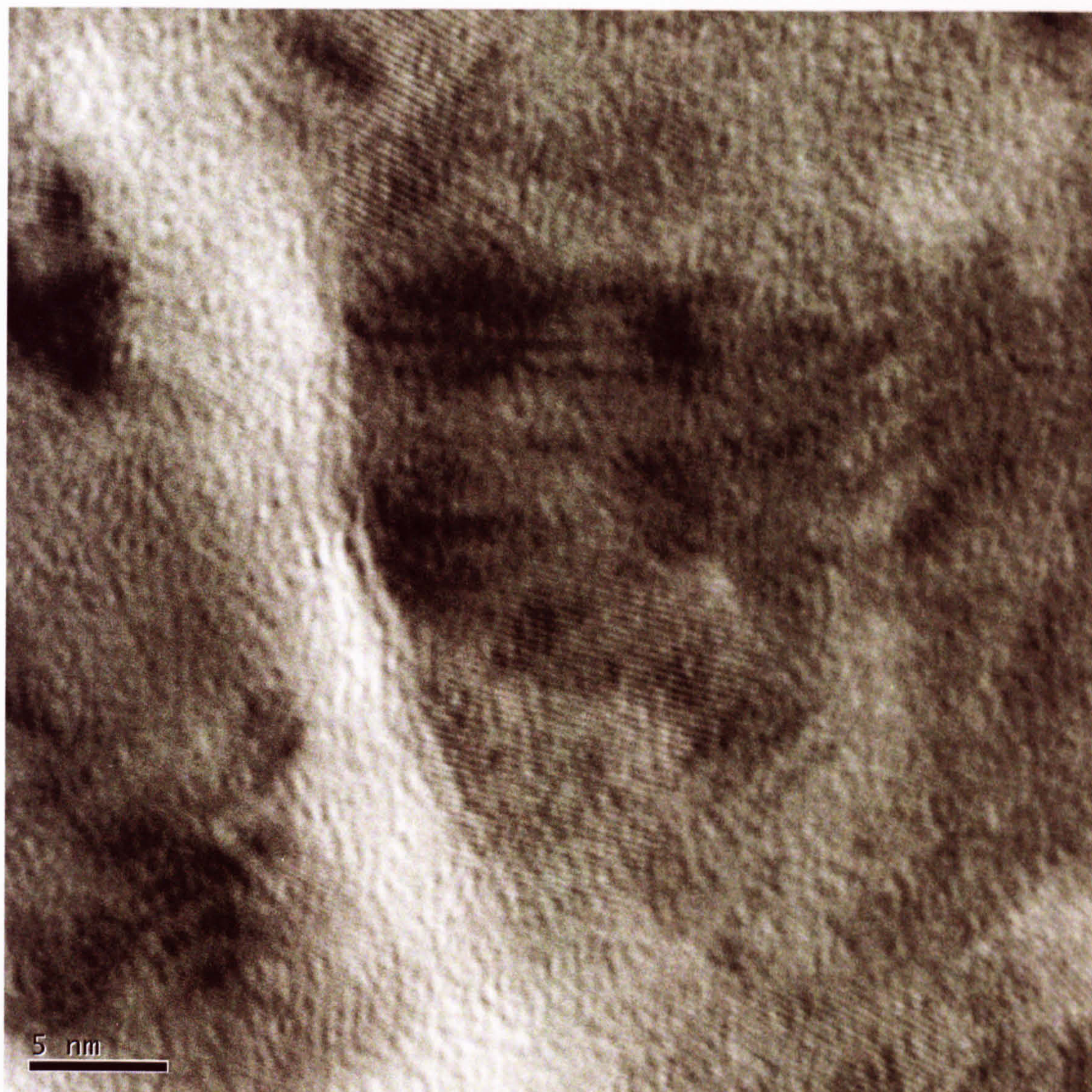


Figure 5. 18 2% Fe in Ho sample clearly showing atomic plane structure

The graph in figure 5.19 plots the atomic diameter of Fe, Ag and Ho and the corresponding atomic spacing of layers of these atoms. The blue graph is a theoretical curve calculated by assuming the atoms are arranged in a simple cubic lattice structure (not close-packed) with atomic spacing equal to 1 atomic diameter.

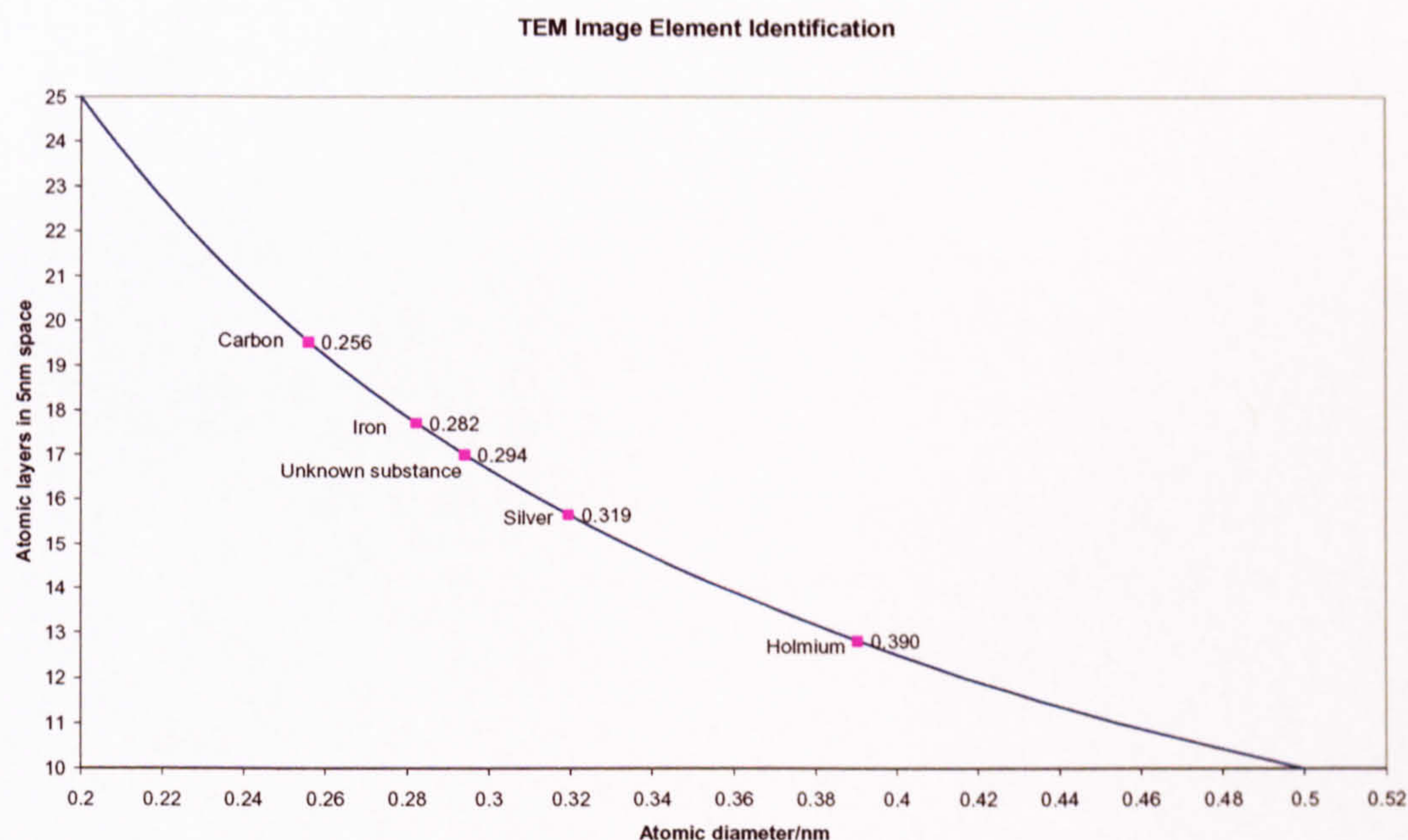


Figure 5. 19 Theoretical curve (blue) and calculated values for specific elements

Fe has an atomic diameter of 0.282nm and this would correspond to ~17.5 atomic layers in a 5nm region. This is close to the measured number of layers, 17, so these crystalline regions are likely to contain Fe. However, an Fe cluster has a diameter of ~2nm which raises an important question. Why are these crystalline structure sites so large? The area of crystalline structure in the centre of figure 5.18 is ~10-15nm in diameter whereas the mass spectrum of the clusters used in this sample show that the mass distribution of the clusters centres around 14,000 a.m.u. corresponding to a cluster diameter of 1.8 nm. Even the full range of the mass spectrum only corresponds to a cluster diameter ranging from 0.9 – 2.7 nm which does not begin to cover the sizes seen in the TEM image.

The answer lies in the suspicions from the XMCD data. The cluster sites seen in the image of figure 5.18 were probably once Fe clusters but are now much larger 'clusters' of one of the iron oxides which are also crystalline in structure. Shaikhutdinov et al reported on the interatomic distances of the oxygen atoms in the three iron oxides⁴⁷. The table in figure 5.20 summarises their data.

Oxide	Structure	Miller indices	Interatomic Spacing (nm)
FeO	HCP	(111)	0.304
α -Fe ₂ O ₃	Corundum	(0001)	0.291
Fe ₃ O ₄	FCC	(111)	0.296

Figure 5. 20 Interatomic spacings of iron oxides.

With the value for the interatomic spacing of 17 atomic layers at 0.294nm the crystalline structure in the centre of the TEM image is likely to be Fe₃O₄ whilst that in the top right is more likely to be Fe₂O₃. This would corroborate the assertion made when taking the XMCD data that the samples had become oxidised.

5.3 H₂(g) coated Fe in Ho

The final batch of samples contained 2 samples; an Fe MBE film and an H₂(g) coated 20% v.f.f. Fe in Ho sample. Hydrogen was added to LUMPS at a partial pressure of 0.5×10⁻⁵ mbar. Isotherms generated were inconclusive but the isofields showed an increase in the temperature at which the proposed SHPT occurred as figure 5.21 shows.

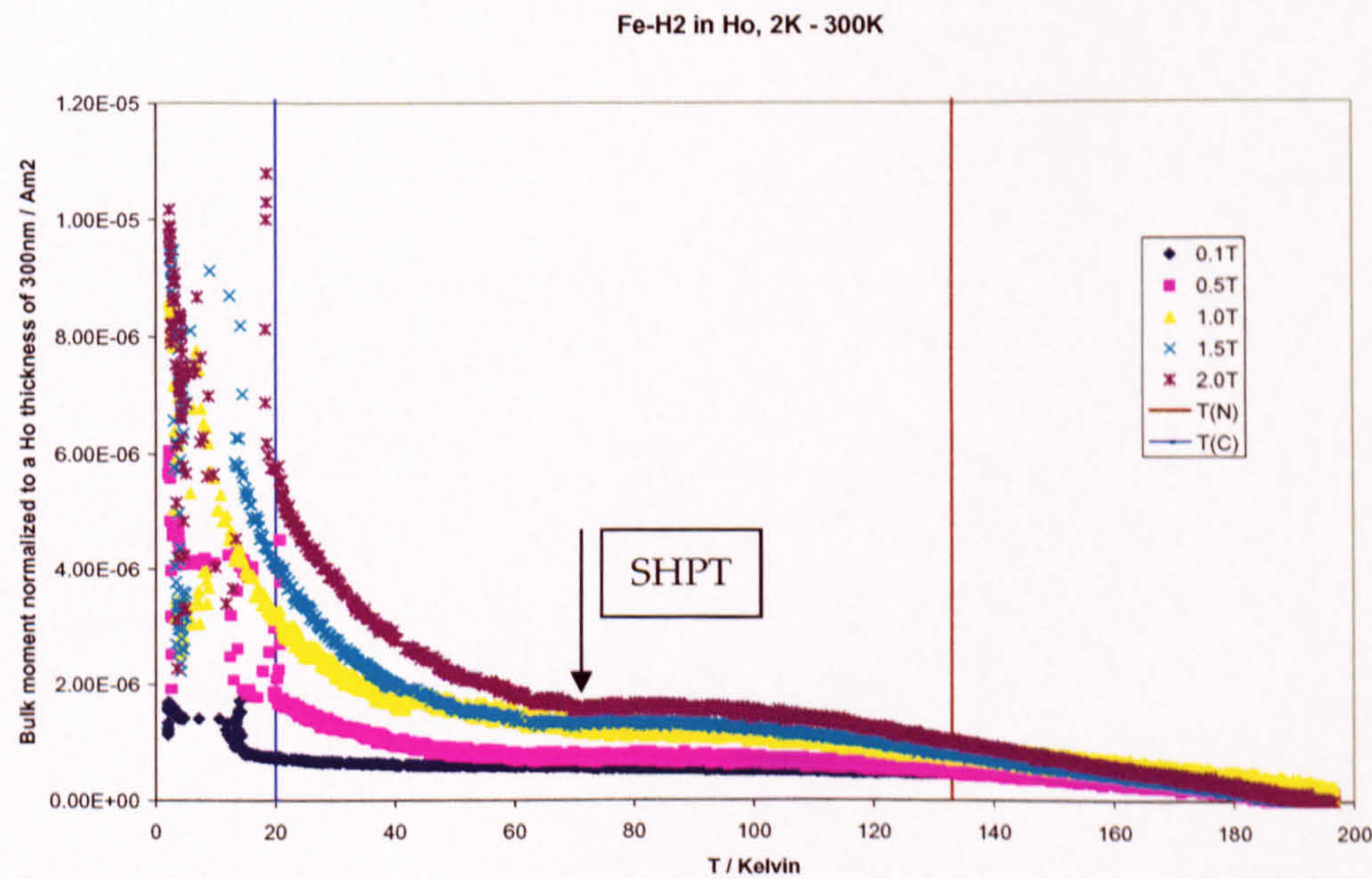


Figure 5. 21 Fe-H₂ in Ho matrix heated to 300K

The transition occurs at 70K, an increase of 20K on the samples without H added. If this sample had not deteriorated and the high field scans could have been executed, the transition at 70K would have become clearer.

5.4 Summary

The saturation magnetisation of all Fe/Ho systems, whilst lower than the bulk Ho, is higher than that of the Fe clusters alone. Different v.f.f.s affect the maximum magnetisation possible. The optimum v.f.f. of ~25% corresponds to the percolation threshold – the point at which clusters in a matrix begin to touch one another.

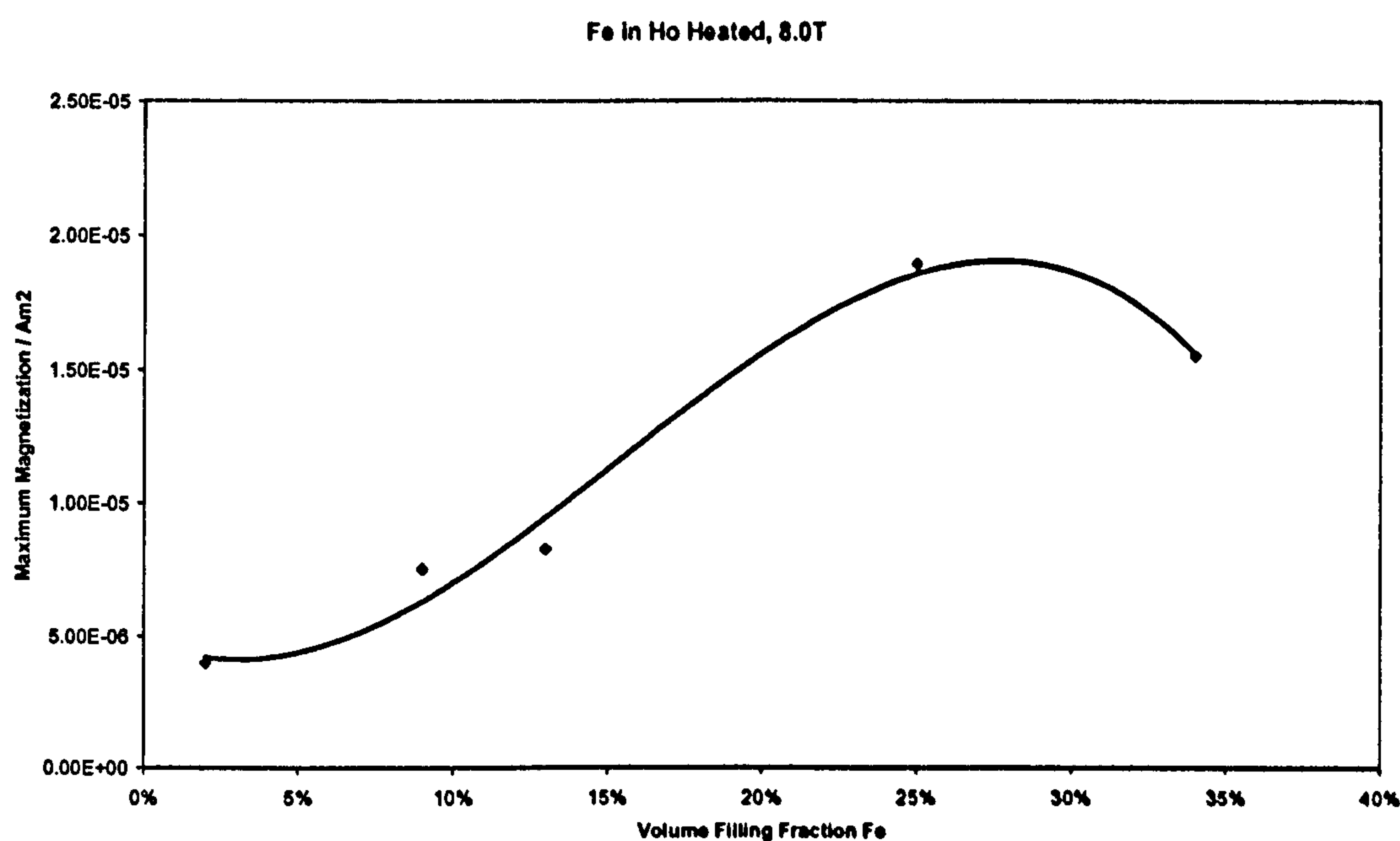


Figure 5.22 Fe vff vs saturation magnetisation for Fe/Ho systems

Long range ordering in the bulk Ho sample is lost in applied fields >1.0T. Addition of the Fe to the Ho decreases the overall magnetisation of the sample and destroys the long-range order of the Ho.

Thermal hysteresis is seen in all samples. For confirmation of a superheating phase transition in the Fe/Ho samples further tests would have to be carried out. The VSM cannot measure the temperature of the sample directly so such tests would have to be conducted using other equipment.

A Langevin function could be fitted to the PM sections of the isofields, that is, at the higher temperatures however, as this function only applies to isolated particles it may only be of use for the 2% Fe in Ho sample.

"The important thing is not to stop questioning. Curiosity has its own reason for existing."

Albert Einstein
(1879-1955)

Chapter 6

Fe clusters in Dy

By 1954 the complexity of the magnetic structure of Dy was well understood with Elliot, Legvold and Spedding describing four distinct magnetic states⁴⁸. With decreasing temperature these are; PM, AFM, FM and some other FM structure. Whilst they identify the fourth region as lying below 25K they make no attempt to explain its structure. Their data additionally indicated a saturation moment of $8.7 \mu_B/\text{atom}$. (Today a value of $10.2 \mu_B/\text{atom}$ is used.)

By the late 1960's investigations had proceeded to greater temperature ranges and more was understood of the various structures. Jordan and Lee proposed a fifth phase in the range $T_C (89\text{K}) < T < 125\text{K}$ when measuring along the c-direction in crystals where the c direction and one other major direction are parallel to the plane of the disk, i.e. either (1120) or (1010) parallel to the surface⁴⁹. They conclude, following a simple analysis, that the first order transition in Dy (i.e. at T_C) is controlled by the strong dependence of the exchange parameters on lattice dimensions rather than the hexagonal anisotropy.

In 1978 the two forms of AFM ordering between T_C and $T_N (176\text{K})$ were fully investigated and found to be dependent upon temperature and applied field. Herz and Kronmuller proposed a magnetic phase diagram for Dy⁵⁰ describing the conditions for the helical and fan structures reproduced in fig 6.1.

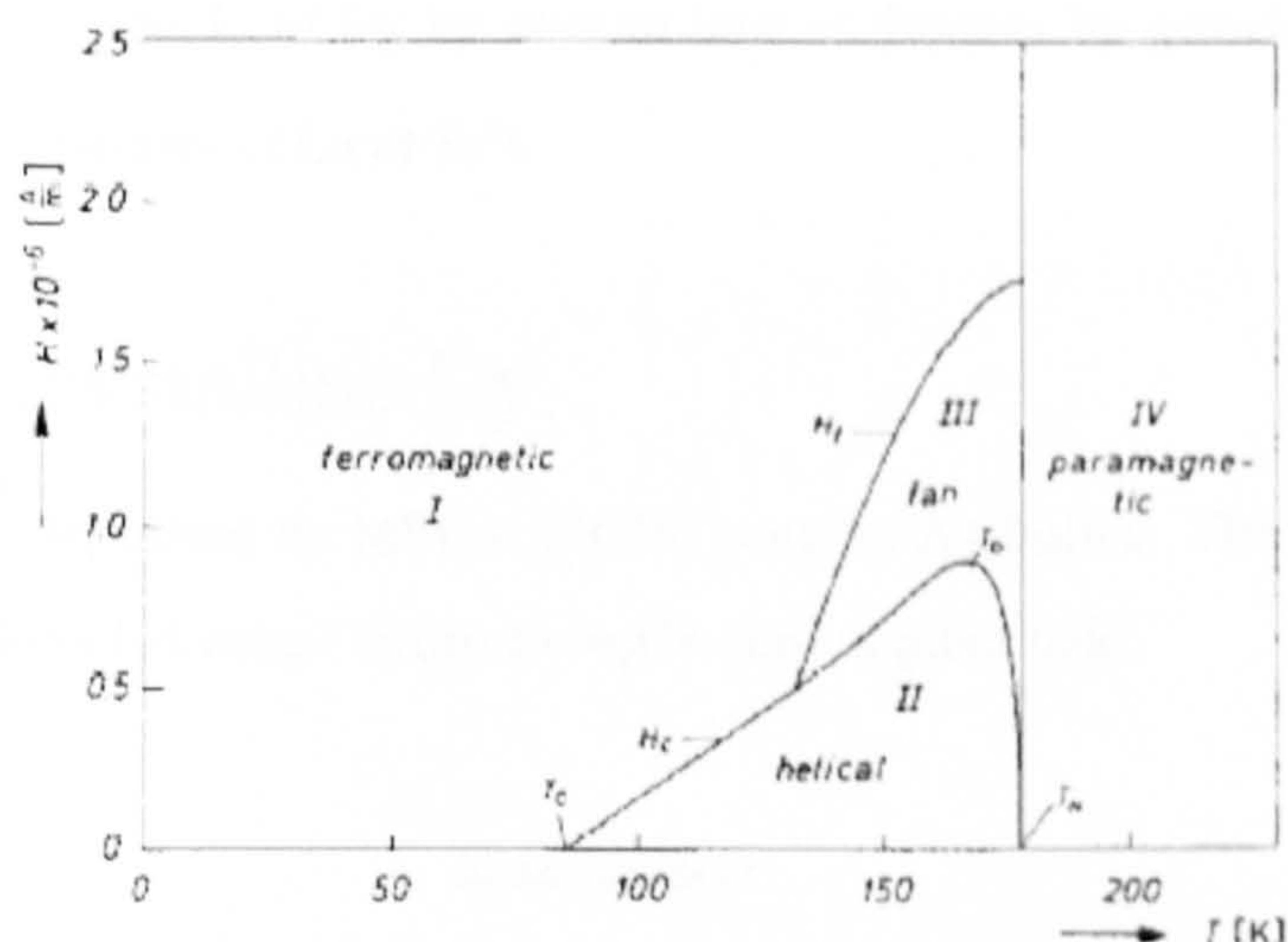


Figure 6. 1 Phase diagram of Dy as derived from magnetisation curves. (Reproduced from ref 48)

They surmise that in the temperature range $T_C < T < T_N$ it is possible to convert the helical phase into the FM (fan) phase by applying a magnetic field in the basal plane.

Bagguley and Howe employ a full mathematical treatment of the spiral spin phases⁵¹ based on a straightforward energy equation with the evolution of the spin structure being obtained from solutions of the Euler-Lagrange equations. They conclude that if anisotropy and magnetostriction are sufficiently high the phase transition can be direct from the helical to the FM configuration.

This work was expanded further by Andrianov, Gaidukov and Vasil'ev who reported differing structures in the FM region dependent upon the direction of the applied field i.e. parallel to the a or b axes⁵².

It is now well known that, in the ground state AFM regime, the structure is helical along the c-axis with the spins rotating from one sheet to the next by a turn angle of 43° . The turn angle decreases to 26.5° at 85K, where a spontaneous first order transition to FM occurs⁵³ all occurring within zero applied field.

Irrespective of the complex structures Dy remains PM above 178K. Any manipulation of Dy would be with the intention of increasing this such that T_N were much closer to room temperature or, ideally, such that T_C were close to room temperature. Dufour et al

managed to increase the T_C of Dy by several tens of degrees by growing thin films (10-350nm thick) on substrates of Lu or Er⁵⁴.

6.1 Polycrystalline Dy

300nm of Dy was deposited by MBE at 1100°C onto an Ag buffer. The ground state was established with a cooled temperature sweep in zero applied field.

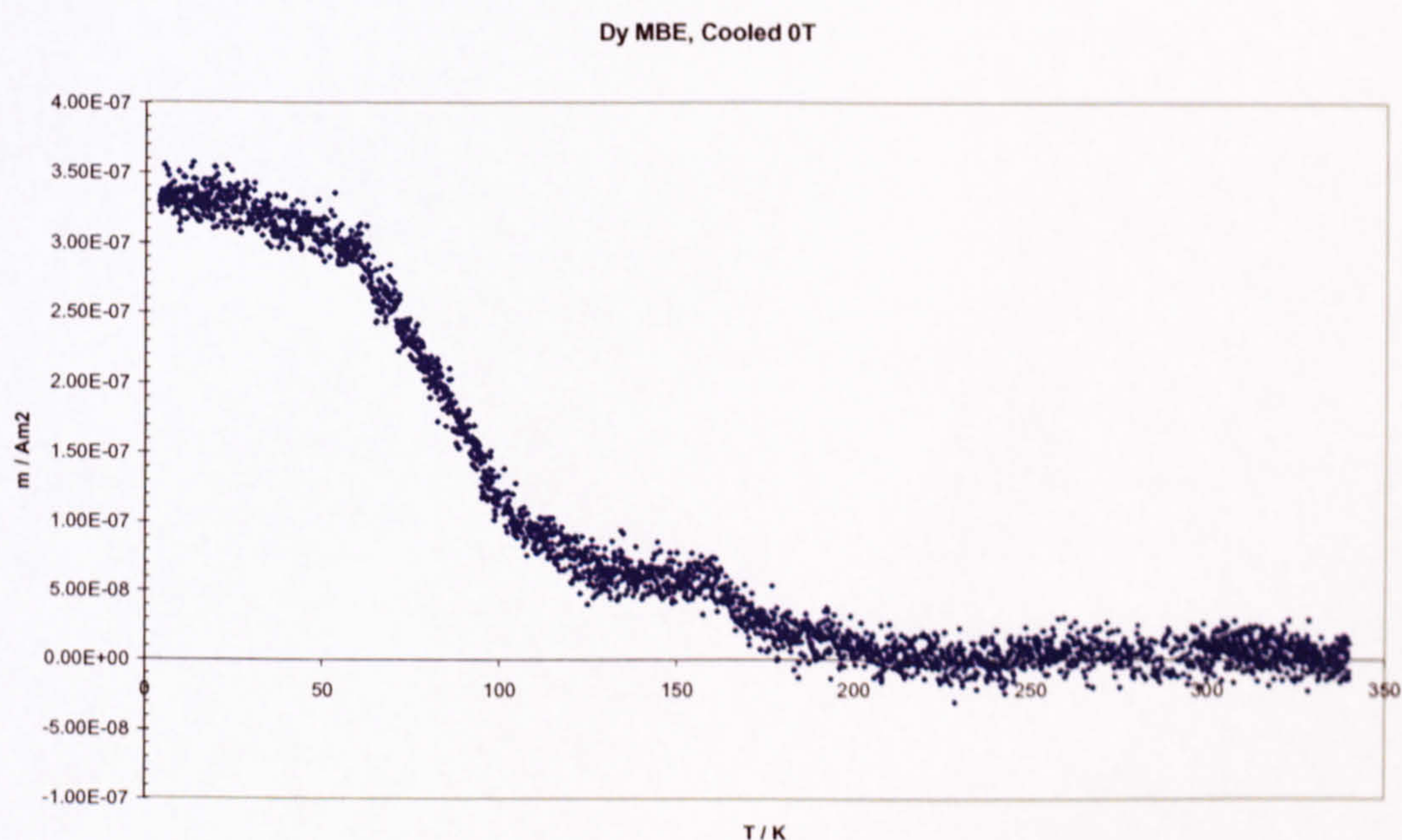


Figure 6. 2 300nm thick Dy MBE film cooled in zero applied field

Figure 6.2 shows exactly the T_N marked by the change in gradient at ~175K, after this the trace remains level at $5 \times 10^{-8} \text{ Am}^2$, this being the AFM stage, then the second change in gradient with a maximum slope at ~80K represents the transition to the FM stage. This FOPT in Dy was characterised by Chaudhary, Garg and Rajput using minor hysteresis loops⁵⁵. The overall scale is two orders of magnitude smaller than expected. In zero applied field the polycrystalline sample is probably arranged into domains which almost entirely cancel generating this very low signal.

Seeing these features in a bulk polycrystalline sample as they would appear in a single crystal provides the valuable reference for all subsequent scans taken on the Fe-Dy alloyed samples.

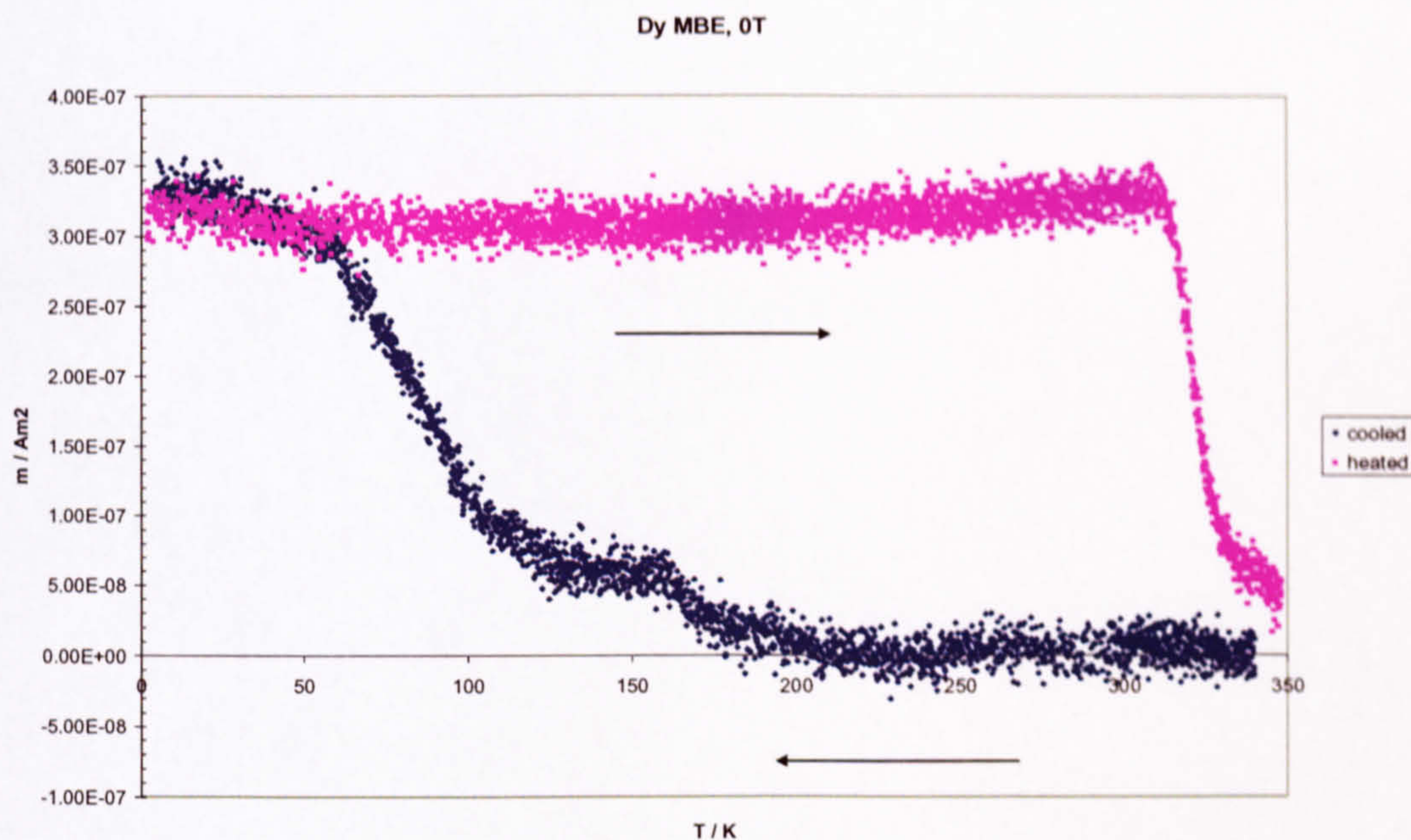


Figure 6.3 300nm thick Dy MBE film heated in zero applied field

Figure 6.3 includes data taken by heating the MBE sample. By starting at a temperature of 2K the moments are locked into their FM configuration which is sufficiently strong to overcome the thermal effects until 325K when the magnetic order collapses and the thermal energy dominates. At this temperature the alignment is lost completely and the sample reverts to a PM state.

Figure 6.4 (a-h) shows the effect of an applied field on T_N and T_C . Heated traces were obtained by starting at room temperature, cooling zfc to 2K, applying the field then heating at a constant rate of 10Kmin^{-1} under the applied field.

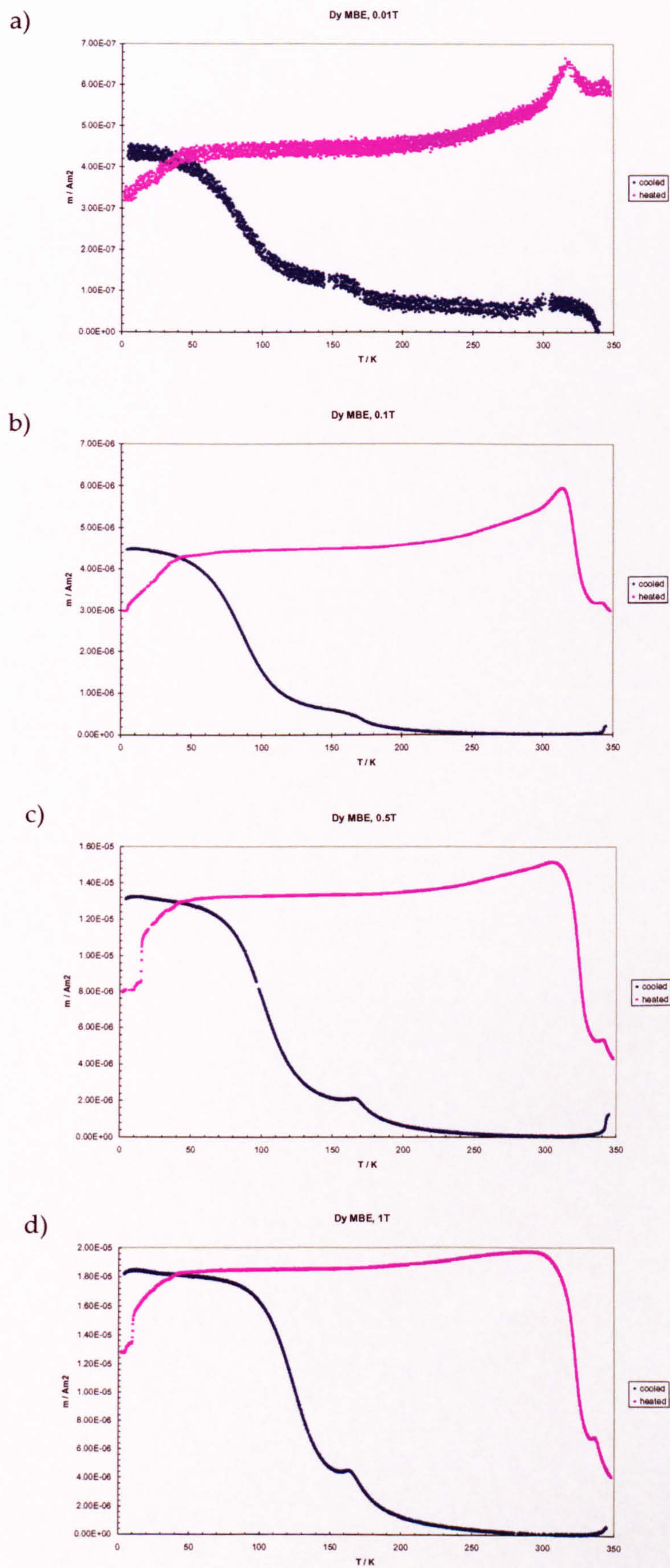


Figure 6. 4 Dy MBE film heated and cooled in applied fields of a) 0.01T, b) 0.1T, c) 0.5T and d) 1.0T. Graphs on different scales.

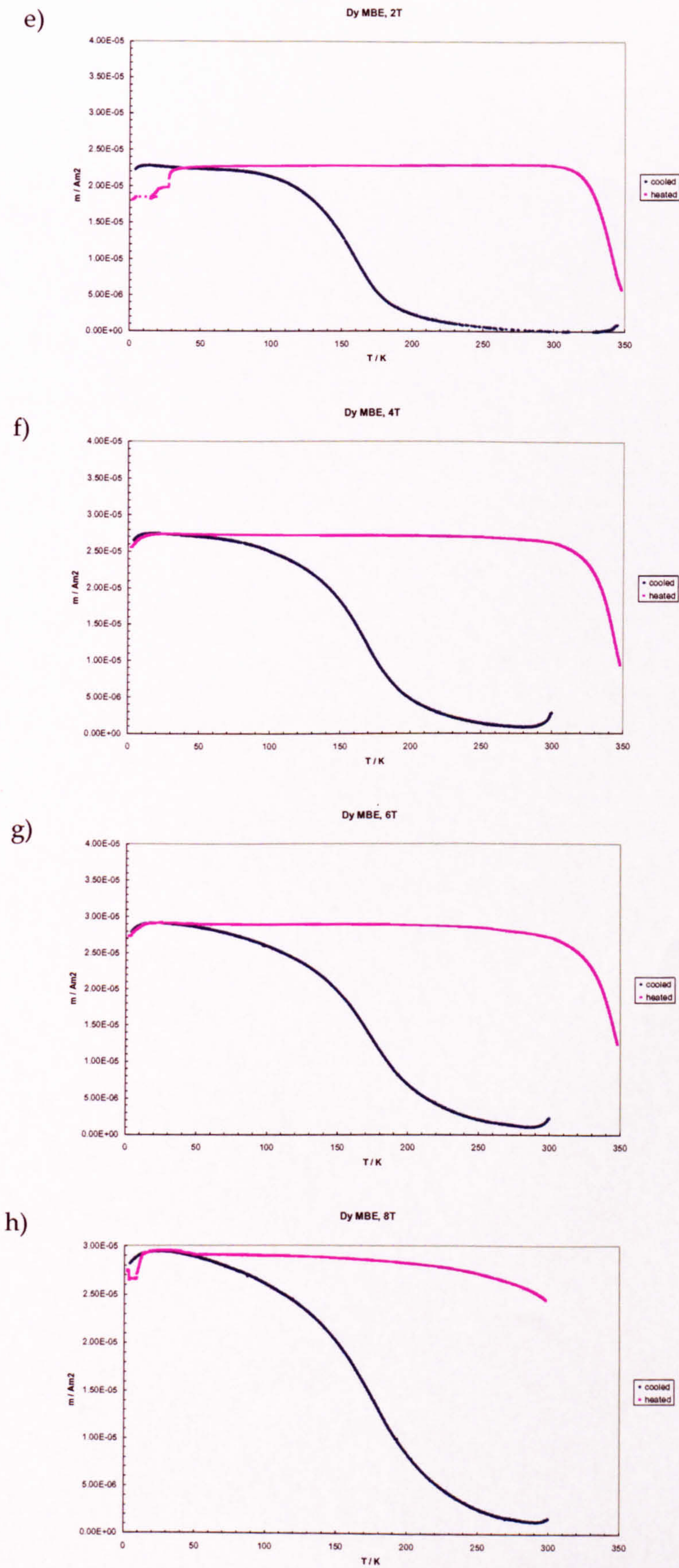


Figure 6.4 Dy MBE film heated and cooled in applied fields of a) 2T, b) 4T, c) 6T and d) 8T. All graphs on the same scale.

Comparing all the graphs of figure 6.4, the first point of interest is that as the applied field is increased the maximum magnetisation achieved by the sample at the lower temperatures is approaching that of saturation ($4.52 \times 10^{-5} \text{ Am}^2$ or $10.2 \mu_B/\text{atom}$). At 8T the maximum magnetisation obtained is $\sim 3 \times 10^{-5} \text{ Am}^2$.

There is a significant difference between heating and cooling the sample. The blue traces represent the cooled isofields and show the T_N quite clearly in the lower applied fields. This becomes smeared out as the field is increased above 1T whereby the sample switches straight from PM to FM. This is the fan phase from figure 6.1. This phase transition occurs at increasing temperatures with increasing applied field such that in 8T $T_C = 175\text{K}$.

The heating isofields have an interesting feature that occurs at $\sim 15\text{K}$. This is not present in the 4T and 6T traces. It is unlikely to be a spin glass transition or a reorientation transition as there is no characteristic sharp peak in the low-field, low-temperature susceptibility as shown in figure 6.5.

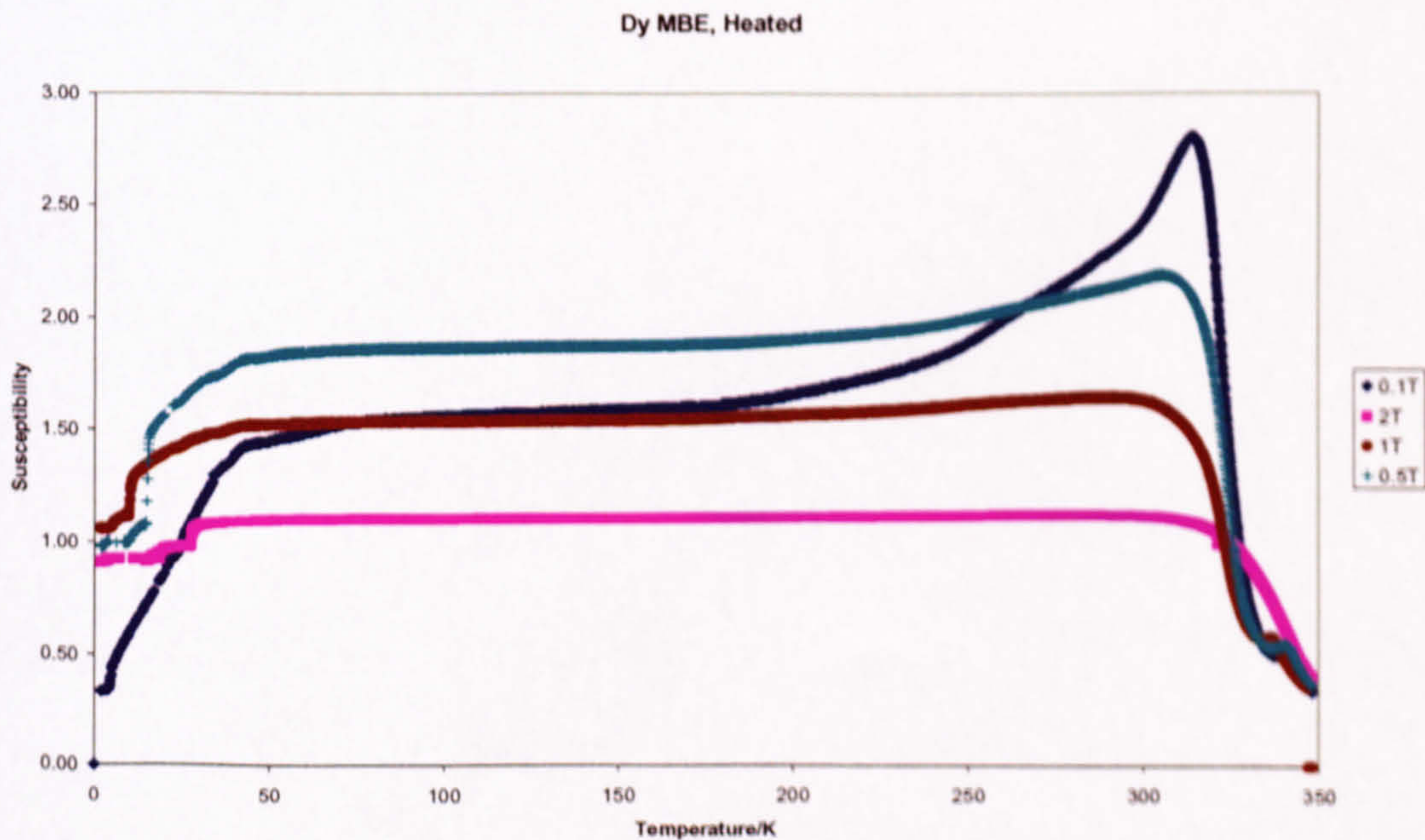


Figure 6. 5 Susceptibility of Dy MBE film

The sharp peak in the susceptibility for the 0.1T heated trace at $\sim 310\text{K}$ represents the phase transition from FM \rightarrow PM.

An attempt was made to reproduce the superheating and supercooling effects seen in high purity polycrystalline Dy as detailed by Gschneider, Jr. and Pecharsky⁵⁶.

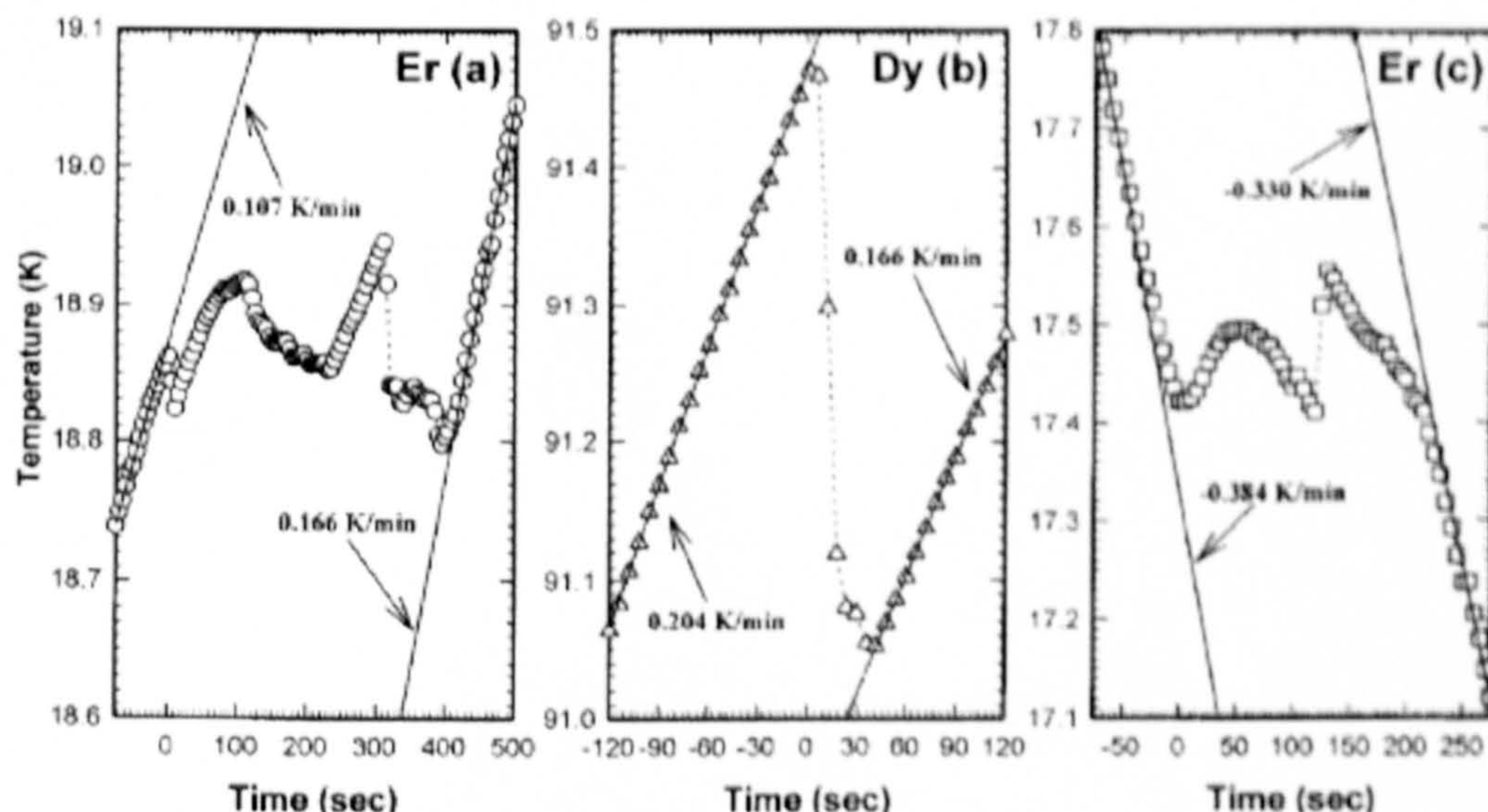


Figure 6. 6 Time-temperature heating a), b) and cooling c) curves for RE metals. (Data reproduced from ref 54.)

The heated Dy curve in figure 6.6 (b) shows the SHPT occurring over a very small temperature range. The attempt to reproduce this result was unsuccessful due to i) inability to measure the temperature of the sample directly and ii) too fast a rate of heating in the VSM (10 K min^{-1}) generating insufficient points with which to see the SHPT.

6.2 Fe/Dy Alloys

A number of different samples were made to investigate the effects of v.f.f. of Fe both as atomic impurities produced by co-depositing with an MBE source or as pre-formed Fe nanoparticles produced by co-depositing with the cluster source.

6.2.1 10% Fe atomic impurity in Dy

The crystallographic structures of TM-RE compounds are trigonal prisms where the corners are occupied by the rare earth atoms and the centre by a smaller transition metal atom. The exchange interactions between the TM atoms are negligible as the TM-TM nearest neighbour distances are large⁵⁷. In this prism arrangement, the RE atoms always

lie in a crystallographic site with very low symmetry. The crystal field reduces or can even cancel the RE magnetic moment.

Subjecting a 10% Fe MBE in Dy sample to the same tests as for the Dy MBE sample, the effect of different applied fields was measured.

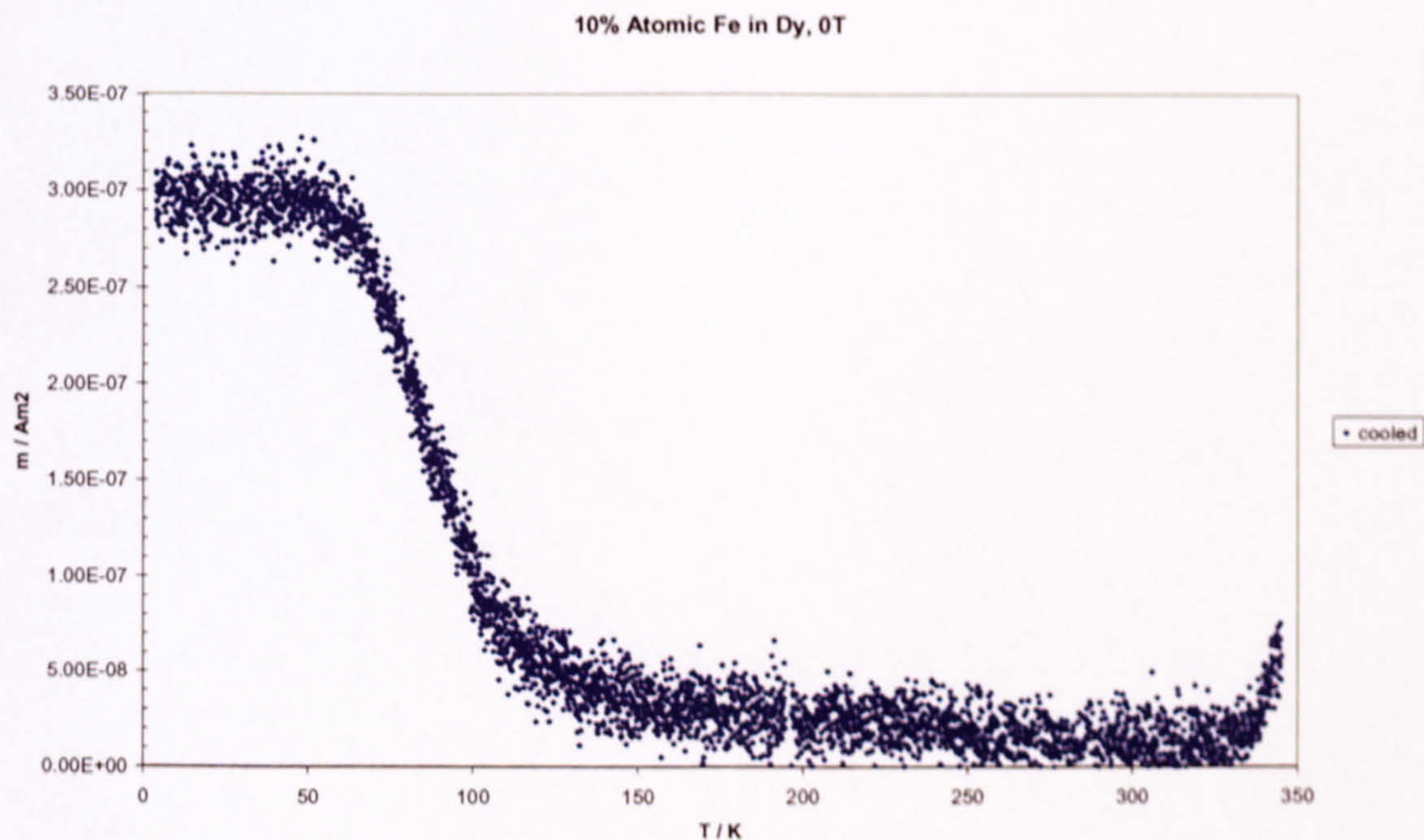


Figure 6. 7 Ground state of 10% Fe deposited using MBE into a Dy matrix

Figure 6.7 shows the ground state of this sample where it is difficult to see T_N but the FM transition occurs at the same T_C as that of the pure Dy film.

The maximum magnetisation of $\sim 2.7 \times 10^{-7} \text{ Am}^2$ is less than that of $\sim 3.3 \times 10^{-7} \text{ Am}^2$ for the pure Dy film. This decrease is too large to be merely a dilution effect, there must be a coupling effect involved. The difference corresponds to the Fe impurity atoms coupled antiferromagnetically to the Dy matrix and corroborates the findings of Tsukahara, Kanayama and Tanoue in their Dy ion implanted Fe films⁵⁸. They report reduction and then destruction of anisotropies and a decrease in magnetization in Dy doped Fe samples.

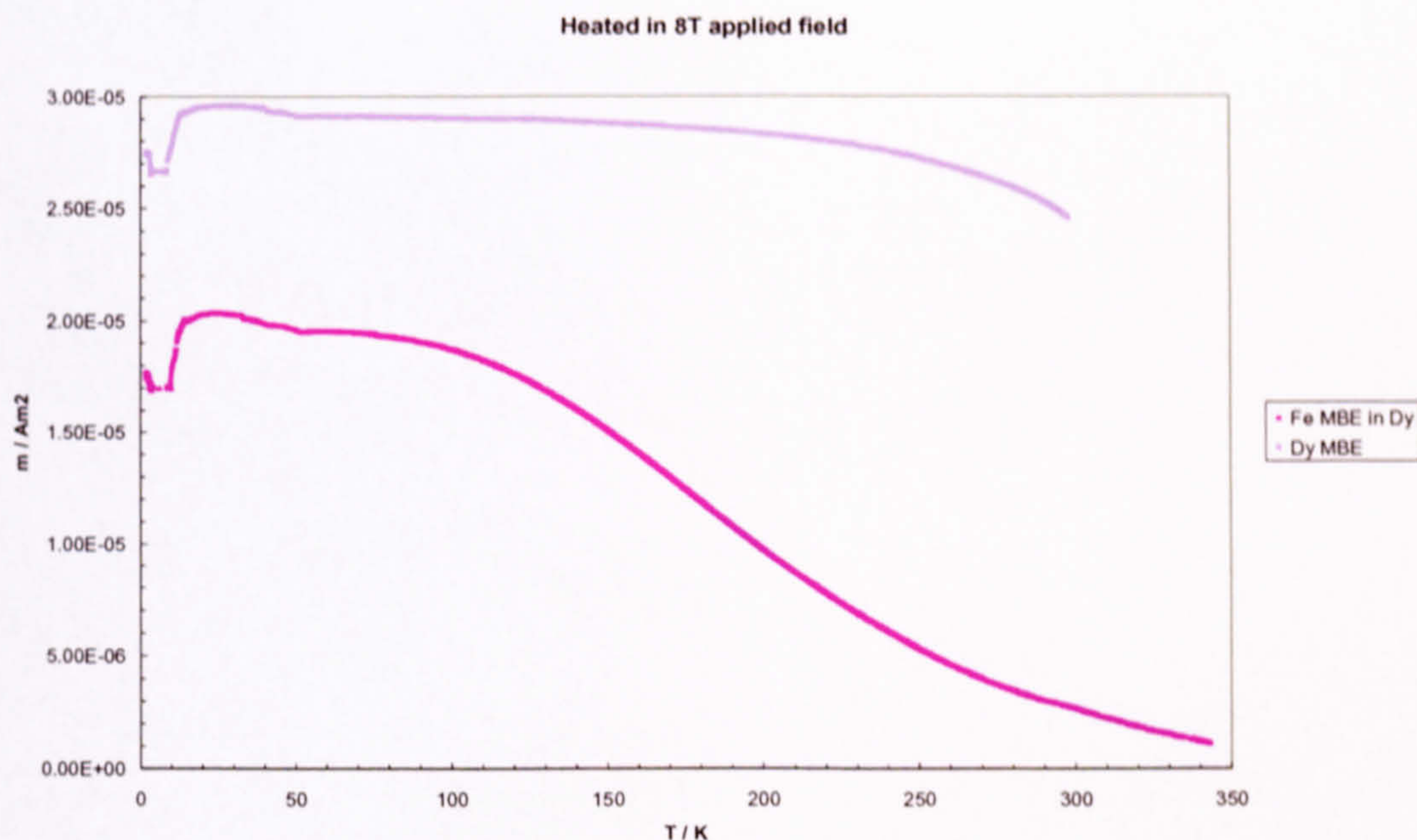


Figure 6.8 Heating isofields of Dy MBE film (lilac trace) and 10% Fe MBE in Dy (pink trace)

Figure 6.8 shows the heating isofield in an 8T applied field for the 10% Fe in Dy sample compared to the pure Dy film. The maximum magnetisation has decreased to ~70% of the Dy MBE value. There is a reorientation at 50K and the tail of the Fe/Dy graph decreases much more rapidly reaching a maximum gradient at ~200K. The near horizontal tail of the Dy MBE film is due to an ability of the RE to hold the FM ordering to high temperatures however, in the Fe/Dy alloy the Fe prevents the Dy from maintaining this order – more evidence of the AFM coupling.

6.2.2 9% Fe clusters in Dy

Addition of 9% Fe nanoparticles into the Dy matrix produces yet another different feature. The cooling isofields in figure 6.9 show a PM response all the way down to low temperatures in all applied fields.

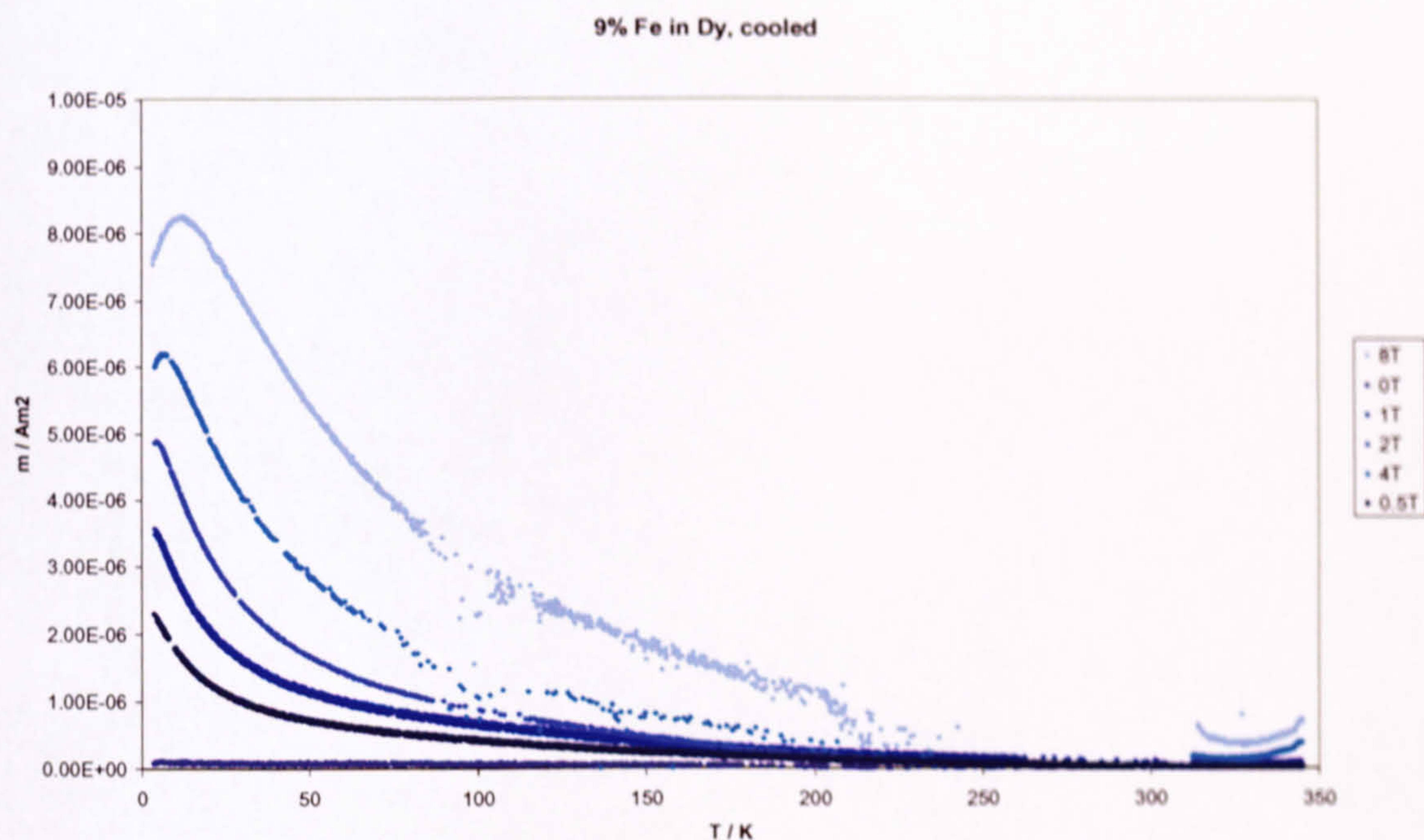


Figure 6. 9 9% Fe clusters in Dy cooled in various applied fields.

This develops into a curve reminiscent of a SPM signature in the very high fields with a peak at $\sim 10\text{K}$. However, with a v.f.f. of 9% there is no possibility that the clusters are isolated, plus they are situated in a magnetic matrix. This is not SPM behaviour. Also, the maximum magnetisation has reduced dramatically. Addition of the Fe clusters to the RE has quenched the overall moment to $\sim 30\%$ that of the Dy MBE.

Figure 6.10 shows the heated 8T curve where the low temperature feature is only $\sim 35\%$ of the entire sample signal.

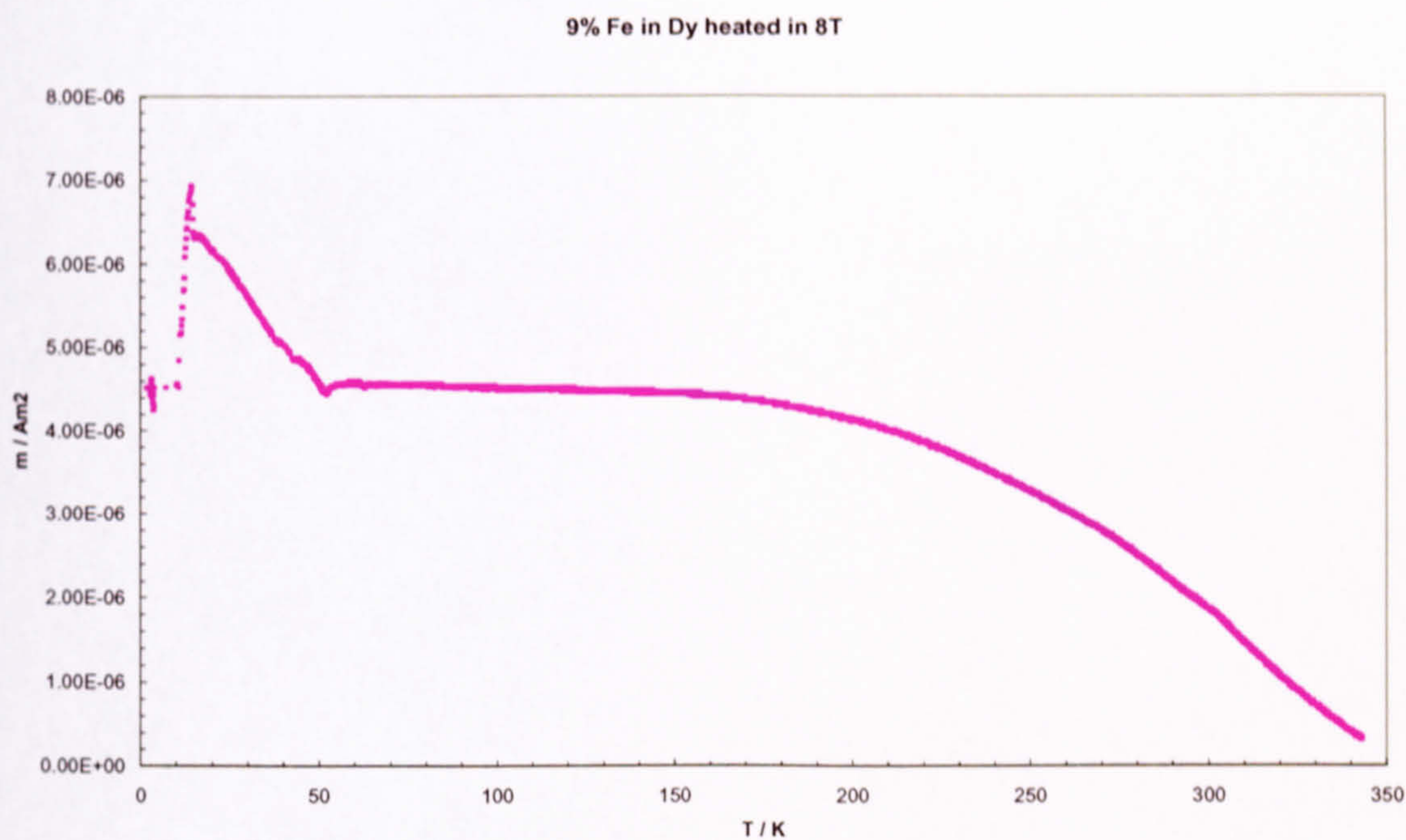


Figure 6. 10 9% Fe clusters in Dy heated in 8T applied field

This dramatic feature at low temperatures in high fields is alignment and reorientation of the Fe clusters within the two competing regimes of a highly FM RE matrix and a very strong applied field.

Comparing the 10% data for atomic Fe and Fe clusters in Dy shows a dramatic difference as shown in figure 6.11.

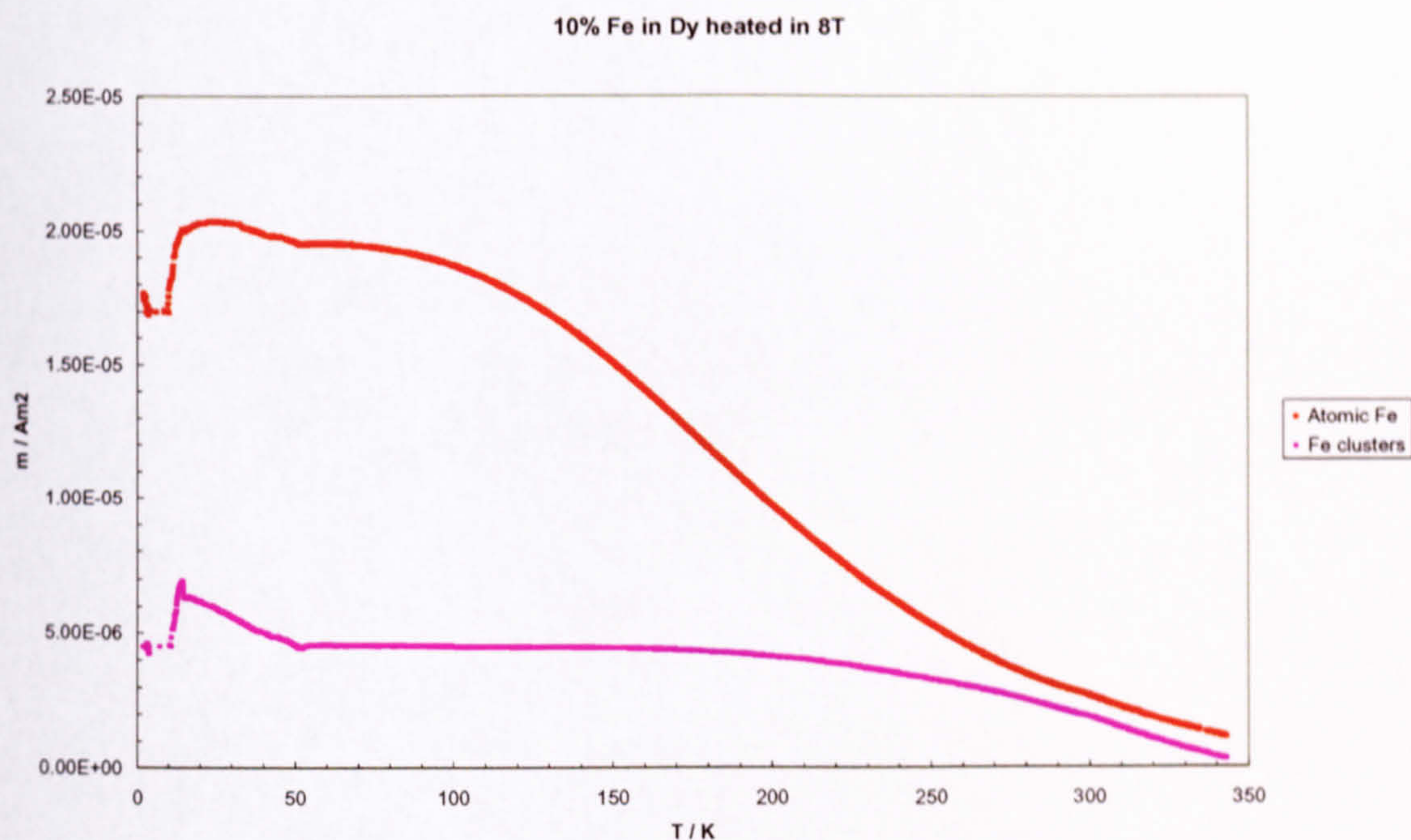


Figure 6.11 10% Fe in Dy

There is an important finding here, which is that if ~10% Fe is added to the Dy it makes a big difference if it is added as an atomic impurity or as pre-formed clusters. As an atomic impurity it couples AFM to the matrix and there is a corresponding drop in the magnetisation. When the same amount is added as clusters there is a much bigger drop in the magnetisation which is due to the Fe clusters disrupting the spin wave structures. With a turn angle between successive planes in Dy of 43° this means the spin wave repeats every 8.37 layers. With a bulk layer spacing in Dy (0 0 0 1) of $\sim 0.28\text{nm}$ ⁵⁹ this equates to a wavelength of the Dy spin wave equal to $\sim 2.34\text{nm}$. A Fe nanoparticle of diameter 2nm will be sufficient to completely disrupt this spin wave and destroy the medium-range order in the RE. The clusters saturate, which provides the FM ordering represented by the horizontal portion of the pink curve in 6.11. Due to their size and giant moment of ~ 450 Bohr magnetons, the RE can not reorientate the clusters until a temperature much closer to room temperature is reached. This is represented by the tail of the graphs above $\sim 250\text{K}$. Overall this sample is FiM whereby the huge cluster moments align with the applied field and the RE couples AFM around the clusters. This accounts for the huge drop in overall magnetisation.

Atomic Fe on the other hand with a diameter of 0.28nm ⁶⁰ is small enough to be incorporated into the spin wave. However, it still couples AFM with the RE which also has the effect of reducing the overall moment, although not to the same extent as in the FiM case.

Camley and Tilley observed the phase transitions in magnetic superlattices composed of alternating TM-RE multilayers³². They observe a reorientation transition in a FeGd system and establish four possible ground-state configurations in the low-temperature low-field limit to account for this behaviour.

It is easy to be misled into thinking that these low temperature features are the signature of a spin glass. Whilst this is characterised by a sharp peak at the freezing temperature (T_g) in the low-field susceptibility, Sarkissian's AC and DC susceptibility measurements on Sc13%Gd found that this peak gradually became smeared out by an applied magnetic field⁶¹. The converse is true here – the sharp peak occurs in high applied fields. Nevertheless some relaxation time measurements were taken to investigate the existence of the spin glass.

Hauser and Waszczak used a process whereby their sample was first cooled in zero field to 4.2K, then a $1 \times 10^{-4}\text{T}$ field was applied and susceptibility was measured with increasing temperature⁶². Conversely, Jung, Ren and O'Connor employed isothermal (IRM) and thermal (TRM) remanent magnetisation measurements⁶³. This involved cooling the spin-glass material to temperatures well below the spin-glass freezing temperature under zero applied field (IRM) or cooling slowly in an applied field to below T_g then switching off the field (TRM). The latter two techniques were both utilised when measuring the 9% Fe in Dy sample.

Figure 6.12 shows that the magnetisation is constant in time; the requirement for the highly frustrated spin glass system is that its magnetism is time dependent.

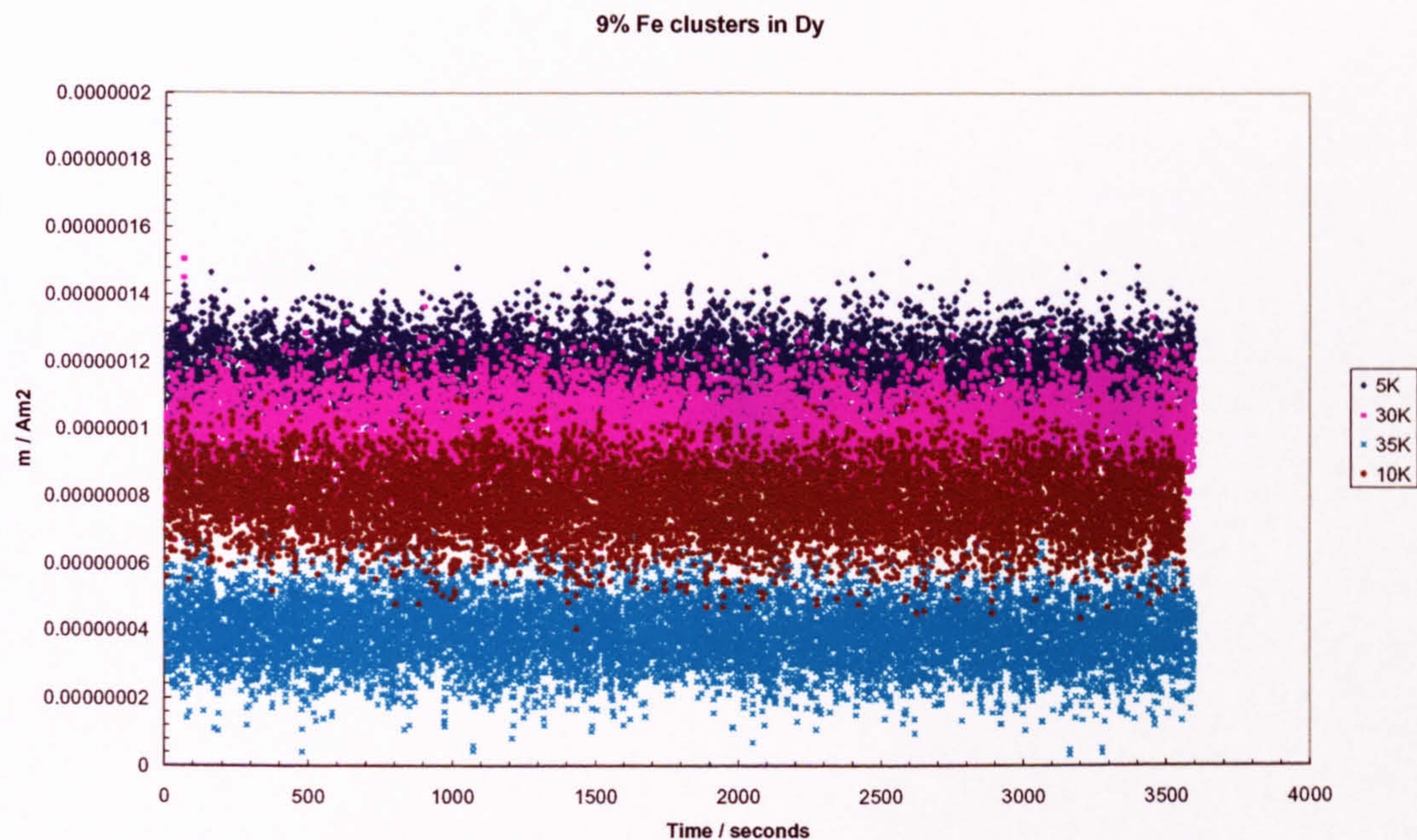


Figure 6. 12 9% Fe clusters in Dy relaxation times

Alternative methods were used to measure the relaxation time all producing the same result – constant magnetisation with respect to time. Longer time frames were used also, up to 4 hours after removal of the applied field but still the magnetisation remained constant. It was therefore concluded that this sample is not a spin glass.

When the method of measuring isofields is changed to straight thermocycling, the 10K feature disappears as shown in figure 6.13. In the process of thermocycling the field remains applied through both the heating and cooling processes.

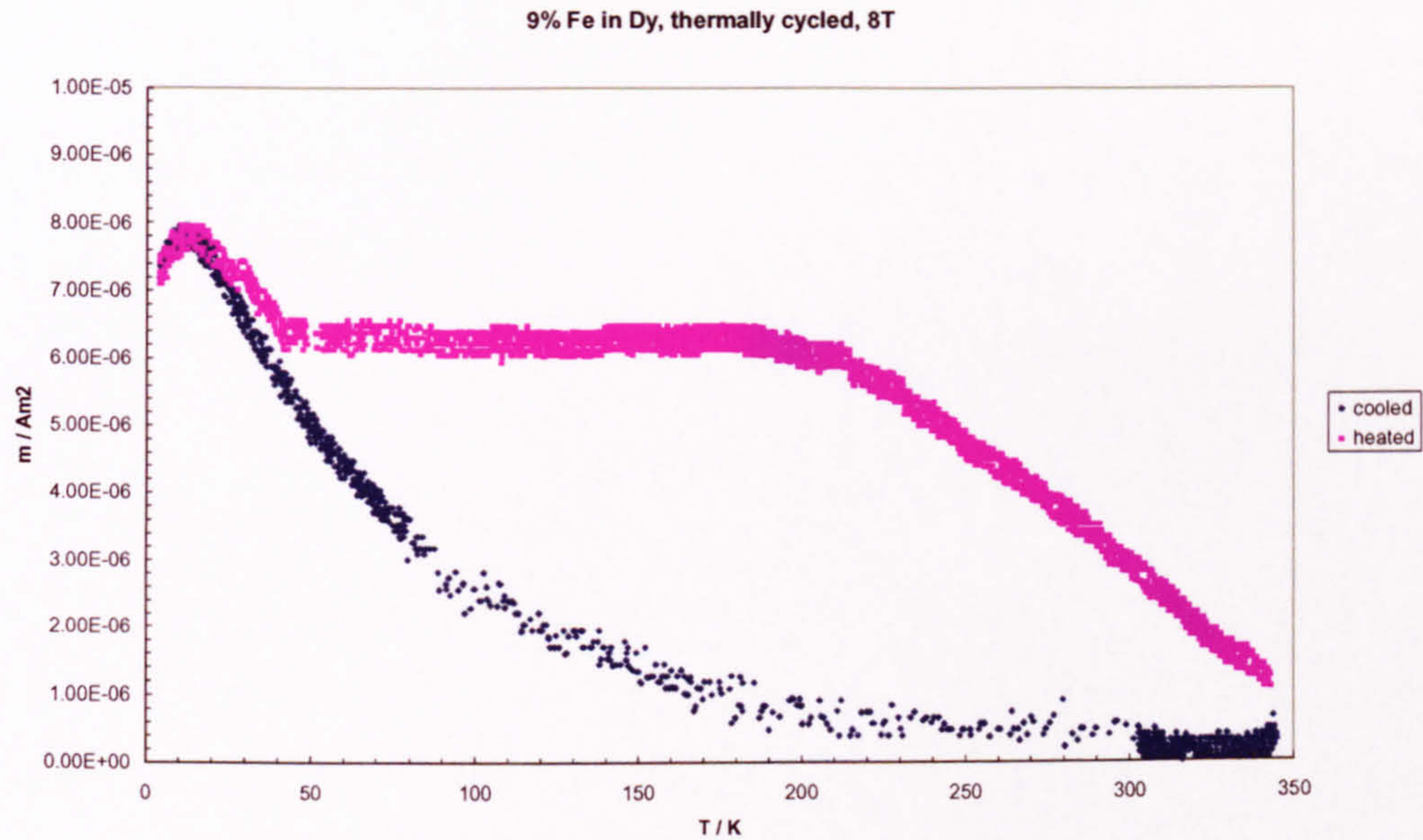


Figure 6. 13 9% Fe clusters in Dy thermocycled in 8T applied field

The stable FiM ordering remains from 50K – 200K as in previous samples.

It is interesting at this point to compare 9% Fe nanoparticles in both the RE matrices. Figure 6.14 shows both Ho and Dy matrices in a heating isofield at 8T applied field.

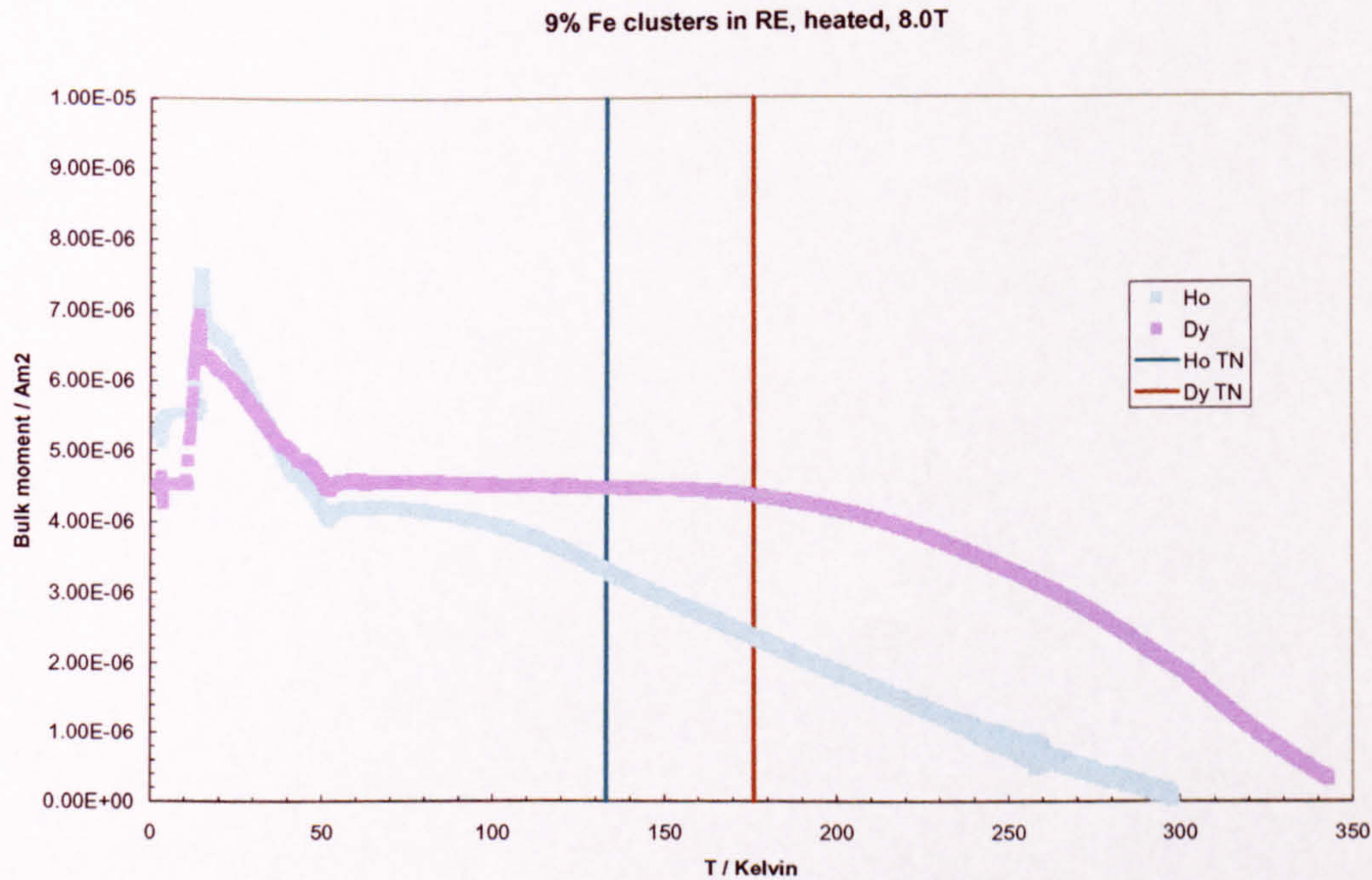


Figure 6. 14 9% Fe clusters in Dy and Ho heated in 8T applied field

The features between 0 and 50K are almost identical suggesting that the Fe clusters are entrily responsible for this behaviour. The two graphs tail off differently which can be attributed to the different rare earths. Dy has a higher T_N than Ho and so takes longer to lose the AFM ordering. The tail of the Dy sample therefore decreases back to zero magnetisation at a slower rate.

6.2.3 24% Fe clusters in Dy

When a much higher v.f.f. of Fe nanoparticles are deposited into the Dy matrix the low-temperature, high-field feature is greatly enhanced. Figure 6.14 shows the heated isofield for 24% Fe clusters in Dy in an 8T field.

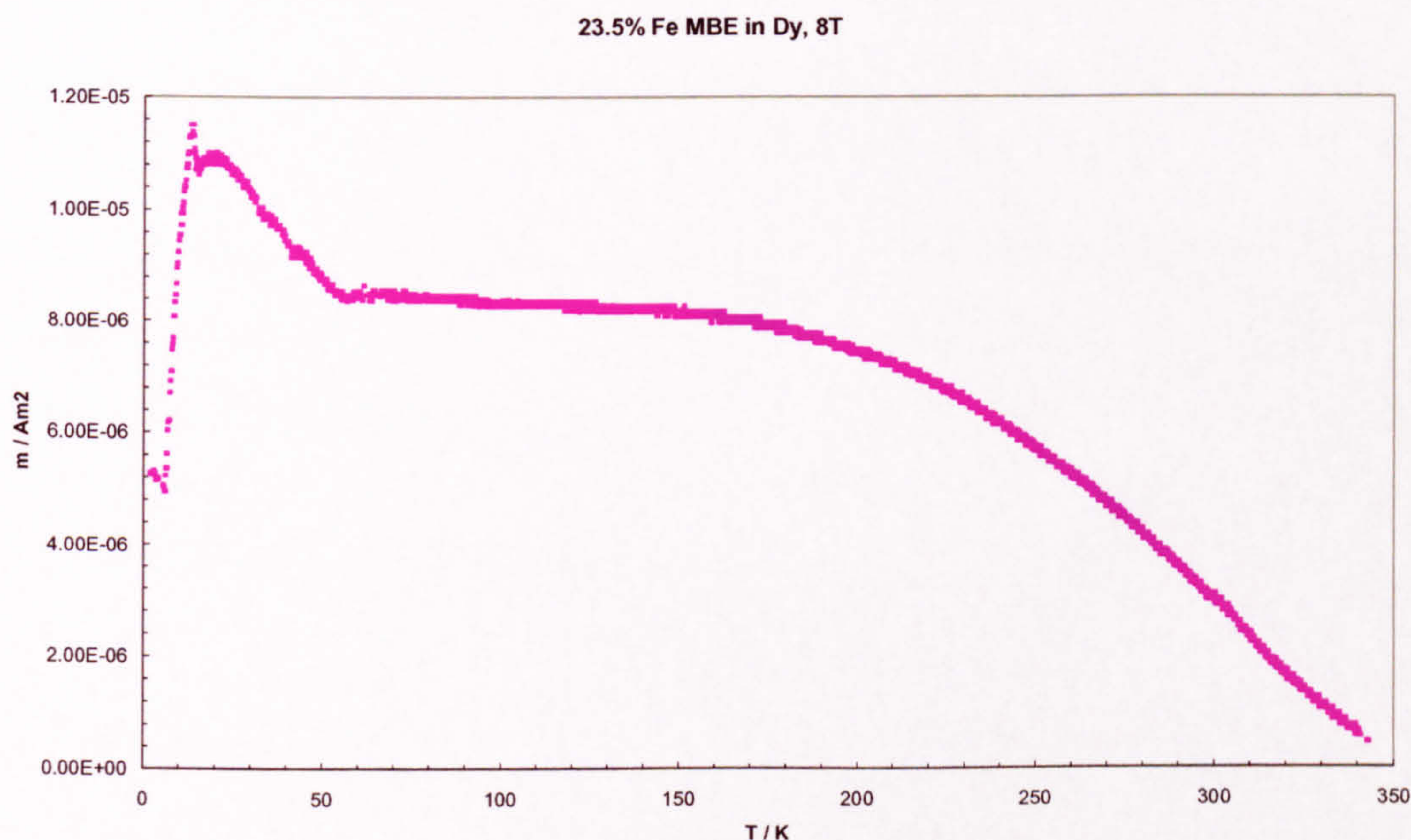


Figure 6. 15 24% Fe clusters in a Dy matrix heated in 8T applied field.

The large feature at 15K represents over half the total signal of the sample. Above 50K the system is stable and in some FiM state. The overall magnetisation is now 3 times smaller than that of the Dy MBE film. Above 200K the system loses its ordering and a slow transition to PM is seen.

Figure 6.16 shows the relationship between maximum magnetisation and applied field for several Fe/Dy alloys and MBE films.

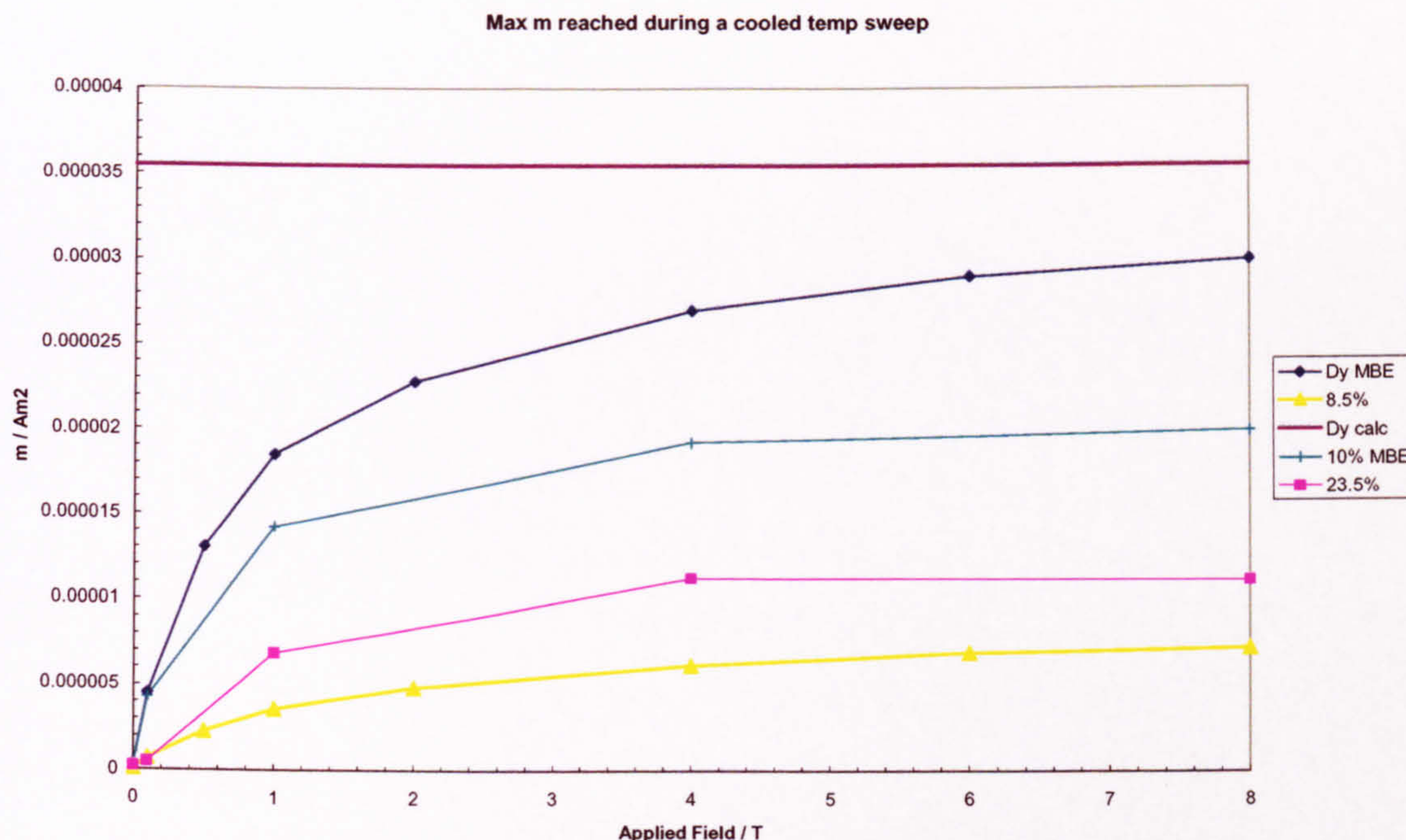


Figure 6. 16 Low temperature magnetisation of all Dy samples obtained during a cooled temperature sweep.

Clearly addition of Fe to the Dy has reduced the moment. The trend of the 10% Fe MBE in Dy curve (teal) in figure 6.16 agrees with the findings of N. Tang et al in that at the lowest fields the magnetisation strongly increases. They attribute this to saturation of a FM impurity phase. Above 1T they find the impurity phase to be saturated and the field-dependence of the magnetization is perfectly linear⁶⁴.

6.3 Structure

The X-ray fluorescence of a 4% Fe in Dy sample on Si (100) was obtained using the EXAFS beamline 7.1 at Daresbury. As shown in figure 6.17 below the Fe K-edge occurs at 7.112 keV and the Dy L_{III}-edge occurs at 7.798 keV.

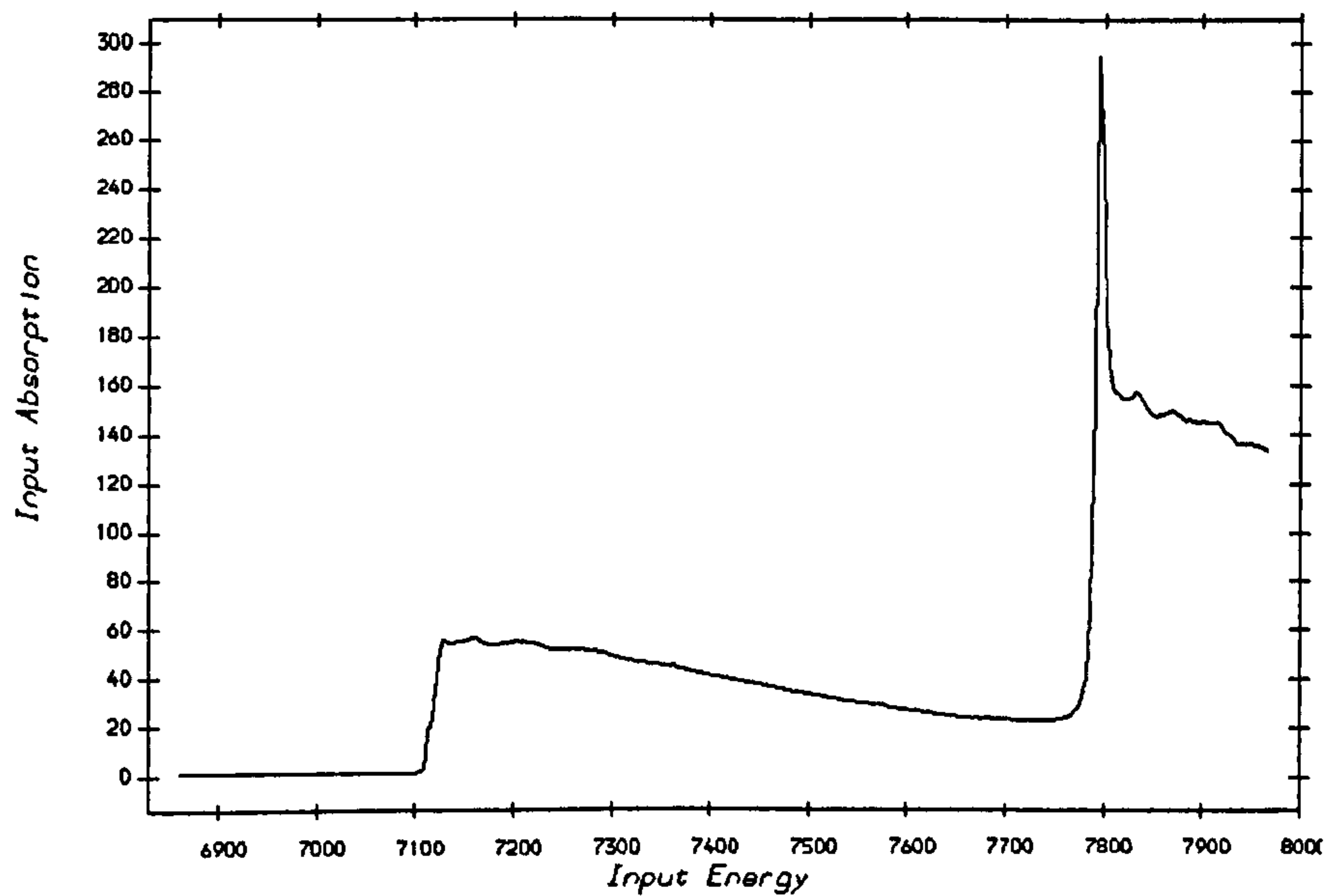


Figure 6.17 Raw EXAFS data showing Fe K-edge and Dy L_{III}-edge

The data is clean, the sample does not appear to be oxidised, both the Fe K-edge and the Dy L-edge can be seen clearly. This confirms a) that the manufacturing technique is valid in terms of keeping the sample clean and b) that the deposition rates of the evaporators are accurate and therefore the relative thicknesses of the metals in the sample can be calculated with a reasonably high level of confidence.

Figure 6.18 shows the theoretical EXAFS fit to the experimental data over the Fe K-edge. Figure 6.19 shows the associated Fourier Transform.

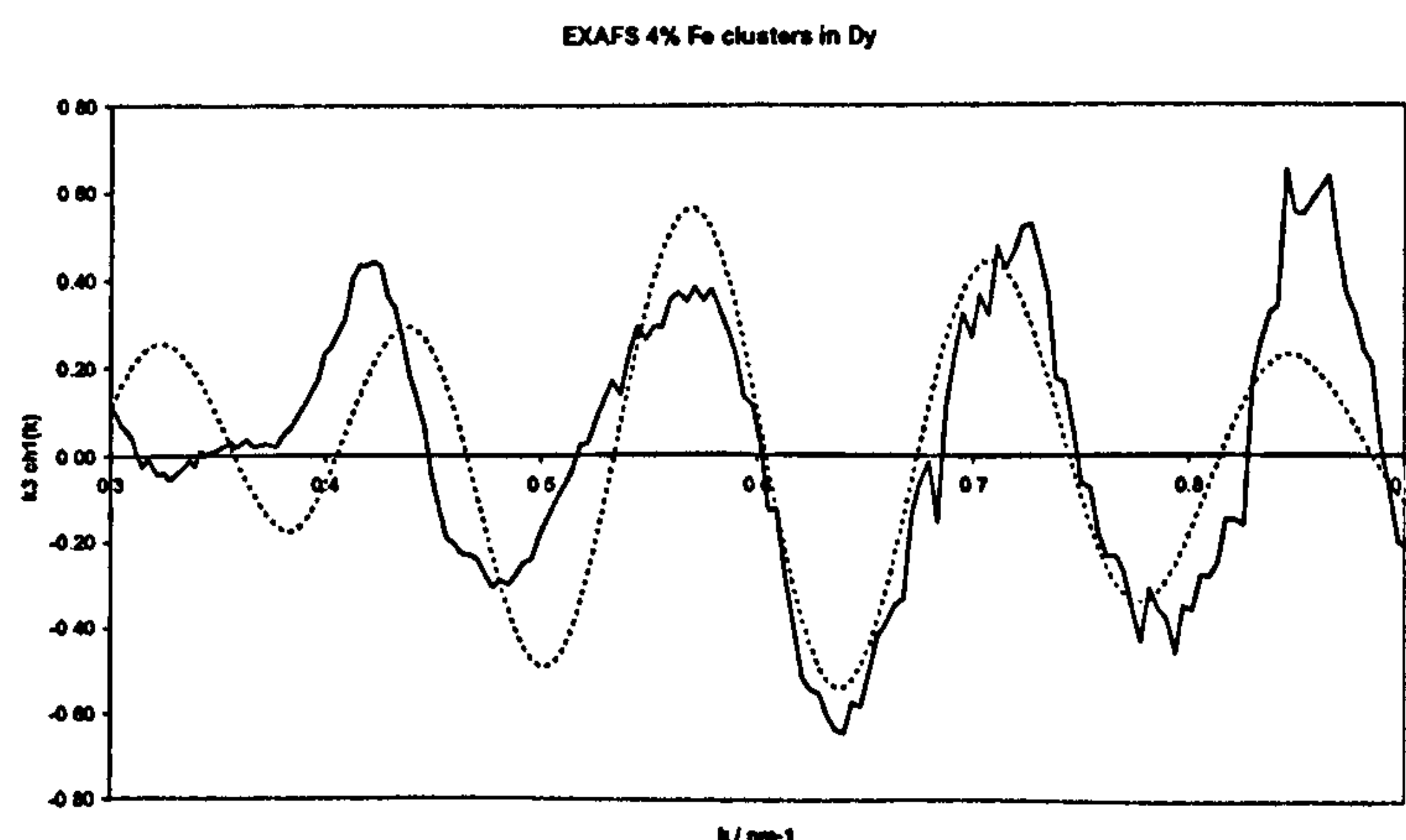


Figure 6.18 EXAFS experimental data (solid line) and theoretical fit (dashed line) for 4% Fe clusters in Dy matrix

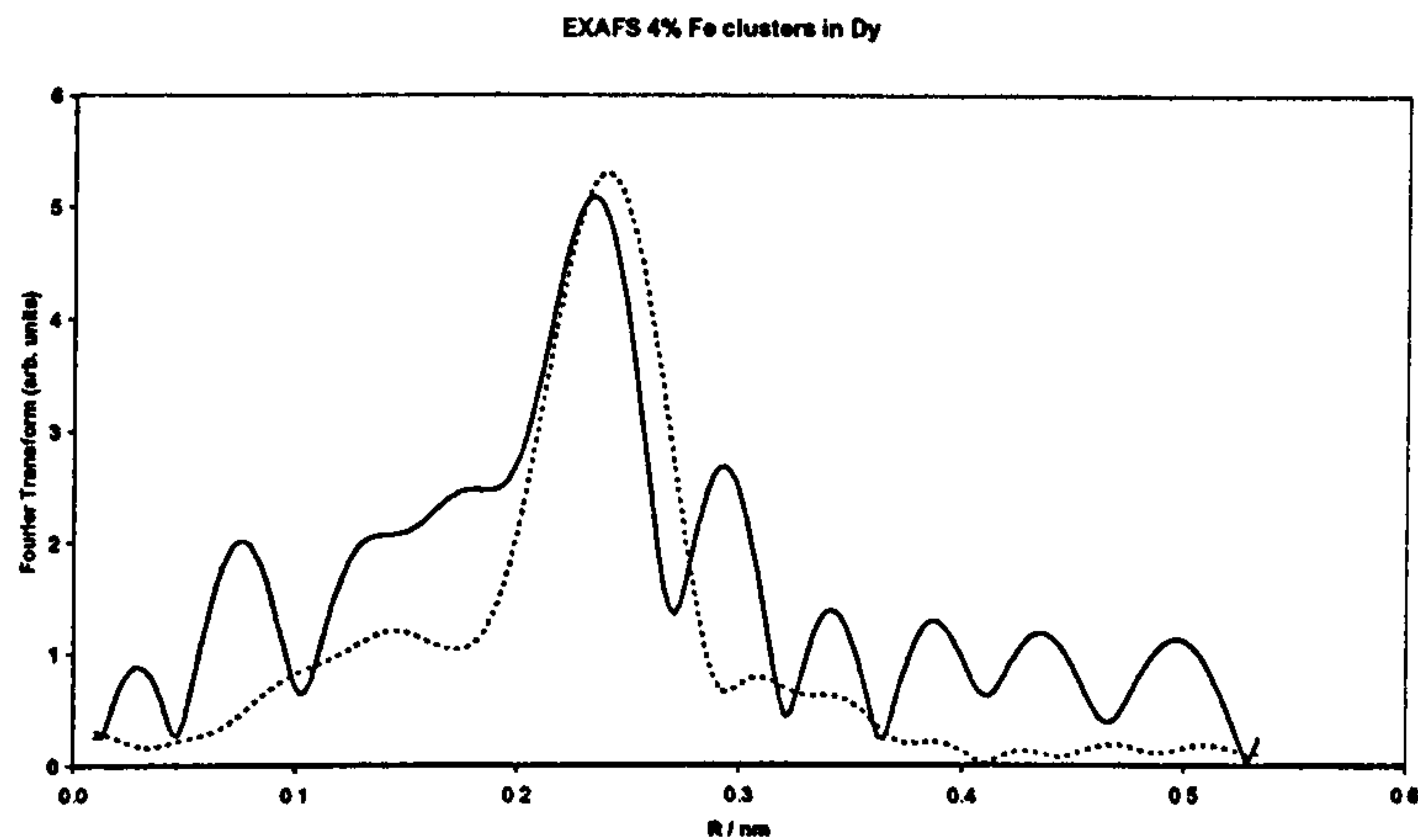


Figure 6.19 Fourier Transform of experimental data (solid line) and theoretical fit (dashed line) of data in figure 6.18.

The data is comparatively poor due to the low amount of Fe in the sample.

Bulk Fe at room temperature has a bcc structure. This has $a_0 = 0.287\text{nm}$ and therefore $r_1 = 0.249\text{nm}$. Above $\sim 1200\text{K}$ Fe changes to a fcc structure with $a_0 = 0.359\text{nm}$ and $r_1 = 0.254\text{nm}$ this is the gamma Fe fcc phase. The plots in figure 6.18 give $r_1 = 0.253 \pm 0.002\text{nm}$ for the Fe in Dy sample suggesting that this sample is either fcc or an expanded bcc structure. At the very least they show that the Fe is grouped into clusters. These results are however only based on using a 1 shell fit to the data with a nearest neighbour of Fe i.e. the Dy has not been considered. An expanded bcc lattice would corroborate the findings of Tsukahara et al for the Dy ion implanted Fe films who report a 1% expansion of the bcc lattice⁴³. This in turn would account for the reduction in magnetic moment seen in all samples of Dy with Fe added.

6.7 Summary

Low temperature features in Dy MBE films and Fe/Dy alloys are not spin glass transitions. The interesting reorientation transitions between 0 and 50K are due to alignment of the clusters flipping between the strong individual RE moments and the high applied field.

A large reduction in magnetisation is seen from the Dy MBE film with addition of Fe.

Atomic Fe couples AFM with the RE matrix whilst Fe nanoparticles disrupt the entire spin wave of Dy reducing the sample to FiM ordering.

Structural data indicates the Fe is no longer in a bcc structure within the Dy matrix but in some expanded lattice.

“The beginning and the end reach
out their hands to each other”

Chinese Proverb

Chapter 7

Conclusions and Further Work

Clusters in rare earth matrices is new science. The temperature dependent magnetic phase transitions encountered are complex and varied. Not only are these phase transitions dependent upon the temperature and applied field of the sample but also on the history of the sample. The work in this thesis has clearly highlighted the difference of adding the transition metal as pre-formed clusters compared to adding it as an atomic impurity.

Gas-coating the Fe nanoparticles is ineffective in enhancing the magnetic moment of the sample or the individual clusters. Both hydrogen and nitrogen coatings have a detrimental effect upon the magnetic moment. This is due to the gas reacting with the cluster surface in some way. Further development of the gas-coating process needs to be modelled in order to understand this effect better.

The saturation magnetisation of all Fe/Ho systems is lower than in bulk Ho but higher than that of bulk Fe. The large decrease in magnetisation implies that addition of the Fe to the Ho has destroyed the medium-range order of the Ho. Thermal hysteresis and phase transitions can be seen clearly with the VSM data.

Addition of atomic Fe to Dy reduces the overall moment of the sample. An even larger reduction in magnetisation is seen with addition of Fe clusters to Dy. The Fe nanoparticles are large enough to disrupt the spin wave of the rare earth. Atomic Fe couples AFM to the Dy whilst Fe clusters produce large FiM coupling effects characterised by a huge drop in magnetisation.

The Fe/rare earth alloys are not spin glass materials but do show interesting reorientation transitions below 50K. These reorientations are as a result of the large clusters flipping between the strong individual rare earth moments and the high applied field.

There are many suggestions for future work but the most interesting effect would be to deposit clusters in a matrix of Gd as it has a high Curie temperature of 293K.

More TEM images of the samples would reveal some surface effects whilst more EXAFS data would produce structural information on the Fe in the samples. XMCD on the rare earths would provide information on the spin and orbital moments which could lead to a clearer picture of the FiM ordering. This would require beamtime at a synchrotron such as the ESRF in order to generate X-rays with a high enough energy to see the L-edges.

It would be useful to develop a proper model of the phase behaviours and to create a full phase diagram for the TM-RE systems that takes into account not just temperature and applied field but high pressures and volume-filling fraction data.

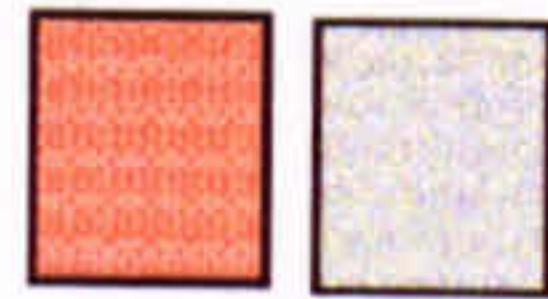
hydrogen 1 H 1.008																		helium 2 He 4.003			
lithium 3 Li 6.941	beryllium 4 Be 9.0122															boron 5 B 10.811	carbon 6 C 12.011	nitrogen 7 N 14.007	oxygen 8 O 15.999	fluorine 9 F 18.998	neon 10 Ne 20.180
sodium 11 Na 22.990	magnesium 12 Mg 24.305															aluminum 13 Al 26.982	silicon 14 Si 28.086	phosphorus 15 P 30.974	sulfur 16 S 32.065	chlorine 17 Cl 35.453	argon 18 Ar 39.948
potassium 19 K 39.098	calcium 20 Ca 40.078	scandium 21 Sc 44.956	titanium 22 Ti 47.867	vanadium 23 V 50.942	chromium 24 Cr 51.996	manganese 25 Mn 54.938	iron 26 Fe 55.847	cobalt 27 Co 58.933	nickel 28 Ni 58.693	copper 29 Cu 63.546	zinc 30 Zn 65.39	gallium 31 Ga 69.723	germanium 32 Ge 72.61	arsenic 33 As 74.922	selenium 34 Se 78.96	bromine 35 Br 79.904	krypton 36 Kr 83.80				
rubidium 37 Rb 85.468	strontium 38 Sr 87.62	yttrium 39 Y 88.906	zirconium 40 Zr 91.224	niobium 41 Nb 92.906	molybdenum 42 Mo 95.94	technetium 43 Tc [98]	ruthenium 44 Ru 101.07	rhodium 45 Rh 102.91	palladium 46 Pd 106.42	silver 47 Ag 107.87	cadmium 48 Cd 112.41	indium 49 In 114.82	tin 50 Sn 118.71	antimony 51 Sb 121.76	tellurium 52 Te 127.60	iodine 53 I 126.90	xenon 54 Xe 131.29				
cesium 55 Cs 132.91	barium 56 Ba 137.33	57-70 ★		lutetium 71 Lu 174.97	hafnium 72 Hf 178.49	tantalum 73 Ta 180.95	tungsten 74 W 183.84	rhenium 75 Re 186.21	osmium 76 Os 190.23	iridium 77 Ir 192.22	platinum 78 Pt 195.08	gold 79 Au 196.97	mercury 80 Hg 200.59	thallium 81 Tl 204.38	lead 82 Pb 207.2	bismuth 83 Bi 208.98	polonium 84 Po [209]	astatine 85 At [210]	radon 86 Rn [222]		
francium 87 Fr [223]	radium 88 Ra [226]	89-102 ★ ★		lawrencium 103 Lr [262]	rutherfordium 104 Rf [261]	dubnium 105 Db [262]	seaborgium 106 Sg [266]	bohrium 107 Bh [264]	hassium 108 Hs [269]	meitnerium 109 Mt [268]	unnilium 110 Uun [271]	ununium 111 Uuu [272]	unbibium 112 Uub [277]	ununseptium 114 Uuq [289]							

* Lanthanide series

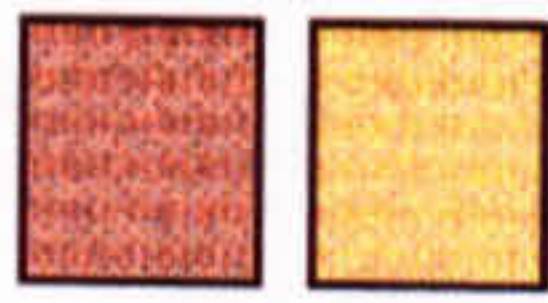
lanthanum 57 La 138.91	cerium 58 Ce 140.12	praseodymium 59 Pr 140.91	neodymium 60 Nd 144.24	promethium 61 Pm [145]	samarium 62 Sm 150.36	europium 63 Eu 151.96	gadolinium 64 Gd 157.25	terbium 65 Tb 158.93	dysprosium 66 Dy 162.50	holmium 67 Ho 164.93	erbium 68 Er 167.26	thulium 69 Tm 168.93	ytterbium 70 Yb 173.04
---------------------------------	------------------------------	------------------------------------	---------------------------------	---------------------------------	--------------------------------	--------------------------------	----------------------------------	-------------------------------	----------------------------------	-------------------------------	------------------------------	-------------------------------	---------------------------------

* * Actinide series

actinium 89 Ac [227]	thorium 90 Th 232.04	protactinium 91 Pa 231.04	uranium 92 U 238.03	neptunium 93 Np [237]	plutonium 94 Pu [244]	americium 95 Am [243]	curium 96 Cm [247]	berkelium 97 Bk [247]	californium 98 Cf [251]	einsteinium 99 Es [252]	fermium 100 Fm [257]	mendelevium 101 Md [258]	nobelium 102 No [259]
-------------------------------	-------------------------------	------------------------------------	------------------------------	--------------------------------	--------------------------------	--------------------------------	-----------------------------	--------------------------------	----------------------------------	----------------------------------	-------------------------------	-----------------------------------	--------------------------------



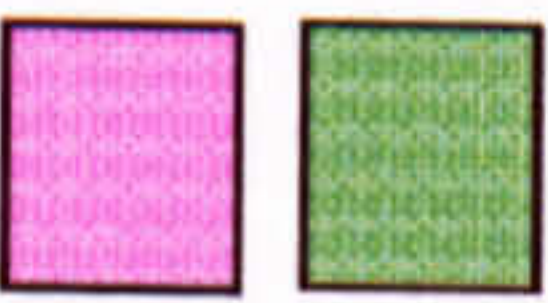
Gas coatings



Cluster materials



RE matrices



Aggregation gases



Buffer and capping materials

3d elements

Element	No. d electrons	m _l =					L	S	J	State
		-2	-1	0	1	2				
Sc	1	↓					2	½	3/2	² D _{3/2}
Ti	2	↓	↓				3	1	2	³ F ₂
V	3	↓	↓	↓			3	3/2	3/2	⁴ F _{3/2}
	4	↓	↓	↓	↓		2	2	0	⁵ D ₀
Cr*, Mn	5	↓	↓	↓	↓	↓	0	5/2	5/2	⁶ S _{5/2}
Fe	6	↓↑	↓	↓	↓	↓	2	2	4	⁵ D ₄
Co	7	↓↑	↓↑	↓	↓	↓	3	3/2	9/2	⁴ F _{9/2}
Ni	8	↓↑	↓↑	↓↑	↓	↓	3	1	4	³ F ₄
	9	↓↑	↓↑	↓↑	↓↑	↓	2	½	5/2	² D _{5/2}
Cu*, Zn	10	↓↑	↓↑	↓↑	↓↑	↓↑	0	0	0	¹ S ₀

* 1 4s electron

4f elements

Element	No. f electrons	m _l =							L	S	J	State
		-3	-2	-1	0	1	2	3				
La, Ce**	1	↓							3	½	5/2	² F _{5/2}
	2	↓	↓						5	1	4	⁴ H ₄
Pr	3	↓	↓	↓					6	3/2	9/2	⁴ I _{9/2}
Nd	4	↓	↓	↓	↓				6	2	4	⁵ I ₄
Pm	5	↓	↓	↓	↓	↓			5	5/2	5/2	⁶ H _{5/2}
Sm	6	↓	↓	↓	↓	↓	↓		3	3	0	⁷ F ₀
Eu, Gd**	7	↓	↓	↓	↓	↓	↓	↓	0	7/2	7/2	⁸ S _{7/2}
	8	↓↑	↓	↓	↓	↓	↓	↓	3	3	6	⁷ F ₆
Tb	9	↓↑	↓↑	↓	↓	↓	↓	↓	5	5/2	15/2	⁶ H _{15/2}
Dy	10	↓↑	↓↑	↓↑	↓	↓	↓	↓	6	2	8	⁵ I ₈
Ho	11	↓↑	↓↑	↓↑	↓↑	↓	↓	↓	6	3/2	15/2	⁴ I _{15/2}
Er	12	↓↑	↓↑	↓↑	↓↑	↓↑	↓	↓	5	1	6	⁴ H ₆
Tm	13	↓↑	↓↑	↓↑	↓↑	↓↑	↓↑	↓	3	½	7/2	² F _{7/2}
Yb	14	↓↑	↓↑	↓↑	↓↑	↓↑	↓↑	↓↑	0	0	0	¹ S ₀

**1 5d electron

Batch	Batch count	Name	For	Sample Type	Materials	Fe / nm	Matrix / nm	Gas coating / mbar	Date made
A	1/2	SQUID01	SQUID	10.7%	Co	10.2	85.0	-	30/06/2004
A	2/2	SQUID02	SQUID	1.1%	Co	10.0	990.0	-	01/07/2004
-		150 x	Mass Spec		Fe			Various	

B	1/3	TDK01	VSM	Clusters	Fe	45.0	-	-	10/12/2004
B	2/3	TDK02	VSM		Fe-H2	3.0	-	5x10-5	13/12/2004
B	3/3	TDK03	VSM		Fe-H2	50.0	-	5x10-5	17/12/2004
C	1/2	TDK04	VSM	Clusters	Fe	27.5	-	-	02/02/2005
C	2/2	TDK05	VSM		Fe-H2	-	-	-	08/02/2005
D	1/4		1 XMCD	9.2%	Fe in Ag	4.1	40.8	-	01/04/2005
D	2/4		2 XMCD	9.3%	Fe-H2 in Ag	4.9	47.5	2x10-5	01/04/2005
D	3/4		3 XMCD	8.7%	Fe-H2 in Ag	4.7	48.8	5x10-5	01/04/2005
D	4/4		4 XMCD	7.8%	Fe-H2 in Ag	4.6	50.4	1.5x10-4	04/04/2005
E	1/2		9 XMCD	Clusters	Fe	5.0	-	-	13/04/2005
E	2/2		10 XMCD		Fe-H2	5.0	-	1.5x10-4	13/04/2005
F	1/3	TDK06	VSM	Clusters	Fe	34.7	-	-	15/09/2005
F	2/3	TDK07	VSM		Fe-N2	34.5	-	5x10-5	19/09/2005
F	3/3	TDK08	VSM		Fe-N2	2.0	-	2x10-5	20/09/2005
G	1/3	TDK09	VSM	Clusters	Fe	34.0	-	-	27/09/2005
G	2/3	TDK10	VSM		Fe-N2	31.6	-	2x10-5	28/09/2005
G	3/3	TDK11	VSM		Fe-N2	32.0	-	1x10-5	13/10/2005
H	1/5		1 XMCD	MBE	Fe	5.1	-	-	18/10/2005
H	2/5		2 XMCD	9.3%	Fe in Ag	5.0	48.5	-	19/10/2005
H	3/5		3 XMCD	9.1%	Fe-N2 in Ag	5.0	50.0	5x10-5	19/10/2005
H	4/5		4 XMCD	9.7%	Fe-N2 in Ag	5.4	50.0	2x10-5	20/10/2005
H	5/5		5 XMCD	10.6%	Fe-N2 in Ag	6.9	58.0	3x10-5	20/10/2005
I	1/6	TDK12	TEM	Clusters	Fe	0.1	-	-	03/03/2006
I	2/6	TDK13	TEM		Fe-H2	0.1	-	2x10-5	03/03/2006
I	3/6	TDK14	TEM		Fe-H2	0.1	-	5x10-5	03/03/2006
I	4/6	TDK15	TEM		Fe-N2	0.1	-	2x10-5	03/03/2006
I	5/6	TDK16	TEM		Fe-N2	0.1	-	5x10-5	03/03/2006
I	6/6	TDK17	TEM		Fe-Ag	0.1	1.0	-	03/03/2006
J	1/5	TDK18	TEM	Clusters	Fe	0.1	-	-	16/03/2006
J	2/5	TDK19	TEM		Fe-N2	0.1	-	2x10-5	16/03/2006
J	3/5	TDK20	TEM		Fe-H2	0.1	-	2x10-5	16/03/2006
J	4/5	TDK21	VSM	Clusters	Fe	26.8	-	-	21/03/2006
J	5/5	TDK22	VSM		Fe/N2	9.0	-	10%	22/03/2006
K	1/2	TDK23	VSM	Clusters	Fe	24.5	-	-	04/04/2006
K	2/2	TDK24	VSM		Fe/N2	22.5	-	10%	07/04/2006

Batch	Batch count	Name	For	Sample Type	Materials	Fe / nm	Matrix / nm	Gas coating / mbar	Date made
L	1/5	TDK25	VSM	MBE	Ho	-	36.0	-	21/06/2006
L	2/5	TDK26	VSM	8.4%	Fe in Ho	33.1	360.0	-	27/06/2006
L	3/5	TDK27	VSM	11.5%	Fe in Ho	30.6	234.7	-	28/06/2006
L	4/5	TDK28	VSM	1.9%	Fe in Ho	30.4	1558.0	-	03/07/2006
L	5/5	TDK29	VSM	Clusters	Fe	31.0	-	-	04/07/2006
M	1/5	TDK30	XMCD	MBE	Ho	-	5.0	-	17/10/2006
M	2/5	TDK31	XMCD	8.9%	Fe in Ho	0.5	5.1	-	17/10/2006
M	3/5	TDK32	XMCD	15.1%	Fe in Ho	0.5	2.82	-	17/10/2006
M	4/5	TDK33	XMCD	40.8%	Fe in Ho	2.0	2.9	-	17/10/2006
M	5/5	TDK34	XMCD	1.9%	Fe in Ho	0.1	5.1	-	17/10/2006
N	1/5	TDK35	VSM	MBE	Ho	-	300.0	-	06/11/2006
N	2/5	TDK36	VSM	13.3%	Fe in Ho	30.1	196.7	-	09/11/2006
N	3/5	TDK37	VSM	MBE	Ho	-	472.5	-	15/11/2006
N	4/5	TDK38	VSM	25.5%	Fe in Ho	32.8	96.2	-	16/11/2006
N	5/5	TDK39	VSM	34.2%	Fe in Ho	31.2	60.0	-	27/11/2006
O	1/2	TDK40	VSM	20.0%	Fe-H2 in Ho	29.6	118.4	5x10-5	18/12/2006
O	2/2	TDK41	VSM	MBE	Fe	30.0	-	-	04/01/2007

P	1/1	GNI42	EXAFS	4%	Fe in Dy	24.0	598.0	-	08/03/07
Q	1/6	GNI43	VSM	23.5%	Fe in Dy	30.2	96.2	-	26/03/07
Q	2/6	GNI44	VSM	MBE	Dy	-	301.2	-	27/03/07
Q	3/6	GNI45	VSM	Clusters	Fe	30.9	-	-	27/03/07
Q	4/6	GNI46	VSM	10.0%	Fe MBE in Dy	30.0	270.0	-	28/03/07
Q	5/6	GNI47	VSM	8.5%	Fe in Dy	31.7	342.0	-	28/03/07
Q	6/6	GNI48	VSM	MBE	Fe	32.8	-	-	09/04/07
R	1/2	GNI49	VSM	7.6%	Fe in Ag	30.1	366.7	-	24/05/07
R	2/2	GNI50	VSM	1.6%	Fe in Dy	16.3	1023.0	-	31/05/07

Characterisation of a Gas Aggregation Source

G. N. Iles, S. H. Baker and C. Binns

Manuscript in preparation for Tech. Phys. Lett.

Fe nanoparticles in rare-earth matrices

G. N. Iles and C. Binns

Manuscript in preparation for Phys. Rev. B.

¹ *Magnetic Susceptibility of Zinc at Liquid Hydrogen Temperatures*

J. A. Marcus

Phys. Rev. 76, 3 (1949)

² *Superparamagnetism*

C. P. Bean and J. D. Livingston

J. App. Phys. 30 (1959) S120-S129

³ *Materials produced by assembling gas-phase nanoclusters*

C. Binns

Current Opinion in Solid State & Materials Science 8 (2004) 203-209

⁴ *Magic numbers in transition metal (Fe, Ti, Zr, Nb and Ta) clusters observed by time-of-flight mass spectrometry*

M. Sakurai et al

J. Chem. Phys. 111 (1999) 1

⁵ *Electronic Shell Structure and Abundances of Sodium Clusters*

W.D. Knight et al

Phys. Rev. Lett. 52 (1984) 2141

⁶ *Adsorbate-induced enhancement of the magnetic moments of iron clusters*

Mark B. Knickelbein

Chem. Phys. Letters 353 (2002) 221-225

⁷ *Magnetism of rare-earth – transition-metal nanoscale multilayers I. Experiments on Dy/Co, Dy/Fe, and Tb/Fe*

Z.S.Shan & D.J. Sellmyer

Phys. Rev. B 42 (1990) 16

⁸ *Methods of fabricating a compositionally modulated electrode in a magnetic tunnel junction device*

United States Patent 7186571

⁹ *Indirect Exchange Coupling of Nuclear Magnetic Moments by Conduction Electrons*

M. A. Ruderman and C. Kittel

Phys. Rev. 96, 99 - 102 (1954)

¹⁰ *Electrical Resistance of Ferromagnetic Metals*

T. Kasuya

Prog. Theor. Phys. 16, 45, 58 (1956)

¹¹ *Magnetic Properties of Cu-Mn Alloys*

K. Yoshida

Phys. Rev. 106, 893 (1957)

¹² *Liquid-gas transition in the spin-ice dysprosium titanate*

T. Sakakibara et al

JMMM 272-276 (2004) 1312-1313

¹³ *Spin Ice State in Frustrated Magnetic Pyrochlore Materials*

S. T. Bramwell & M. J. P. Gingras

Science 294 (2001)

¹⁴ *High-pressure magnetic susceptibility experiments on the heavy lanthanides Gd, Tb, Dy, Ho, Er and Tm*

D.D. Jackson et al

Phys. Rev. B 71, 184416 (2005)

-
- ¹⁵ *Calculations of Exchange Bias in Thin Films with Ferromagnetic/Antiferromagnetic Interfaces*
N. C. Koon
Phys. Rev. Lett. 78, 4865 - 4868 (1997)
- ¹⁶ *Superparamagnetic relaxation of Fe deposited on MgO(001)*
Y. Park et al
Phys. Rev. B 52 (1995) 17
- ¹⁷ *Spin-glass transition of a dilute Ag-Mn alloy in a magnetic field*
M.A. Novak, O.G. Symko & D.J. Zheng
Phys. Rev. B 33 (1986) 1
- ¹⁸ *Enhanced orbital magnetic moment on Co atoms in Co/Pd multilayers: A magnetic circular x-ray dichroism study*
Y. Wu et al
Phys. Rev. Lett. 69 (1992) 2307
- ¹⁹ *X-Ray Circular Dichroism as a Probe of Orbital Magnetization*
B.T. Thole et al
Phys. Rev. Lett. 68 (1992) 1943-1946
- ²⁰ *X-Ray Circular Dichroism and Local Magnetic Fields*
P. Carra et al
Phys. Rev. Lett. 70 (1993) 5
- ²¹ *Experimental Confirmation of the X-Ray Magnetic Circular Dichroism Sum Rules for Iron and Cobalt*
C.T. Chen et al
Phys. Rev. Lett. 75 (1995) 1

²² *The construction of a gas aggregation source for the preparation of size-selected nanoscale transition metal clusters*

S. H. Baker et al

Rev. Sci. Instr. 71 3178 (2000)

²³ *A compact electron-beam metal vapour source with integral cooling and shutter*

J S G Taylor & D A Newstead

J. Phys. E: Sci. Instrum. 20 1288-1289 (1987)

²⁴ *X-ray magnetic circular dichroism at the Gd L_{2,3} absorption edges in GdN layers: The influence of lattice expansion*

F. Leuenberger et al

Phys. Rev. B 73, 214430 (2006)

²⁵ *Magnetic interactions in transition metal clusters embedded in matrices prepared by LECBD technique*

V. Dupuis et al

Zeitschrift für Physik D Atoms, Molecules and Clusters 40 (1997) 155-159

²⁶ *The behaviour of nanostructured magnetic materials produced by depositing gas-phase nanoparticles*

C. Binns et al

J. Phys. D: Appl. Phys. 38 (2005) R357-R379

²⁷ *Spin and orbital magnetic moments of deposited small iron clusters studied by x-ray magnetic circular dichroism spectroscopy*

J. T. Lau et al

New Journal of Physics 4 (2002) 98.1–98.12

²⁸ *Magnetisation of Fe and Co Nanostructured Materials*

S. Louch

University of Leicester, Thesis (2005)

²⁹ *Structure and Magnetic Properties of RF sputtered Fe-N films*

Y. F. Chen et al

J. Phys. D: Appl. Phys. **37** (2004) 1429-1433

³⁰ *Nitrogen (Web Elements Periodic Table)*

M. Winter

Copyright 1993-2007 [The University of Sheffield and WebElements Ltd, UK]

³¹ *Reactions of iron clusters with hydrogen. Composition of the fully hydrogenated products*

E. K. Parks et al

J. Chem. Phys. **82** (1985) 5470-5474

³² *Covered Clusters: The Composition Of Hydrogenated Iron And Nickel Clusters*

E. K. Parks et al

J. Phys. Chem. **91** (1987) 2671-2674

³³ *Band structure theory of magnetism in 3d-4f compounds*

M. Richter

J. Phys. D: Appl. Phys. **31** (1998) 1017-1048

³⁴ *Magnetic X-Ray Scattering Studies of Holmium Using Synchrotron Radiation*

Gibbs et al

Phys. Rev. Lett. **55** (1985) 2

³⁵ *The magnetic structure of holmium: I*

Cowley and Bates

J. Phys. C: Solid State Phys. **21** (1988) 4113-4124

³⁶ *The magnetic structure of holmium: II*

Bates et al

J. Phys. C: Solid State Phys. **21** (1988) 4125-4141

³⁷ *Dynamic x-ray speckle patterns of the magnetic superstructure peak of an ultrathin Ho film*

S. Konings

konings@science.uva.nl 2007

³⁸ *Electrical and Magnetic Properties of Holmium Single Crystals*

D. Strandburg, S. Legvold and F. Spedding

Phys. Rev. **127** (1962) 6

³⁹ *Observation of transitions to spin-slip structures and splitting of the Neel temperature of holmium in magnetic fields*

Willis et al

J. App. Phys. **67** (1990) 5277-5279

⁴⁰ *Novel magnetic phases in holmium*

J. Jensen and A. R. Mackintosh

J. Mag. Mag. Mat. **104** (1992) 1481-1484

⁴¹ *Rare Earth Magnetism*

www.ill.fr/YellowBook/D10/EDIT99/experiments.html

⁴² *Magnetic phase diagram of holmium/dysprosium superlattices*

A. del Moral et al

J. Mag. Mag. Mat. **226** (2001) 1700-1701

⁴³ *Study of magnetic properties of single crystal holmium in weak magnetic fields*

Snigirev, Tishin and Volkozub

J. Mag. Mag. Mat. 94 (1991) 342-346

⁴⁴ *Tunable magnetic thermal hysteresis in transition metal (Fe, Co, CoNi)/rare earth (Gd) multilayers*

S. Demirtas et al

Phys. Rev. B 72 (2005) 184433

⁴⁵ *Second- and First-Order Phase Transitions in the Magnetic Reorientation of Ultrathin Fe on Gd*

C.S. Arnold and D.P. Pappas

Phys. Rev. Lett. 83 (1999) 16

⁴⁶ *Phase transitions in magnetic superlattices*

R.E. Camley and D. R. Tilley

Phys. Rev. B. 37 (1988) 7

⁴⁷ *Structure and reactivity of iron oxide structures*

Shaikhutdinov et al

Faraday Discuss. 114 (1999) 363-380

⁴⁸ *Some Magnetic Properties of Dy metal*

Elliott, Legvold & Spedding

Phys. Rev. 94 (1954) 5

⁴⁹ *Low-Temperature Magnetic Properties of Dysprosium Single Crystals*

R. G. Jordan and E. W. Lee

Proc. Phys. Soc. (1967) 92

⁵⁰ *Field-induced Magnetic Phase Transitions in Dysprosium*

R. Herz and H. Kronmuller

JMMM 9 (1978) 273 – 275

⁵¹ *Magnetisation of a Spiral Spin System*

D.M.S. Bagguley and F.A. Howe

JMMM 58 (1986) 191-201

⁵² *The magnetic phase diagrams of dysprosium*

A. V. Andrianov, Yu.P. Gaidukov, A. N. Vasil'ev

JMMM 97 (1991) 246-250

⁵³ *Magnetic order in Dy/Lu superlattices*

R.S. Beach et al

JMMM 104-107 (1992) 1915-1917

⁵⁴ *Shifts of Curie temperature of epitaxial dysprosium films*

C. Dufour et al

JMMM 156 (1996) 425-426

⁵⁵ *Investigations of the first order magnetic phase transition in dysprosium*

S. Chaudhary, P. Garg and S. Rajput

Solid S. Comm. 132 (2004) 293-297

⁵⁶ *Novel Thermal Effects at the First Order Magnetic Phase Transition in Erbium, and a Comparison with Dysprosium*

K. A. Gschneider, Jr. and V. K. Pecharsky

Phys. Rev. Lett. 78 (1997) 22

⁵⁷ *Magnetic Properties and Structures of the Rare Earth Compounds $\text{FNi}_{1-x}\text{Cu}_x$ with the FeB-type structure*

D. Gignoux and J.C. Gomez-Sal

JMMM 1 (1976) 203-213

⁵⁸ *Structure and Magnetic Domain Walls of Dy Ion Implanted Fe Films*

S. Tsukahara, T. Kanayama and H. Tanoue

JMMM 35 (1983) 319-322

⁵⁹ *Novel structural phases of Dy thin films on W(1 1 2)*

N. Moslemzadeh, S.D. Barrett and J. Ledieu

Surface Science 600 (2006) 559–564

⁶⁰ *Fe (Web Elements Periodic Table)*

Mark Winter

Copyright 1993-2007 [The University of Sheffield and WebElements Ltd, UK]

⁶¹ *Low-field susceptibilities of rare earth spin glass alloys: The role of single-ion anisotropy*

B.V.B. Sarkissian

J. Phys. F: Metal Phys. 7 (1977) 5

⁶² *Spin-glass transition in MnO*

J. J. Hauser & J. V. Waszczak

Phys. Rev. B 30 (1984) 9

⁶³ *Electric, Magnetic and Photomagnetic Properties of the Amorphous Metallic Spin-Glass $\text{Ni}_3(\text{SbTe}_3)_2$*

J-S Jung, L. Ren & C.J. O'Connor

J. Mater. Chem. 2(8) (1992) 829-832

⁶⁴ *The dysprosium-transition-metal interaction in Dy(Co,Ni)₁₀Si₂ compounds*

N. Tang et al

JMMM 157/158 (1996) 397-398